Simultaneous Measurement of Fluctuating Velocity and Pressure in Complex Turbulent Shear Flow Associated with Large-Scale Vortex Structure

Thesis submitted for the degree of Doctor of Philosophy
August 2014

Takuya Kawata

School of Science for Open and Environmental Systems

Graduate School of Science and Technology
Keio University

Acknowledgements

A part of this research was financially supported by Japan Society for the Promotion of Science (JSPS), Grant-in-Aid for JSPS Fellows, 23-3679, 2011, and the Global COE program, Center for Education and Research of Symbiotic, Safe and Secure System Design, from the Ministry of Education, Culture, Sport and Technology of Japan.

I wish to express deepest gratitude to my supervisor, Professor Shinnosuke Obi, whose encouragement and support with constructive advices I greatly appreciate.

I appreciate Professors Toshihisa Ueda, Koichi Hishida, and Koji Fukagata for invariable discussions that have remarkably improved quality of this thesis. Especially, I would like to thank Professor Koji Fukagata for his helpful suggestions through the discussions at weekly seminars of the Obi-Fukagata laboratory. I also appreciate Dr. Yoshitsugu Naka for his many advices about my research topic and, particularly, for helping me to conduct experiment when I was an undergraduate and master course student. In addition, I have a great sense of appreciation to Professor Kuniaki Toyoda of Hokkaido Institute of Technology for giving me many substantial advices about fluctuating pressure measurement.

I also would like to thank the members of the Obi-Fukagata laboratory. Especially, I appreciate Dr. Hiroya Mamori, Dr. Takashi Naito, Dr. Yukinori Kametani, Fuminori Hioki, Alex Jhon Sepnov, and Nguyen Hai Long not only for meaningful discussions about research topics, but also for many funny daily conversations that have made my study life in the laboratory enjoyable. Of course, I do appreciate my family for supporting me all the time.

Abstract

In the present thesis, the following three contributions are made aiming at further development of techniques for simultaneous measurement of fluctuating velocity and pressure in complex turbulent flow:

- Validation of an existing measurement technique
- Development of a new technique for simultaneous velocity and pressure measurement in a three-dimensional turbulent flow
- Development of a hybrid method of direct pressure measurement by static-pressure probes and particle image velocimetry (PIV)

In the first topic, applicability of an existing measurement technique, in which a static-pressure probe and a hot-wire probe are combined, was examined by a quantitative comparison with reference data obtained by a numerical simulation. Experimental results of the pressure-related statistics were in quantitatively good agreement with the computational results and reliability of the existing measurement technique was confirmed. In the second topic, a new probe system comprising a triple-sensor hot-film probe and a total-pressure probe was developed for measurement in three-dimensional turbulent flows, and a wingtip vortex flow was chosen for the test case. All components of the velocity-pressure correlation were successfully measured, and contribution of the velocity-pressure correlation to turbulence transport was found to be significant. In the third topic, a hybrid method of direct pressure measurement by static-pressure probes and PIV was developed. Instantaneous pressure field was numerically evaluated based on the PIV data and the fluctuating pressure directly measured by the static-pressure probe was used as a reference signal for the PIV-based pressure evaluation. The pressure-related statistics were successfully measured in a wake immediately behind a circular cylinder, and they were found to play an important role in turbulence transport.

Contents

3 Validation of Measurement Technique by Combination of Hot-Wire Probe and Static-Pressure Probe 23

4 Simultaneous Measurement of Three Velocity Components and Pressure in Three-Dimensional Turbulent Flow 55

List of Figures

List of Tables

Nomenclature

Roman Symbols

A	Amplitude ratio
B	Fourier coefficient of fluctuating pressure
$\hat{B}$	Corrected Fourier coefficient
C	In Chaps. 2 and 5: elastic compliance of pressure sensor, in Chap. 3 : capacitance of condenser microphone
$C_{ij}, D^v_{ij}, D^t_{ij}, D^p_{ij}, P_{ij}$	Convection, molecular diffusion, turbulent-diffusion, pressure-diffusion, and production rate of Reynolds stress $\overline{u_i u_j}$
$C_k, D^v_k, D^t_k, D^p_k, P_k$	Convection, molecular diffusion, turbulent-diffusion, pressure-diffusion, and production rate of turbulent kinetic energy
C_p	Pressure coefficient
coh	Coherence
D	Diameter of circular cylinder
d	Outer diameter of SP-probe
E_a	Output voltage of CTA
Er	Systematic error caused by temperature drift of output of CTA
F_u	Flatness factor of streamwise velocity fluctuation
f	Frequency
I	Inertance of fluid inside pressure-measuring system

$\mathcal{I}$	Imaginary part of complex quantity
K	Bulk modulus of fluid inside pressure cavity of pressure transducer
k	Turbulent kinetic energy
L_1,L_2	Length of static-pressure probe
l	Length of thin tube in analytical model of pressure-measuring model
P	Mean static-pressure
p	Static-pressure fluctuation
p_m	Fluctuating pressure measured by pressure transducer
p_s	In Chaps. 2 and 5: true value of fluctuating pressure at pressure source, in Chap. 4: static-pressure fluctuation indirectly evaluated from directly measured total- and dynamic-pressure fluctuations
p_t	Total-pressure fluctuation
Q	Volumetric flow rate entering pressure cavity of pressure transducer
Q_X	Symmetric matrix for POD analysis
Re	Reynolds number
R	In Chaps. 2 and 5: fluid resistance of pressure-measuring system, in Chap. 3, input resistance of pre-amplifier
R_{ab}	Correlation coefficient between fluctuating quantities a and b
$\mathcal{R}$	Real part of complex quantity
S	In Chap. 2 and Chap. 5:Cross-sectional area of thin tube in analytical model of pressure-measuring system, in Chap. 6: Source term of discretized Poisson equation for pressure
S_{ab}	Cross spectrum between a and b
S_k	Precision index of X_k
S_t	Strouhal number

S_u	Skewness factor of streamwise velocity fluctuation
T_a,T_0	Atmosphere temperature in calibration of hot-wire probe and that during measurement
T_w	Temperature of sensor wire of X- and THF-probe
U_i	Mean velocity
Uc	Convection velocity of disturbance
U_∞	Free stream velocity
$\mathbf{u}$	Velocity vector
u, v, w	fluctuation of velocity component
$\overline{u_iu_j}$, $\overline{u^2}$, $\overline{v^2}$, $\overline{w^2}$, $\overline{uv}$,$\overline{uw}$,$\overline{vw}$	Reynolds stress
V_{ol}	Volume of pressure cavity of pressure transducer
V_t	Magnitude of mean velocity vector
v_t	Fluctuation of magnitude of mean velocity vector
X	Data matrix for POD analysis
X_k	Arbitrary statistical quantity
x_i	Axis in i-direction of Cartesian coordinates
x, y, z	Cartesian Coordinate in streamwise, transverse and spanwise directions

Greek Symbols

α	Over-heat ratio of CTA
α_0	Temperature coefficient of CTA
$\Delta\theta$	Phase lag
Δx	Streamwise distance between hot-film probe and TP-probe
Δx, Δy, Δz	Measuring-point spacing in x-, y- and z-direction
Δz	Spanwise distance between X-probe and SP-probe

ε_{ij}	Dissipation rate of Reynolds stress $\overline{u_i u_j}$
ε_k	Dissipation rate of turbulent kinetic energy
η_k	POD base of streamwise velocity component
γ_k	kth eigen vector in POD anaylis
Λ	Integral length scale
λ_k	kth eigen value in POD analysis
μ	Molecular viscosity
ν	Kinetic viscosity
Ω	Intermittency factor defined as $\Omega = 3/F_u$
ω	Angular frequency
ω_n	Natural frequency of pressure-measuring system
ϕ	In Chap. 2: arbitrary quantity, in Chaps. 3-6: angle of attack of flow
ϕ_{ij}	Redistribution of Reynolds stresses
ϕ_k	POD base of streamwise pressure gradient
Π_{ij}	Velocity pressure-gradient correlation
ψ_k	POD base of transverse pressure gradient
ρ	Density
τ	Time lag between velocity and pressure signals
θ	Phase
ξ_k	POD base of transverse velocity component
ζ	Damping factor of pressure-measuring system

Superscripts

$[]^*$	Non-dimensionalized quantities

$[]'$	Root-mean-square value of fluctuating quantities

Subscripts

$[]_1,[]_2$	Quantity measured by main and reference condener microphone in calibration of dynamic response
$[]_{\mathrm{cor}}$	Corrected values
$[]_{ijk}$	Indexing subscripts
$[]_k$	Quantity of kth POD mode
$[]_{\mathrm{lut}}$	Velocity evaluated based on look-up-table
$[]_{\mathrm{pitot}}$	Velocity measured by Pitot tube in calibration
$[]_{\mathrm{spp}}$	Value directly measured by SP-probe
$[]_{t_n}$	Quantities measured at $t = t_n$
$[]_{\mathrm{true}}$	True value of velocity components in calibration

Other Symbols

$\overline{[]}$	Averaged quantity
$\tilde{[]}$	Instantaneous quantity
$\hat{[]}_m$	Quantities reconstructed based on first m POD modes

Acronyms

CTA	Constant Temperature Anemometer
DIA	Direct Interaction Approximation
DNS	Direct Numerical Simulation
EDQNM	Eddy-Damped Quasi-Normal Markovian
EVM	Eddy-Viscosity Model
LDV	Laser Doppler Velocimetry

LES	Large Eddy Simulation
NLEVM	Non-Linear Eddy-Viscosity Model
PDF	Probability Density Function
PIV	Particle Image Velocimetry
POD	Proper Orthogonal Decomposition
PSD	Power Spectral Density
PTV	Particle Tracking Velocimetry
RANS	Reynolds Averaged Navier-Stokes
RNG	Renormalizaton Group
RSM	Reynolds Stress Model
SP-probe	Static-pressure probe
THF-probe	Triple-hot-film probe
TP-probe	Total-pressure probe
TSDIA	Two-Scales Direct-Interaction Approximation
X-probe	X-type hot-wire probe

Chapter 1

Introduction

1.1 Background

1.1.1 Turbulent Flow and Its Coherent Structure of Vortices

Turbulent flow is found in many practical engineering problems, such as inside a pipeline for transport of fossil fuel, around a vehicle moving in air, and inside a turbomachinery such as a gas turbine and a jet engine. Understanding, predicting, and controlling turbulent flow have been important research targets in engineering research field, because the nature of turbulence that it enhances fluid mixing leads to many important consequences such as increase of skin friction drag, suppression of flow separation, and enhancement of heat transfer, all of which are strongly related to energy problems.

Although the turbulent flow has been a research topic to be concerned by engineers, physicists, and mathematicians over more than 100 years, the phenomenon has still not been fully understood. Due to strong non-linearity of the Navier-Stokes equation, it is impossible to derive analytical solution under the turbulent flow condition, and the statistical theories developed so far, such as the eddy-damped quasi-normal Markovian (EDQNM, Orszag, 1970; Tatsumi et al., 1978), the direct interaction approximation (DIA, Kraichnan, 1959), and the renormalization group closure (RNG, Smith and Woodruff, 1998), are applicable only to the ideal isotropic turbulence. The direct numerical simulation (DNS) of a practical turbulent flow with a high Reynolds number is still unrealizable in terms of computational cost despite the recent rapid growth of computational power.

Important feature of turbulent flow is that it consists of a huge number of vortices with a wide range of length scales. The non-linear term in the Navier-Stokes equation physically represents interaction between these vortices, by which small vortices are produced from larger vortices. The gap between the smallest and largest length scales of vortices becomes larger as the Reynolds number increases, and those vortices with various length scales compose a structure with a certain coherence, so called *coherent vortex structure*.

The coherent vortex structure has been observed in many turbulent flows. For example, it is well known that there are organized structures of quasi-streamwise vortices with relatively large length scale (with a diameter of about 25-30 wall-units and a streamwise length of about 150-300 wall-units) in the buffer layer of wall turbulence (e.g., Jeong et al., 1997; Kasagi et al., 1995; Kim et al., 1987; Kline et al., 1967; Smith and Metzler, 1983), and they are responsible to the production of the turbulent kinetic energy and the Reynolds shear stress (e.g., Kida and Yanase, 1999; Robinson, 1991b). In addition, a larger structure than those in the buffer layer appears in the very high-Reynolds-number flows (Adrian et al., 2000; Iwamoto et al., 2005).

Coherent vortex structures have been also investigated in turbulent shear flows (e.g., Hussain and Hayakawa, 1987; Mumford, 1982). In the turbulent mixing layer, the large-scale vortices caused by the Kelvin-Helmholtz instability, so called *roller vortices*, can be observed, and they contain smaller-scale streamwise vortices, so called *rib vortices*, that are produced from the rib vortices by the non-linear vortex interaction (e.g., Brown and Roshko, 1974). A similar vortex structure is found in the vortex street of turbulent wake of bluff bodies (e.g., Bernard and Wallace, 2002).

These coherent structures of vortices greatly affect transport phenomenon in turbulent flow and result in the aforementioned important engineering problems: for example, the quasi-streamwise vortices in the wall turbulence transport the high-speed fluid away from the wall to the wall vicinity, which results in increase of skin friction and heat transfer on the wall. A massive flow separation and subsequent vortex shedding are often found in the turbulent free shear flows such as the wake of bluff bodies, and they result in lift fluctuation and sound-noise generation. Thus, the existence of the coherent large-scale vortex structure in turbulent flow is closely related to several engineering problems, and investigation on such vortex structures is important, for example, to develop an effective flow controlling scheme.

Furthermore, investigating the turbulent vortex structure is also important to develop a method for numerical simulation of the practical engineering turbulent flows with a quite high Reynolds number. In such high-Reynolds-number flows, the vortex structures in the near wall region is so small that a quite heavy computational cost is required to resolve them even by the large-eddy simulation (LES). In order to predict such flows, incorporating the turbulence models based on the Reynolds-Averaged Navier-Stokes equation (RANS) is useful, and the hybrid RANS-LES approaches have been extensively studied in recent years (e.g., Haase et al., 2009). Further development in turbulence models enable us to simulate the high-Reynolds-number turbulent flows by less computational cost, and detailed information of vortex structures in the high-Reynolds-number turbulent flow is necessary to further develop the turbulence models.

1.1.2 Investigation on Coherent Vortex Structure

Up to now, a great number of both experimental and computational studies have been devoted to investigation of the coherent structure in turbulent flow. In the early stage of this topic, the vortex structures were observed by means of experimental techniques, such as flow visualization, multi-point correlation measurement, and conditional averaging of fluctuating velocity (some reviews are available: e.g., Cantwell, 1981; Ho and Huerre, 1984; Hussain, 1983; Hussain and Zaman, 1987).

The DNS has been recently used for study of the coherent turbulence vortex structure, as it can provide instantaneous three-dimensional fields of fluctuating velocity and pressure without introducing any turbulence model. Especially, the DNS has been playing a significant role in the recent studies on the vortex structures in the wall turbulence (e.g., Jeong et al., 1997; Kim et al., 1987; Schoppa and Hussain, 2002), and several models of the mechanism of streamwise vortex generation have been proposed based on those information provided by the DNS studies (e.g., Robinson, 1991a).

The turbulent flows intensively investigated by the DNS up to now are, however, the canonical flows with a relatively low Reynolds number and a simple geometry, and it still requires extremely heavy computational cost to investigate the practical turbulent flows with a quite high Reynolds number and a complex geometry by means of the DNS. Although large-scale DNSes of the wall turbulence using a super computer have been recently performed (e.g., Hoyas and Jimenez, 2006; Iwamoto et al., 2005; Schlatter and Örlü, 2010), the flow fields investigated in these studies are also the canonical flow with simple geometries. Therefore, experimental investigation will be important to further explore the vortex structures of the turbulent flows with quite high Reynolds number and complex geometries.

1.1.3 Importance of Fluctuating Pressure Measurement for Investigation on Vortex Structure

Fluctuating pressure is closely related to the large-scale vortex motions. The helical motion of fluid in the large vortices results in low-pressure region in the vortex core, and the motion of those vortices produces strong pressure fluctuation as well as velocity fluctuation. Mathematically, the Laplacian of pressure is, for incompressible turbulent flow, equivalent to the second invariant of the velocity-gradient tensor (so-called *Q value*), which is the criteria most widely used to visualize the vortex structure. In terms of experimental investigation, it may be easier to use the pressure information than the Q values, because the pressure is a scalar quantity while all components of the velocity-gradient tensor are required to calculate the Q value. In fact, eduction of the vertex structure based on the fluctuating pressure measurement was performed in some earlier studies (e.g., Sakai et al., 2007; Toyoda et al., 1994).

Interaction between fluctuating pressure and velocity fields is the other important aspect of the flow field associated with the coherent vortex structure. Motion of the organized structure of large-scale vortices results in a significant correlation between the fluctuating velocity and pressure fields. Especially, the velocity-pressure correlation and the pressure strain-rate correlation are closely related to turbulence transport process caused by the large-scale vortices, as they appear in the transport equation of the Reynolds stress as the *pressure diffusion* and *redistribution* terms, respectively; the pressure diffusion represents the turbulence transport driven by the pressure fluctuation, and the redistribution does the energy exchange between different components of the Reynolds stresses.

In particular, the pressure diffusion often plays a significant role in the transport equation of the turbulent kinetic energy or the Reynolds stress in the flow regions associated with the large-scale vortex motion (e.g, Johansson and Andersson, 2005; Yao et al., 2001). As these flow regions are those where the conventional RANS-based turbulence models often fail in accurate prediction, appropriately modeling the pressure diffusion might significantly improve the performance of the RANS-based turbulence models.

Thus, investigating interaction between the fluctuating velocity and pressure is indispensable to understand the turbulence transport phenomena caused by the coherent vortex structure. However, knowledge about the pressure fluctuation is still rare partly because of absence of a sophisticated technique for fluctuating pressure measurement.

Further development in measurement techniques, especially for simultaneous measurement of fluctuating velocity and pressure, is desired.

1.2 Earlier Studies on Simultaneous Measurement of Fluctuating Velocity and Pressure

Techniques for simultaneous measurement of fluctuating velocity and pressure is still under development. The technical difficulties mainly underlie fluctuating pressure measurement at arbitrary positions in turbulent flow. Up to now, some measurement techniques were proposed such as direct measurement technique using a hot-wire probe and a miniature Pitot tube and numerical evaluation of pressure field based on measurement data of PIV. But each of them has both advantages and disadvantages, and still has room for further improvement. In the following, earlier works for the velocity-pressure correlation measurement are summarized.

1.2.1 Direct Measurement Technique

Simultaneous measurement of velocity and pressure in turbulent flow has been attempted since 1950s. Technical difficulties was mainly underlying in fluctuating pressure measurement at an arbitrary point remote from the wall in turbulent flow. In order to capture static-pressure fluctuation, it is inevitable to use a pressure probe such as the Pitot tube, intrusive nature of which might results in serious contamination on measurement. Many possible sources of measurement error were pointed out by Fuchs (1972) and George et al. (1984) and, thus, fluctuating pressure measurement using a pressure probe was considered extremely difficult, in contrast with fluctuating wall-pressure measurement, which has become a popular technique in turbulence research; the point measurement using a pressure tap on the wall has become a standard technique (Eckelmann, 1989; Willmarth, 1975), and the surface measurement by pressure-sensing paint (PSP) is also being intensively studied (e.g., Klein et al., 2005; MacLachlan et al., 1993; Tropea et al., 2007).

1.2.1.1 Combination of static-pressure probe and hot-wire anemometry

Kobashi (1957) and Kobashi et al. (1960) overcame such technical difficulties in fluctuating pressure measurement by developing a miniature Pitot-tube-type probe, and they conducted measurement using a condenser microphone as a pressure sensor. They combined this pressure measurement technique with a hot-wire anemometry and investigated the velocity-pressure correlation in a wake of a circular cylinder, for the first time.

On the Basis of the pioneering work by Kobashi (1957) and Kobashi et al. (1960), Shirahama and Toyoda (1993) and Toyoda et al. (1994) further optimized geometrical configuration of the static-pressure probe. The pressure probe has a circular cone on its tip and the outer- and inner-diameter of the tube were 1.0 mm and 0.8 mm, respectively. A condenser microphone for a pressure sensor was directly embedded in a joint part of the pressure probe, and nearly flat frequency response of the pressure probe up to 2 kHz was achieved. Using this measurement technique, Shirahama and Toyoda (1993) and Toyoda et al. (1994) successfully investigated the velocity-pressure correlation and the coherent vortex structure in an oscillated noncircular jets.

Inspired by the successful measurement by Shirahama and Toyoda (1993) and Toyoda et al. (1994), the pressure probe of the same type was adopted in some experimental studies, e.g., investigating scaling law of pressure fluctuation (Tsuji et al., 2007; Tsuji and Ishihara, 2003) and source of acoustic sound noise (Iida et al., 1999).

Simultaneous measurement of velocity and pressure using the pressure probe of the same type with a hot-wire anemometry was also performed. Naka et al. (2006) combined a miniature static-pressure probe with an X-type hot-wire probe and measured the velocity-pressure correlation in a turbulent planer mixing layer, and pointed out that the measured profiles of the velocity-pressure correlation agree with those evaluated from the velocity triple-correlation based on the classical model for the velocity-pressure correlation proposed by Lumley (1978) in the flow region with equilibrium state, but disagree in the flow region out of equilibrium state.

Sakai et al. (2007) also performed simultaneous measurement of fluctuating pressure and velocity to investigate vortex structure in the self-preserving region of a plane jet. They used a semiconductor pressure transducer in order to capture pressure fluctuation in low frequency range and a static pressure probe with eight pressure-sensing holes following Ishida et al. (1995).

In the measurement techniques mentioned above, a hot-wire probe and static-pressure probe are placed adjacent to each other, and both the fluctuating pressure and velocity are measured directly. In such probe system, certain spatial distance is between the probes in order to avoid the probe interference, which results in low spatial resolution.

1.2.1.2 Improvement of spatial resolution

Naka and Obi (2009) and Naka (2009) improved the spatial resolution of the measurement technique used by Naka et al. (2006) by using a miniature total-pressure probe instead of the static-pressure probe, the idea of which was based on the measurement technique developed by Giovanangeli (1988) and Nasseri and Nitsche (1991). The fluctuating velocity and total pressure were simultaneously measured, and the static-pressure fluctuation was indirectly evaluated from the dynamic and total pressure. In the proposed probe arrangement, the tip of the total-pressure probe was inserted into the measurement volume of the hot-wire probe. Hence, the spatial resolution was equivalent to that of single use of the hot-wire probe, which was much improved as compared to combination of the hot wire- and the static-pressure-probes. Furthermore, the measurement by the total-pressure probe is less affected by the cross flow compared to that by the static-pressure probe.

1.2.1.3 Problems in the direct measurement technique

As described above, some technique for simultaneous velocity-pressure measurement by combination of a hot-wire probe and a pressure probe have been performed, and a certain amount of data has been provided. However, the measurement by these techniques is limited to sing-point measurement, and they cannot be applied to three-dimensional flows as velocity measurement by an X-type hot-wire probe may be contaminated by error caused by the out-of-plane velocity component.

Furthermore, due to the nature of direct measurement by probe, both the hot-wire probe and the pressure probe have limitation in measuring range of angle of attack of the velocity vector to the probe axis. Therefore, the direct measurement techniques cannot be applied to flow regions where the instantaneous flow direction has too large angle of attack to the probe axis, such as flow regions with quite high turbulent intensities or the recirculation region.

In addition, validity of the measurement results by these techniques has not been examined enough. There are quite few studies in which the validity of the measurement results was addressed by quantitative comparison with reference data provided by, for example, numerical simulation (as long as the author knows, only Naka et al., 2006; Tsuji and Ishihara, 2003). Even the validations in these earlier studies were conducted in the self-preserving region in the free shear flows, where the turbulence intensity is rather moderated. However, the flow region where the velocity-pressure correlation plays a significant role is often out of the equilibrium state and associated with the relatively large lateral velocity fluctuation due to the large-scale vortex motion, and the applicability of this measurement technique should be further investigated in such flow region.

1.2.2 Numerical Evaluation of Instantaneous Pressure Field Based on PIV Measurement Results

Mathematically, pressure and velocity are not independent valuable from each other, but related by the Navier-Stokes equation or the Poisson equation for pressure, as will be described in Chap. 2. Hence, it is possible to derive pressure from velocity if one has enough information of velocity field, such as temporal and spatial gradient of instantaneous velocity distribution.

With this concept, some attempts to numerically evaluate pressure field form velocity measured by a particle image velocimetry (PIV) have been made since the late 1990s. Increase of capabilities of the PIV has extended application of the derivation of pressure based on PIV data from evaluation of two-dimensional steady pressure field (e.g., Baur and Köngeter, 1999; Fujisawa et al., 2004; Gurka et al., 1999) to that of instantaneous pressure field. Hosokawa et al. (2003) applied the pressure evaluation based on the PIV measurement to two phase flow, and evaluated the pressure distribution around a bubble. Fujisawa et al. (2005) evaluated fluid force acting on a rotating circular cylinder by applying the PIV-based pressure evaluation, and investigated enhancement/reduction of the fluid force. Obi and Tokai (2006) applied this technique to an oscillatory flow between two bluff bodies and investigated contribution of the velocity pressure-gradient correlation to the transport of the Reynolds stresses. Ishii et al. (2008) performed pressure field evaluation based on a stereoscopic PIV in a turbulent wingtip vortex flow and evaluated the pressure-related statistics produced by unsteady meandering motion of the wingtip vortex.

A number of contribution has been devoted to improvement of the PIV-based pressure evaluation; some numerical techniques to derive pressure field from the PIV data were developed such as direct integration of pressure gradient based on the Navier-Stokes equation (Baur and Köngeter, 1999; Liu and Katz, 2006), solving the Poisson equation for pressure (e.g., De Kat and van Oudheusden, 2012; Hosokawa et al., 2003) and the Lagrangian approach to evaluate the material derivative (Violato et al., 2011). Charonko et al. (2010) compared various numerical techniques mentioned above and assessed the effect of different numerical approach used for pressure evaluation, spatial resolution of the PIV measurement and filtering methods.

In particular, recent increase of capabilities of the PIV technique toward the time-resolved three-dimensional measurement, e.g., tomographic PIV (Elsinga et al., 2006), enabled us to derive pressure field without omitting any terms in the Navier-Stokes equation or the Poisson equation for pressure. De Kat and van Oudheusden (2012) performed evaluation of the instantaneous pressure field behind a square cylinder comparing the results obtained by a time-resolved planer PIV and a time-resolved tomographic PIV, and demonstrated the advantages of taking into account the out-plane component of the instantaneous velocity gradient. Ghaemi et al. (2012) applied the pressure evaluation based on a time-resolved tomographic-PIV to a turbulent boundary layer flow, and investigated relation between the vortex structure in the boundary layer and the pressure fluctuation. Pröbsting et al. (2013) also performed instantaneous pressure-field evaluation and investigated relationship between the wall-pressure fluctuation and the pressure fluctuation caused by vortex structure near the wall. A review of recent development on the PIV-based pressure evaluation including those by the time-resolved three-dimensional PIV measurement is available in (van Oudheusden, 2013)

The PIV-based pressure evaluation is quite useful to investigate the pressure-related statistics not only the velocity-pressure correlation but also the pressure-strain correlation as both the instantaneous pressure and velocity field are simultaneously obtained. Moreover, thanks to the non-intrusive nature of the PIV measurement, this method can be applied to flow regions where the direct measurement technique cannot be used.

Despite such great advantages, there remain issues of the PIV-based pressure evaluation that need to be further addressed, such as specification of the boundary condition. Information of velocity primarily gives the Neumann-type boundary condition as the pressure gradients are supplied by evaluating the terms in the momentum equation, while some extra efforts are required to identify the Dirichlet-type boundary condition; the most straightforward way is to directly measure the pressure in the PIV measurement domain, which has never been attempted in earlier studies (at least, to the best of the authors$'$ knowledge) partly due to the technical difficulties in measuring fluctuating pressure. Alternatively, in some of the earlier studies, the pressure on the boundary was estimated from the measured velocity data by assuming a potential flow or a steady flow (e.g., De Kat and van Oudheusden, 2012; Ghaemi et al., 2012).

The PIV-based pressure evaluation has another shortcoming, in that the pressure evaluation is easily affected by the noise involved in PIV data (Charonko et al., 2010; De Kat and van Oudheusden, 2012). The equation used to derive pressure, such as the Poisson equation for pressure, contains spatial and temporal derivatives of instantaneous velocity, the evaluation of which amplifies the effect of the measurement noise in PIV data. Thus, the direct single-point measurement by the pressure probe still has advantages over the PIV-based pressure evaluation, although it also has the aforementioned limitations. Therefore, it may be possible to further improve quality of simultaneous measurement of fluctuating velocity and pressure by the PIV-based pressure evaluation with the direct pressure measurement by the pressure probe.

1.2.3 Other Possible Measurement Techniques

For other possibility of simultaneous measurement of instantaneous velocity and pressure field, use of PSP coated particles has been proposed (Abe et al., 2004; Kimura et al., 2006, 2010). This method can be quite useful method for direct simultaneous measurement of velocity and pressure field, but still under development.

1.3 Scope and Objectives of the Present Thesis

The present thesis aims at following three targets:

- Assessment of reliability of the direct measurement technique, in which a miniature static-pressure probe is combined with a hot-wire probe
- Development of a technique for simultaneous measurement of all three velocity components and fluctuating pressure in three-dimensional turbulent flow
- Development of hybrid method of direct single-point measurement by static-pressure probes and the PIV-based pressure evaluation

For the first target, the measurement technique where an X-type hot-wire probe and a miniature static-pressure probe are combined was applied to a relatively near region of wake of a circular cylinder. Several pressure probes with different diameters and lengths were used to investigate the effect of geometrical configuration of static-pressure probe, and the validity of the measurement results was addressed by a quantitative comparison with reference data obtained by a numerical simulation. This will be described in Chap. 3.

For the second, a technique for simultaneous measurement of three velocity components and fluctuating pressure was newly developed on the basis of the technique developed by Naka and Obi (2009) and Naka (2009). A triple-sensor hot-film probe and a miniature total pressure probe were combined, and the static-pressure fluctuation was evaluated from the directly measured velocities and total pressure fluctuation. Calibration technique to take into account the effect of probe interference was developed, and the measurement technique was applied to three-dimensional turbulent flow, a turbulent wingtip vortex. This will be described in Chap. 4.

For the third target, a technique for fluctuating pressure measurement in water was developed at first so that it could be combined with the house-made PIV system for measurement in water. This will be described in Chap. 5. In Chap. 6, a hybrid method of the direct measurement and the PIV-based pressure evaluation is described. Instantaneous pressure field was numerically evaluated from the PIV data, and the fluctuating pressure directly measured by the static-pressure probe was used as a reference signal for the PIV-based pressure evaluation. The simultaneous measurement of velocity and pressure was performed in the very near wake of a circular cylinder, and the pressure-related statistics in the flow region immediately behind the cylinder, inside and near the recirculation region, were experimentally investigated.

Chapter 2

Theoretical Considerations

2.1 Governing Equations

2.1.1 Governing Equations for Instantaneous Flow Field

Throughout this thesis, we handle only incompressible flow of Newtonian fluid. The governing equations are the continuity equation and the equation of motion, which is called the Navier-Stokes equation:

$$\nabla \cdot \tilde{\mathbf{u}} = 0, \tag{2.1}$$

$$\rho \left(\frac{\partial \tilde{\mathbf{u}}}{\partial t} + (\tilde{\mathbf{u}} \cdot \nabla)\, \tilde{\mathbf{u}} \right) = -\nabla \tilde{p} + \mu \nabla^2 \tilde{\mathbf{u}}, \tag{2.2}$$

where $\tilde{[\,]}$ stands for the instantaneous quantities, $\mathbf{u}$ and p represent velocity vector and pressure, and ρ and μ stand for density and viscosity of the fluid, respectively. In the Cartesian coordinates, the continuity equation and the Navier-Stokes equation are written as

$$\frac{\partial \tilde{u}_i}{\partial x_i} = 0, \tag{2.3}$$

$$\rho \left(\frac{\partial \tilde{u}_i}{\partial t} + \tilde{u}_j \frac{\partial \tilde{u}_i}{\partial x_j} \right) = -\frac{\partial \tilde{p}}{\partial x_i} + \mu \frac{\partial \tilde{u}_i}{\partial x_j x_j}, \tag{2.4}$$

with x_i and $\tilde{u}_i$ representing i-th axis of the Cartesian coordinates and instantaneous velocity component in x_i-direction, respectively. The first and second terms in the right-hand-side of Eq. (2.4) represent contribution by pressure gradient and viscosity, respectively. The left-hand-side of Eq. (2.4) has a non-linear tem which represents acceleration along the streamline. Although the equation system comprising Eqs. (2.3) and (2.4) is closed, it is impossible to solve this equation system under the turbulent flow condition mainly due to the nonlinearity of the Navie-Stokes Equation (2.4).

For seeing the relationship between pressure and velocity, it may be more convenient to derive an equation which relates velocity to pressure. Taking divergence of the Navier-Stokes equation Eq. (2.4) and using the continuity equation Eq. (2.3), one can also obtain the Poisson equation for instantaneous pressure:

$$\frac{\partial^2 \tilde{p}}{\partial x_i^2} = -\rho \frac{\partial \tilde{u_j}}{\partial x_i} \frac{\partial \tilde{u_i}}{\partial x_j}. \tag{2.5}$$

As the terms in the right-hand-side of this equation consists of only the velocity, the pressure can be obtained from the velocity field using this equation Eq. (2.5). As Eq. (2.5) is an elliptic equation, it is indicated that the pressure is not determined by local information but affected by the entire velocity field.

2.1.2 Governing Equations for Reynolds-Averaged Flow Fields

2.1.2.1 Reynolds-averaged Navier-Stokes equation

To derive the equations for averaged quantities, instantaneous value of an arbitrary quantity ϕ are divided into averaged part and fluctuation from it as

$$\tilde{\phi} = \Phi + \phi. \tag{2.6}$$

This procedure is called *Reynolds decomposition*, and the capital and small letters in Eq. (2.6) stand for the averaged and fluctuating quantities, respectively.

By applying Eq. (2.6) to Eqs. (2.3) and (2.4) and taking average, one obtains the continuity equations for averaged and fluctuating velocity components as:

$$\frac{\partial U_i}{\partial x_i} = 0, \tag{2.7}$$

$$\frac{\partial u_i}{\partial x_i} = 0. \tag{2.8}$$

In the same manner, the Reynolds Averaged Navier-Stokes (RANS) equation is obtained as

$$\rho \left(\frac{\partial U_i}{\partial t} + U_j \frac{\partial U_i}{\partial x_j} \right) = -\frac{\partial P}{\partial x_i} + \frac{\partial}{\partial x_j} \left(\mu \frac{\partial U_i}{\partial x_j} - \rho \overline{u_i u_j} \right). \tag{2.9}$$

The additional term $\overline{u_i u_j}$ appears in the second term of the right-hand-side, which is called *Reynolds stress* and represents the effect of velocity fluctuation on the mean velocity field. The Poisson equation for the mean pressure also can be obtained by applying the same procedure to Eq. (2.5) as

$$\frac{\partial^2 P}{\partial x_i^2} = -\rho\left(\frac{\partial U_i}{\partial x_j}\frac{\partial U_j}{\partial x_i} + \frac{\partial^2 \overline{u_i u_j}}{\partial x_i \partial x_j}\right). \tag{2.10}$$

By subtracting this equation for the mean pressure from that for the instantaneous pressure Eq. (2.5), one obtains the Poisson equation for pressure fluctuation:

$$\frac{\partial^2 p}{\partial x_i^2} = -\rho\left(-2\frac{\partial U_i}{\partial x_j}\frac{\partial u_j}{\partial x_i} + \frac{\partial^2}{\partial x_i \partial x_j}\left(u_i u_j - \overline{u_i u_j}\right)\right). \tag{2.11}$$

The first and second terms in the right hand side represent the effect by the mean flow field and that by the velocity fluctuation, respectively, and the former is often referred to as the *rapid part*, because it would immediately reflect the effect of change in the mean flow field to pressure field as it explicitly include the mean velocity gradients. On the other hand, the latter is often called the *slow part* as it contains only the fluctuating velocities.

2.1.2.2 Transport equation of Reynolds stress and turbulent kinetic energy

The equations for the averaged flow field introduced above contain the Reynolds stresses $\overline{u_i u_j}$. Therefore, the transport equation of the Reynolds stress is helpful to understand the structure of the averaged flow field. The transport equation of the Reynolds stress is obtained from the Navier-Stokes equation. Terms in the Reynolds stress transport equation are classified according to their physical interpretation:

$$\begin{aligned}
&\underbrace{\frac{\partial \overline{u_i u_j}}{\partial t}}_{Unsteady} + \underbrace{U_k \frac{\partial \overline{u_i u_j}}{\partial x_k}}_{Convection: C_{ij}} = \\
&\qquad \underbrace{-\frac{\partial}{\partial x_k}\overline{u_i u_j u_k}}_{TurbulentDiffusion: D^t_{ij}} \underbrace{-\frac{1}{\rho}\frac{\partial}{\partial x_k}\left(\overline{p u_i}\delta_{jk} + \overline{p u_j}\delta_{ik}\right)}_{PressureDiffusion: D^p_{ij}} + \underbrace{\nu \frac{\partial}{\partial x_k}\frac{\partial \overline{u_i u_j}}{\partial x_k}}_{ViscousDiffusion: D^\nu_{ij}} \\
&\underbrace{-\left(\overline{u_j u_k}\frac{\partial U_i}{\partial x_k} + \overline{u_i u_k}\frac{\partial U_j}{\partial x_k}\right)}_{Production: P_{ij}} \underbrace{+\frac{1}{\rho}\overline{p\left(\frac{\partial u_i}{\partial x_j} + \frac{\partial u_j}{\partial x_i}\right)}}_{Redistribution: \phi_{ij}} \underbrace{-2\nu \overline{\frac{\partial u_i}{\partial x_k}\frac{\partial u_j}{\partial x_k}}}_{Dissipation: \varepsilon_{ij}}
\end{aligned} \tag{2.12}$$

Among these terms, the re-distribution and the pressure-diffusion terms which originally comes from the velocity-pressure-gradient term contain the fluctuating pressure.

The transport equation of the turbulent kinetic energy can be obtained by taking the trace of the Eq.(2.12) as

$$\frac{\partial k}{\partial t} + U_k \frac{\partial k}{\partial x_k} = -\frac{1}{2}\frac{\partial \overline{u_i u_i u_j}}{\partial x_j} - \frac{1}{\rho}\frac{\partial \overline{u_i p}}{\partial x_i} - \nu \frac{\partial^2 k}{\partial x_i^2} - \overline{u_i u_j}\frac{\partial U_i}{\partial x_j} - \nu \overline{\left(\frac{\partial u_i}{\partial x_j}\right)^2} \tag{2.13}$$

The terms in the right-hand-side are the turbulent diffusion D_k^t, pressure diffusion D_k^p, molecular diffusion D_k^ν, production rate P_k and dissipation rate ε_k. It should be noted that the redistribution term ϕ_{ij} disappear in the transport equation of k because of $\phi_{ii} = 0$.

The description of each term in the transport equation of the Reynolds stress Eq. (2.12) is noted below.

- Convection: C_{ij}
  This term means the variation of the Reynolds stresses along the streamline of the mean flow field. It can also be viewed as the residual of the balance among other terms in the transport equation.

- Production rate: P_{ij}
  By deriving the transport equation of U_iU_j, one can easily see that $-P_{ij}$ appears in it, which implies that P_{ij} represents the transport of energy from the mean flow field to the fluctuation field.

- Diffusion terms: D_{ij}^t, D_{ij}^p, D_{ij}^ν
  These terms has the form of the divergence, which means that these terms represent only the transport in space and never can be source nor sink of the Reynolds stresses.

  Turbulent diffusion: D_{ij}^t

  This term represents the spatial transport of the Reynolds stresses caused by the velocity fluctuation. In the conventional turbulence model, this term is modeled based on the idea of “gradient diffusion”.

  Pressure-diffusion: D_{ij}^p

  This term can be interpreted as the transport of the Reynolds stresses in space by the pressure fluctuation, and is originated from the velocity pressure-gradient correlation. Since the effect of the fluctuating pressure is non-local being different from the effect of the fluctuating velocity, it is not appropriate to model this term by the gradient-diffusion hypothesis.

Viscous-diffusion: D^{v}_{ij}

This term indicates the diffusion of the Reynolds stress due to the viscosity. As for the high-Reynolds number free shear flows, this term can be neglected.

- Re-distribution: ϕ_{ij}
  This term is also originated from the velocity pressure-gradient correlation term. The physical meaning of this term can be interpreted as the transfer of energy between different components of the Reynolds stresses because $\phi_{ii} = 0$ for the incompressible flow. This affects always the Reynolds stress tensor to be isotropic i.e. this term affects so that the difference between the normal components components becomes small and the shear components are vanished.

- Dissipation: ε_{ij}
  This term is originated form the viscous force term in the Navier-Stokes equation and the normal components of this term always play the negative contribution to the energy balance. Therefore, the physical meaning of this term is interpreted as the dissipation of the kinetic energy of the turbulent flow field into the heat.

In the framework of the RANS-based turbulence modeling, the transport equation of the Reynolds stress, Eq. (2.12), or that of the turbulent kinetic equation, Eq. (2.13), is often used together with the continuity and momentum equations, Eqs. (2.7) and (2.9), in order to enclose the equation system to be solved. The former equation, Eq. (2.12), is used in the Reynolds stress model (RMS), by which the Reynolds stress is directly obtained by solving its transport equation. The latter equation, Eq. (2.13) is often used in the eddy viscosity models (EVM), such as the k-ε model (Jones and Launder, 1972) or the k-ω (Wilcox, 1993) model. In either case of the EVM or RSM, the transport equation contains new unknown terms that need to be modeled, including the pressure-related terms, and the models for those terms are required to enclose the whole equation system.

2.1.2.3 Treatment for the pressure-related terms in the RANS-based turbulence models

Importance of the redistribution has been well recognized, as it has a significant contribution to the Reynolds stresses distributions in near wall region; it redistributes energy from the streamwise normal stress produced by the shear production to the wall-normal component and the spanwise component. Several models of the redistribution term has been proposed (e.g., Launder et al., 1975; Speziale et al., 1991).

On the other hand, contribution of the pressure diffusion has been disregarded despite the aforementioned importance of the velocity-pressure correlation. In the conventional RANS model, the pressure diffusion is treated as a part of turbulent diffusion, and the contribution is not explicitly taken into account. Although some attempts to incorporate the near wall behavior of the velocity-pressure correlation have been reported (e.g., Nagano and Tagawa, 1990), those to take into account the importance of the velocity-pressure correlation in the flow region away from the wall are quite rare. Even in the classical model by Lumley (1978), which is one of the rare explicit models of the pressure diffusion, the pressure-diffusion is expressed as sub process of the turbulent diffusion. Such disregard of the pressure diffusion is based on the fact that the velocity-pressure correlation is negligibly small except wall vicinity in the canonical shear flow, such as a channel flow, but it is also one of the reasons that knowledge of the velocity-pressure correlation is still limited, partly due to lack of the popular techniques for simultaneous measurement of fluctuating velocity and pressure.

After Yao et al. (2001) reported significant contribution of the pressure diffusion, some attempts with focus on the importance of the velocity-pressure correlation have been reported. Yoshizawa (2002) pointed out importance of taking into account the effect of the mean velocity gradient on the velocity-pressure correlation, and proposed a model based on the two-scale direct-interaction approximation (TSDIA). Suga (2004a) and Suga (2004b) also proposed a model for pressure diffusion on the basis of the model developed by Yoshizawa (2002) and reported certain improvement. For accelerating such efforts for improving performance of the RANS-based turbulence models, further construction of database of the velocity-pressure correlation is indispensable.

2.2 Analytical Considerations on Dynamic Response of Pressure-Measuring System

In this section, the dynamic response of the pressure-measuring system is analytically considered. The pressure-measuring system is now simplified as schematically shown in Fig. 2.1. The pressure-measuring point is connected to the pressure cavity of the pressure transducer by a thin tube, and p_s and p_m represent the true value of the fluctuating pressure at the measuring point and the pressure measured by the pressure

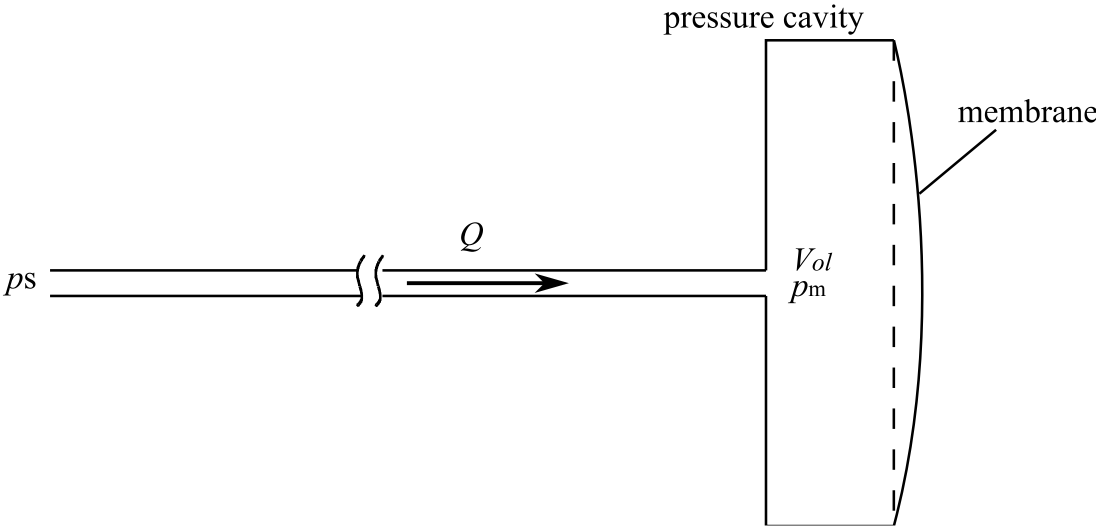

Figure 2.1: Analytical model of pressure-measuring system

transducer, respectively. The pressure transducer measures p_m by deformation of the membrane. The equation which relates p_s and p_m is derived in the following.

Flow inside the tube is driven by the pressure difference between the pressure-measuring point and inside of the pressure cavity, and damped by the viscosity of the fluid. Hence, behavior of the volumetric flow rate across the cross section of the tubing Q can be modeled as:

$$I\frac{dQ}{dt} + RQ = -\left(p_\mathrm{m} - p_\mathrm{s}\right), \tag{2.14}$$

where I is the fluid inertance, and R is the resistance of the system mainly caused by the viscosity of the working fluid. By the mass flow rate entering the pressure cavity, the mass in the pressure cavity ρV_{ol}, with V_{ol} being the cavity volume, changes as;

$$\begin{aligned}\rho Q &= \frac{d}{dt}\left(\rho V_{ol}\right)\\ &= \frac{d\rho}{dt}V_{ol} + \rho\frac{dV_{ol}}{dt}\end{aligned} \tag{2.15}$$

The first term in the right-hand-side represents the compressibility effect of the fluid inside the cavity, and the second term indicates the change of the cavity volume due to the deformation of membrane. The fluid density ρ and cavity volume V_{ol} are the functions of the pressure inside the cavity p_m, which is the function of time. Hence, Eq. (2.15) is rewritten as

$$
\begin{aligned}
\rho Q &= V_{ol}\frac{d\rho}{dp_m}\frac{dp_m}{dt} + \rho\frac{dV_{ol}}{dp_m}\frac{dp_m}{dt} \\
\therefore\quad Q &= \left(\frac{V_{ol}}{K} + C\right)\frac{dp_m}{dt}, \qquad (2.16) \\
\text{where}\quad K &= \rho\frac{dp_m}{d\rho} \quad C = \frac{dV_{ol}}{dp_m}.
\end{aligned}
$$

K and C are the bulk modulus of the fluid in the pressure cavity and the elastic compliance of the pressure transducer. Letting $C' = V_{ol}/K + C$ and substituting Eq. (2.16) into Eq. (2.14), one obtains an equation relating p_s and p_m ;

$$
IC'\frac{d^2 p_m}{dt^2} + RC'\frac{dp_m}{dt} + p_m = p_s \qquad (2.17)
$$

This equation indicates that the behavior of the measuring system is equivalent to that of a damped harmonic oscillator, and the damping ratio ζ and the undamped natural frequency ω_{n} of the system are given as

$$
\zeta = \frac{R}{2}\sqrt{\frac{C'}{I}}, \qquad (2.18)
$$

$$
\omega_{\mathrm{n}} = \sqrt{\frac{1}{IC'}}. \qquad (2.19)
$$

One can easily see that the ideal value of C' is zero because it gives $\omega_{\mathrm{n}} = \infty$ and $\zeta = 0$, which means frequency response of the pressure-measuring system is completely flat.

As mentioned in Sect. 1.3, fluctuating pressure measurement is conducted in both air and water in the present thesis. Now, C' introduced above is roughly evaluated to show that the pressure measuring-system has non-flat frequency response in both case in air and water. in the experiment in air, the bulk modulus of air was roughly evaluated as $K = 101$ kPa assuming the perfect gas, and C was evaluated based on specification of pressure sensor and pressure probe. Then, C' in the experiment in air is given as;

$$
C' = \frac{V_{ol}}{K} + C \approx 1.9 \times 10^{-13} + 6.1 \times 10^{-13} = 8.0 \times 10^{-13},
$$

which implies that the effect of compressibility of the fluid and elasticity of the membrane are of same importance. On the other hand, in the case of the measurement in water, the bulk modulus was evaluated as $K \approx 2.2 \times 10^9$ Pa (White, 2006), and V_{ol} and C were also evaluated based on specification of pressure transducer. The value of C' is roughly evaluated as;

$$C' = \frac{V_{ol}}{K} + C \approx 7.3 \times 10^{-17} + 1.9 \times 10^{-10} \approx 1.9 \times 10^{-10},$$

which implies that the compressibility effect of water is completely negligible.

The fluid inertance can be roughly estimated by regarding the flow inside the tube as the Hargen-Poiseuille flow as

$$I = \frac{\rho l}{S}, \tag{2.20}$$

with l and S being length and cross-sectional area of the tube. With the evaluated values of I, values of the natural frequency ω_n in each cases of experiment in air and water are obtained as roughly 3 kHz and 10 Hz, respectively. As these evaluated natural frequency are located near the frequency range of the present pressure measurements, careful calibration of the frequency response of the pressure-measuring system is necessary for accurate measurement in either experiment in air or water. It should be emphasized here that even in the experiment in water the frequency response of the pressure-measuring system is not flat due to elasticity of membrane of the pressure transducer although the compressibility of the working fluid is negligible.

Chapter 3

Validation of Measurement Technique by Combination of Hot-Wire Probe and Static-Pressure Probe

3.1 Motivation and Outline of This Chapter

As mentioned in Chap. 1, the measurement technique in which a hot-wire probe and a miniature static-pressure probe are aligned together has been used in some earlier studies of simultaneous measurement of fluctuating velocity and pressure, and some data of the velocity-pressure correlation have been provided. However, validity of the measurement results by this method has not been addressed enough. Applicability of this measurement technique should be further examined especially in flow region associated with large-scale vortex structure.

In this chapter, simultaneous measurement of fluctuating velocity and pressure is performed using a miniature static-pressure probe and an X-type hot-wire probe, and the validity of the experimental results of the velocity-pressure correlation is examined by a quantitative comparison with reference data obtained by a numerical simulation. Near wake of a circular cylinder was chosen for the test case because the velocity-pressure correlation is expected to be significant due to strong effect of the large-scale vortices periodically shed from the cylinder. In the experiment, several pressure probes with different diameters and lengths were employed for the velocity-pressure correlation measurement in a near wake of a circular cylinder, and effect of geometrical configuration of the pressure probe were also investigated in addition to validity of the measurement results.

Table 3.1: List of SP-probes (dimensions in mm)

Name	d	L_1	L_2	Name	d	L_1	L_2
d05-1	0.5	7.5	15.0	d05-5	0.5	17.5	15.0
d05-2	0.5	10.0	15.0	d07-1	0.7	12.0	20.0
d05-3	0.5	12.5	15.0	d07-2	0.7	17.0	20.0
d05-4	0.5	15.5	15.0	d10	1.0	19.5	24.0

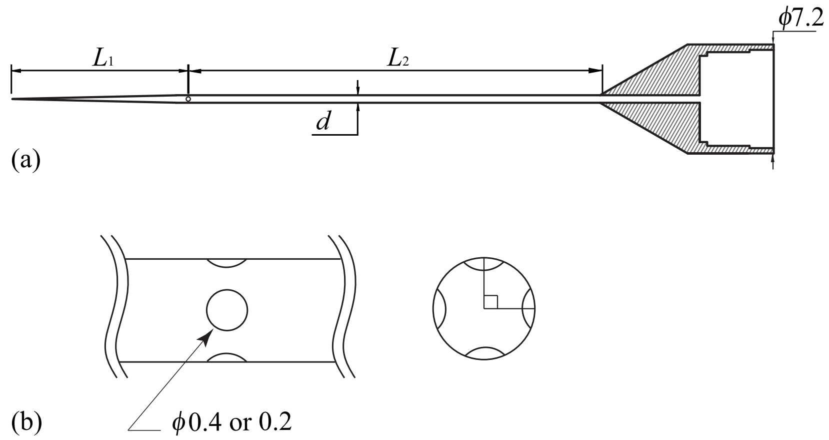

Figure 3.1: Schematics of SP-probe; (a) overall view, (b) zoom up view of configuration of pressure-sensing holes.

3.2 Experimental Setup

3.2.1 Technique for Fluctuating Static-Pressure Measurement

3.2.1.1 Static-pressure probe

A miniature Pitot-tube-type probe for static-pressure measurement (SP-probe) used in the presnet experiment is schematically shown in Fig. 3.1. The SP-probe consisted of a thin pipe with a circular cone on its tip and the flare part for joint to a condenser microphone. There were four small pressure-sensing holes on the surface to capture the fluctuating static-pressure in turbulent flow, and they were separated by 90° in the circumferential direction.

Eight SP-probes were employed in the present study to investigate the effect of the shape on the velocity-pressure correlation measurement. The diameters and lengths of each SP-probe are summarized in Table 3.1, where d is the outer diameter, and L_1 and L_2 are the length from the tip to the pressure-sensing holes and that from the pressure-sensing holes to the flare part, respectively (see Fig. 3.1). The probe d10 has the same dimensions as those proposed by Toyoda et al. (1994) and the others have smaller dimensions. The probes d05-1 to d05-5 have d of 0.5 mm and different values of L_1 in order to investigate the effect of the length of the tip section. There were other set of SP-probes with d of 0.5 mm and different length L_2, but they are omitted in Table 3.1 because the difference in L_2 showed only minor effect. The probes d07-1 and d07-2 have d of 0.7 mm, and L_1 of 12.0 mm and 17.0 mm, respectively. The thickness of SP-probe and the diameter of the pressure-sensing holes were 0.05 mm and 0.2 mm for the probes d05-1 to d05-5, and 0.1 mm and 0.4 mm for the probes d07-1, d07-2, and d10.

The error in the pressure measurement caused by the cross flow was experimentally investigated. The SP-probe was placed in a uniform flow, and the static pressure was measured with various angle of attack of the flow to the axis of the SP-probe. Figure 3.2 shows the variation of the measured pressure against the angle of attack of the flow. The pressure coefficient C_p was defined as

$$C_p = \frac{p - p_0}{\rho U_\infty^2}, \tag{3.1}$$

with p_0 being the value of the pressure measured with the flow angle of 0°. It is shown in Fig. 3.2 that the pressure values were underestimated when the flow direction is not parallel to the axis of the SP-probe, and there is not any significant difference between the directional response of the various SP-probes except that the characteristics of the probe d05-1 was relatively worse than the other SP-probes. For any SP-probe, the measurement error due to the cross-flow effect was less than $0.03\rho U_\infty^2$ with the flow angle smaller than 20°.

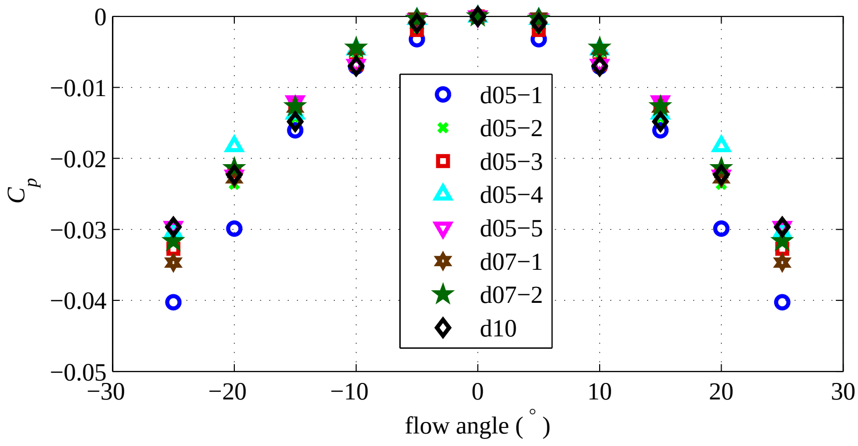

Figure 3.2: Error in static-pressure measurement due to effect of cross flow.

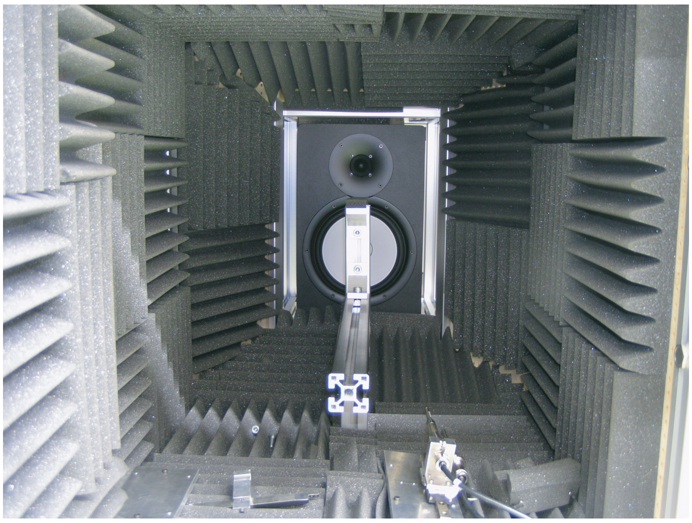

Figure 3.3: Photo of anechoic box used for calibration of dynamic response of pressure probes.

3.2.1.2 Pressure sensor and amplifier

A 1/4-inch condenser microphone (UC-29, Rion), with the sensitivity of 20.4 mV/Pa and the flat response in frequency the range from 25 Hz to 10 kHz, was used as a pressure sensor, being flushed inside the flare part of the SP-probe. The output voltage of the microphone was amplified by the pre-amplifier (NH-05A, Rion) and the main amplifier (UN-04, Rion).

Due to the characteristics of the electric circuit in the microphone and the pre-amplifier, certain phase delay occurs on the measured pressure signals. According to the manufacture, this phase delay can be evaluated as:

$$\Delta\theta = -\pi + \tan^{-1}\left(\frac{1}{2\pi CRf}\right), \tag{3.2}$$

where C and R stand for the electronic capacitance of the condenser microphone and the input resistance of the pre-amplifier, respectively, and f is the frequency of the fluctuating pressure. In the present study, the values of C and R were 6 pF and 10 GΩ, respectively, according to the hardware specification. The phase lag caused by the electric circuit was corrected in the post processing base on Eq. (3.2), as will be described in Sect. 3.2.1.4.

3.2.1.3 Dynamic response of SP-probe

The effect of the compressibility of the air inside the SP-probe were investigated prior to the experiments in an echoic box by the same manner as the previous experiments (e.g., Naka and Obi, 2009; Sakai et al., 2007, etc.) in an anechoic box shown in

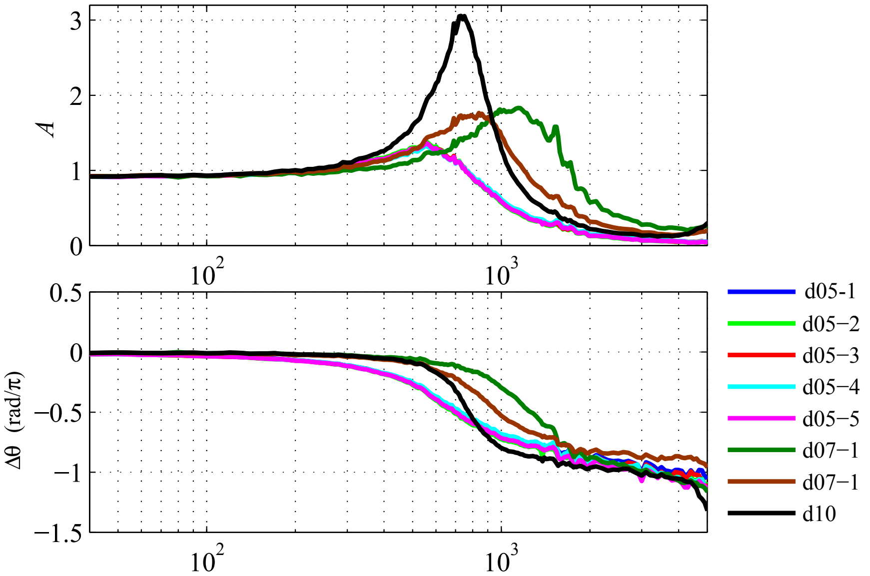

Figure 3.4: Dynamic response of various SP-probes.

Fig. 3.3. The SP-probe attached on the condenser microphone was placed in front of a loud speaker (YAMAHA, HS80S) with another microphone, which was not attached to the SP-probe. The pressure-sensing holes of the SP-probe and the surfaces of the reference microphone were located at the same distance from the speaker, and the sound signal was measured simultaneously in the frequency range of 40Hz $\leq f \leq$ 20kHz. The amplification/attenuation of amplitude and phase lag of the fluctuating pressure were obtained at each frequency by comparing the fluctuating pressure measured by the microphones with and without the SP-probe.

Figure 3.4 shows the variation of the amplitude ratio A and the phase delay $\Delta\theta$, which are respectively defined as

$$A = p'_1/p'_2, \tag{3.3}$$

$$\Delta\theta = \theta_1 - \theta_2, \tag{3.4}$$

where p' and θ stand for the root-mean-square of the pressure fluctuations and the phase, respectively, and the subscripts 1 and 2 denote the values measured by the condenser microphone with the SP-probes and the reference microphone. The variations in the frequency range lower than 5 kHz are presented. It is shown in Fig. 3.4 that the probes with relatively large diameters, d07-1, d07-2 and d10, have a significant peak of M around the frequency of 1 kHz. On the other hand, the probes with d being 0.5 mm does not have such significant peak of M, and the phase begins to delay from 300 Hz.

3.2.1.4 Post processing of pressure signals

As investigated Sect. 3.2.1.1, the amplitude and the phase of the measured signals of the fluctuating pressure might be changed due to the dynamic response of the SP-probe. Besides, additional phase delay occurs owing to characteristics of the electric circuit in the condenser microphone and the pre-amplifier. Therefore, the amplitude and the phase of the measured signals of the pressure was corrected in the post processing by the manner described following.

Applying the Fourier transform to the measured pressure signals, one can evaluate the complex Fourier coefficient B_n of the measured pressure signals at the nth frequency f_n. The amplitude change and the phase delay caused by the dynamic response of the SP-probe at this frequency, namely A_n and $\Delta\theta_n^{\mathrm{spp}}$ can be evaluated by interpolating the measured variation of A and $\Delta\theta$ in Fig. 3.4. The additional phase delay caused by the electric circuit in the microphone and the pre-amplifier $\Delta\theta_n^{\mathrm{spp}}$ was obtained by Eq. (3.2). Using these values of $\Delta\theta_n^{\mathrm{spp}}$ and $\Delta\theta_n^{\mathrm{ec}}$, the Fourier coefficient B_n was corrected as:

$$\hat{B_n} = \frac{B_n}{A_n \left\{ \cos(\Delta\theta_n^{\mathrm{spp}} + \Delta\theta_n^{\mathrm{ec}}) + j\sin(\Delta\theta_n^{\mathrm{spp}} + \Delta\theta_n^{\mathrm{ec}}) \right\}}, \tag{3.5}$$

and the pressure signals were reconstructed by inverse Fourier transform as

$$p = \sum_{n=1}^{N} \hat{B_n} \exp\left(-j2\pi f_n t\right), \tag{3.6}$$

where j is the imaginary unity. As the sampling time in the present measurement was 120 s (this sampling time was determined by the random error analysis in Sect. 3.2.5), the frequency resolution of the Fourier transform was 1/120 Hz, and the FFT and the interpolation included in the above procedures were conducted by using the function "`fft`" and "`interp1`" available in the MATLAB® library.

The background noise contained in the measured pressure signals, such as acoustic noise from surrounding or the mechanical vibration of the probe support, was reduced by means of an optimal filtering scheme proposed by Naguib et al. (1996). A secondary SP-probe which has identical dimensions to the probe d10 was placed at the same streamwise location as the main SP-probe but outside of the wake, and the optimal values for the filter coefficient was determined based on the signals of the fluctuating pressure measured by the main and sub SP-probe. The noise signal involved in the pressure signals measured by the main SP-probe was estimated by applying the filtering with the optimized coefficients and was subtracted from the pressure signal measured by the main SP-probe.

Due to the non-flat dynamic response of the microphone in the low frequency range and the dynamic response of the SP-probe shown in Fig. 3.4, the band-pass filtering was applied on the measured signals of fluctuating velocity and pressure with the passed frequency range of 20 Hz $\leq f \leq$ 650 Hz using “`filtfilt`”, a function for applying filtering without phase shift available in MATLAB® library. By the band-pass filtering, the streamwise velocity fluctuation $\overline{u^2}$ was underestimated to 80% of the raw data, because a certain amount of the power spectra of u were distributed in the lower frequency range than 20 Hz; and they were filtered out. On the other hand, the transverse velocity fluctuation $\overline{v^2}$ decreased only by 2% because most of the power was concentrated around the vortex shedding frequency (113 Hz). As the velocity-pressure correlation was mainly produced by the velocity and pressure fluctuation at the vortex shedding frequency, it can be reasonably considered that the velocity-pressure correlation was underestimated only weakly by the band-pass filtering.

3.2.2 Velocity Measurement

For the fluctuating velocity measurement, a commercial dual-sensor hot-wire probe (55P64, Dantec) was used as the X-probe and operated with a constant temperature anemometer (CTA; Model 1011, Kanomax). Two velocity components of the instantaneous velocity vector was evaluated from the output voltage of the CTA by means of the look-up-table method (Lueptow et al., 1988). In the calibration of the X-probe, the calibration range of the yaw angle and the velocity magnitude were between ±42° with increment of 4.2°, with the free-stream velocity of 2.5, 5.0, 7.0, and 9.5 m/s. For samples falling out of the table (approximately 0.9 % of the total number of the samples), the velocity was evaluated based on the effective angle method (Browne et al., 1989).

The relation between the true values of the velocity components and the output voltage of the CTA may change during the experiment owing to the change in the sounding environment, mainly the change in the temperature in the free stream of the wind tunnel. This effect of the temperature change was corrected by the following equation according to the DANTEC Practical Guide (Jørgensen, 2002):

$$E_{\mathrm{corr}} = \left(\frac{T_w - T_0}{T_w - T_a} \right)^{0.5} E_a, \tag{3.7}$$

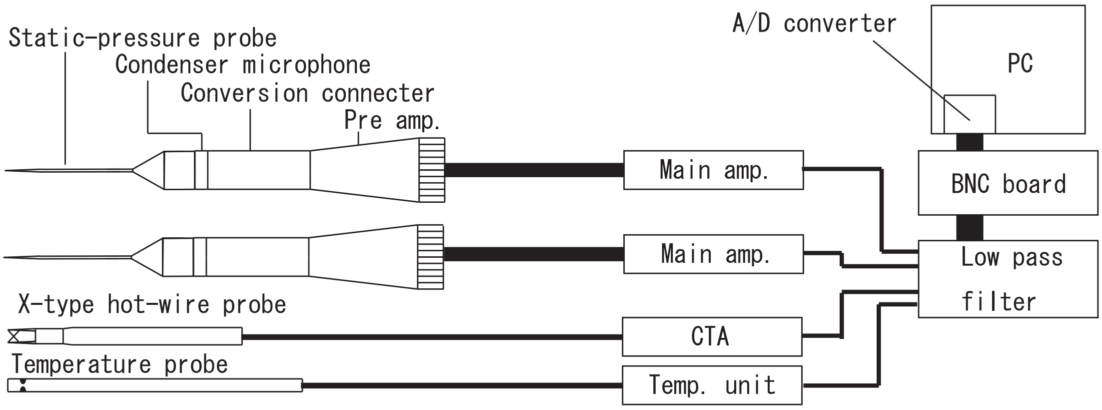

Figure 3.5: Diagram of system for velocity-pressure correlation measurement.

where E_a is the output voltage of the CTA, T_0 and T_a are the atmosphere temperature in the calibration and during the measurement, respectively, and T_w is the temperature of the wire of the X-probe evaluated as $T_w = \alpha/\alpha_0 + T_0$ with α and α_0 being the over-heat ratio and the temperature coefficient of the CTA, respectively. The recorded output voltage of the CTA was corrected base on Eq. (3.7) in the post processing. The calibration of the X-probe was conducted before and after the every experiment run, and the shift of the output voltage of the CTA was checked by comparing the calibration results. The systematic error due to this temperature drift is evaluated in Sect. 3.2.5.

3.2.3 Data Acquisition and Other Hard- and Softwares

A diagram of the system for the velocity-pressure correlation measurement is show in Fig. 3.5. The X-probe, two SP-probes and a temperature probe were in use for the simultaneous measurement of two velocity components and static pressure, and the signals from these probes were acquired by a data-acquisition board (PCI-6621, National Instruments) after filtered by an analog low-pass filter (DT-6LF2, NF CORPOLATION). The resolution and the scan rate of the data-acquisition board were 16 bits and 250 kS/s, respectively. With five channels in use, the maximum time lag of data acquisition between the channels was 0.02 ms. The low-pass filter was operated with the cut-off frequency of 10 kHz, and the sample rate of data acquisition was 20 kHz. The integration time to evaluated the statistics was determined based on the random error analysis described in Sect. 3.2.5. Data acquisition was managed by LabVIEW® (National Instruments), and further data processing including those previously mentioned in Sect. 3.2.1.4 was conducted by programs written in MATLAB®.

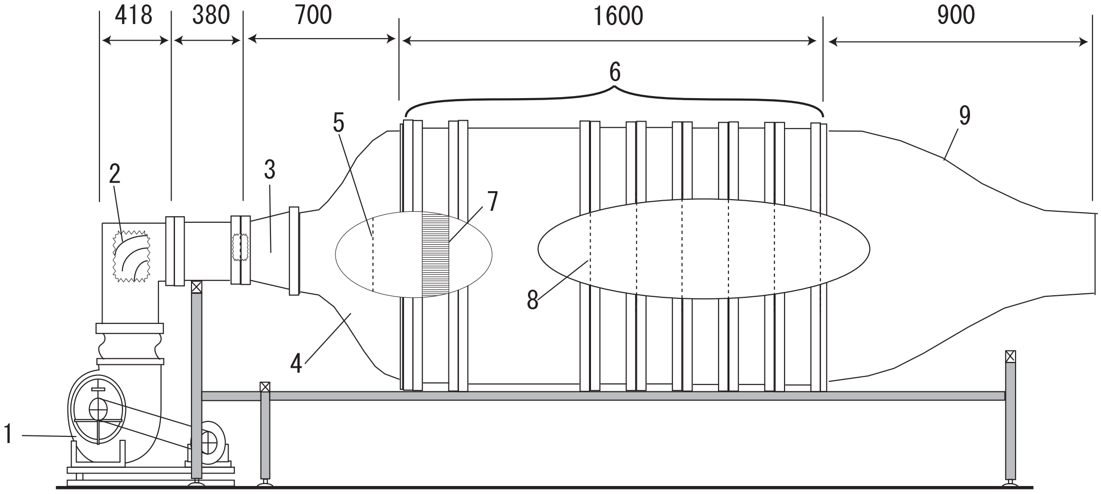

1	Blower	4	Main diffuser	7	Honeycomb
2	Corner bane	5	Punching metal	8	Screen mesh
3	Pre diffuser	6	Camber	9	Nozel

Figure 3.6: Schematic of low-speed wind tunnel.

The other hardware used in the present experiment, such as the traverse units, a low-range pressure transducer and a Pitot tube used for calibration of the X-probe and the temperature measuring unit and etc., are summarized in Appendix A. The low-speed wind-tunnel used in the experiments described in Chaps. 3 and 4 is schematically shown in Fig. 3.6. It was open-blowing type with an exit cross-sectional area of 350×350 mm^2, and the maximum free-stream velocity and the turbulence intensity were 9.5 m/s and about 0.23%, respectively.

3.2.4 Flow Condition and Probe System

Simultaneous measurements of the fluctuating velocity and pressure were undertaken in the free stream of the open-blowing wind-tunnel. A circular cylinder, which had a diameter D of 10 mm and a length L longer than the width of the wind-tunnel exit, was placed in the free stream; both the aspect ratio D/L and the blockage ratio D/H (H is the height of the wind-tunnel exit) were 0.029. The coordinates was defined as shown in Fig. 3.7(a); the origin was fixed at the center of the cylinder and $x-$, $y-$ and $z-$axes were taken in the streamwise, transverse and spanwise directions. The free-stream velocity U_∞ was 5.9 m/s with turbulence intensity of 0.2%, and the Reynolds number based on the cylinder diameter and the free stream velocity, $\mathrm{Re} = U_\infty D/\nu$, was 3900.

Figure 3.7: Experiment condition; (a) coodinate system, (b) probe configuration.

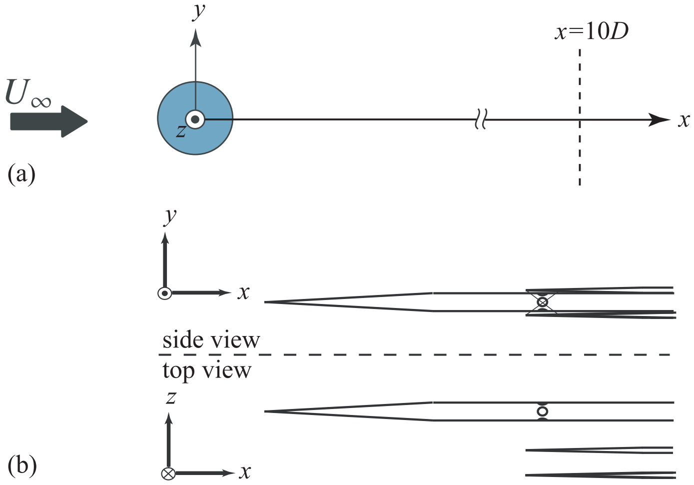

The vortex shedding frequency was 113 Hz, which corresponds to a Strouhal number, $S_t = fD/U_\infty$, of 0.19.

In the velocity-pressure correlation measurements, the SP-probe was combined with an X-type hot-wire probe (X-probe) as schematically shown in Fig. 3.7(b). The probes were arrayed in the spanwise direction so that the X-probe and the SP-probe were virtually at the same (x,y) position. The distance between the X- and SP-probe was carefully determined based on the experimental investigation of the probe interference, as will be described in Sect. 3.14.

Measurements were conducted at $x/D = 10$, where a relatively large lateral velocity fluctuation exists. The velocity profile was measured by the X-probe prior to the simultaneous measurements, and it was found that at the wake center the flow-angle fluctuation was about 20°; the instantaneous flow angle was mostly below 25°, while it reached 40° at the maximum.

3.2.5 Uncertainty Analysis

In the present study, the statistical quantities, such as the mean velocity, the Reynolds stresses and the velocity-pressure correlations, are evaluated by taking average based on the samples of the velocity and pressure measured for certain integration time with sampling rate being 10 kHz. In order to determine the proper integration time, the random error analysis was conducted based on the data measured at the wake center. The fluctuating velocity was measured by the X-probe for 1 hour, and the variation of the statistics against the integration time was investigated. Figure 3.8 presents the variation of the mean streamwise velocity U and the Reynolds stresses $\overline{u^2}$, $\overline{v^2}$ and $\overline{uv}$ evaluated with various integration times. The half width of the error bar indicates the

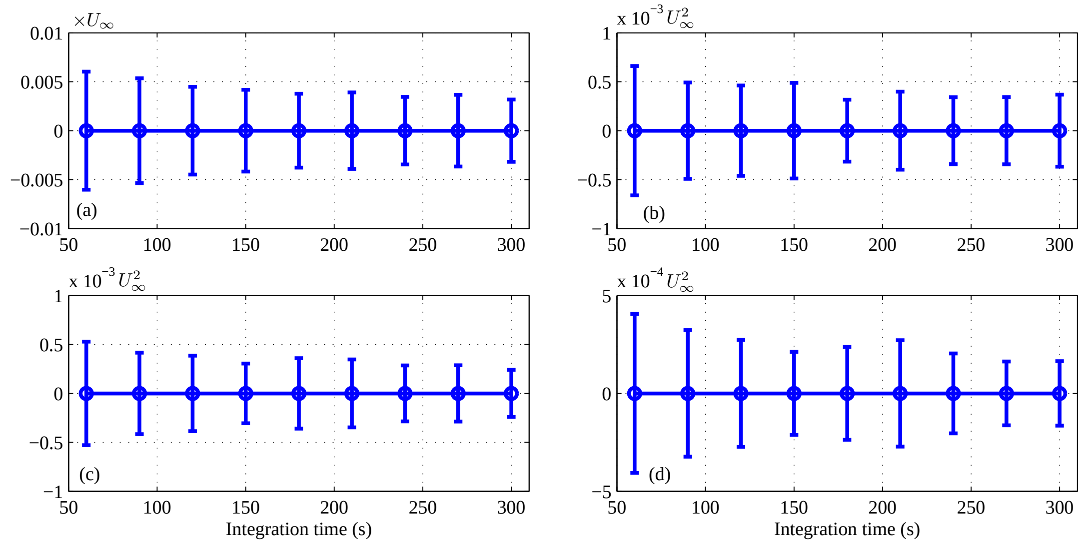

Figure 3.8: Variation of statistics with integration time: (a) mean streamwise velocity U, (b) Reynolds normal stress $\overline{u^2}$, (c) Reynolds normal stress $\overline{v^2}$, (d) Reynolds shear stress $\overline{uv}$.

possible range of the random error, which was evaluated as tS_x with t being the student t-value and S_x being the precision index of the statistical quantity X defined as:

$$S_x = \left[\frac{\sum_{k=1}^{N} \left(X_k - \overline{X_k} \right)^2}{N-1} \right]^{1/2} . \tag{3.8}$$

The student t-value was provided by ASME PTC 19.1 (1985) according to the number of freedom. For example, when the integration time was 120 s, the number of freedom was 30 (because the data measured for 1 hour was used) and the student t-value t was 2.18.

In Fig. 3.8, it is shown that the width of the error bar gradually decreases as the integration time increases in the range where the integration time is shorter than 120 s but does not show clear dependency in the range of the longer integration time. With the integration time of 120 s, the uncertainty due to the random error was less than $0.05U_\infty$ for evaluation of the mean streamwise velocity and $5 \times 10^{-4} U_\infty^2$ for the Reynolds stresses $\overline{u^2}$, $\overline{v^2}$ and $\overline{uv}$, which are fairly small compared with the variation of these statistics at $x = 10D$. Therefore, the proper integration time for the measurement was determined to be 120 s.

Next, the systematic error involved in the present measurement is addressed. The largest possible cause of the systematic error is the temperature draft of the CTA output previously mentioned in Sect. 3.2.3. The error due to the drift of the CTA output was

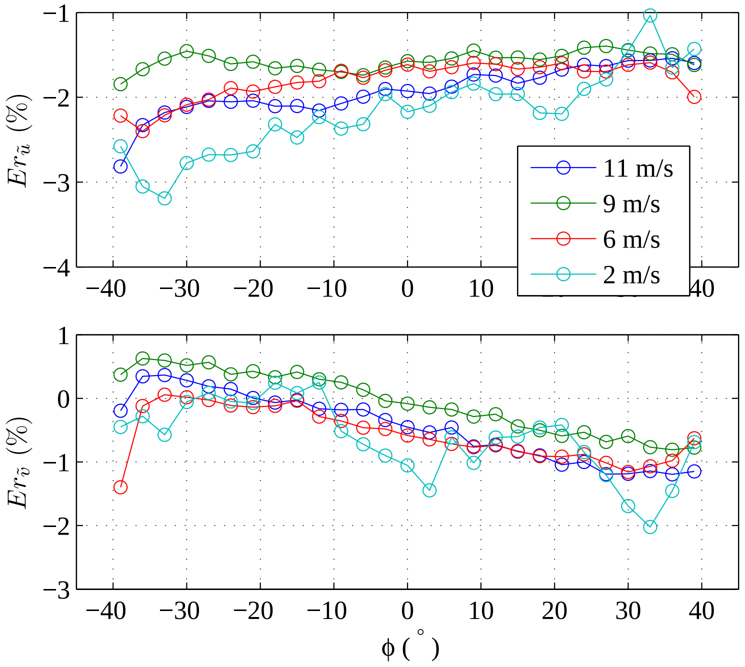

Figure 3.9: Error in velocity measurement due to drift of CTA output.

investigated by comparing the data of the calibrations conducted before and after the experiment. Figure 3.9 shows the error due to the drift of the CTA output, which was evaluated as:

$$Er_u = \frac{u_{\mathrm{lut}} - u_{\mathrm{true}}}{u_{\mathrm{pitot}}}, \tag{3.9}$$

$$Er_v = \frac{v_{\mathrm{lut}} - v_{\mathrm{true}}}{u_{\mathrm{pitot}}}, \tag{3.10}$$

where u_{lut} and v_{lut} are the values of the velocity components which were evaluated based on the output signals recorded in the calibration after the measurement and the look-up-table constructed by the calibration before the experiment, and u_{true} and v_{true} are the true values of each velocity component obtained as

$$u_{\mathrm{true}} = u_{\mathrm{pitot}} \cos\phi, \tag{3.11}$$

$$v_{\mathrm{true}} = u_{\mathrm{pitot}} \sin\phi, \tag{3.12}$$

with u_{pitot} and ϕ being the free stream velocity measured by a Pitot tube in the calibration and the angle of attack of the velocity vector to the axis of the X-probe, respectively. It is shown that the magnitude error does not have clear dependency on the velocity magnitude nor the flow angle, and is within the range of $\pm 3\%$ of the free stream velocity.

Other possible causes of the systematic error in the velocity-pressure correlation measurement are listed below:

1. Error in the pressure measurement caused by the cross-flow effect
2. Interference between the X- and SP-probe
3. Insufficient spatial resolution of the combined probe
4. Phase lag between the signals of the velocity and pressure

The error caused by the cross-flow effect in the pressure measurement was already addressed in Sect. 3.2.1.1. As the fluctuation of the instantaneous flow angle was roughly evaluated as 15°, the values of the instantaneous pressure may be underestimated by $0.015\rho U_\infty^2$ according to Fig. 3.2.

The effect of the probe interference and the low spatial resolution of the combined probe of the X- and SP-probes will be experimentally addressed prior to the main velocity-pressure correlation measurement in Sect. 3.4.1.

The phase lag between the pressure and velocity signals could be the cause of fatal error in the velocity-pressure correlation measurement. The largest possible cause is the phase delay of the pressure signals caused by the dynamic response of the SP-probe and the electric circuit in the microphone and the pre-amplifier. Although these are already corrected was corrected as described in Sect. 3.2.1.4, there may be the other cause of the phase delay, such as the other electric circuit or the disturbance to the flow caused by the intrusion of the probes. The phase lag between the velocity and pressure signals also will be experimentally explored prior to the main measurement as will be described in Sect. 3.4.2.

3.3 Computation

3.3.1 Numerical Setup

A large-eddy simulation (LES) of a flow around a circular cylinder with the Reynolds number of 3900 was performed to obtain reference data for the validation of the experimental results. An open-source CFD software, OpenFOAM version 2.0.1, was used for carrying out the simulation. Dynamic Smagorinsky model (available as “`homogeneousDynSmagorinsky`” in the OpenFOAM library) was adopted for the sub-grid scale (SGS) model, and “`pisoFoam`”, which is a solver based on the PISO method, was used for velocity-pressure coupling. Numerical schemes used for discretization are summarized in Table 3.2.

Table 3.2: Numerical schemes used in LES

Numerical schemes	Used option
`ddtSchemes`	`backward`
`gradSchemes`	`Gauss linear`
`divSchemes`	`limittedLinear 1`
`interpolationSchemes`	`Linear`
`snGradScheme`	`corrected`

A square-shaped computational domain with the H-type computational grids concentrated around and in the downstream of the cylinder as shown in Fig. 3.10 was used, in order to maintain the sufficient spatial resolution at the downstream location $x = 10D$. The domain size was $-15 \leq x/D \leq 30$, $-15 \leq y/D \leq 15$ and $-1.5 \leq z/D \leq 1.5$ in the streamwise, transverse, and spanwise directions. The number of computational grids was 6.6 million; 134,000 grids were in the $xy-$ plane with the closest grids to the cylinder wall located at $2.0 \times 10^{-3}D$ distance from the wall, and 49 grids were placed in the spanwise direction.

As for the boundary conditions, the inlet velocity and pressure were uniformly fixed at 6 m/s and 0 Pa, respectively, without fluctuation, and "`zeroGradient`" option was applied to both velocity and pressure on the sides and downstream boundaries of the domain. No-slip and "`zeroGradient`" conditions were applied to velocity and pressure on the cylinder wall, respectively, and periodic boundary condition was used

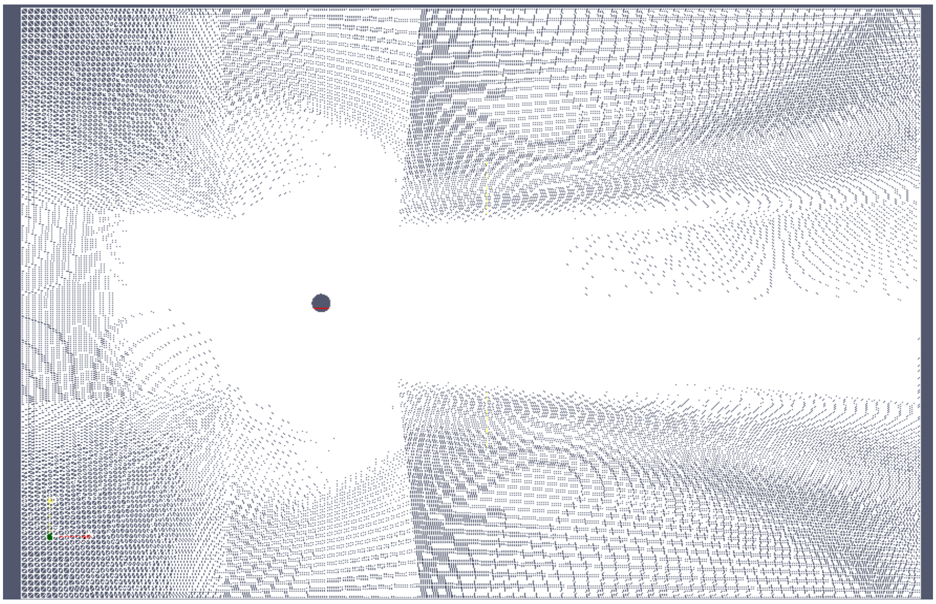

Figure 3.10: Computational grids.

Figure 3.11: Distribution of mean streamwise velocity along the center line: solid line, present LES; black bars, variation of reference data from Beaudan and Moin (1994); Kravchenko and Moin (2000); Lourenco and Shih (1993); Mittal and Moin (1997); Parnaudeau et al. (2008)

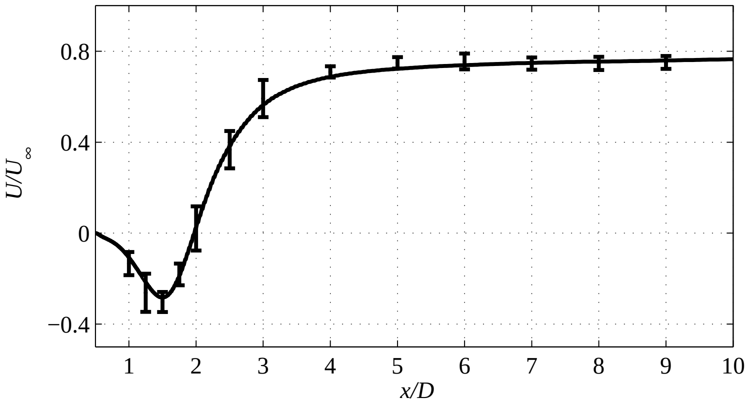

Figure 3.12: Pressure coefficient distribution of the cylinder surface: solid line, present LES; circles, Norberg (1987); chain line, (Ma et al., 2000, DNS, Case I)

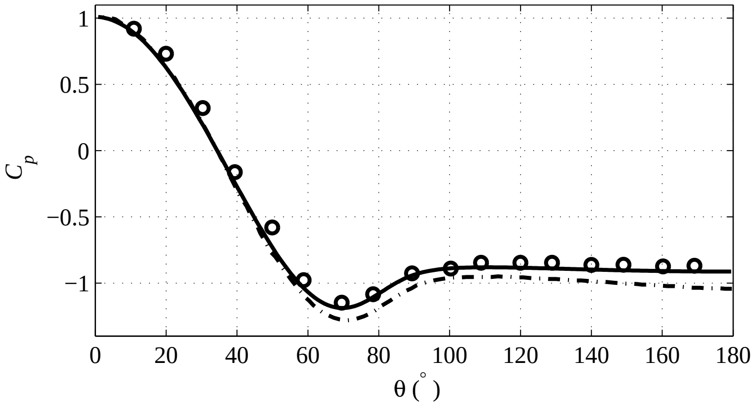

in the spanwise direction. Statistical quantities were obtained by averaging samples both in space and in time; spatial averaging was taken in the spanwise direction and integration time for temporal averaging was 0.3 s, which corresponds to about 30 vortex pairs.

3.3.2 Preliminary Results

Figures 3.11 and 3.12 show distribution of the mean streamwise velocity along the center line and the pressure coefficient on the cylinder surface, comparing with experimental and computational reference data (Beaudan and Moin, 1994; Kravchenko and Moin, 2000; Lourenco and Shih, 1993; Ma et al., 2000; Mittal and Moin, 1997; Norberg, 1987; Parnaudeau et al., 2008). It is shown that the profile of U and C_p provided by the present LES are in satisfactory agreement with reference data.

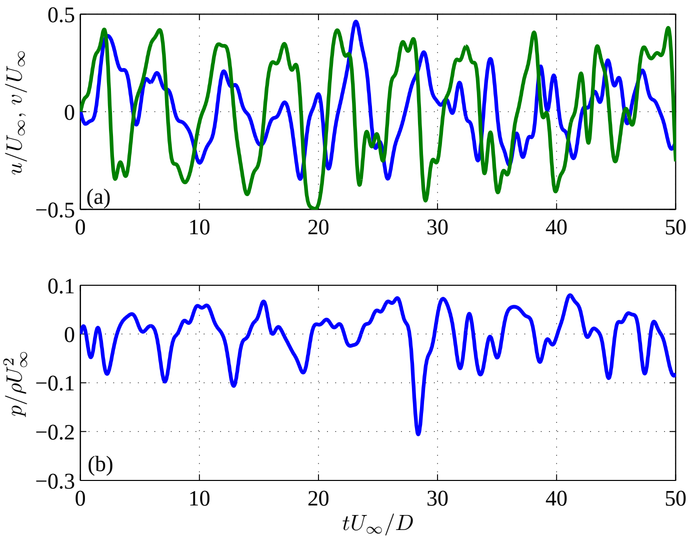

Figure 3.13: Time sequence of fluctuating component of velocities and pressure measured by the X-probe and the probe d05-3 with probe distance of $\Delta z = 3.0$ mm at $(x/D,\ y/D) = (10,\ -0.5)$: (a) fluctuating component of streamwise (blue) and transverse (green) velocities; (b) fluctuating pressure.

3.4 Experimental and Computational Results

3.4.1 Probe Interference

The effect of the probe interference was investigated for the various SP-probes. The X-probe and the SP-probe were placed at $(x/D,\ y/D) = (10,\ -0.5)$. The velocity and pressure were measured simultaneously with spanwise different probe distances Δz, and the variations of the measured statistics were investigated. Figure 3.13 presents time sequences of fluctuating component of velocities and pressure measured by the X- and d05-3 probes with the probe distance $\Delta z = 3.0$ mm. It can be seen that both the velocities and pressure were fluctuating with the period roughly being $5U_\infty/D$.

Figure 3.14 shows the variation of measured values of the mean streamwise velocity U, the Reynolds stresses $\overline{v^2}$ and $\overline{uv}$, and the velocity-pressure correlation coefficient $R_{\overline{up}} = \overline{up}/(u' \cdot p')$. The values of U, $\overline{v^2}$ and $\overline{uv}$ are scaled by reference values measured by a single use of the X-probe. In Fig. 3.14, the colors of the symbols indicate the dimater of the SP-probe; the blue, red, and black symbols stand for the SP-probe with the dimater of 0.5 mm (from d05-1 to d05-5), 0.7 mm (d07-1 and -2), and 10 mm (d10). The mean streamwise velocity$U$ and the Reynolds stresses $\overline{v^2}$ and $\overline{uv}$ monotonously approach to unity as Δz increases. The velocity-pressure correlation $R_{\overline{up}}$ also indicates similar behavior approaching to the value of -0.25. The variations of $\overline{v^2}$ and $\overline{uv}$ obviously show that the velocity measurement by the X-probe was more significantly affected by the probe interference as the diameter of the SP-probe became larger, and the length of the SP-probe L_1 did not affect the probe interference. For the probe d07-1, -2, and d10, distance of 4.0 mm was required so that the X-probe was free from

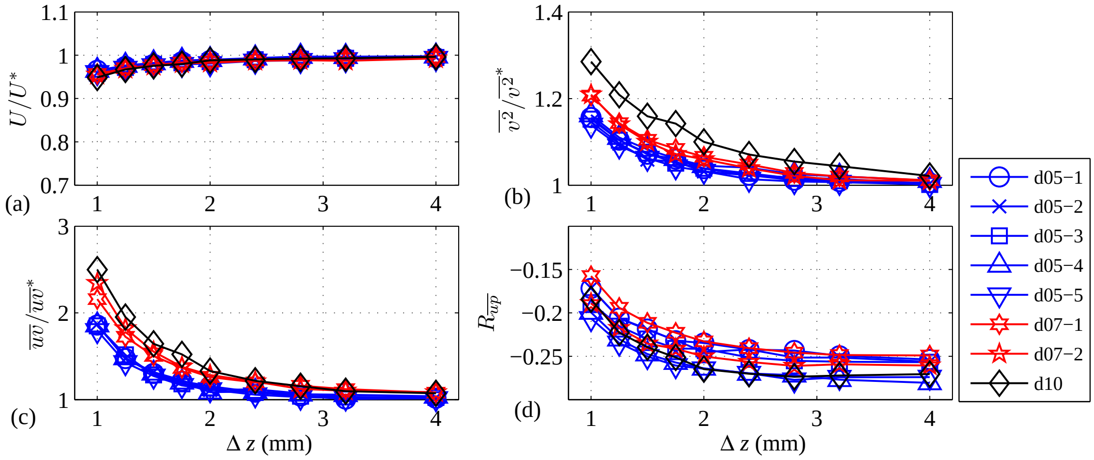

Figure 3.14: Variation of statistics against the probe separation Δz measured at $(x/D,\ y/D) = (10,\ -0.5)$: (a) mean streamwise velocity U; (b) Reynolds normal stress $\overline{v^2}$; (c) Reynolds shear stress $\overline{uv}$; (d) velocity-pressure correlation coefficient $R_{\overline{up}}$.

the probe interference, while the probe distance of 3.0 mm was enough for the probe with d of 0.5 mm. Therefore, the reasonable probe distance to avoid the probe interference was determined to be 3.0 mm for probes for d05-1 to d05-5 and 4.0 mm for the probes d07-1, -2, and d10.

The correlation between the fluctuating velocity and pressure at a single point was measured by two probes spatially separated by distance of 3.0 mm or 4.0 mm. In order to address appropriateness of this spatial resolution, a two-point correlation measurement was performed. Figure 3.15 shows the measured auto-correlation functions

$$R_{uu}(\Delta z) = \frac{\overline{u(z)u(z+\Delta z)}}{\overline{u^2}(z)}. \tag{3.13}$$

Integrating $R_{uu}(\Delta z)$ with respect to Δz, the integral scale Λ was evaluated as $\Lambda =$

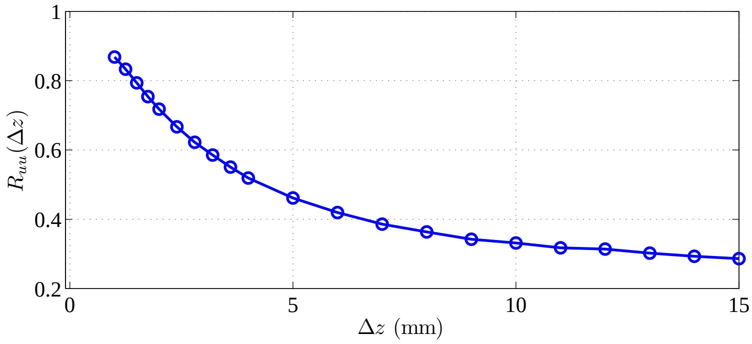

Figure 3.15: Two-point correlation coefficient of fluctuating streamwise velocities at $(x/D,\ y/D) = (10,\ 0)$ measured by two single-sensor hot-wire probes.

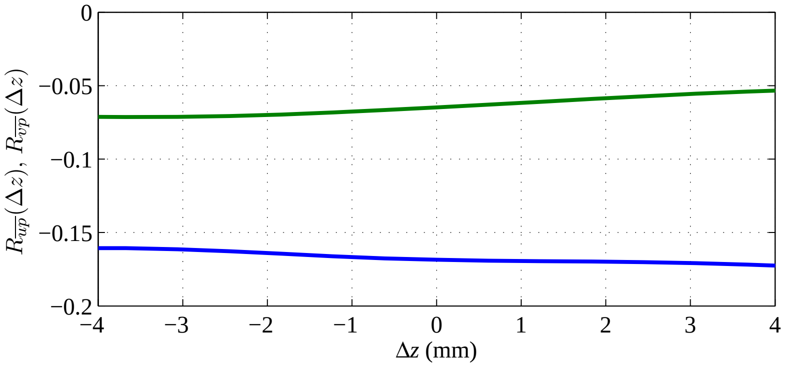

Figure 3.16: Two-point correlation coefficients between fluctuating velocities and pressure at $(x/D,\ y/D) = (10,\ 0.5)$ obtained by LES: blue, $R_{\overline{up}}(\Delta z)$; green, $R_{\overline{vp}}(\Delta z)$

6.50 mm. Hence, the probe distance is in the same order as the integral scales.

In order to examine the effect of such a low spatial resolution on evaluation of the velocity-pressure correlation, the velocity-pressure two-point correlation coefficients $R_{\overline{up}}(\Delta z)$ and $R_{\overline{vp}}(\Delta z)$ evaluated based on the computational results are shown in Fig. 3.16. As shown, the velocity-pressure correlations remained nearly constant against Δz. Therefore, it can be reasonably considered that the error in the velocity-pressure correlation measurement caused by the probe separation was not significant.

3.4.2 Time-lag between signals of fluctuating velocity and pressure

The time-delay between the signals of the fluctuating velocity and pressure measured by the X- and the SP-probes, respectively, was investigated prior to the velocity-pressure correlation measurement, according to the manner proposed by Toyoda et al. (1994). In the potential flow region, one can predict the true fluctuating pressure from the fluctuating velocity as (Fuchs, 1972):

$$p = -\rho u \left(U - U_c\right), \tag{3.14}$$

where U and U_c are the local mean streamwise velocity and the convection velocity of the disturbance, respectively. Equation (3.14) indicates that the fluctuating pressure p should be at the same phase as $-u$. We measured the fluctuating velocity and pressure simultaneously outside the wake at $x/D = 10$, and evaluated the time lag between the velocity and pressure signals by comparing the measured p to $-u$.

In order to seek the proper location in the wake of the circular cylinder to investigate the time lag between the velocity and pressure signals based on Eq. (3.14), the

Figure 3.17: Distribution of third and fourth moment of streamwise velocity fluctuation at $x = 10D$; (top) skewness factor S_u, (bottom) intermittency factor $\Omega = 3/F_u$.

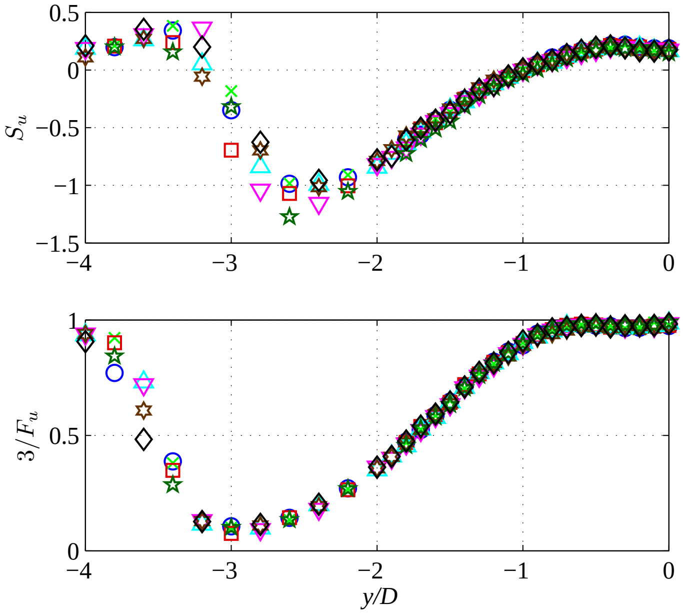

higher moments of the velocity fluctuation were investigated. The skewness factor and the flatness factor of the streamwise velocity fluctuation were evaluated as:

$$S_u = \frac{\overline{u^3}}{\overline{u^2}^{1.5}}, \tag{3.15}$$

$$F_u = \frac{\overline{u^4}}{\overline{u^2}^{2}}, \tag{3.16}$$

respectively, and their distributions are shown in Fig. 3.17. The Flatness factor is shown as $\Omega = 3/F$, which can be interpreted as intermittency factor (e.g., Hinze, 1959). In the center region of the wake, the skewness factor S was nearly zero and the intermittency factor Ω was almost unity, which indicates the nearly random nature of the velocity fluctuation u in this region. As the location moved to the outer region of the wake, S showed significant negative values and Ω decreased to nearly zero at $y/D = -3$. The small values of Ω was due to large value of the flatness factor F_u caused by intermit behavior of fluctuation of u at this location. In the further outer region, the intermittency factor Ω again increased to unity at $y/D = -4.0$, and the skewness factor S_u was nearly zero. This random nature of the velocity fluctuation may be due to the effect of the noise because the velocity fluctuation was already as small as the noise near $y/D = -4.0$. Hence, the flow is still intermittently turbulent at $y/D = -3.0$ as indicated by the small value of Ω, but the measured signal seems to be contaminated by the noise at $y/D = -4.0$. Therefore, it may be reasonable to consider that $y/D = -3.6$,

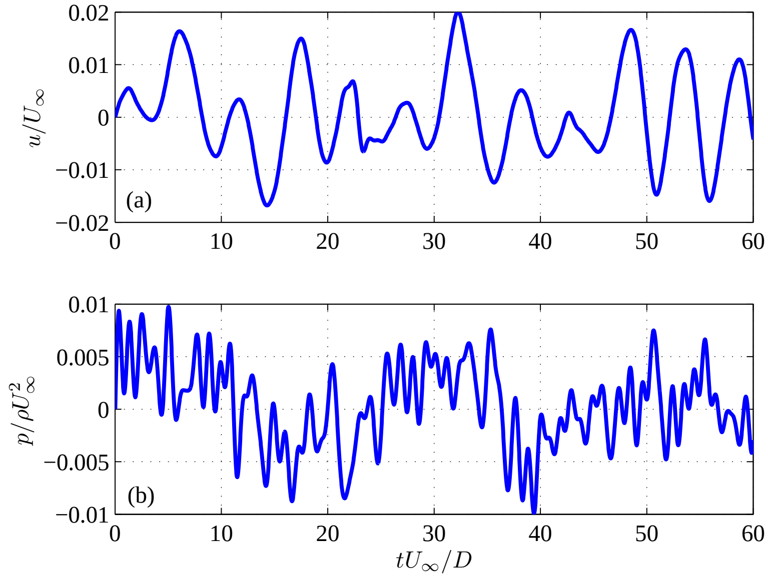

Figure 3.18: Time sequences of fluctuating streamwise velocity and pressure used for evaluation of time lag between velocity and pressure signals: (a) fluctuating streamwise velocity; (b) fluctuating pressure. They were measured by the X-probe and the probe d05-3 at $(x/D,\ y/D) = (10,\ -3.6)$.

where the skewness factor S_u is zero but the intermittency factor is still fairly smaller than 1, was the most valid location to use Eq. (3.14).

Simultaneous measurements of the fluctuating velocity and pressure were conducted with the probe distance determined in Sect. 3.4.1 at $(x/D,\ y/D) = (10,\ -3.6)$. Figure 3.18 presents time sequences of fluctuating component of streamwise velocity and pressure, measured by the X- and the d05-3 probes, respectively. The fluctuating streamwise velocity shows a smooth and periodic time sequence, while effect of background noise is apparent in the time sequence of fluctuating pressure. The power spectra density (PSD) of these time sequences of $-u$ and p are shown in Fig. 3.19. The PSD of $-u$ has a significant peak at the frequency of the vortex shedding (113 Hz),

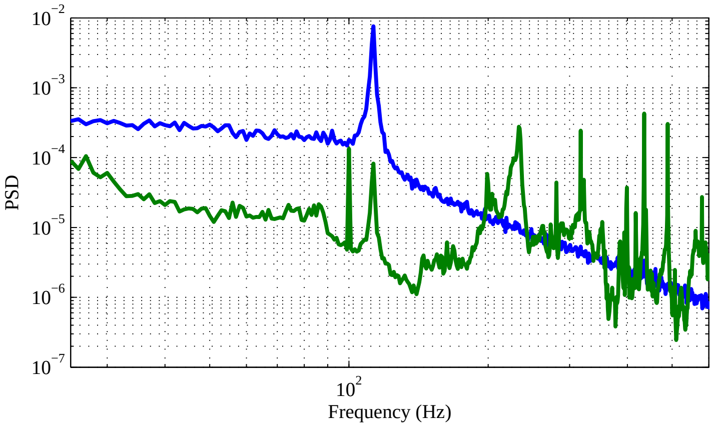

Figure 3.19: Power spectrum density of fluctuating velocity and pressure shown in Fig. 3.18.

Table 3.3: Time lag between measured signals of velocity and pressure.

Name	L_1 (mm)	τ (ms)	Name	L_1 (mm)	τ (ms)
d05-1	7.5	-0.19	d05-5	17.5	-0.33
d05-2	10.0	-0.26	d07-1	12.0	-0.25
d05-3	12.5	-0.29	d07-2	17.0	-0.29
d05-4	15.0	-0.32	d10	19.5	-0.42

while that of p has not only a peak at the vortex shedding frequency, but also many other larger peaks originating from background noise. The time lag between $-u$ and p was evaluated as:

$$\tau = \frac{1}{2\pi f_{\mathrm{sh}}} \tan^{-1} \frac{B_{-u}(f_{\mathrm{sh}})B_p^*(f_{\mathrm{sh}}) + B_{-u}^*(f_{\mathrm{sh}})B_p(f_{\mathrm{sh}})}{j\left(B_{-u}(f_{\mathrm{sh}})B_p^*(f_{\mathrm{sh}}) - B_{-u}^*(f_{\mathrm{sh}})B_p(f_{\mathrm{sh}})\right)}, \tag{3.17}$$

where f_{sh} is the vortex shedding frequency, the superscript $[]^*$ stands for the conjugate complex, and B_{-u} and B_p are the Fourier complex coefficients of $-u$ and p, respectively.

The time lag between the measured signals of $-u$ and p were evaluated by Eq. (3.17) and are summarized in Table 3.3. A time lag of about 0.2-0.4 ms was observed in all cases. Since the period of the Karman vortex shedding was about $D/0.2U_\infty \approx 8$ ms, the time lag between the velocity and pressure signals was relatively small. Comparing these values, we can see the tendency that the observed time lag between the velocity and pressure signals increases with the length L_1 of the SP-probe.

3.4.3 Velocity-pressure Correlation Measurements

The simultaneous measurements of fluctuating velocity and pressure at $x/D = 10$ in the wake of a circular cylinder were conducted with the previously determined probe distances. Figure 3.20 presents profiles of the mean streamwise velocity and the Reynolds stresses at $x/D = 10$, comparing those measured by the X-probe in the presence of various SP-probes with the reference data provided by the previous experiments (Ong and Wallace, 1996; Zhou and Antonia, 1993). The present experimental results coincided with each other. The profiles of the mean streamwise velocity U had the minimum of $0.75U_\infty$ at the center of the wake. The streamwise normal Reynolds stress $\overline{u^2}$ had two peaks beside the wake center, and the transverse normal stress $\overline{v^2}$ showed a single significant peak at the wake center with magnitude of $0.07U_\infty^2$, which was more than two times larger than that of the peaks of $\overline{u^2}$. The Reynolds shear stress $\overline{uv}$ showed an

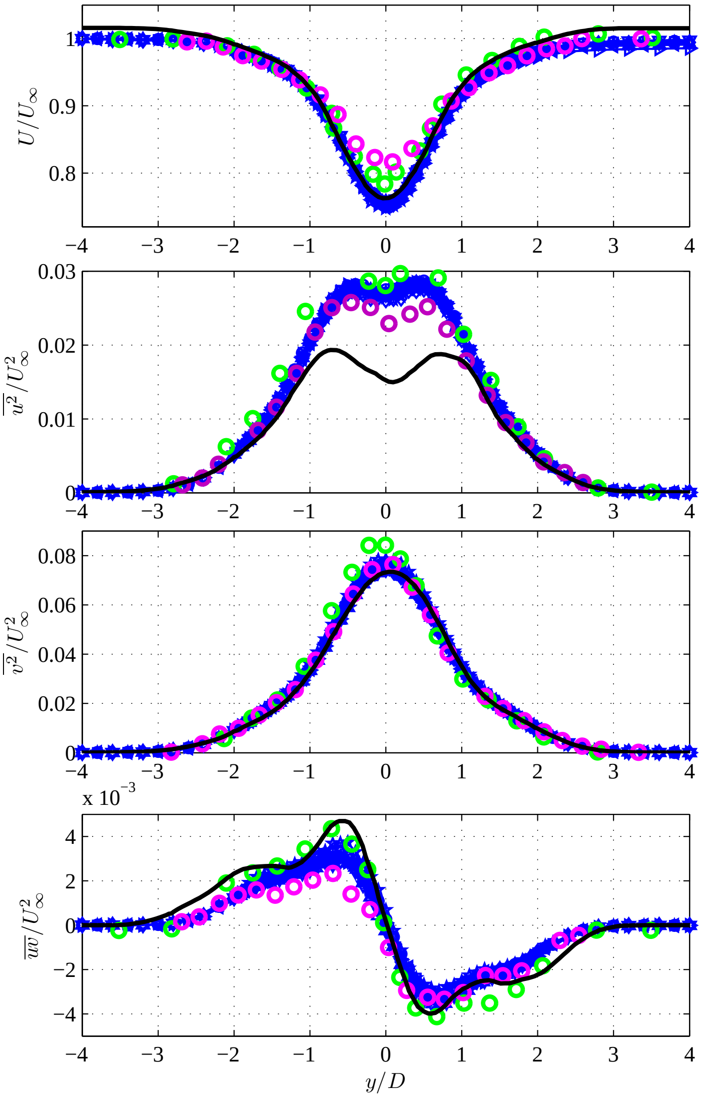

Figure 3.20: Distributions of mean streamwise velocity and Reynolds stresses measured by the X-probe in the presence of SP-probe in simultaneous measurement of velocity and pressure. Results of all the cases of the various SP-probes are shown as various blue symbols and compared with reference data by Zhou and Antonia (1993) (purple circle), Ong and Wallace (1996)(green circle) and present LES (black line).

anti-symmetric profile about $y/D = 0$. It is also shown that the present experimental results strongly agreed with the reference data provided in the previous experiment by (Zhou and Antonia, 1993) and Ong and Wallace (1996).

The results obtained by the present LES are also shown in Fig. 3.20 by the black solid lines. Comparing the experimental and computational results, one can see that while the streamwise normal Reynolds stresses were somewhat underestimated in the computation, the present experimental and the computational results were also in acceptable agreement with each other. In addition, it can be seen that the mean streamwise velocity U by the LES exceeded unity at $y/D \pm 4$, which might be attributable to acceleration of the flow due to the blockage effect of the cylinder.

Figure 3.21 presents the PSD of the fluctuating velocity measured at the center of the wake. The transverse velocity component v shows a significant spike of the

Figure 3.21: Power spectrum density of fluctuating velocity u and v measured at $(x/D,\ y/D) = (10,\ 0)$.

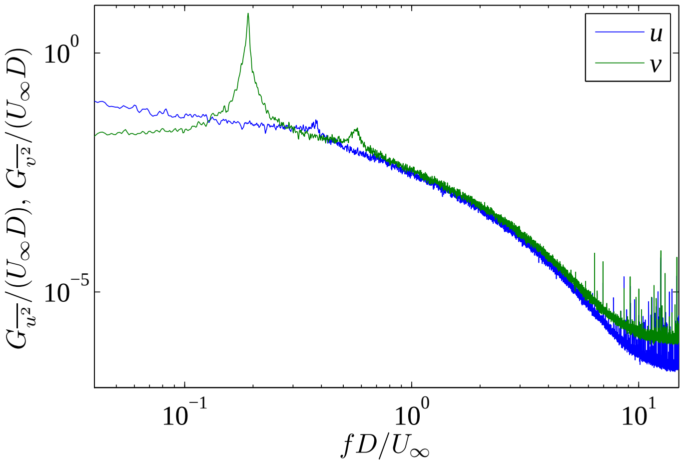

fluctuation at the frequency of $f = 0.19U_\infty/D$ (113 Hz in dimensional frequency). On the other hand, the fluctuation of the streamwise velocity component u did not show any peak at this frequency, but showed a smaller peak at the double of the vortex shedding frequency, $f = 0.38U_\infty/D$, which resulted from effect of vortices shed from both sides of the cylinder.

Figure 3.22 shows the profiles of the root-mean-square of the pressure fluctuation p'. The profiles of p' measured by the various SP-probes agreed well with each other: they have two peaks of the pressure fluctuation beside the wake center similarly to the profile of the streamwise velocity fluctuation $\overline{u^2}$, and the peak magnitude was about

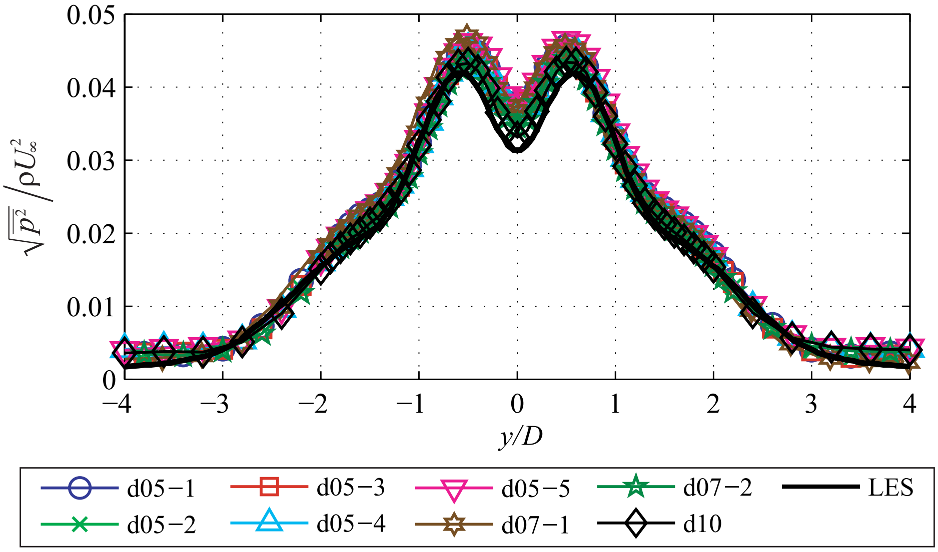

Figure 3.22: Pressure fluctuation $\sqrt{\overline{p^2}}$ at $x/D = 10D$ measured by the various SP-probes in simultaneous measurement of velocity and pressure. Experimental results are presented by various symbols and computational result is shown by a black solid line.

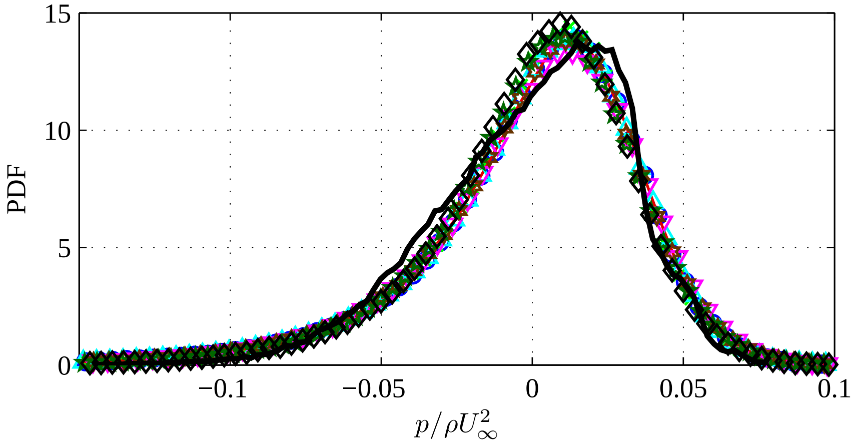

Figure 3.23: Probability density function of pressure fluctuation measured at $(x/D,\ y/D) = (10,\ 0)$. Symbols and black solid line indicate the same results in Fig. 3.22.

$0.045\rho U_\infty^2$. Comparing with the computational results, one can see that the profiles of p' measured by the present experiment were in strong agreement with the computational results.

The probability density function (PDF) of the pressure fluctuation p measured at the wake center $(x/D,\ y/D) = (10,\ 0)$ is presented in Fig. 3.23. The PDFs of p measured by the various SP-probe showed the profiles with negative skewness, and were in good agreement with each other. The computational result shown together also indicated the distribution with negative skewness and agreed well with the experimental results, indicating that the fluctuating pressure was successfully measured in the present measurement.

Figure 3.24 presents the PSD of the pressure fluctuation measured at $(x/D,\ y/D) = (10,\ 0.5)$, comparing the various experimental results with the computational result. The experimental results showed the profiles of the PSD with a significant peak at the Strouhal number of 0.19 and the second peak at 0.38. The computational result also showed similar profile with two obvious peaks, and their peak magnitudes were in good agreement with those of the experimental results, while a certain disagreement was seen in the frequencies of the vortex shedding; the computational result showed the peaks of the PSD at the Strouhal numbers of 0.21 and 0.42. This discrepancy between the vortex shedding frequencies might be attributable to the flow acceleration observed in the LES results, shown in Fig. 3.20a.

The signal-to-noise ratio and the uncertainty of the fluctuating static-pressure measurement by the SP-probe were roughly estimated based on the above measurement results. As illustrated in Figs. 3.18 and 3.19, the fluctuating pressure measured in

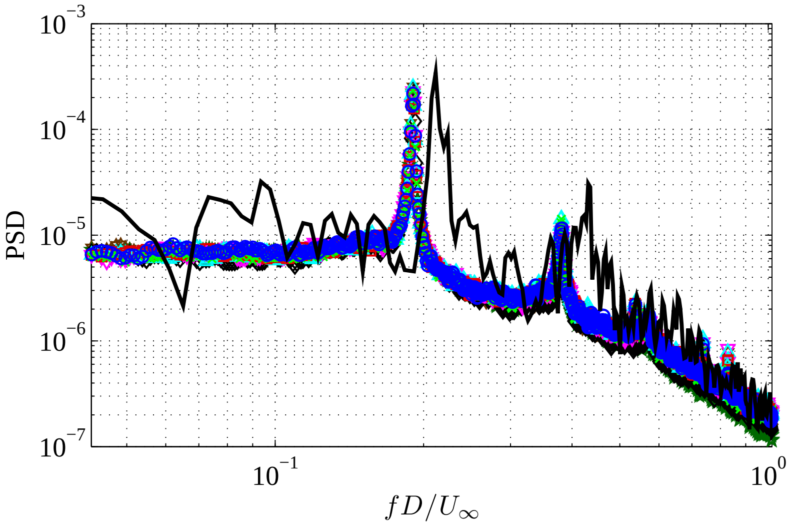

Figure 3.24: Power spectrum density of pressure fluctuation at $(x/D,\ y/D) = (10,\ 0.5)$. Symbols and black solid line indicate the same results in Fig. 3.22.

$|y/D| \geq 3.6$ was mainly the background noise. Hence, the signal-to-noise ratio of the measurement was evaluated as the ratio of the peak magnitude of the measured pressure fluctuation to the pressure fluctuation measured at $y/D = 4.0$. As the values of p' at the peak location and at $y/D = 4.0$ were $4.5 \times 10^{-2}\rho U_\infty^2$ and $3.5 \times 10^{-3}\rho U_\infty^2$, respectively, the signal-to-noise ratio was approximately 13-to-1; this was relatively smaller than that of the velocity measurement by the X-probe, which was roughly evaluated by the same manner to be 35-to-1.

On the other hand, the discrepancy between the experimental and computational results in Fig. 3.22 was approximately $0.005\rho U_\infty^2$ at the wake center, which corresponded to 10% of the peak magnitude of the pressure fluctuation. Hence the uncertainty in the fluctuating pressure measurement by the SP-probe was approximately 10%.

Next, the velocity-pressure correlations $\overline{up}$ and $\overline{vp}$ are presented in Figs. 3.25 and 3.26. In each figure, the results evaluated with/without the correction of the time-lag shown in Sect. 3.4.2 are compared, and the computational results are also shown together by the black solid line. As shown in Fig. 3.25, the profiles of $\overline{up}$ were mainly negative across the wake with two significant negative peaks located near $y/D = \pm 1$. The profiles of $\overline{up}$ measured with the X- and various SP-probes agreed well each other, and were not affected by the correction of the time lag between the velocity and pressure signals. Comparing the experimental and the computational results, one can see that they were in fairly good agreement with each other.

Figure 3.25: Velocity-pressure correlation $\overline{up}$ at $x/D = 10$; (a) without correction of time lag, (b) with correction of time lag. The symbols and solid line indicate the same results as in Fig. 3.22.

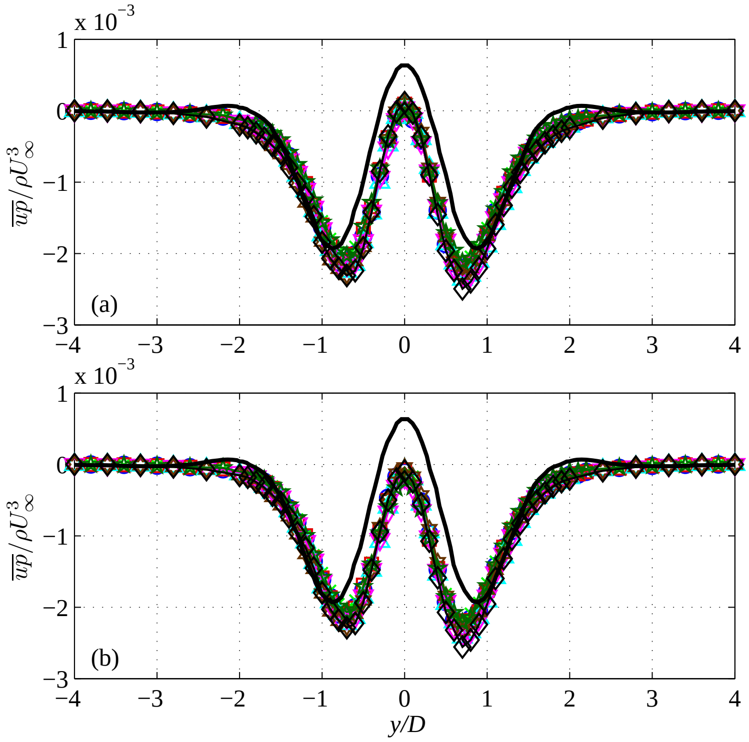

The velocity-pressure correlations $\overline{vp}$ measured by the X- and various SP-probes are shown in Fig. 3.26. The profiles of $\overline{vp}$ were the anti-symmetric profiles about $y/D = 0$, and were similar to each other, while certain quantitative difference in the magnitude of the positive/negative peak at $y = \pm 0.5D$ can be observed. Comparing the profiles evaluated with/without the correction of the time lag, one can obviously see that $\overline{vp}$ sensitively changed its profiles by the time-lag correction. The values in the center region of the wake $-1 \leq y/D \leq 1$ were significantly affected and changed the sign, while the effect of the time-lag correction was not seen much in the outer region of the wake, $|y/D| \geq 1$. Comparing the experimental and the computational results, one can see that the experimental results evaluated with the time-lag correction were in acceptable agreement with the computational results.

The uncertainty in the velocity-pressure correlation measurement was also roughly estimated based on the comparison between the experimental and computational results. In Fig. 3.25b, the discrepancy between the experimental and computational results of $\overline{up}$ was notable at the vortex center, and the deviation was about $0.5 \times 10^{-3} \rho U_\infty^2$. In Fig. 3.26b, the experimental results showed a certain dispersion of about 0.5×10^{-3} at the peak location, and the discrepancy between the experimental and computational results was notable in the region $1 \leq |y/D| 2$; both the dispersion of the experimental results and the deviation between the experimental and computa-

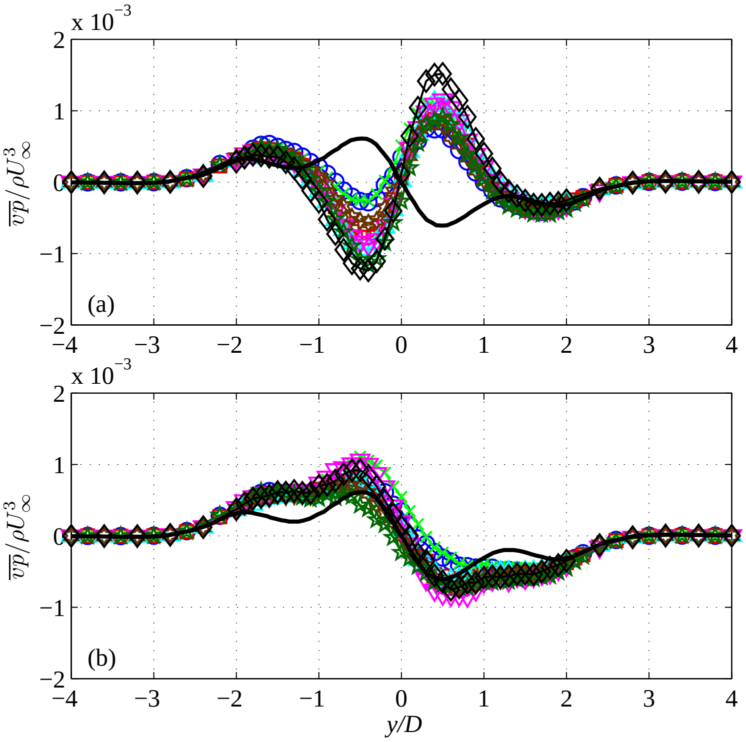

Figure 3.26: Velocity-pressure correlation $\overline{vp}$ at $x/D = 10$; (a) without correction of time lag, (b) with correction of time lag. The symbols and solid line indicate the same results as in Fig. 3.22.

tional results were about $0.5 \times 10^{-3}\rho U_\infty^2$. Therefore, it is reasonable to consider that the uncertainty in the velocity-pressure correlation was about $0.5 \times 10^{-3}\rho U_\infty^2$ for both the measurement of $\overline{up}$ and $\overline{vp}$, which corresponded to 25% and 50% of the peak magnitudes of $\overline{up}$ and $\overline{vp}$, respectively.

3.5 Discussion

For further discussion on the experimental and the computational result of the velocity-pressure correlation, the velocity-pressure cross-correlations $\overline{u(t)p(t+\tau)}$ and $\overline{v(t)p(t+\tau)}$ were evaluated based on the computational results. Figure 3.27 presents the profiles of $\overline{u(t)p(t+\tau)}$ and $\overline{v(t)p(t+\tau)}$ evaluated from the computational results. The experimental results of $\overline{up}$ and $\overline{vp}$ measured by the X- and d05-3 probes (without the time-lag correction) are also shown together by the black circle plot for comparison. It is shown that the profile of $\overline{u(t)p(t+\tau)}$ is insensitive to the values of τ, but $\overline{v(t)p(t+\tau)}$ is sensitively affected; and in the case where $\tau = 0.3$ ms, the computational result of $\overline{v(t)p(t+\tau)}$ agrees well with the experimental result of $\overline{vp}$ without the time-lag correction. It should be noted that this value of τ has almost the same magnitude but the opposite sign of the time lag experimentally observed in Sect. 3.4.2.

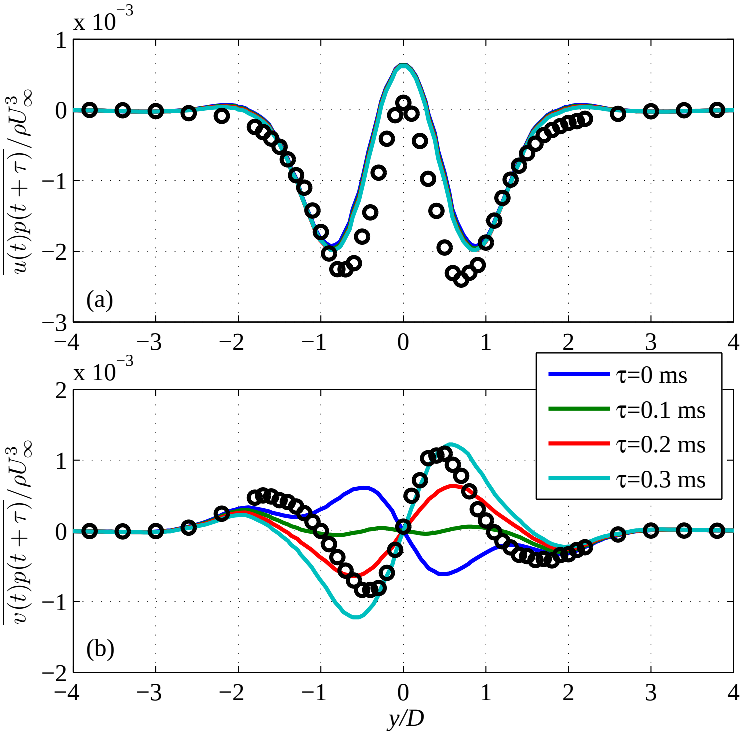

Figure 3.27: Velocity-pressure cross-correlation at $x/D = 10$ evaluated from the computational result: (a) $\overline{u(t)p(t+\tau)}$; (b) $\overline{v(t)p(t+\tau)}$. Experimental result measured by the X- and d05-3 probes is shown by black circles for comparison.

The transport equation of the turbulent kinetic energy k is investigated below in order to further validate the experimental results of the velocity-pressure correlation. The production P_k, convection C_k, and turbulent diffusion D_k^{t}, were evaluated from the experimental results measured by single use of the X-probe as:

$$P_k = -\overline{uv}\frac{\partial U}{\partial y} - \overline{v^2}\frac{\partial V}{\partial y}, \tag{3.18}$$

$$C_k = -U\frac{\partial k}{\partial x} - V\frac{\partial k}{\partial y}, \tag{3.19}$$

$$D_k^{\mathrm{t}} = -\frac{\partial}{\partial y}\left(\frac{\overline{u^2 v} + \overline{v^3}}{2}\right). \tag{3.20}$$

The streamwise gradient of k in Eq. (3.19) was evaluated using values of k measured at $x/D = 10$ and 11. The pressure-diffusion term D_k^{p} was evaluated from the results of the velocity-pressure correlation measurement as

$$D_k^{\mathrm{p}} = -\frac{1}{\rho}\frac{\partial \overline{vp}}{\partial y}, \tag{3.21}$$

respectively. Figure 3.28a presents profiles of the pressure diffusion D_k^p evaluated with/without the time-lag correction based on the measurement results by the X- and d05-3 probes, comparing them with the other terms of the transport equation.

Figure 3.28: Distribution of terms in the transport equation of the turbulent kinetic energy at $x/D = 10$: (a) pressure diffusion, blue ○ (experiment, with time-lag correction), green ○ (experiment, without time-lag correction) and red solid line (LES); turbulent diffusion, ◇ (experiment) and chained line (LES); production, +; convection, ×; (b) dissipation rate obtained based on experimental results; by Eq. (3.22), blue (with time-lag correction) and green (without time-lag correction); by Eq. (3.23), black. Experimental results of pressure-diffusion term were measured by the X- and d05-3 probes and those of the other terms were measured by single use of the X-probe.

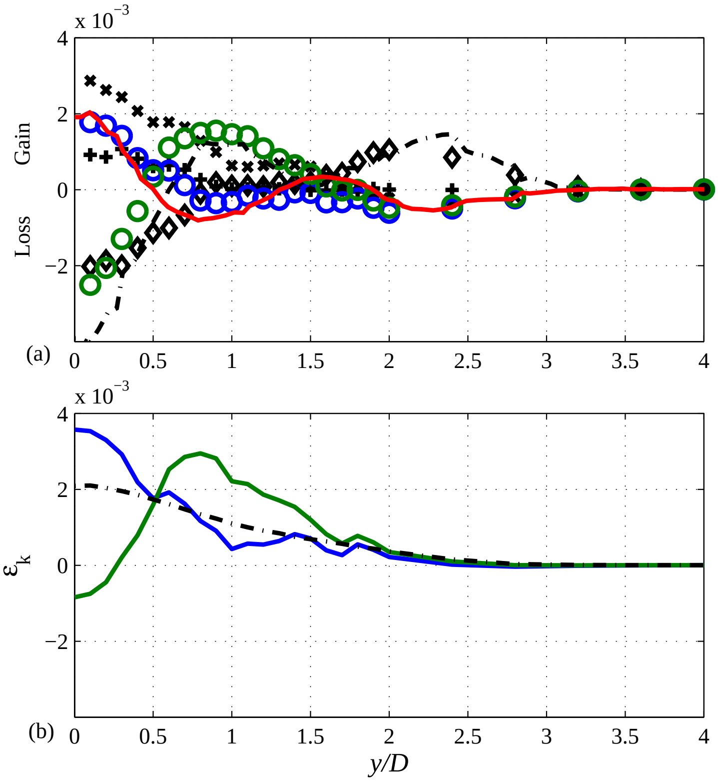

It is shown that the pressure-diffusion term is as large as the other terms regardless with/without the time-lag correction, indicating the importance the role of the velocity-pressure correlation in the transport of k. With the time-lag correction, the profile of the pressure diffusion is similar to the profile of the turbulent diffusion, but with the opposite sign. On the other hand, the profile of the pressure-diffusion D_k^p evaluated without the time-lag correction has a significant negative peak at the wake center and is not similar to that of the turbulent-diffusion D_k^t.

The pressure diffusion and turbulent-diffusion terms evaluated based on the computational results are also shown in Fig. 3.28a for comparison. Comparing the experimental and computational results of the pressure-diffusion term, one can see that the experimental result of the pressure diffusion evaluated with the time-lag correction was in better agreement with the computational result than that obtained without the time-lag correction. The fairly good agreement between the experiment and the computation was also achieved for the turbulent diffusion, while the experimental results were somewhat underestimated at the wake center. It should be mentioned that the computational result of D_k^t was evaluated by Eq. (3.20) omitting the contribution of $\overline{vw^2}$ for fair comparison, but adding $\overline{vw^2}$ does not significantly change the profile of D_k^t.

Figure 3.28b presents the dissipation rate of the turbulent kinetic energy which was indirectly evaluated from the other terms as,

$$\varepsilon_k = P_k + C_k + D_k^{\mathrm{t}} + D_k^{\mathrm{p}}. \tag{3.22}$$

According to the definition, $\varepsilon_k = \nu\overline{(\partial u_i/\partial x_j)^2}$, the dissipation rate ε_k should be always positive. In the case the time-lag correction, the dissipation rate keeps the positive values across the wake, while the profile in the case of without the time-lag correction shows negative values at the wake center due to the significant negative peak of the pressure diffusion.

The dissipation rate was also roughly evaluated from the time series of the fluctuating streamwise velocity measured by single use of the X-probe. According to the Taylor′s frozen hypothesis (e.g., Bernard and Wallace, 2002) and the identity for the isotropic turbulence (e.g., Pope, 2000), the dissipation rate can be obtained as

$$\begin{aligned} \varepsilon_k &= \nu\overline{\left(\frac{\partial u_i}{\partial x_j}\right)^2} \approx 15\nu\overline{\left(\frac{\partial u}{\partial x}\right)^2} \\ &\approx 15\nu\overline{\left(-\frac{1}{u}\frac{\partial u}{\partial t}\right)^2}. \end{aligned} \tag{3.23}$$

The dissipation rate evaluated with Eq. (3.23) are also plotted in Fig. 3.28b and compared to those indirectly evaluated by Eq. (3.22). It is shown that the dissipation rate evaluated with the time-lag correction are in better agreement with that evaluated by Eq. (3.23). Thus, investigation on the budget of the transport equation of the turbulent kinetic energy supports that the experimental results of $\overline{vp}$ evaluated with the time-lag correction is more feasible.

The velocity-pressure correlation $\overline{vp}$ is found to be quite sensitive to the time lag between the velocity and pressure signals while $\overline{up}$ is insensitive. Figure 3.29 shows the variation of the velocity-pressure cross-correlation with the time lag measured at $(x/D,\ y/D) = (10,\ 0)$ (by the probe d05-3, again, for instance). Due to the periodic fluctuation of the velocity and the pressure, $\overline{u(t)p(t+\tau)}$ and $\overline{v(t)p(t+\tau)}$ indicates the periodic variation with τ. In the variation of $\overline{u(t)p(t+\tau)}$, the node is near $\tau = 0$ s while the anti-node is near $\tau = 0$ s in the variation of $\overline{v(t)p(t+\tau)}$. Thus, $\overline{v(t)p(t+\tau)}$ is quite sensitive to change of τ around $\tau = 0$ s, while $\overline{u(t)p(t+\tau)}$ is not.

In addition, the measurement of $\overline{vp}$ was found to be also sensitively affected by the geometrical configuration of the pressure-sensing holes, while the measurements of p' and $\overline{up}$ were, again, insensitive. Details is described in Appendix B.

Figure 3.29: Variation of cross-correlation coefficients against time lag τ measured at $(x,y) = (10D, 0.5D)$ by probe d05-3.

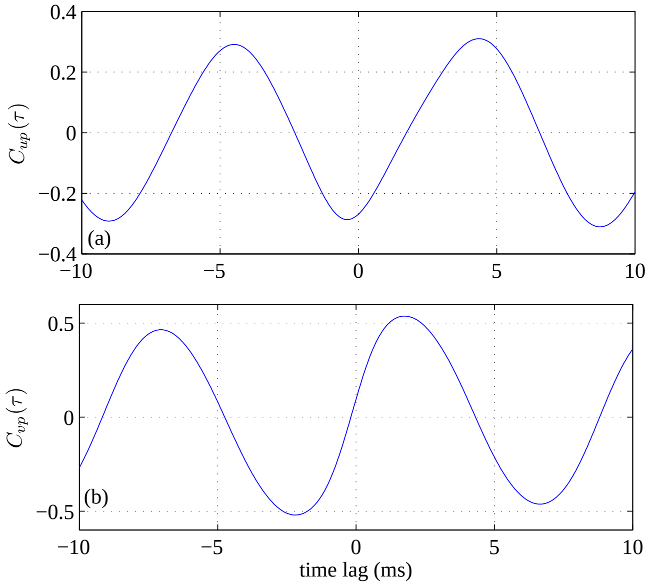

3.6 Summary of this chapter

Simultaneous measurement of fluctuating velocity and pressure by an SP- and X-probes was performed in a near wake of a circular cylinder, in order to strengthen reliability of the measurement method. For this purpose, the measurement results were validated by a quantitative comparison with reference data obtained by a large-eddy simulation, and the effect of geometry of the static-pressure probe was examined by comparing the performance of the various pressure probes with different diameters and lengths.

It was found that the interference between the probes mainly depends on the tube diameter of the static-pressure probe, and only weakly on the length of the tip section. The smallest probe distance achieved in the present measurement was 3.0 mm, which was comparable to the integral length scale of the flow field. The error due to the low spatial resolution was found to be not significant based on the computational result.

The signal-to-noise ratio of the static-pressure measurement was approximately 13-to-1, and the experimental results of the pressure fluctuation was in strong agreement with the computational result.

For evaluation of the velocity-pressure correlation, a certain time lag between the velocity and pressure signals was observed in the experiment, and it was corrected based on the preliminary measurement results. It was revealed that the measurement of correlation between the transverse velocity component and the static pressure $\overline{vp}$ was extremely sensitive to such small time lag between the signals, despite the measurement of correlation between the streamwise velocity component and pressure $\overline{up}$

was insensitive. With the time-lag correction, the experimental results of the velocity-pressure correlation were in quantitatively good agreement with the computational results, and reliability of the measurement technique was confirmed.

Therefore, it can be reasonably concluded that combination of a hot-wire probe and a static-pressure probe is a reliable measurement technique for velocity-pressure correlation measurement, but careful attention is necessary for accurate measurement of correlation between fluctuating pressure and lateral velocity component.

Chapter 4

Simultaneous Measurement of Three Velocity Components and Pressure in Three-Dimensional Turbulent Flow

4.1 Motivation and Outline of This Chapter

Simultaneous measurements of fluctuating velocity and pressure in earlier studies have been mainly performed in two-dimensional turbulent flow fields, such as a wake of a circular cylinder (those described in Chap. 3 and, e.g., Kobashi et al., 1960; Shirahama and Toyoda, 1993), a planer jet (Sakai et al., 2007; Terashima et al., 2012), and a planer mixing layer (Naka et al., 2006). However, the most of practical engineering flows are the three-dimensional turbulent flow, and it is, therefore, important to develop a measurement technique applicable to such three-dimensional turbulent flows.

The measurement technique in which a hot-wire probe is aligned side-by-side with a static-pressure probe is not appropriate for measurement in three-dimensional flow, because the hot-wire probe may be in the wake of the pressure probe depending on the flow direction. On the other hand, the technique proposed by Naka and Obi (2009), in which a total-pressure probe is inserted to the measuring volume of a hot-wire probe, is less likely to be affected by the probe interference.

In this chapter, a technique for simultaneous measurement of the three velocity components and the fluctuating pressure is developed on the basis of the work by Naka and Obi (2009), in order to investigate the velocity-pressure correlation in three dimensional turbulent flows. A triple hot-film probe (THF-probe) was used for the velocity measurement to capture all the three velocity components, and a miniature bent-type total-pressure probe (TP-probe) was developed for combination with the

THF-probe. The fluctuating static-pressure was evaluated based on the fluctuating velocity and total pressure directly measured by the THF- and TP-probes, and the formula for static-pressure evaluation proposed by Naka and Obi (2009) was modified in order to properly incorporate the contribution of the cross-flow velocity components. The THF-probe was carefully calibrated in the presence the TP-probe by means of the look-up-table method, so that the effect of probe interference was taken into account. The newly developed measurement technique was applied to a turbulent wingtip vortex flow, and the role that the velocity-pressure correlation plays was investigated.

4.2 Indirect Evaluation of Static-Pressure Fluctuation

In the previous study (Naka and Obi, 2009), the fluctuating static pressure p_s is calculated from the fluctuating total pressure p_t and the velocity in the streamwise direction using following relationship:

$$p_s = p_t - \frac{\rho}{2}\left(2Uu + u^2 - \overline{u^2}\right) + \frac{\rho}{2}\frac{\partial u}{\partial t}\Delta x, \tag{4.1}$$

where U and u are the mean and fluctuating streamwise velocity components, respectively, and Δx is the probe distance. Eq. (4.1) is derived from the unsteady Bernoulli equation in differential form along the streamline stagnating onto the tip of the TP-probe, and the velocity along the streamline is replaced by the streamwise velocity component assuming that the flow angle of attack is not very large.

In the present study, the velocity magnitude v_s is used instead of u to obtain a better applicability to flows at large angles of attack. Accordingly, the relationship between the instantaneous velocity and pressure is written as

$$\tilde{p}_s = \tilde{p}_t - \frac{\rho}{2}\tilde{v}_s^2 + \frac{\rho}{2}\frac{\partial \tilde{v}_s}{\partial t}\Delta x, \tag{4.2}$$

where $\tilde{[]}$ denotes the instantaneous quantity. Here, $\tilde{v}_s$ is evaluated as $\tilde{v}_s = \sqrt{\tilde{u}^2 + \tilde{v}^2 + \tilde{w}^2}$, with $\tilde{u}$, $\tilde{v}$, $\tilde{w}$ being the instantaneous velocities in x-, y-, z-directions, which are measured by the THF-probe. The fluctuating components are then obtained by further applying the Reynolds decomposition to Eq. (4.2),

$$p_s = p_t - \frac{\rho}{2}\left(2V_s v_s + v_s^2 - \overline{v_s^2}\right) + \frac{\rho}{2}\frac{\partial v_s}{\partial t}\Delta x. \tag{4.3}$$

The difference between the results obtained by Eqs. (4.1) and (4.3) represents the influence of cross flow on the pressure measurement. Its remarkably large effect on the

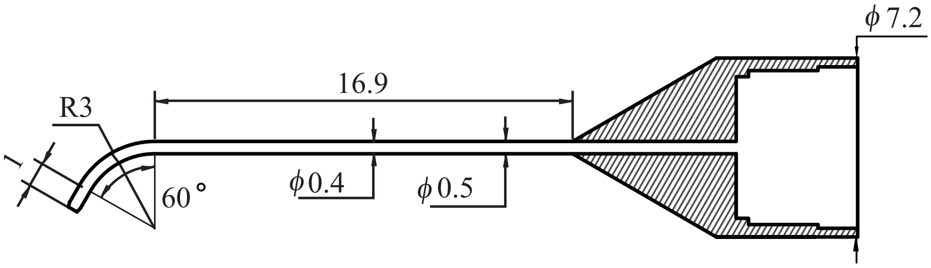

Figure 4.1: Schematic of the bent-type total pressure probe (dimensions in mm)

wingtip vortex measurements will be demonstrated by inspecting the velocity-pressure correlation.

4.3 Measurement Technique

4.3.1 Measurement of Fluctauting Total Pressure

A miniature bent-type probe schematically shown in Fig.4.1 was used for the fluctuating total-pressure measurement. It consists of a bent thin pipe and the joint-screw part. The inner and the outer diameters of the pipe were 0.4 mm and 0.5 mm, respectively, and the tip section had a straight part with a length of 1.0 mm, and the following part was bent by 60° with a curvature radius of 3 mm, so that the tip could be inserted into the measuring volume of the THF-probe from the side. The tip was rounded in order to maintain good angle response.

The error caused by the cross flow in the fluctuating total-pressure measurement was already well investigated by Naka and Obi (2009) using a total-pressure probe with the same inner- and outer-diameter, and it was found that the cross-flow error is less than 2% of $0.5\rho U_\infty^2$ (ρ and U_∞ are the density of the fluid and the free stream velocity, respectively). Although the present TP-probe was bent, the angle response of this probe can be regarded the same as that of the probe used by Naka and Obi (2009).

The dynamic response of the TP-probe was explored through the same manner as performed in Sect. 3.2.1.1 using the sound signal generated by a loud speaker. Two condenser microphones (one with a TP-probe and the other without) were mounted in front of a loud speaker placed in an anechoic box. The loud speaker generated sound signals with the frequency in the range from 40 Hz to 10 kHz, and the pressure fluctuation was measured simultaneously by the two condenser microphones. The amplitude ratio A and the phase delay $\Delta\theta$ at each frequency of the pressure fluctuation were evaluated by comparing the pressure signals. Figure 4.2 shows the variation of

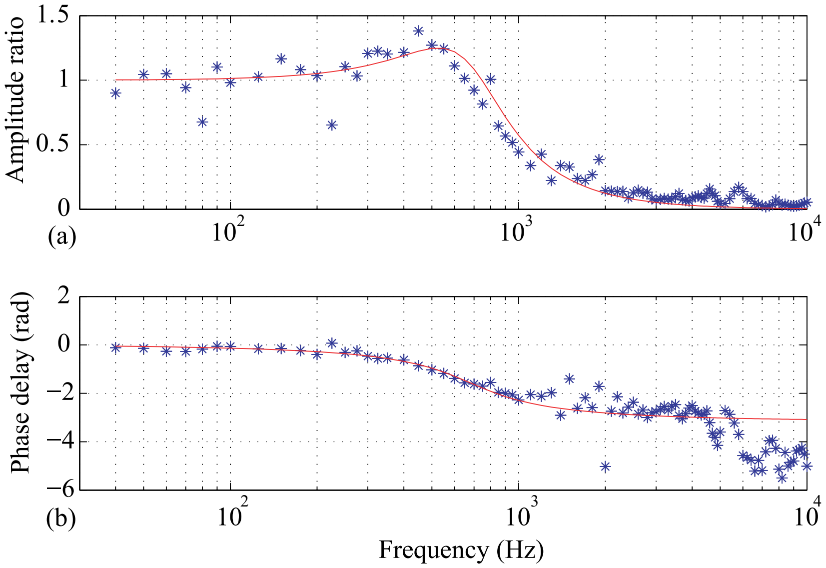

Figure 4.2: dynamic response of the TP-probe; (a) amplitude ratio A, (b) phase delay $\Delta\theta$

the amplitude ratio and the phase delay of the pressure fluctuation measured by the microphone with the TP-probe. The amplitude increases for frequencies near 500 Hz and decays at higher frequency ranges. The phase also delays in the high frequency range.

In order to compensate for these frequency responses, the oscillating air inside the pipe was modeled as the forced damping oscillation system, and the dynamic response was approximated to the solution of the normalized equation of motion according to the following expression:

$$A = \frac{1}{\sqrt{(1-\omega^*)^2 + (2\zeta\omega^*)^2}}, \tag{4.4}$$

$$\Delta\theta = \tan^{-1}\left(\frac{2\zeta\omega^*}{1-\omega^{*2}}\right), \tag{4.5}$$

where, ω^* and ζ are the frequency of the sound signal ω normalized by the natural frequency of the air inside the TP-probe ω_n and the damping ratio, respectively. The values of ω_n and ζ were optimized by fitting to the data by using the "`fminsearch`" function available in MATLAB ®, and the amplitude ratio and the phase delay calculated by Eqs. (4.4) and (4.5) were indicated by the red lines in Fig. 4.2. The amplitude and phase of the pressure fluctuations were corrected using these equations in post processing by the similar manner described in 3.2.1.4.

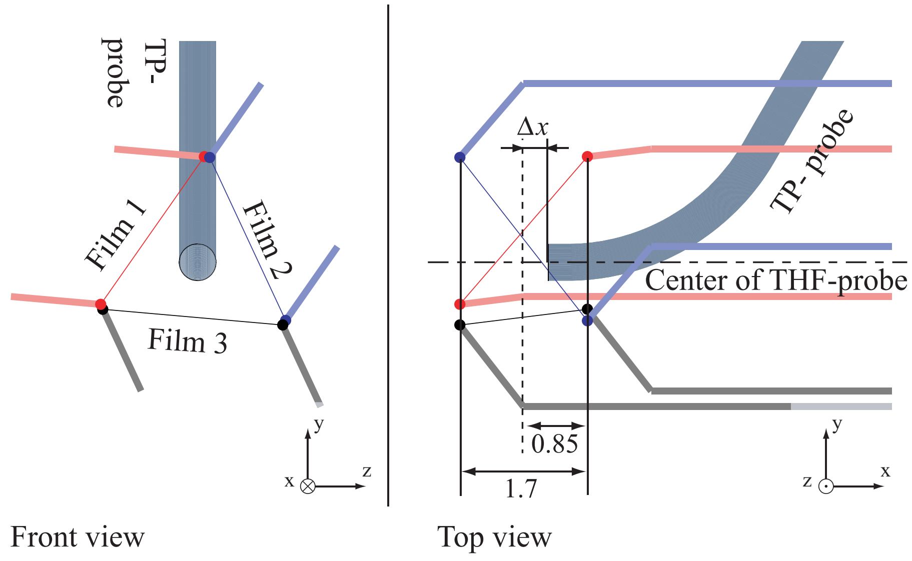

Figure 4.3: Arrangement of new combined probes

4.3.2 Arrangement of TP- and TPF-Probe

The arrangement of the new combined probe, which consists of the TP- and the THF-probe is shown in Fig. 4.3. Each film of the THF-probe had the sensitivity length of 1.25 mm (the whole length was 3 mm), and each film was positioned perpendicular to other two. The measurement volume of the THF-probe was a sphere with a diameter of 3 mm. The TP-probe was inserted inside the measurement volume of the THF-probe for the simultaneous measurement of velocity and pressure. The mouth of the TP-probe was set normal to the axis of the THF-probe, and the distance between the tip of the TP-probe and the center of the measurement volume of the THF-probe, Δx, was determined by the investigation of the effect of the probe proximity as described in Sect. 4.3.3.

4.3.3 Determination of Probe Distance

The distance between the center of the measurement volume of the THF-probe and the tip of the TP-probe Δx should be determined by taking both the probe interference and the spatial resolution of the combined probe into consideration; Δx should be large enough to avoid the probe interference, but use of Eq. (4.2) for evaluation of the static pressure fluctuation requires strong correlation between the total pressure measured by the TP-probe and the dynamic pressure measured by the THF-probe. The location of the tip of the TP-probe inside of the measurement volume of the THF-probe should be

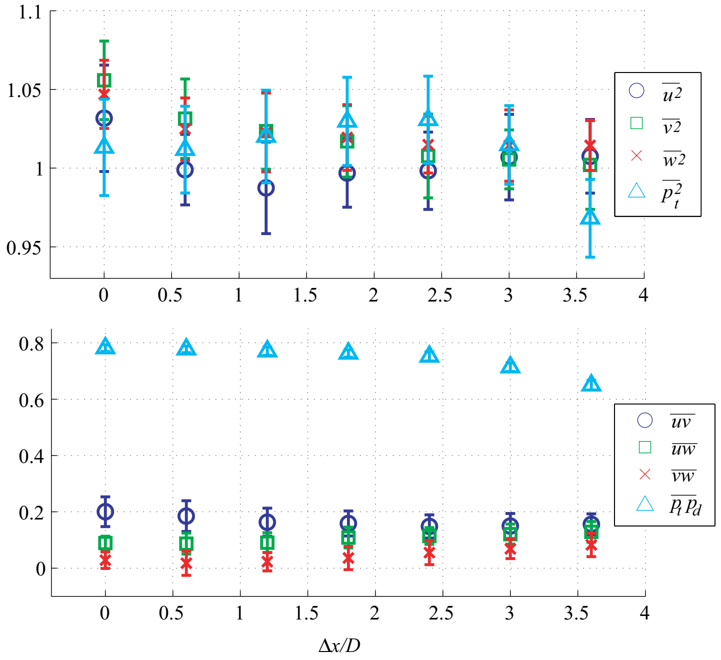

Figure 4.4: Effect of probe proximity measured in a turbulent wingtip vortex; (top) variation of Reynolds normal stresses and total-pressure fluctuation, (bottom) correlation coefficients between three velocity components and that between total pressure and dynamic pressure.

determined after thorough consideration of the trade-off. The effect of probe proximity was experimentally observed prior to each of the measurements in a wingtip vortex.

The preliminary measurement was undertaken at the vortex center in the streamwise location of one-chord-length distance downstream from the trailing edge of an airfoil. The fluctuating velocities and total pressure were simultaneously measured with different probe distance Δx, and the sampling rate and the sampling time were same as in the main experiments. The variations of the measured statistics against the probe distance are shown in Fig. 4.4, with the probe distance scaled by the diameter of the TP-probe d. The error bar indicates the range of 95% confidence interval evaluated based on 12 samples of each statistics. Figure 4.4(a) shows the root-mean-square values of the velocity/total-pressure fluctuation, normalized by the reference values measured by single use of the THF- and TP-probes, respectively. Figure 4.4(b) presents variation of the cross correlation coefficients between the different velocity components or between the total- and dynamic-pressure fluctuations. It is shown that the turbulence intensities $\overline{u^2}$, $\overline{v^2}$, $\overline{w^2}$, and $\overline{p_t^2}$ were almost equal to the reference values between $\Delta x/d = 1$ and 2. The correlation coefficients between three velocity components, which should be zero at the center of the wingtip vortex, approached to zero at $\Delta x/d = 2$. The correlation between the total pressure fluctuation p_t and the dynamic pressure fluctuation p_d gradually decreased as the probe distance increased. In order to retain the correlation between p_t and p_d and, at the same time, reduce the interference between the probes, the optimal probe distance was determined to be $1.2D$,

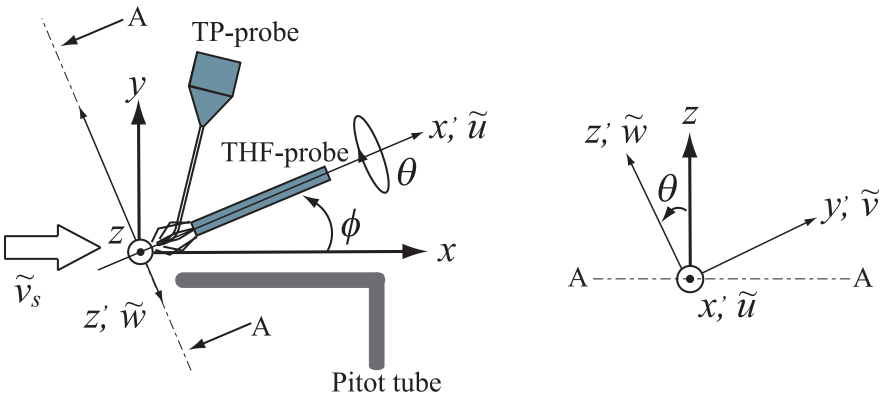

Top view

Section AA

Figure 4.5: Configuration at calibration of THF-probe

which corresponds to 0.6 mm, based on these observation. With this probe distance, the tip of the TP-probe was placed inside the measurement volume of the THF-probe. Therefore, the spatial resolution of the new combined probe was equivalent to that of single use of the THF-probe; the sphere with a diameter of 3.0 mm.

4.3.4 Calibration of THF-probe

The output signals from the films of the THF-probe were converted into the three components of instantaneous velocity vector by means of the look-up-table method. Since the static pressure fluctuation is evaluated using the velocity, the accuracy of the velocity measurement is important for static pressure fluctuation measurement. The look-up-table method was chosen because it does not require any simplification such as neglecting non-orthogonal configuration of sensors and the flow angle dependency of coefficients in Jϕrgensen’s equation in contrast with the calibration technique based on concept of the effective cooling velocity (Jørgensen, 1971).

In order to take into account the effect of the probe interference, the THF-probe was mounted with the TP-probe inside of its measuring volume during the calibration. The output signals from the three sensors, E_1, E_2, and E_3, were recorded with yaw- and the rotation-angles of the probe. These angles represent the difference between two coordinate systems as illustrated in Fig. 4.5 where the global coordinate system xyz was fixed to the laboratory while the probe coordinate system $x'y'z'$ was fixed to the probe. By introducing the relationship between the instantaneous velocity $\tilde{v}_s$ and the

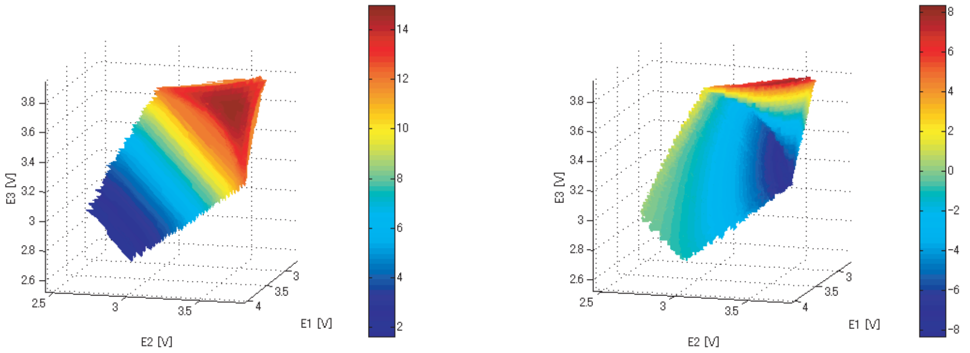

(a) $\tilde{u}$ v.s. voltages.

(b) $\tilde{v}$ v.s. voltages.

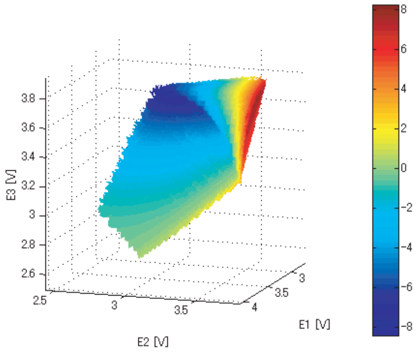

(c) $\tilde{w}$ v.s. voltages.

Figure 4.6: Iso-contour of the three velocity components, $\tilde{u}$, $\tilde{v}$ and $\tilde{w}$, against the combination of the output voltages of the THF-probe.

velocity components $\tilde{u}$, $\tilde{v}$, and $\tilde{w}$, which are defined on the probe coordinate system,

$$\tilde{u} = \tilde{v}_s \cos\phi, \tag{4.6}$$

$$\tilde{v} = \tilde{v}_s \sin\phi \cos\theta, \tag{4.7}$$

$$\tilde{w} = \tilde{v}_s \sin\phi \sin\theta, \tag{4.8}$$

where ϕ and θ are the yaw- and the rotation-angles, respectively, one can determine the direction of measured velocity with respect to the laboratory coordinate from the relationship between ϕ, θ, E_1, E_2, and E_3. The calibration data were obtained at various $\tilde{v}_s$, ϕ, and θ: 2.5 m/s $\leq \tilde{v}_s \leq$ 10.2 m/s (4 points), $0^\circ \leq \phi \leq 33^\circ$ (8 points) and $0^\circ \leq \theta \leq 360^\circ$ (31 points) giving 960 combinations of $\tilde{u}$, $\tilde{v}$, $\tilde{w}$, E_1, E_2 and E_3 in total. The iso-contours of the three velocity components on the typical look-up table are presented Fig 4.6. In addition, samples falling out of the look-up-table were converted using the effective angle technique with a coefficient optimally determined (Ligeza and

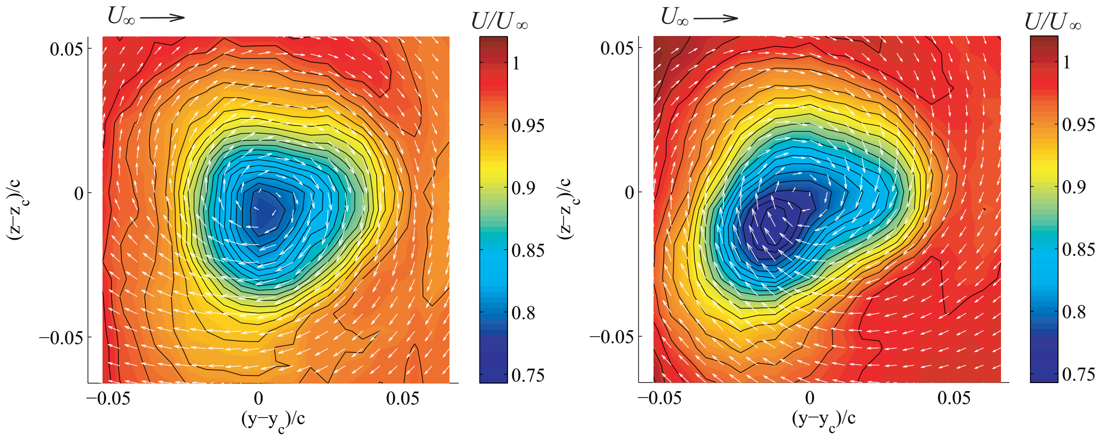

(a) Single use of THF-probe.

(b) Combined probe (calibrated without TP-probe).

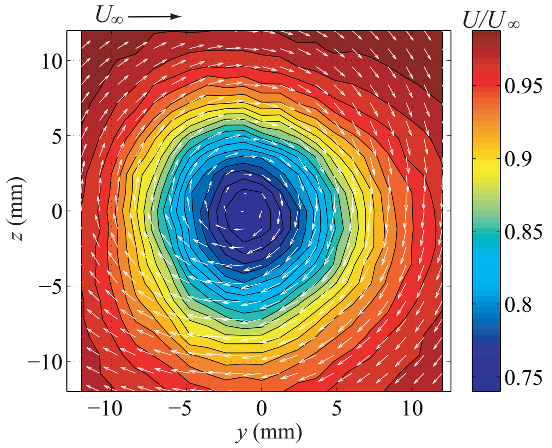

(c) Combined probe (calibrated with TP-probe).

Figure 4.7: Effect of existence of TP-probe inside the measuring volume of THF-probe. Means streamwise velocity at $x/c = 1.0$ (c is chord length of airfoil) are compared.

Socha, 2007).

The effect of calibrating the THF-probe in the presence of the TP-probe is demonstrated in Fig. 4.7. The distribution of the mean streamwise velocity at $x/c = 1$ (x and c are the streamwise location from the trailing edge of the airfoil and the chord length, respectively) measured by single use of THF-probe is compared with those measured by the new combined probe. The color indicates the values of the mean streamwise velocity, and the white arrows show the mean cross-flow components. Figure 4.7a presents the results measured by single use of the THF-probe, and one may notice that the shape of the contour shows somewhat triangular shape, which may be attributable to the non-axisymmetric configuration of the hot-film sensors; due to the non-axisymmetric sensor configuration, the measurement range of flow-angle of the

THF-probe, so-called "*the acceptance domain*" was not axisymmetric (e.g., Bruns and Dengel, 1998; Roseman et al., 1996), and consequently the sensitivity to the flow direction was non-axisymmetric.

Figures 4.7b and c compare the results measured by the new combined probe calibrated with and without the TP-probe. It is obviously shown that the result obtained by the calibration without the TP-probe was affected by the probe interference, although the probe distance was determined based on the investigation of the effect of the probe interference. On the other hand, the result obtained by the calibration with the TP-probe agrees well with that measured by single use of the THF-probe.

4.3.5 Instruments and Data Processing

A commercial triple hot-film probe (Dantec, 55R91) was used for measurement of three velocity components with a constant temperature anemometer (CTA, Kanomax, 1011). For the fluctuating pressure measurement, the same condenser microphone, the pre- and the main-amplifier as in Chap. 3 were used with the TP-probe. The analog signals from the CTA and the pressure-measuring system were acquired by a 16-bit A/D board (PCI-6221, Instrument) with the sampling rate of 10 kHz after through an analog low-pass filter operated with the cut-off frequency of 2 kHz.

The dynamic response of the TP-probe was compensated for by the same manner described in Sect. 3.2.1.4. The measured pressure signals were Fourier transformed. The amplitude change and the phase delay at each frequency were evaluated using Eqs. (4.4) and (4.5), and the Fourier coefficients of the pressure signals were corrected by Eq. 3.5. The signals of the total pressure fluctuation was reconstructed based on the corrected Fourier coefficient by Eq. 3.6. It should be also mentioned that the temperature drift on the CTA output and the phase delay caused by the electric circuit in the microphone and the pre-amplifier was also corrected by the same manner described in the previous chapter.

The reduction of the background noise contained in the total-pressure signals was also conducted as described in Sect. 3.2.1.4. The secondary TP-probe that had the identical geometric configuration to that of the main TP-probe was placed at the same streamwise location but outside the turbulent shear layer, and monitored the background noise. The filter coefficient was optimally determined by the signal measured by the secondary probe, and the background noise in the signals measured by the main probe was reduced.

Figure 4.8: Typical temperature drift of CTA output (with free steam velocity of 9.5 m/s)

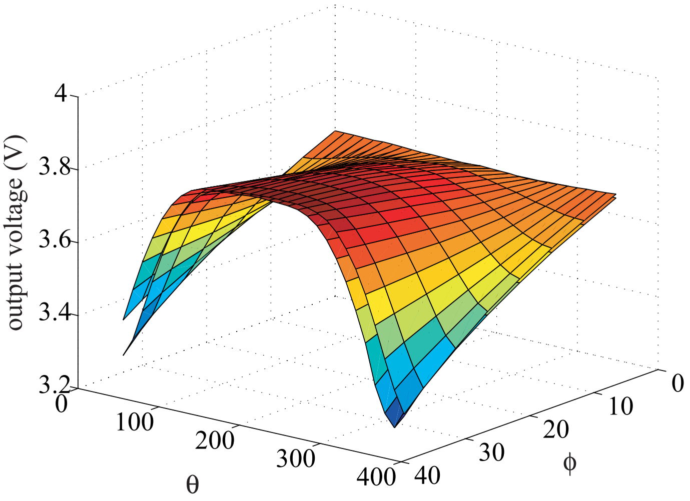

The use of Eq. (4.2) requires the frequency characteristics of velocity and pressure signals to be identical. The condenser microphone does not capture signals with frequencies lower than 20 Hz, and the pressure fluctuation at frequencies higher than 650 Hz is attenuated as shown in Fig. 4.2. Therefore, the band-pass filtering was applied also in this experiment to both of the velocity and pressure signals before applying Eq. (4.1) or (4.3). The passed frequency range was from 25 Hz to 650 Hz, and the MATLAB® function "`filtfilt`" was used to apply the filtering as in the previous Chapter. In the following section, the filtered signal was used only for the calculation of the pressure-related statistics, such as the static pressure fluctuation and velocity-pressure correlations, and the velocity statistics, such as the mean velocity and Reynolds stress, were calculated from the unfiltered signals.

4.3.6 Uncertainty Analysis

The random error analysis was also conducted for the measurement in the turbulent wingtip vortex by the same manner described in Sect. 3.2.5. As the number of the measurement points was large in this experiment, the integration time for statistics evaluation was 30 s at each measurement point, so that the total measurement-duration did not exceeds 4-5 hours. (If the measurement duration was too long, the temperature drift of the CTA output may seriously contaminate the measurement result). The uncertainty by the random error with this integration time was evaluated to be, as a ratio to the peak value of the each quantity, 0.4% in evaluation of the mean streamwise velocity, 5% in evaluation of the Reynolds stresses.

The systematic error caused by the temperature drift was also checked by the same manner described in the previous chapter. Figure 4.8 shows the typical change in the CTA output measured in the calibration of the THF-probe before and after the experiment run. The surfaces in the figure indicates the variation of the output voltage from one of the sensor of the THF-probe against various yaw and pitch angles under a constant free-stream velocity; the upper and lower surfaces indicate the calibration results before and after the experiment run, respectively. Although the output voltages measured after the experiment were corrected based on Eq. (3.7), a certain shift of the CTA output can be seen between the before- and after-calibrations. By the similar manner described in Sect. 3.2.5, the error caused by the temperature shift was evaluated to be 7% of the free stream velocity.

The other possible cause of the systematic error, such as insufficient of the spatial resolution of the combined probe and the phase lag between the velocity and pressure signals. The overall accuracy of the fluctuating static-pressure measurement will be discussed by a comparison with reference data measured by single use of the SP-probe in Sect. 4.4.2.2.

4.4 Velocity-Pressure Correlation Measurement in a Turbulent Wingtip Vortex

A turbulent wingtip vortex was chosen as the test case to perform the simultaneous measurement of three velocity components and pressure. As the wingtip vortex increases the drag and decreases the lift force acting on the wing, there have been a number of studies on the wingtip vortex by both experimental and numerical approaches from industrial point of view. Several measurements have been performed to characterize the wingtip vortex (e.g., Birch and Lee, 2005; Chow et al., 1997; Devenport et al., 1996; Gerontakos and Lee, 2006; Heyes et al., 2004), and there are also some computational studies (e.g., Craft et al., 2006; Duraisamy et al., 2007); in addition, some attempts to control the wingtip vortex have been also reported (e.g., Boesch et al., 2010; Margaris and Gursul, 2006; Okada and Hiraoka, 2003).

On the other hand, the wingtip vortex flow is a representative example of a three-dimensional turbulent flow field associated with coherent vortex structure. The swirling motion of fluid in the wingtip vortex produces significant gradients of both the velocity and pressure, and the unsteady motion, which is called *meandering*, results in significant velocity and pressure fluctuations. Therefore, it is expected that the velocity-pressure correlation plays an important role in the transport phenomena in this flow, but the number of earlier studies which focus on this point of view is only few.

Figure 4.9: Experimental condition of velocity-pressure correlation measurement in a turbulent wingtip vortex.

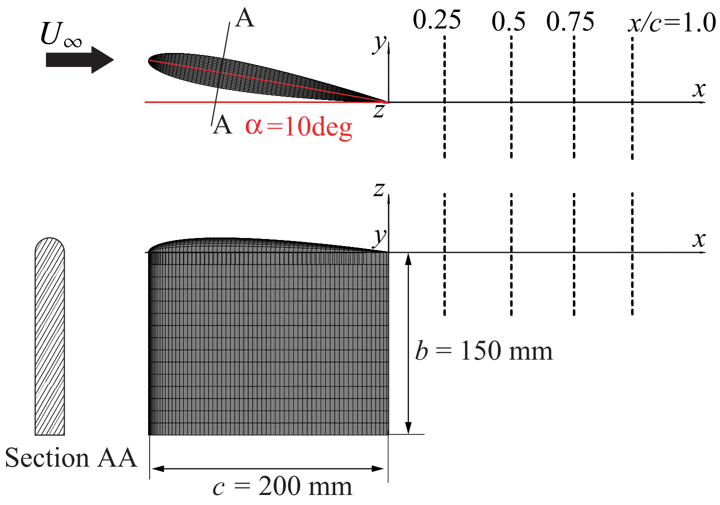

Table 4.1: Measurement range and spacing between measuring points at each streamwise location.

x/c	Δy, Δz	measurement range
0.25	0.8 mm	-1 mm$\leq y \leq$15 mm, -10 mm$\leq z \leq$6 mm
0.5	1.0 mm	-4 mm$\leq y \leq$12 mm, -11.5 mm$\leq z \leq$4.5 mm
0.75	1.0 mm	-8,5 mm$\leq y \leq$11.5 mm, -12.5 mm$\leq z \leq$7.5 mm
1.0	1.2 mm	-14.5 mm$\leq y \leq$9.5 mm, -13.5 mm$\leq z \leq$10.5 mm

4.4.1 Experimental Condition

The condition of the simultaneous measurement of velocity and pressure is schematically shown in Fig. 4.9. A blowing wind tunnel with exit square cross section of 350×350 mm^2 was used, and a NACA0012 wing model with a chord length of $c = 200$ mm and a semi-span length of $b/2 = 150$ mm was mounted in the immediate downstream of the exit of the wind tunnel. The angle of attack α was fixed at 10 °, and the free-stream velocity and turbulence intensity were 9.5 m/s and 0.6 %, respectively; consequently, the Reynolds number based on the chord length and the free stream velocity $Re_c = U_\infty c/\nu$ was 1.4×10^5.

The origin of the Cartesian coordinate system was defined at the end of the trailing edge of the airfoil, and x-, y-, and, z-axes were taken in the streamwise, transverse, and spanwise directions. Measurements were performed on planes perpendicular to the $x-$axis at various streamwise locations, $x/c = 0.25$, 0.5, 0.75, and 1.0. The number of the measurement points at each streamwise location was 21 points in each $y-$ and $z-$directions, namely 441 points in total. The measurement range and the spacing between the measurement points at each streamwise location were chosen according to the location and the size of the wingtip vortex, and they are summarized in Table 4.1.

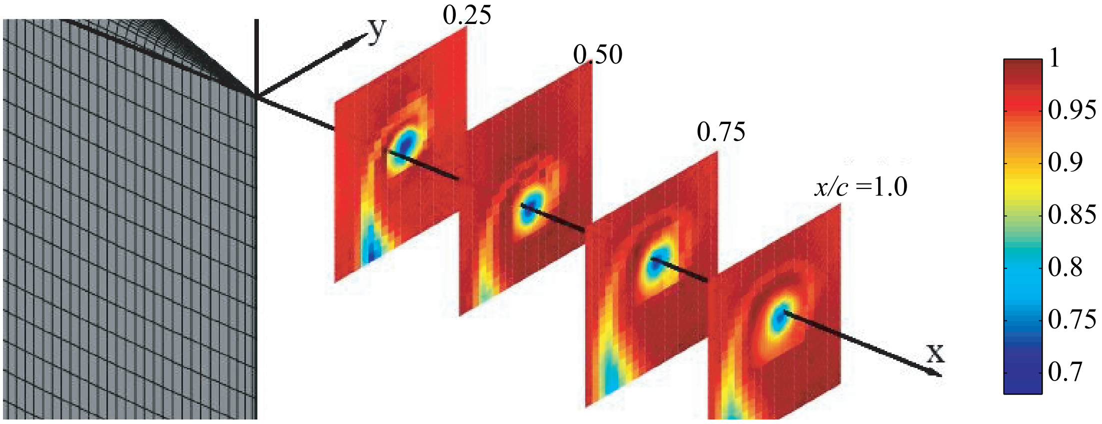

Figure 4.10: Development of mean streamwise velocity distribution

4.4.2 Results

4.4.2.1 Velocity measurement

Development of the mean streamwise velocity and the Reynolds normal stresses are presented in Figs. 4.10 and 4.11. The values are scaled by the free-stream velocity U_∞. It should be mentioned that the distributions measured with the measurement range and the point spacing given in Table 4.1 are superimposed upon those measured with a wider measurement range and point spacing (Δy, Δz=3 mm), in order to capture an entire picture of the wingtip vortex at each streamwise location. It is shown in Fig. 4.10 that the wingtip vortex changed its location across x-axis as it went downstream, and the minimum value at the vortex center increased from $0.75U_\infty$ at $x/c = 0.25$ to $0.8U_\infty$ at $x/c = 1.0$.

In Fig. 4.11a, it is shown that the streamwise normal stress $\overline{u^2}$ had a characteristic distribution at the most downstream location with two peaks located upper and lower sides of the vortex center. On the other hand, the transverse and the spanwise normal stress $\overline{v^2}$ and $\overline{w^2}$ had a single significant peak at the vortex center. It should be noted that $\overline{u^2}$, $\overline{v^2}$ and $\overline{w^2}$ are presented in different color scales in Fig. 4.11, and the magnitude of the streamwise normal stress $\overline{u^2}$ was smaller by nearly one order than that of the transverse normal stress $\overline{v^2}$. It is also shown that the Reynolds normal stresses near the vortex center increased as the measurement location went downstream, while those in the shear layer rolling up from the wing decreased.

Such excessively large lateral velocity fluctuation apparent near the vortex center implies that they did not originate from so-called shear production, but were caused by the meandering motion of the wingtip vortex. It was already pointed out in many earlier studies (e.g., Bailey and Taboularis, 2006; Heyes et al., 2004) that the velocity

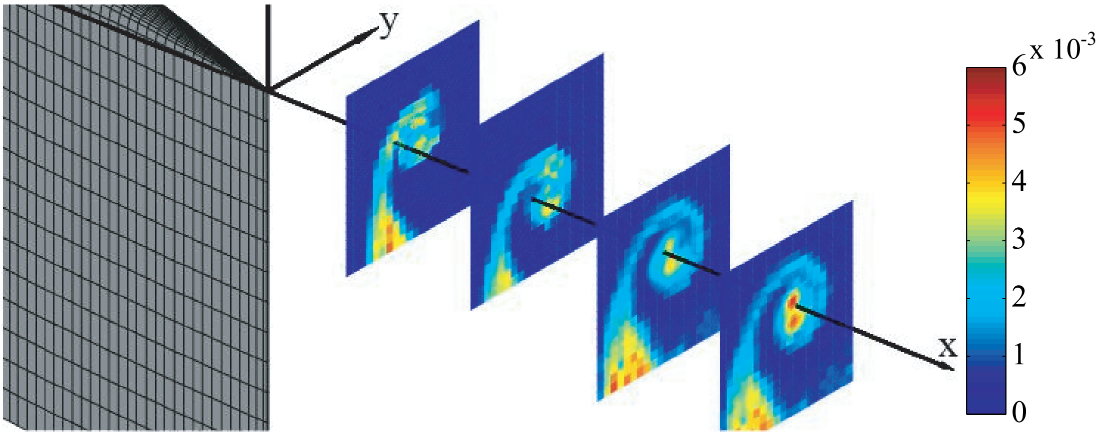

(a) Distribution of $\overline{u^2}$.

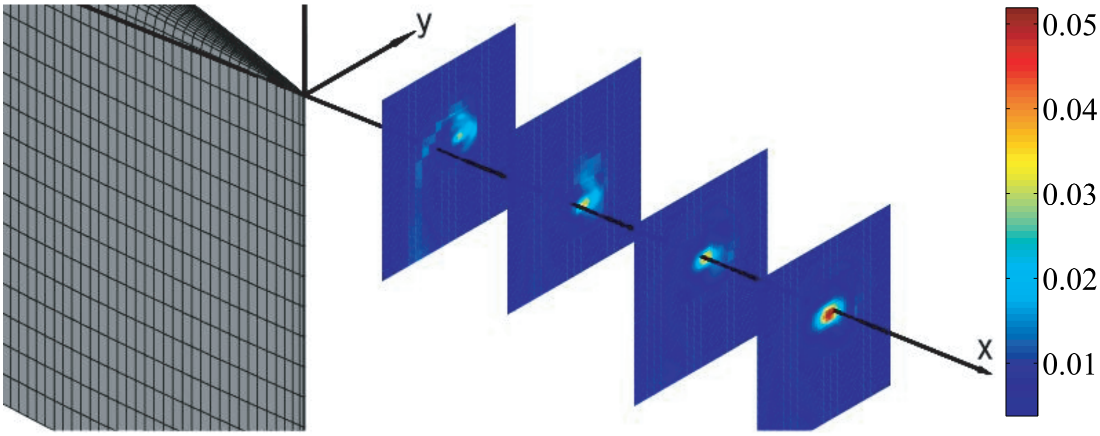

(b) Distribution of $\overline{v^2}$.

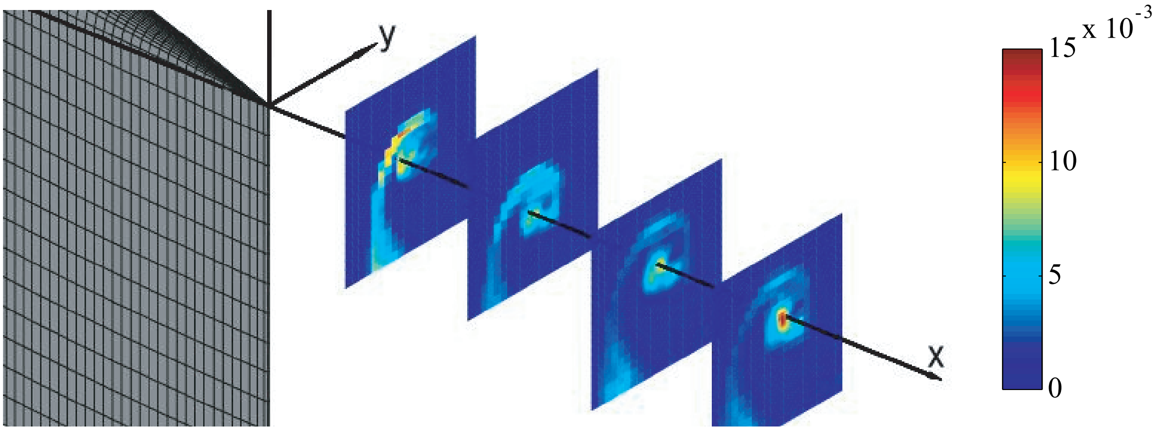

(c) Distribution of $\overline{w^2}$.

Figure 4.11: Development of distribution of Reynolds normal stresses.

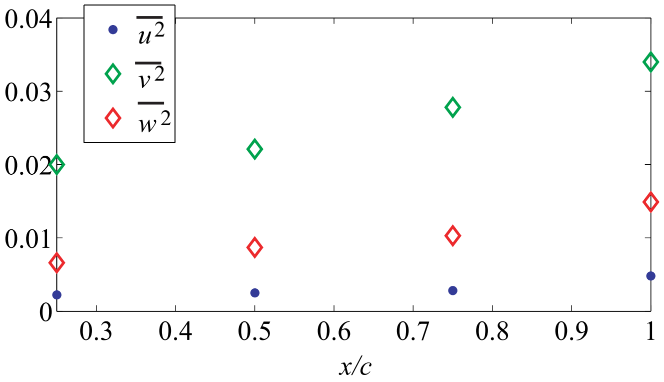

Figure 4.12: Variation of Reynolds normal stresses at vortex center in streamwise direction.

Figure 4.13: Power spectrum density of transverse velocity at center of wingtip vortex.

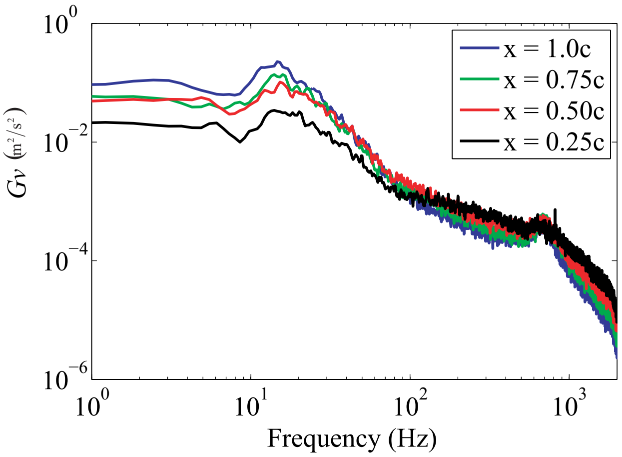

fluctuation in the wingtip vortex is mostly produced by the unsteady meandering motion of the vortex, and the magnitude of the velocity fluctuations linearly increases in the streamwise direction (Devenport et al., 1996). Figure 4.12 presents the variation of the Reynolds normal stresses at the vortex center in the streamwise direction. The tendency of the velocity fluctuation caused by the vortex meandering mentioned above is clearly indicated.

The characteristic of the velocity fluctuation caused by the vortex meandering also can be seen in the distribution of the power spectrum density (PSD). Figure 4.13 presents the PSD of the transverse velocity component v at the vortex center measured in various streamwise locations. The PSDs of v was mainly distributed in the lower frequency range than 100 Hz, and they increased as the measurement location went downstream while those in the higher frequency range decreased, which indicates that the meandering motion of the wingtip vortex occurred mainly in the frequency region lower than 100 Hz. The minor peak appeared near 680 Hz, which corresponded to the vortex roll-up that occurred in the shear layer surrounding the wingtip vortex.

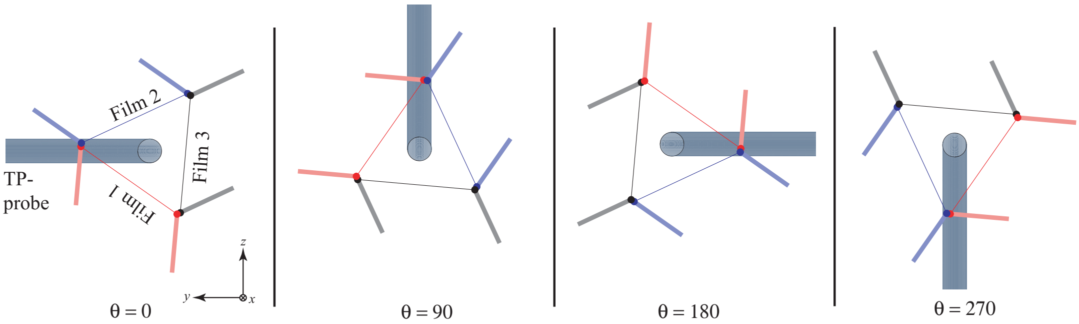

Figure 4.14: Arrangement of the new combined probe in simultaneous velocity and pressure measurement.

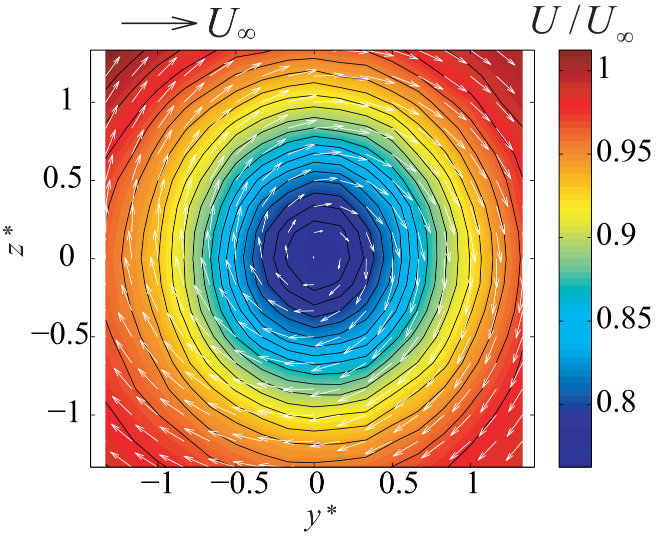

Figure 4.15: Mean streamwise velocity distribution at $x/c = 1.0$ measured by the new combined probe. Colors show values of the mean streamwise velocity, and white arrows indicate cross-flow vector pattern. The values of mean velocities were obtained by averaging results measured by four different probe position shown in Fig. 4.14.

As shown above, the wingtip vortex had the characteristic velocity distributions due to the meandering motion at the most downstream location $x/c = 1.0$. The rest of this section and the discussion is mainly focused in the results measured at this streamwise location. In addition, the velocity measurement was somewhat affected by the non-axisymmetric directional sensitivity of the THF-probe, as already pointed out in Sect. 4.3.4. In order to minimize this influence, the statistics presented below were obtained by averaging results measured by the four different probe orientations schematically shown in Fig. 4.14. The sampling time was 8 s for each probe position, and consequently the integration time for statistics evaluation was 32 s.

The distribution of the mean streamwise velocity U at $x/c = 1.0$ is presented in Fig. 4.15 with white arrows indicating the mean cross-flow pattern. The y- and z-coordinates are shown in a non-dimensional form denoted by the asterisk: $(y^*,\ z^*) = ((y-y_c)/R,\ (z-z_c)/R)$, where (y_c, z_c) and R are the center location and radius of the wingtip vortex, which are defined as the location at which the cross-flow mean velocity magnitude $|V| \equiv \sqrt{V^2+W^2}$ became its minimum, and the distance between (y_c, z_c)

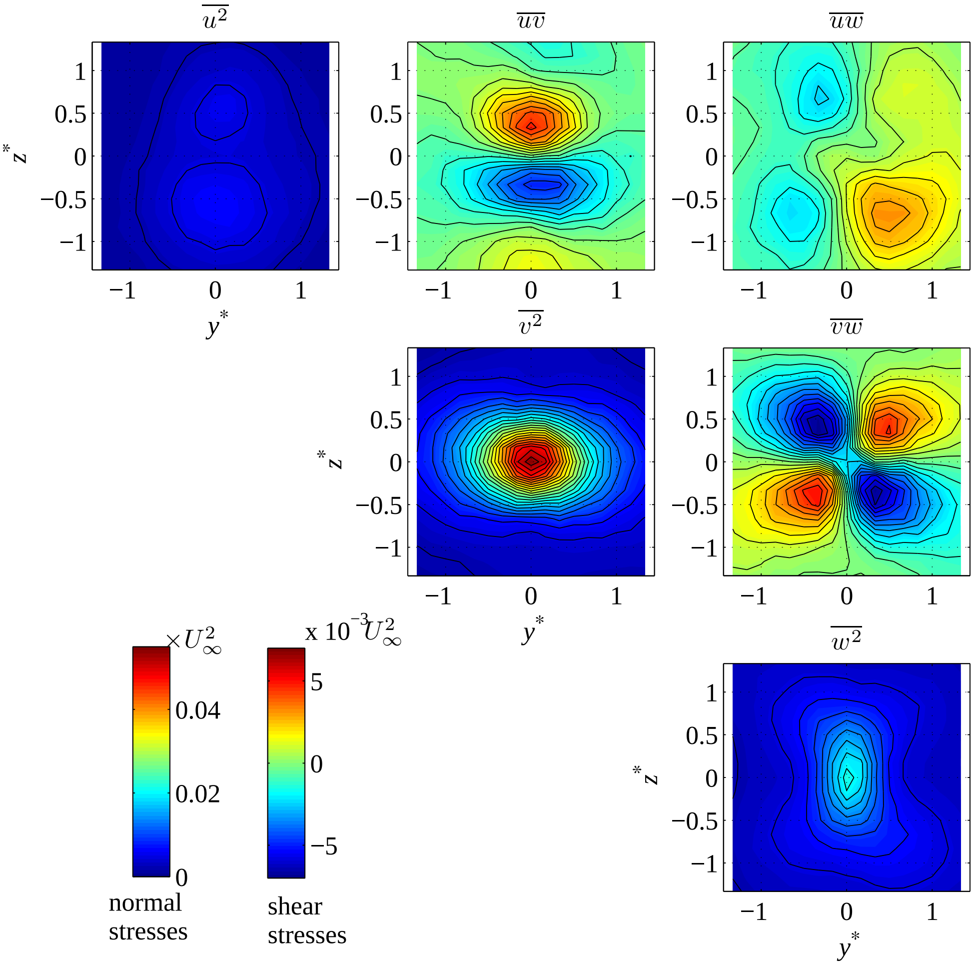

Figure 4.16: Distribution of Reynolds stresses measured at $x/c = 1.0$.

and the maximum location of $|V|$; in addition, the vortex radius R was approximately 6 mm at $x/c = 1.0$. The measurement result of U were somewhat improved by averaging the results measured by the four different probe positions, in that the contour lines showed almost circular shape, unlike the results shown in Fig. 4.7.

Figure 4.16 presents the distributions of all components of the Reynolds stress at $x/c = 1.0$. It should be noted that the normal and shear stresses are shown in different color scales. As previously mentioned, the distribution of the normal stress component $\overline{u^2}$ had two peaks on upper and lower sides of the vortex center. The peak magnitude was approximately $6.9 \times 10^{-3}U_\infty^2$. In contrast, the transverse and spanwise normal stress components $\overline{v^2}$ and $\overline{w^2}$ showed a significant single peak at the vortex center, and the peak magnitudes were $0.05U_\infty^2$ and $0.02U_\infty^2$, respectively. The peak magnitude of $\overline{v^2}$ was almost by an order of magnitude larger than that of $\overline{u^2}$. The shear stress components, $\overline{uv}$, $\overline{uw}$, and $\overline{vw}$ showed symmetric distributions with the $\overline{vw}$ component being

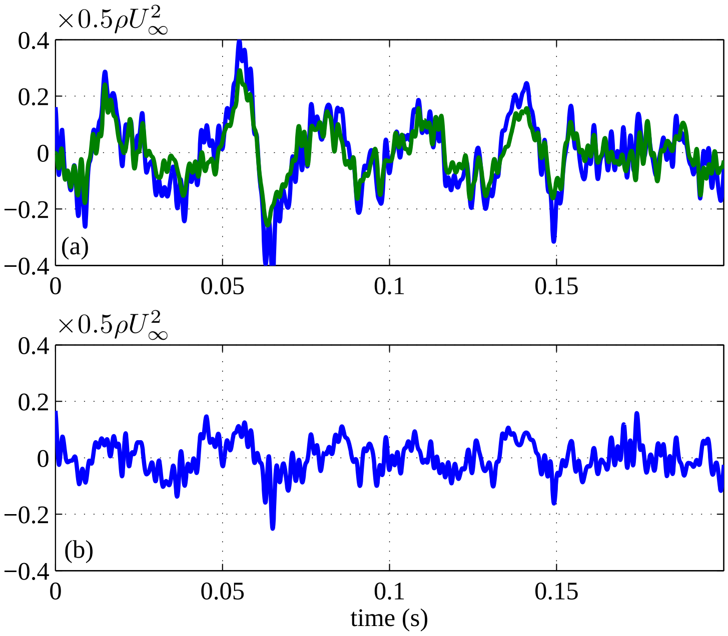

Figure 4.17: Time sequences of pressure fluctuations measured at center of a wingtip vortex $(y^*, z^*) = (0, 0)$: (a) total pressure fluctuation (blue) and dynamic pressure fluctuation (green) directly measured by the TP- and THF-probes, respectively; (b) static-pressure fluctuation evaluated from the total and dynamic pressure fluctuation shown in (a).

substantially larger magnitude than the others. Such extraordinarily strong anisotropy of the Reynolds stress was also observed in earlier studies (e.g., Devenport et al., 1996), and the vortex meandering was considered to be the reason for such an anomaly (Heyes et al., 2004), as will be explained in Sect. 4.4.3.

4.4.2.2 Fluctuating static-pressure measurement

The static-pressure fluctuation p was evaluated based on the instantaneous velocities and total pressure fluctuation directly measured by the combined probe, by the manner described in Sect. 4.2. The time sequences of the total- and dynamic-pressure fluctuations at the vortex center are presented in Fig. 4.17a. The values are scaled by $0.5\rho U_\infty^2$, and the dynamic pressure fluctuation was evaluated as that in Eq. (4.3) taking into account the contribution from the cross-flow velocity components. As shown in Fig. 4.17a, the time sequence of the dynamic-pressure fluctuation measured by the THF-probe was quite similar to that of the total-pressure fluctuation measured by the TP-probe, which was the expected behavior of them, because the static-pressure fluctuation is usually much smaller than the dynamic-pressure fluctuation. The correlation coefficient between the total- and dynamic-pressure fluctuations was about 0.81. The pressure fluctuation evaluated from the total- and dynamic-pressure fluctuations based on Eq. (4.3) is shown in Fig. 4.17b.

Figure 4.18 presents the distribution of the root-mean-square values of the static-pressure fluctuation p', comparing those obtained using Eqs. (4.1) and (4.3), in order

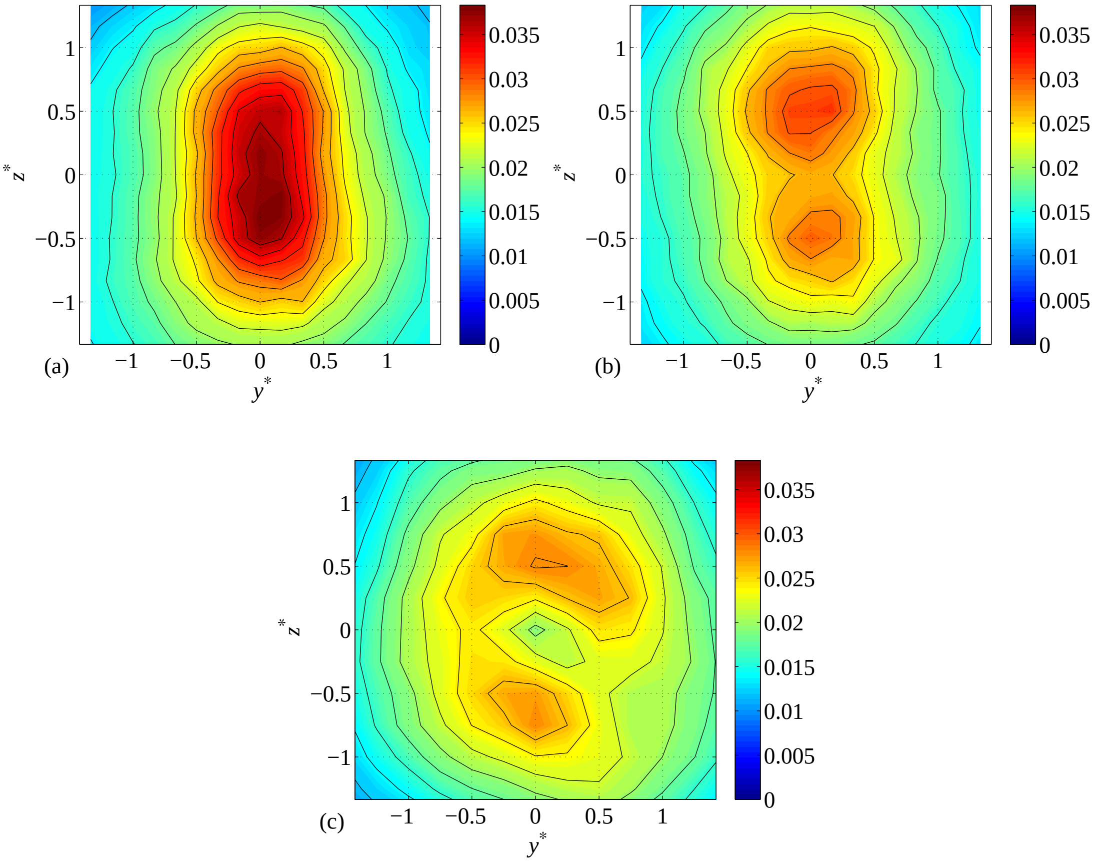

Figure 4.18: Distributions of static-pressure fluctuation at $x/c = 1.0$: (a) Evaluated by Eq. (4.1); (b) Evaluated by Eq. (4.3); Directly measured by SP-probe (Naka and Obi, 2009). The values are scaled by ρU_∞^2 in each figure.

to address the effect of incorporating the cross-flow velocity components. The direct measurement result by the SP-probe provided by Naka and Obi (2009) is also given in Fig. 4.18c as a reference. It is obviously seen that the pressure fluctuation obtained by Eq. (4.1) was larger in magnitude than that by Eq. (4.3) due to absence of the cross-flow effect contributions. It is also seen that the result given by Eq. (4.3) was in stronger agreement with the direct measurement result by the SP-probe; both results showed two significant peaks at the location corresponding to those of the streamwise Reynolds normal stress $\overline{u^2}$, while the result by Eq. (4.1) showed a single broad hill. This resemblance between the distributions of p' and $\overline{u^2}$ can be explained by the meandering of the vortex in z-direction, as will be described in Sect. 4.4.3.

The line plots of the static-pressure fluctuations through the vortex center at $y^* = 0$ is also presented in Fig. 4.19. The result obtained by Eq. (4.3) strongly agreed with that directly measured by the SP-probe, although a certain discrepancy of about $0.006\rho U_\infty^2$, which corresponded to 20% of the peak pressure fluctuation, was seen at the vortex

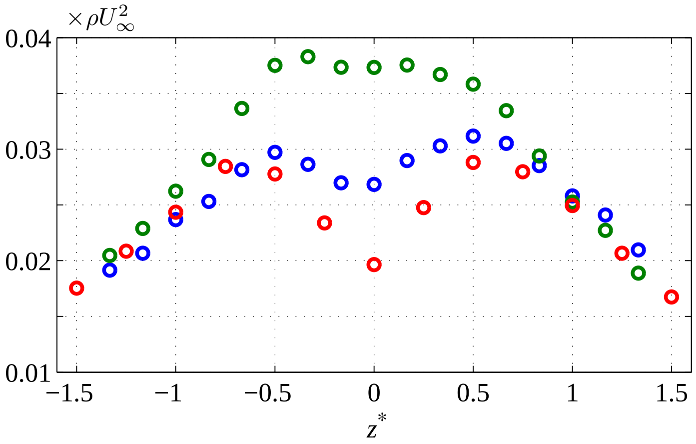

Figure 4.19: Line plot of static-pressure fluctuation though a center of wingtip vortex at $y^* = 0$: blue, evaluated by Eq. (4.3); green, evaluated by Eq. (4.1); red, directly measured by SP-probe (Naka and Obi, 2009).

center. Thus, the measurement uncertainty in the static-pressure measurement was roughly estimated to be 20%.

The signal-to-noise ratio of the static-pressure measurement was roughly estimated. In a separate measurement, the static-pressure fluctuation was measured by the new combined probe at $(y^*, z^*) = (2.17, -1.83)$, the location far enough from the vortex center that the measured pressure fluctuation was mainly the background noise, and it was $0.01\rho U_\infty^2$. On the other hand, the maximum magnitude of static-pressure fluctuation shown in Fig. 4.18 was $0.031\rho U_\infty^2$ at $(y^*, z^*) = (0.5, 0)$, and consequently, the signal-to-noise ratio was roughly estimated to be 3.1-to-1. The signal-to-noise ratio of the directly measurement by the SP-probe was also estimated by the similar manner, and it was approximately 5.2-to-1. Therefore, the drawback of the present method compared to the direct static-pressure measurement by the SP-probe is the lower signal-to-noise ratio of the indirect static-pressure fluctuation.

4.4.2.3 Velocity-pressure correlation measurement

Figure 4.20 presents the distribution of the velocity-pressure correlations $\overline{up}$, $\overline{vp}$, and $\overline{wp}$ measured at $x/c = 1.0$, comparing those obtained by Eq. (4.1) and (4.3). The distributions of the velocity-pressure correlation $\overline{up}$ evaluated by Eq. (4.1) and (4.3) agreed well with each other; both of them showed positive values over the entire range of the measuring area with two slightly visible peaks located upper and lower sides of the vortex center, which is somewhat similar to the distributions of $\overline{u^2}$ and p'.

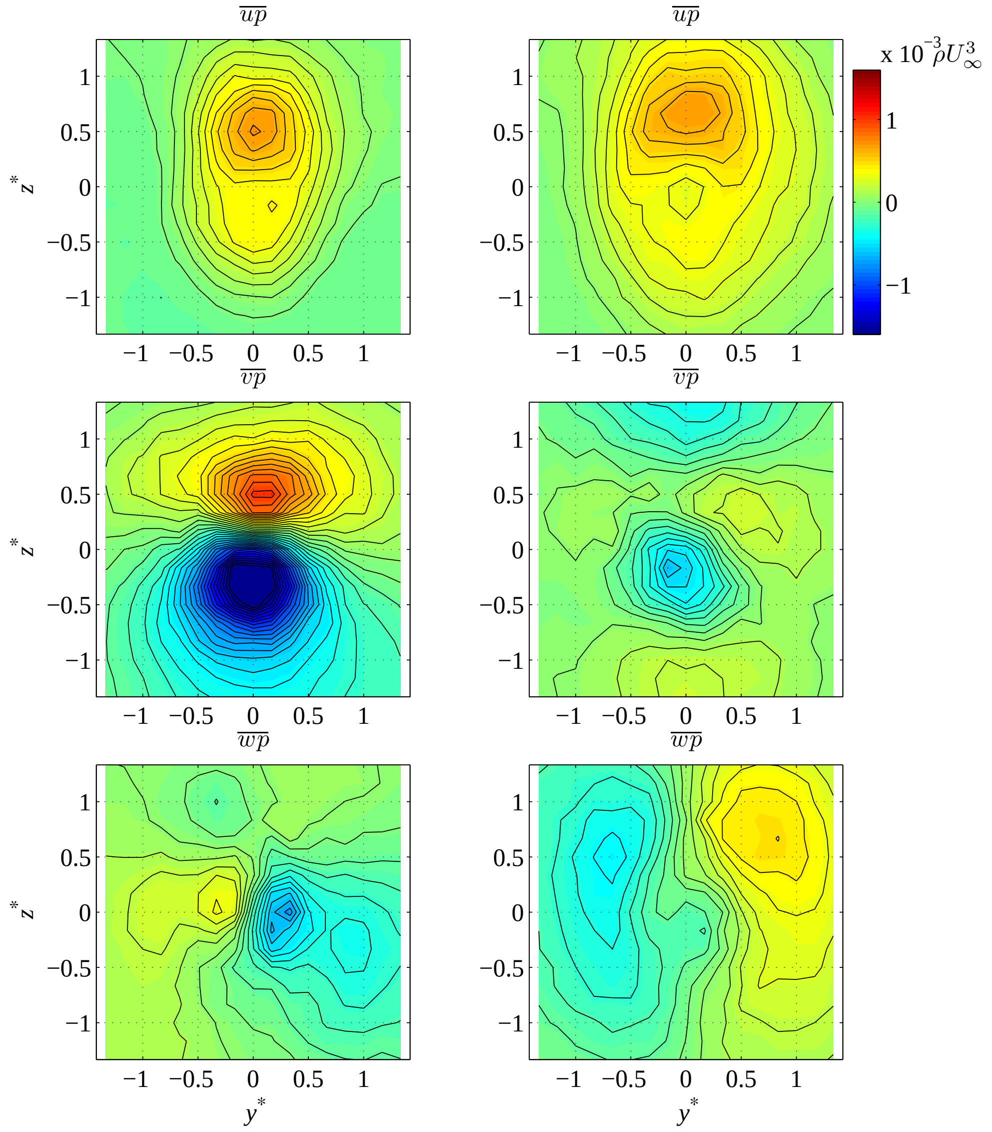

Figure 4.20: Distribution of velocity-pressure correlation $\overline{up}$, $\overline{vp}$ and $\overline{wp}$ at $x = 1.0c$; (left) obtained by Eq. (4.1), (right) obtained by Eq. (4.3).

On the other hand, the measurement results of $\overline{vp}$ and $\overline{wp}$ showed obviously different distribution depending on Eq. (4.1) or (4.3). The result by Eq. (4.1) had distinct positive and negative peaks located upper and lower side of the cortex center, while that obtained by Eq. (4.3) changed the sign three times across the measurement range in the y-direction. The distributions of $\overline{wp}$ evaluated by different equations indicated the opposite sign to each other. Thus, the modification in the indirect evaluation of the static pressure from Eq. (4.1) to (4.3) resulted in a significant difference between the evaluated distributions of $\overline{vp}$ and $\overline{wp}$, while the modification did not result in apparent difference in the results of $\overline{up}$. The reason of this will be discussed in the next section.

4.4.3 Discussion

4.4.3.1 Effect of modification in formula for static-pressure evaluation

It has been demonstrated that Eqs. (4.1) and (4.3) provide remarkably different values of the velocity-pressure correlation, particularly for the $\overline{vp}$ and $\overline{wp}$ components. The reason for this is now addressed by inspecting the contents of these equations. By multiplying the fluctuating pressure provided by Eq. (4.3) with each fluctuating velocity component and taking the average, one obtains the following relationships to describe the velocity-pressure correlations:

$$\begin{aligned}
\overline{up} &= \left[\overline{up_t} - \frac{\rho}{2}\left(\underline{2U\overline{u^2}} + \overline{u^3}\right)\right] - \frac{\rho}{2}\left(2V\overline{uv} + 2W\overline{uw} + \overline{uv^2} + \overline{uw^2}\right), && (4.9)\\
\overline{vp} &= \left[\overline{vp_t} - \frac{\rho}{2}\left(2U\overline{uv} + \overline{u^2 v}\right)\right] - \frac{\rho}{2}\left(\underline{2V\overline{v^2}} + 2W\overline{vw} + \overline{v^3} + \overline{vw^2}\right), && (4.10)\\
\overline{wp} &= \left[\overline{wp_t} - \frac{\rho}{2}\left(2U\overline{uw} + \overline{u^2 w}\right)\right] - \frac{\rho}{2}\left(2V\overline{vw} + \underline{2W\overline{w^2}} + \overline{v^2 w} + \overline{w^3}\right). && (4.11)
\end{aligned}$$

It should be noted that the unsteady terms such as $\overline{u\partial v_s/\partial t \Delta x}$ are omitted as they had only a minor contribution. The first terms bracketed by [] on the right hand side of each equation represents the velocity-pressure correlations evaluated by Eq. (4.1), while the second term represents the additional contribution of the mean cross-flow components that is introduced in Eq. (4.3).

The dominant terms in each equation, marked by the underline, comprise the product of the mean velocity and the normal component of the Reynolds stress. The magnitude of these three terms, $U\overline{u^2}$, $V\overline{v^2}$, and $W\overline{w^2}$, are nearly the same although $\overline{u^2}$ is significantly smaller in comparison to the other normal stresses, because it is multiplied by U, which is the largest among the mean velocity components. As these dominant terms appear in the additional term in the equation for $\overline{vp}$ and $\overline{wp}$, it is evident that they were responsible for the aforementioned remarkable difference in distributions of $\overline{vp}$ and $\overline{wp}$ provided by the different formulae for static-pressure evaluation. In contrast, $\overline{up}$ was mostly unchanged because the dominant term was already contained in the first term in Eq. (4.9), and the additional term had only a minor effect.

4.4.3.2 Effect of meandering motion of wingtip vortex

In order to further verify the present measurement results of the velocity-pressure correlations, the relationship between the vortex meandering motion and the induced velocity/pressure fluctuations is discussed below. If the velocity fluctuations measured by the THF-probe was mainly produced by the vortex meandering, the magnitude

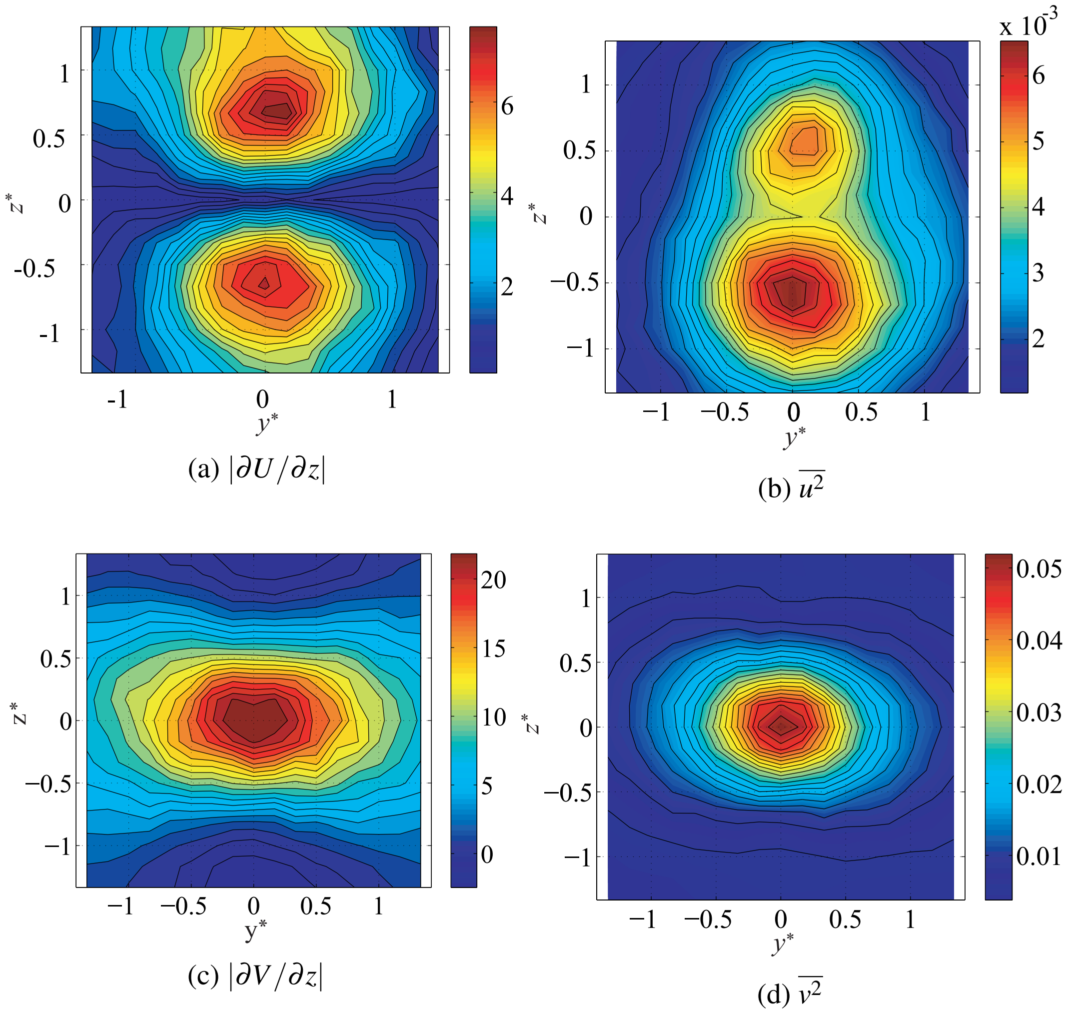

(a) $|\partial U/\partial z|$

(b) $\overline{u^2}$

(c) $|\partial V/\partial z|$

(d) $\overline{v^2}$

Figure 4.21: Comparison between mean velocity-gradient and Reynolds normal stresses.

of the measured velocity fluctuation should depend on the velocity gradient. Figure 4.21 compares the magnitude of the spanwise gradients of the mean-velocity and the Reynolds normal stresses $\overline{u^2}$ and $\overline{v^2}$. As shown, the mean-velocity-gradient $\partial U/\partial z$ had two significant peaks at the upper and lower side of the vortex center, and $\partial V/\partial z$ had a single significant peak at the vortex center, which were in quite strong agreement with the distributions of $\overline{u^2}$ and $\overline{v^2}$. This strong resemblance between the distributions of the Reynolds stresses and the spanwise mean-velocity-gradients implies that the wingtip vortex was meandering mainly in spanwise direction, and the measured Reynolds stresses were induced by it.

Next, effect of the vortex meandering on the distribution of the Reynolds shear stresses is also discussed by similar consideration. The sign of the Reynolds shear stresses should depend on that of product of the mean velocity gradients. Figure 4.22

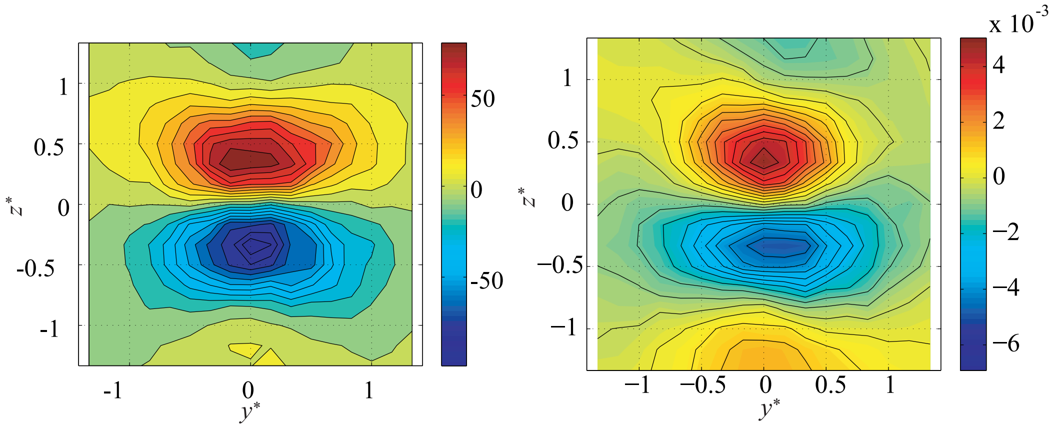

(a) $\partial U/\partial z \cdot \partial V/\partial z$ (b) $\overline{uv}$

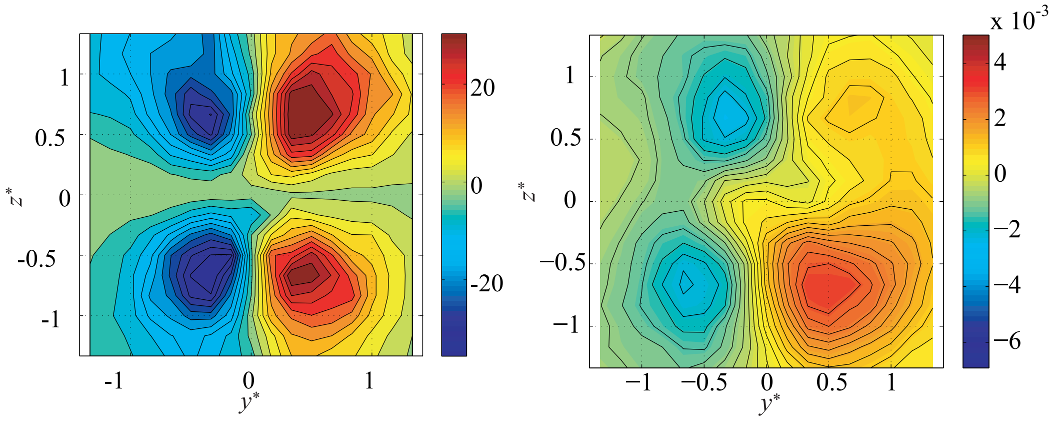

(c) $\partial U/\partial z \cdot \partial W/\partial z$ (d) $\overline{v^2}$

Figure 4.22: Comparison between product of mean velocity-gradients and Reynolds shear stresses.

compares the Reynolds shear stresses $\overline{uv}$ and $\overline{uw}$ with the products of the spanwise mean-velocity-gradients $\partial U/\partial z \cdot \partial V/\partial z$ and $\partial U/\partial z \cdot \partial W/\partial z$, respectively. It is also obviously shown that the sign patterns of the Reynolds shear stresses were quite similar to those of the products of the mean-velocity gradients. Therefore, it is reasonably considered that the velocity fluctuations at $x/c = 1.0$ were mainly caused by the meandering motion in z-direction of the wingtip vortex. The distribution patterns of the other statistics such as the velocity-pressure correlation also can be estimated by the similar consideration.

As the distribution of the pressure fluctuation p' was similar to that of the Reynolds normal stress $\overline{u^2}$ (compare Figs. 4.21b and 4.18), the behavior of the pressure fluctuation can be considered to be similar to that of the streamwise velocity fluctuation. Hence, it is reasonably inferred that the distribution of the velocity-pressure correlation $\overline{up}$ should be similar to those of $\overline{u^2}$ and p'. The present measurement result captured this tendency (see Fig. 4.20). By the same reason, the distributions of $\overline{vp}$ and $\overline{wp}$ should

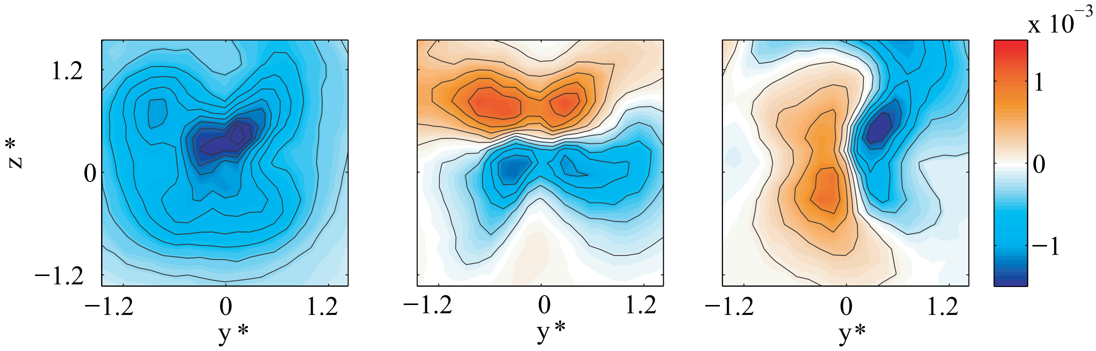

Figure 4.23: Reference results by Naka and Obi (2009). (left) $\overline{up}$, (center) $\overline{vp}$, (right) $\overline{wp}$

be similar to those of $\overline{uv}$ and $\overline{uw}$, respectively, and such expected tendency was shown in the results obtained by Eq. 4.3 in Fig. 4.20. Therefore, it can be concluded that the characteristics of the velocity-pressure correlation in the wingtip vortex flow were appropriately captured by the present measurement method.

Now, the present measurement results are compared to those provided in the previous study (Naka and Obi, 2009), measured in the same experiment condition by the X-probe and a straight-type TP-probe, in order to examine the superiority of the present measurement method over the previous measurement technique. The measurement result by the previous measurement technique (Naka and Obi, 2009) is shown in Fig. 4.23. It is shown that the distributions of $\overline{vp}$ and $\overline{wp}$ were similar to the present measurement results evaluated by Eq. (4.1), as the contribution of the cross-flow components was not taken into account in the previous study. The most remarkable difference between the previous and present measurement results was observed between the distributions of the velocity-pressure correlation $\overline{up}$. The previous result indicated negative values over the entire measuring range, while the present result showed the positive values. The negative values of $\overline{up}$ in the previous measurement might be attributable to error in velocity measurement by the X-probe caused by the velocity components perpendicular to the wire plane of the X-probe. Thus, it has been shown that the velocity-pressure correlation measurement in a turbulent wingtip vortex flow was obviously improved as compared to the previous study by the present measurement technique.

4.4.3.3 Transport of turbulent kinetic energy

The transport equation of turbulent kinetic energy was investigated in order to shed light on the role that the velocity-pressure correlation plays in the transport phenomena in the wingtip vortex flow. By ignoring the terms containing the streamwise derivative,

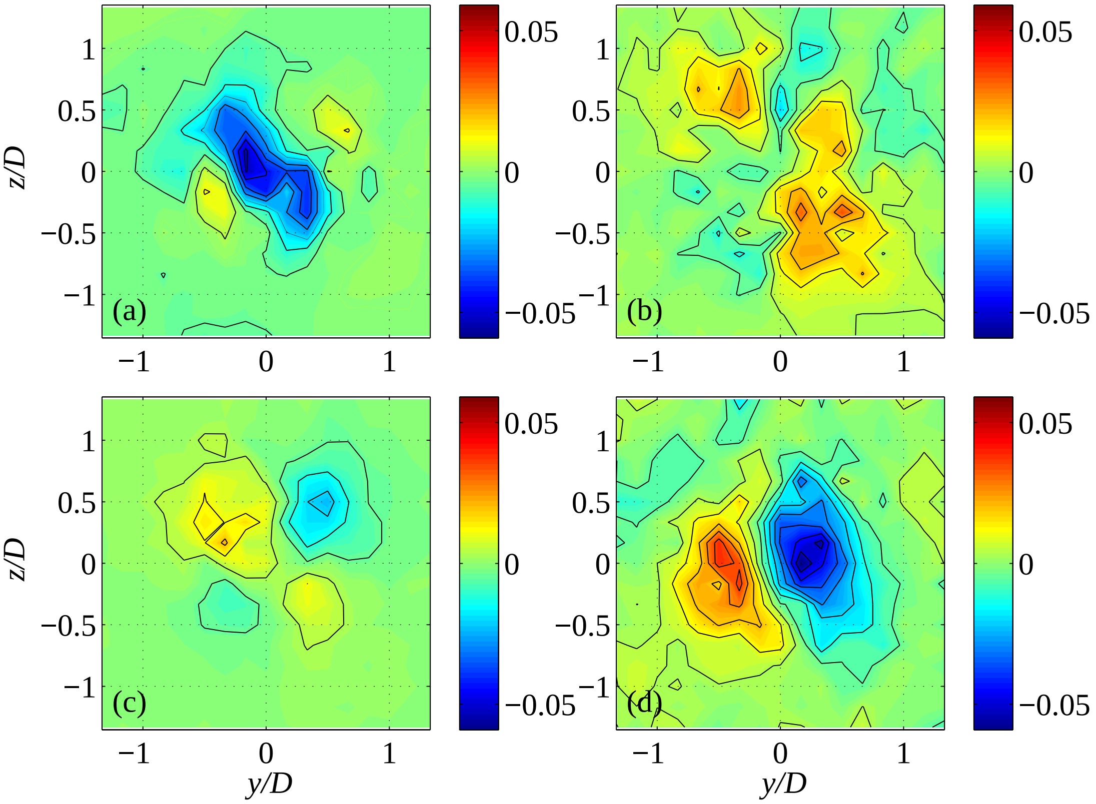

Figure 4.24: Distribution of the individual terms in the transport equation of turbulent kinetic energy; (a) production, (b) convection, (c) turbulent diffusion, (d) pressure diffusion. The values are scaled by U_∞^3/c.

$\partial/\partial x$, one obtains the following expressions:

$$P_k \simeq -\overline{v^2}\frac{\partial V}{\partial y} - \overline{w^2}\frac{\partial W}{\partial z} - \overline{uv}\frac{\partial U}{\partial y} - \overline{uw}\frac{\partial U}{\partial z} - \overline{vw}\left(\frac{\partial V}{\partial z} + \frac{\partial W}{\partial y}\right), \tag{4.12}$$

$$C_k \simeq V\frac{\partial k}{\partial y} + W\frac{\partial k}{\partial z}, \tag{4.13}$$

$$D_k^t \simeq -\frac{1}{2}\left(\frac{\partial \overline{u^2v}}{\partial y} + \frac{\partial \overline{v^3}}{\partial y} + \frac{\partial \overline{vw^2}}{\partial y} + \frac{\partial \overline{u^2w}}{\partial z} + \frac{\partial \overline{v^2w}}{\partial z} + \frac{\partial \overline{w^3}}{\partial z}\right), \tag{4.14}$$

$$D_k^p \simeq -\frac{1}{\rho}\left(\frac{\partial \overline{vp}}{\partial y} + \frac{\partial \overline{wp}}{\partial z}\right), \tag{4.15}$$

with P_k, C_k, D_k^t, and D_k^p representing the production, convection, turbulent diffusion, and pressure diffusion of the turbulent kinetic energy. Figure 4.24 presents the distributions of these terms. The production rate P_k was negative near the vortex center and the reason for this is examined later. The convection C_k was smaller compared to production and also changed the sign on the cross section; it should be noted that C_k

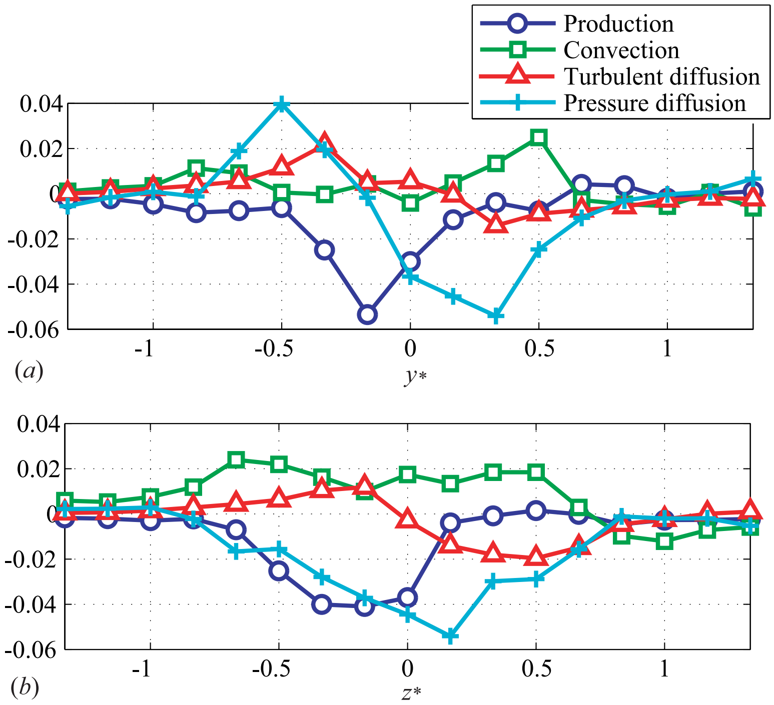

Figure 4.25: Individual terms in the transport equation of turbulent kinetic energy; (a) in y-direction at $z^* = 0.16$, (b) in z-direction at $y^* = 0.33$

is shown with negative sign to facilitate the comparison with other terms. It is seen that the turbulent diffusion D_k^t partly compensated for the negative production. The pressure-diffusion D_k^p changed sign from positive to negative across the vortex center. This occurred from the left to right in a symmetric manner about the z-axis as a consequence of the symmetric distributions of $\overline{vp}$ and $\overline{wp}$ (see Fig. 4.16, right).

The balance of each term is presented in the form of a line plot in Fig. 4.25, cutting through the peaks of the distribution of the diffusion terms. Figures 4.25a and b indicate the y-direction line plots at $z^* = 0.16$ and the z-direction line plots at $y^* = 0.33$, respectively. In both graphs, the pressure-diffusion indicated consistently larger values than the turbulent-diffusion , which is not typical for simple shear flows where the pressure diffusion can be treated as a fraction of the turbulent diffusion term, as suggested by a classic model of pressure diffusion (Lumley, 1978). Admittedly, the sum of the terms shown in Fig. 4.25 would yield a finite residual. This is partly because of the under-estimation of spatial derivatives due to rather coarsely located measuring locations, and partly because of the insufficient accuracy of the pressure-velocity correlation.

The contents of the production rate P_k are now investigated in order to shed light on the anomalous behavior of the wingtip vortex flow. It is obvious in Fig. 4.26 that

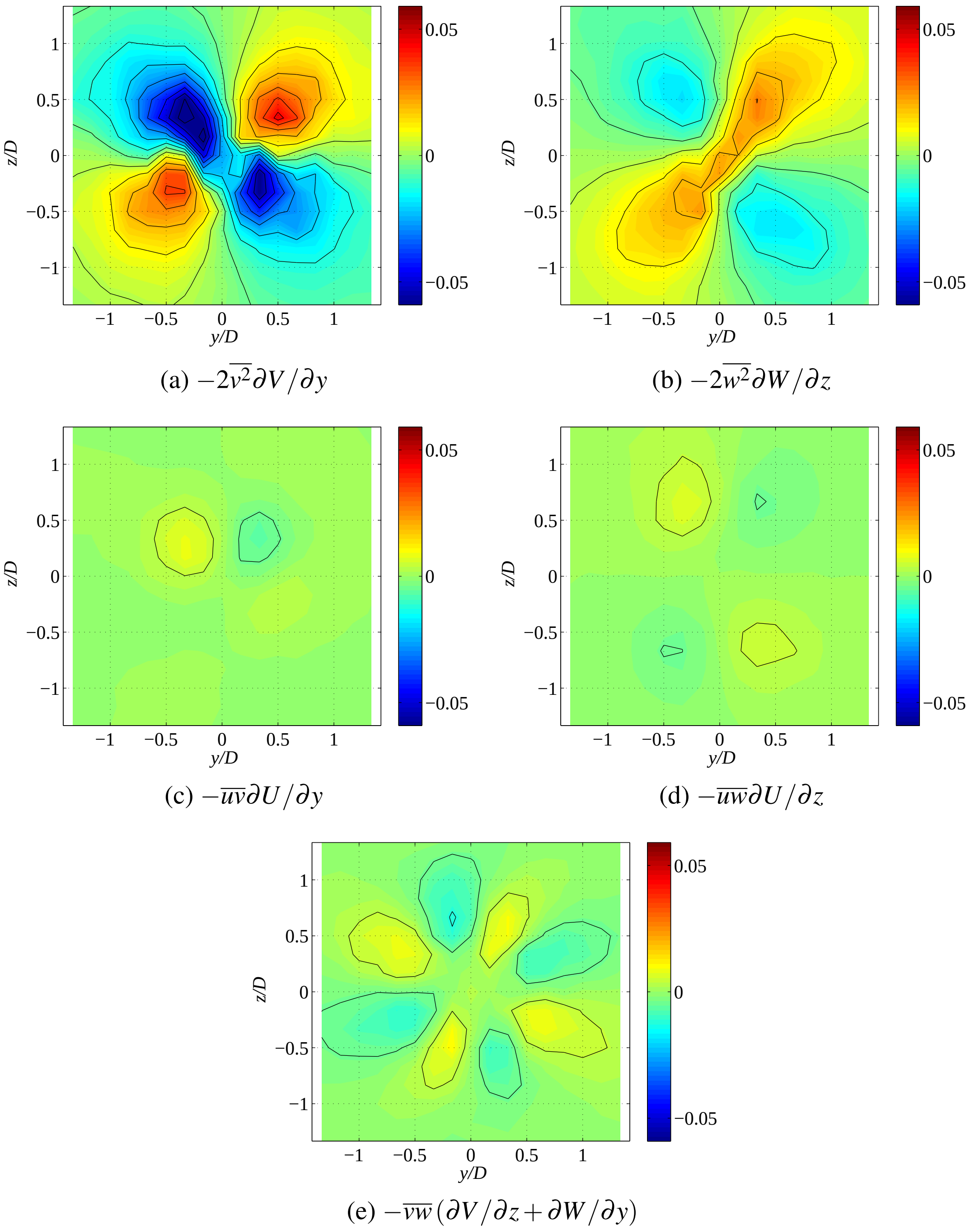

(a) $-2\overline{v^2}\partial V/\partial y$

(b) $-2\overline{w^2}\partial W/\partial z$

(c) $-\overline{uv}\partial U/\partial y$

(d) $-\overline{uw}\partial U/\partial z$

(e) $-\overline{vw}\,(\partial V/\partial z+\partial W/\partial y)$

Figure 4.26: Contents of the production term

the components related to $\overline{v^2}$ or $\overline{w^2}$ showed significant negative values and dominated others. This is a consequence of the fact that these normal components of the Reynolds stress are very large as compared to other stress components as a consequence of the vortex meandering.

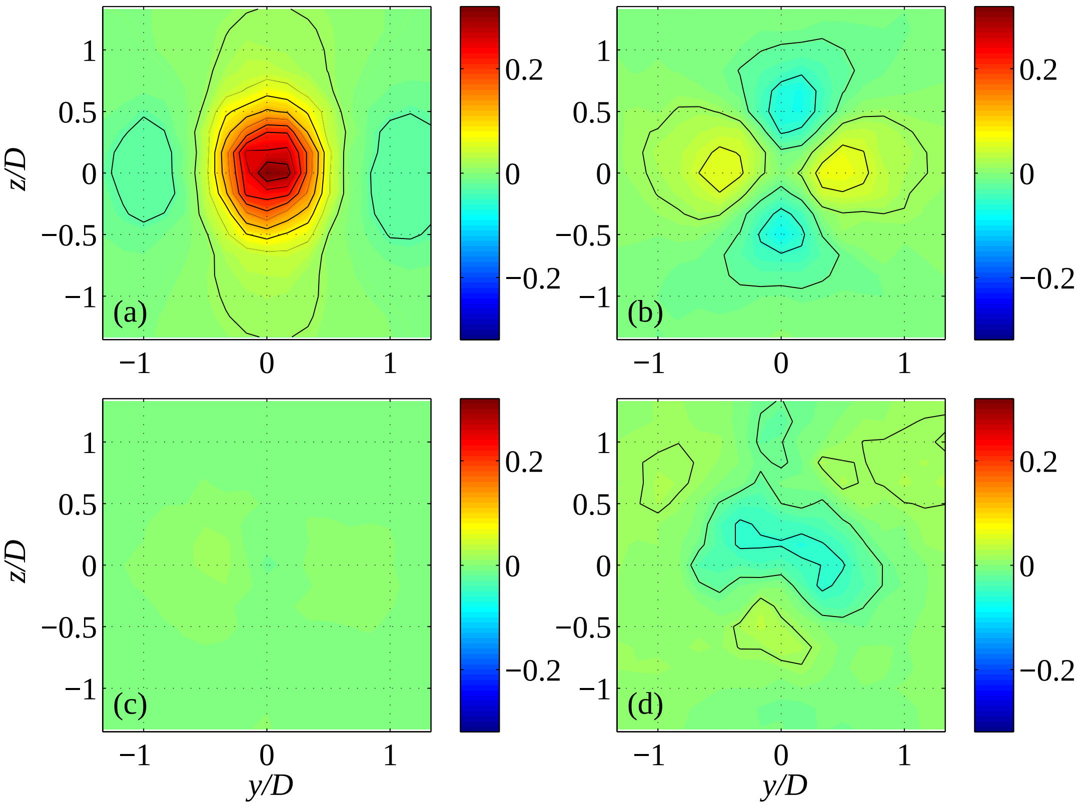

Figure 4.27: Distribution of the individual terms in transport equation of Reynolds shear stress $\overline{vw}$; (a) production, (b) convection, (c) turbulent diffusion, (d) pressure diffusion. The values are scaled by U_∞^3/c.

4.4.3.4 Transport of Reynolds stress $\overline{vw}$

The transport equation of the Reynolds shear stress $\overline{vw}$ was also investigated, because it showed the most significant magnitude and characteristic distribution among the shear stresses. The production, convection, turbulent diffusion, and pressure diffusion were evaluated neglecting the streamwise gradient contributions as:

$$P_{23} = -\overline{v^2}\frac{\partial W}{\partial y} - \overline{w^2}\frac{\partial W}{\partial z} - \overline{vw}\left(\frac{\partial V}{\partial y} + \frac{\partial W}{\partial z}\right), \tag{4.16}$$

$$C_{23} = -V\frac{\partial \overline{vw}}{\partial y} - W\frac{\partial \overline{vw}}{\partial z}, \tag{4.17}$$

$$D^t_{23} = -\frac{\partial \overline{v^2 w}}{\partial y} - \frac{\partial \overline{vw^2}}{\partial z}, \tag{4.18}$$

$$D^p_{23} = -\frac{1}{\rho}\left(\frac{\partial \overline{vp}}{\partial z} + \frac{\partial \overline{wp}}{\partial y}\right). \tag{4.19}$$

The production rate P_{23} showed a single distinct positive peak at the vortex center,

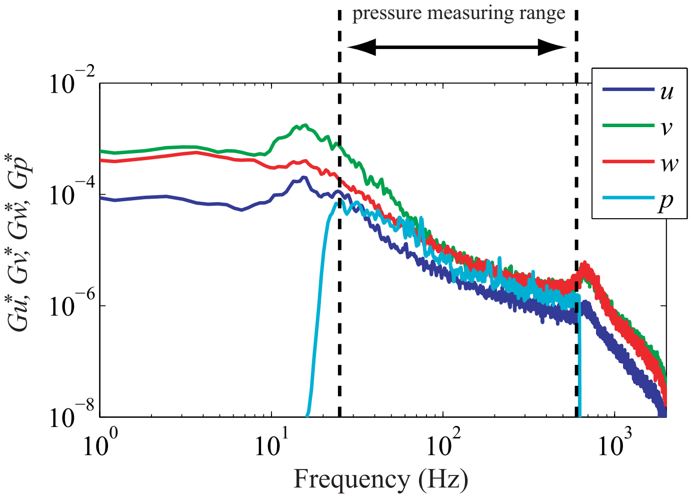

Figure 4.28: PSDs of velocity and pressure fluctuation measured at the vortex center at $x = 1.0c$.

which was mostly contributed by the first tem in Eq. (4.16), the products of the transverse Reynolds normal stress $\overline{v^2}$ and the spanwise mean-velocity-gradient $\partial W/\partial y$. The convection C_{23} showed a symmetric distribution with respect to both y- and $z-$axes, with two positive and negative peaks located near the vortex center, and the magnitude of those peaks were relatively small, but still comparable to the distinct peak of the production at the vortex center.

The pressure diffusion D^p_{23} showed negative values in the center region of the vortex and slightly positive values around the negative region, indicating that $\overline{vw}$ produced by P_{23} at the vortex center was transported by D^p_{23} to the surrounding region, but the magnitude was much smaller than that of the peak of P_{23}. On the other hand, the turbulent diffusion was negligibly small. Also in the transport of the Reynolds shear stress $\overline{vw}$, contribution of the pressure diffusion was more significant than that of the turbulent diffusion, as a consequence of the significant velocity-pressure correlations $\overline{vp}$ and $\overline{wp}$ produced by the meandering of the wingtip vortex. As no term is found to be in balance with the production, the production may be mainly compensated by the redistribution or the dissipation, which are not measured in the present experiment.

4.4.3.5 Frequency range of velocity-pressure correlation measurement

As mentioned in Sect. 4.3.5, the frequency range of simultaneous measurement of velocity and pressure was 25 Hz$\leq f \leq$ 650 Hz, because of the dynamic response of the microphone and the TP-probe. The effect of this limited frequency range on the velocity-pressure correlation measurement is addressed in the following.

Figure 4.28 compares the PSDs of the fluctuating velocities and static pressure measured at the vortex center in the streamwise location of $x/c = 1.0$. As shown, the profiles of the PSDs of fluctuating velocities had a broad hill located around 18 Hz, which was outside of the measurement frequency range of the measurement of static-pressure fluctuation. on the other hand, the PSD of fluctuating static-pressure showed a similar profiles to those of fluctuating velocities in the measurement frequency range, and, therefore, it is inferred that the PSD of the fluctuating static-pressure also would have a broad hill near 18 Hz similarly to those of fluctuating velocities. The velocity fluctuation distributed in the frequency range lower than 25 Hz was evaluated to be 50-60% of the total fluctuation. Therefore, the velocity-pressure fluctuation may be underestimated by 40-50% due to the limited frequency range in the present measurement, and the true role of the velocity-pressure correlation in turbulence transport would be more significant than that observed in the present experiment.

4.5 Summary of This Chapter

In this chapter, a method for simultaneous measurement of three velocity components and fluctuating pressure was developed by using a new probe arrangement comprising a bent-type total pressure probe and a triple-sensor hot-film probe. The tip of the TP-probe was inserted into inside of the measurement volume of the THF-probe. Hence the spatial resolution of the new combined probe was equivalent to that of single use of the THF-probe; a sphere with a radius of 3 mm. The fluctuating static pressure was indirectly evaluated from the fluctuating total pressure and velocity, and the formula for the static-pressure evaluation was modified so that the contribution of the cross flow was properly taken into account.

Simultaneous measurement of three velocity components and fluctuating pressure was performed in a turbulent wingtip vortex. The signal-to-noise ratio of the static-pressure measurement by the new combined probe was roughly estimated to be 3.1-to-1. The present method provided distribution of the static-pressure fluctuation which quantitatively agreed with that obtained by a direct measurement by the SP-probe. The velocity-pressure correlations measurement based on the newly modified formula provided remarkably different results from those evaluated by the old formula, and the results provided by the new method were found to be consistent with the Reynolds stress distribution, which supports validity of the results by the new method. It is clarified that the improvement is due to the inclusion of the lateral velocity components in the dynamic pressure calculation introduced in the new formulation. The investigation on the budget of turbulent kinetic energy and the Reynolds shear stress indicated an anomalous structure of turbulence in the wingtip vortex flow, where the role of pressure diffusion is found to be important.

Chapter 5

Development Fluctuating Hydraulic Pressure Measurement

5.1 Motivation

While the fluctuating pressure measurements at arbitrary positions using an SP-probe has been performed in some earlier studies by experiment in air (e.g., Iida et al., 1999; Sakai et al., 2007; Toyoda et al., 1994; Tsuji et al., 2007), the attempt to conduct fluctuating pressure measurement by the SP-probe in a liquid flow has never been reported, and up to now the hydraulic pressure measurement has been limited to fluctuating wall-pressure measurement. However, the technique for measuring fluctuating pressure at arbitrary positions in liquid flow would be useful in the measurement, for example, in multiphase flow or the non-Newtonian fluid flow.

The hydraulic pressure measurement at arbitrary positions in turbulent flow is difficult in that the typical measurement technique for the experiment in air cannot directly converted to the hydraulic measurement. In the experiment in air, a pressure transducer is attached directly to an SP-probe and placed inside the flow field of interest with the SP-probe, which is difficult in the experiment in liquid as the whole part of a pressure transducer is usually not waterproofed. In addition, a pressure transducer sensitive and applicable to hydraulic pressure measurement has a sensor diaphragm with too large diameter to be placed inside the flow. Hence in the hydraulic pressure measurement, the pressure transducer would be placed outside the flow and connected to the SP-probe by a tube with a certain length. Therefore, the length and/or the shape of the tube might affect the fluctuating pressure measurement. A technique to investigate the characteristics of such a pressure-measuring system is necessary to conduct fluctuating pressure measurement in liquid flow.

In this chapter, a technique to calibrate dynamic response of a pressure-measuring system which consists of a pressure transducer, a tube, and an SP-probe is developed in order to conduct fluctuating pressure measurement by the SP-probe in liquid turbulent flow. A model of the dynamic response of the pressure-measuring system is derived similarly to those studied in earlier works of the fluctuating hydraulic wall-pressure measurement, and techniques to evaluate unknown coefficient in the dynamic response model, i.e. the natural frequency and the damping ratio, are proposed. The measurement technique developed in this chapter is used in Chap. 6 in order to develop a new measurement method, in which direct single-point-measurement by the SP-probe is combined with pressure-field evaluation based on PIV measurement.

5.2 Analytical Model for Dynamic Response of Pressure Measuring System

In earlier studies of fluctuating hydraulic-wall-pressure measurement, a strain-gage-type pressure transducer was used as a pressure sensor and connected to the pressure tap on the wall by tubing. Dynamic response of such pressure-measuring system has been investigated in the previous studies of the wall-pressure measurement (Geddes et al., 1984; Hansen, 1950), and it was pointed out that the dynamic response was non-flat mainly due to elasticity of the pressure sensor while effect of compressibility of the fluid is negligible (c.f. Sect. 2.2). The method to correct these effects has been studied in literatures (Aydin, 1998; Donovan et al., 1994, 1991; Taylor and Donovan, 1992). In these studies, the behavior of the pressure-measuring system was modeled to be equivalent to that of a harmonic oscillator with one degree of freedom, and the natural frequency and damping factor was determined by calibration. In the following, a model of the dynamic response of a pressure-measuring system for the pressure measurement at an arbitrary point in liquid flow is considered.

The system, which enables us the fluctuating static-pressure measurement at an arbitrary point in water, is schematically shown in Fig. 5.1a. It comprises the SP-probe, tubing and the pressure transducer, and can be simplified as a tube with sudden contraction connected to the pressure source and the pressure transducer as shown in Fig. 5.1b. Although the model drawn in Fig. 5.1b is more complicated than that in Fig. 2.1 because of the sudden change of cross sectional area at the joint of the SP-probe and the tube, the same expression of fluid motion inside the pressure-measuring

Figure 5.1: (a) Schematics of pressure-measuring system; (b) its model.

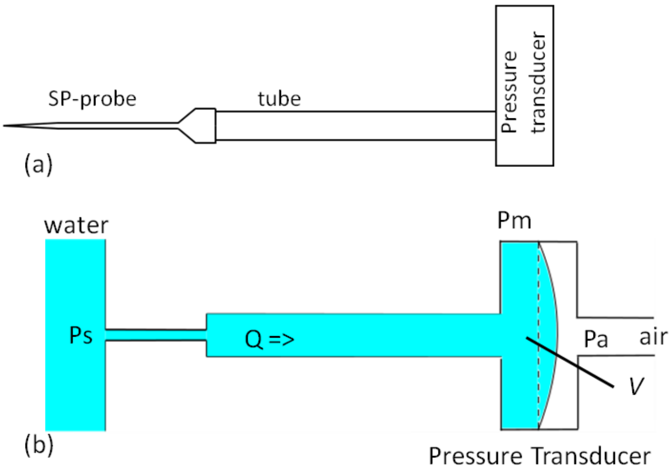

system as Eq. (2.14) is used in the following considerations:

$$I\frac{dQ}{dt}+RQ=-\left(p_{\mathrm{m}}-p_{\mathrm{s}}\right).$$

It can be considered that the effect of the thin entrance part at the pressure source is taken into account by the value of the resistance R. As mentioned in Sect. 2.2, $V_{ol}/K \ll C$ in experiment in water. Hence, $C' \simeq C$. The equation which relates the true fluctuating pressure at the pressure source p_s to the pressure value measured by the transducer p_m is obtained as

$$IC\frac{d^2p_{\mathrm{m}}}{dt^2}+RC\frac{dp_{\mathrm{m}}}{dt}+p_{\mathrm{m}}=p_{\mathrm{s}}, \tag{5.1}$$

and the damping ratio and the undamped natural frequency (in rad/s) of the system are given as:

$$\zeta=\frac{R}{2}\sqrt{\frac{C}{I}}, \qquad \omega_{\mathrm{n}}=\sqrt{\frac{1}{CI}}, \tag{5.2}$$

respectively. Solving Eq. (5.1) with a pressure input p_s fluctuating at a constant frequency ω, one obtains amplitude ratio A and phase lag $\Delta\theta$ between p_{m} and p_{s} as:

$$A = \frac{1}{\sqrt{(1-\omega^{*2})^2+4\zeta^2\omega^{*2}}}, \tag{5.3}$$

$$\Delta\theta = \tan^{-1}\left(\frac{2\zeta\omega^*}{1-\omega^{*2}}\right), \tag{5.4}$$

where ω^* is the non-dimensional frequency defined as $\omega^*=\omega/\omega_{\mathrm{n}}$. The profiles A and $\Delta\theta$ against the frequency of the input pressure fluctuation were measured by the

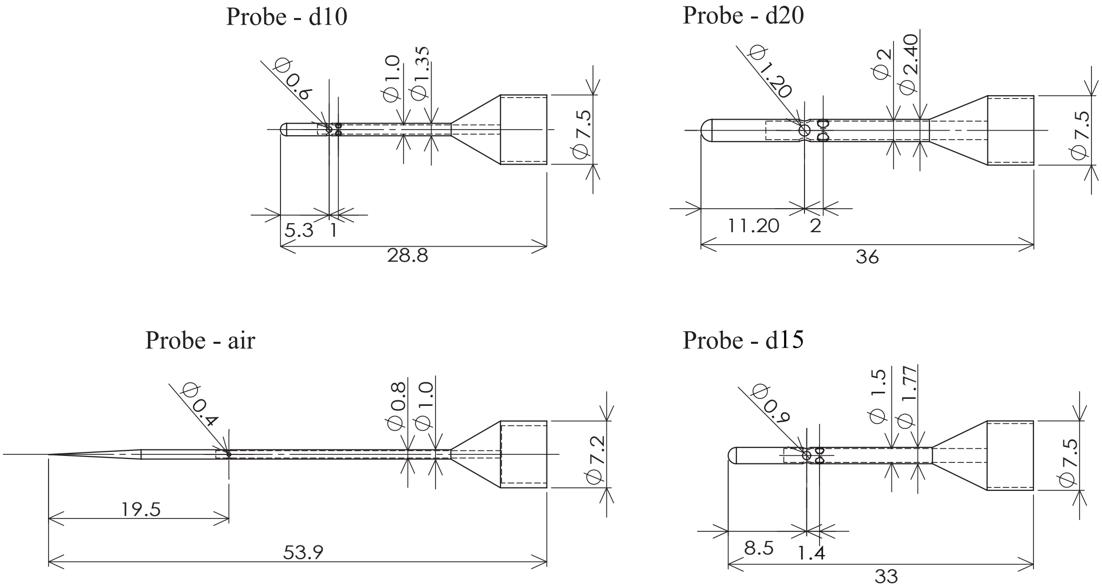

Figure 5.2: Schematics of static-pressure probes.

dynamic-response calibration, and the damping ratio ζ and the natural frequency ω_{n} were evaluated by fitting measured variations of A and $\Delta\theta$ to Eq. (5.3) and (5.4).

5.3 Experimental Apparatus

5.3.1 Pressure-measuring system

Static-Pressure Probe The SP-probes employed in the present study are schematically presented in Fig. 5.2. There were four types of the SP-probe; the probe-air, d10, d15 and d20. The probe-air had similar geometric configuration to those employed in previous experiments in the air (Naka et al., 2006; Toyoda et al., 1994). It consisted of a thin tube with a circular corn tip, and the outer and inner diameters were 1.0 and 0.8 mm, respectively. There were four pressure-sensing holes on the surface separated by 90° in the circumferential direction and the diameter was 0.4 mm.

The probe d10, d15 and d20 were designed for the hydraulic pressure measurement. The diameters and lengths for each probe are presented in Fig. 5.2. They were made of transparent material so that one could check if the bubbles remained inside of the SP-probe, and the tip was semispherical shape. The number of the pressure-sensing holes was eight, and their diameter ϕ was determined so that the impedance of the pressure-measuring system was retained low. To accomplish this, it was assumed that the pressure loss caused by the eight pressure-sensing holes were equal to that in the

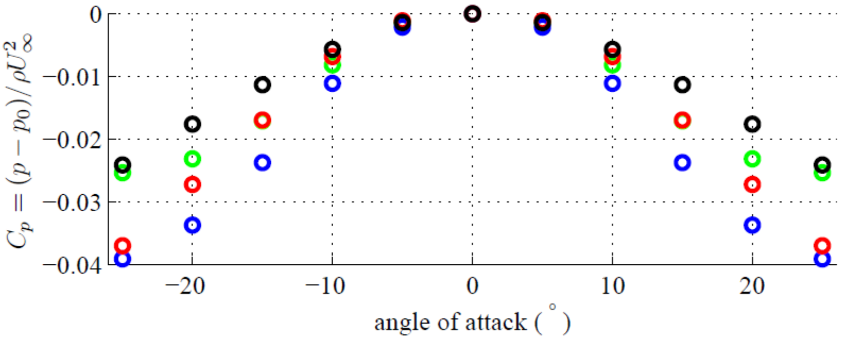

Figure 5.3: Error in pressure measurement due to cross flow: blue, probe-d20; green, probe-d15; red, probe-d10; black, probe-air.

tube of the SP-probe for the same volume flow rate. Under the assumption that the flow through the tube of the SP-probe and that through the eight pressure-sensing holes are approximated by the Hagen-Poiseuille flow, the volume flow rat in the former and that through the latter are proportional to d^4 and $8\phi^4$, respectively:

$$\begin{aligned} \frac{8\phi^4}{d^4} &= 1 \\ \frac{\phi}{d} &= \left(\frac{1}{8}\right)^{1/4} = 0.59. \end{aligned} \tag{5.5}$$

Therefore, the diameters of the pressure-sensing holes were determined to be 60% of the tube diameter of the SP-probe. The analysis based on the Hagen-Poiseuille flow would overestimate the pressure loss caused by the pressure-sensing holes, as there would be only minor viscous effect. Hence the diameter of the pressure-sensing holes determined above should be large enough not to cause a major influence to the dynamic response of the pressure-measuring system.

Error in the pressure measurement by the SP-probes caused by the cross flow was experimentally explored. The SP-probe was placed in an uniform flow of a wind tunnel, and the pressure was measured with various angles of attack. Figure 5.3 shows the variation of the pressure coefficient defined as

$$C_p = \frac{p - p_0}{\rho U_\infty^2}, \tag{5.6}$$

with p_0 being the pressure value measured with the flow angle of 0°. It is shown that pressure is underestimated when the flow direction is not parallel to the axis of the probe. The probe-air shows better angle characteristics than those of the other SP-probes, which may be attributable to difference in the shape of the tip.

Table 5.1: Characteristics of pressure transducer; s, sensitivity; V volume of pressure cavity; $\Delta V_{\max}$, maximum volumetric displacement.

	Range (Pa)	s (Pa/V)	V (cc)	$\Delta V_{\max}$ (cc)	C (mm^3/Pa)
DP45-1	±84	16.7	0.16	0.016	0.192
DP45-2	±167	33.2	0.16	0.016	0.0967
DP103	±28	5.7	0.57	0.057	1.96

Pressure Transducer A low-range strain-gage-type pressure transducer was used for pressure sensor in order to sensitively measure the small pressure fluctuation in a low frequency range. In order to investigate the effect of the elastic compliance C, three pressure transducers with different C were used for comparison: DP45-1, DP45-2 and DP103 (Validyne) were employed, and their characteristics are summarized in Table 5.1.

Tubing A plastic tube was used for tubing between the SP-probe and the pressure transducer placed outside the flow. The inner diameter and the thickness were 6 mm and 0.5 mm, respectively, and the length was 0.96 m.

5.3.2 Other instruments and data acquisition

The experiments were undertaken in a closed-loop water tunnel with maximum free stream velocity of 0.28 m/s. For the other hardware, a carrier modulator (PA501, Validyne) was used for amplification of the signals from the pressure transducer, and an analog low-pass filter (DT-6LF2, NF CORPOLATION) and 16 bit A/D convertor (PCI-6221, National Instruments) were used for filtering and acquisition of samples.

5.4 Dynamic response of Pressure-Measuring System

5.4.1 Response to sinusoidal pressure fluctuation

Response of the pressure-measuring system against pressure input oscillating at a constant frequency was experimentally explored. The system for this calibration is schematically shown in Fig. 5.4. The pressure-measuring system to be calibrated was set up as it was in the main measurement; the SP-probe was placed in the water channel and connected to the pressure transducer located outside by a tube that was identical to that used in the main experiment. Oscillatory pressure was generated in a pressure chamber by driving a piston connected to the pressure chamber using an oscillator,

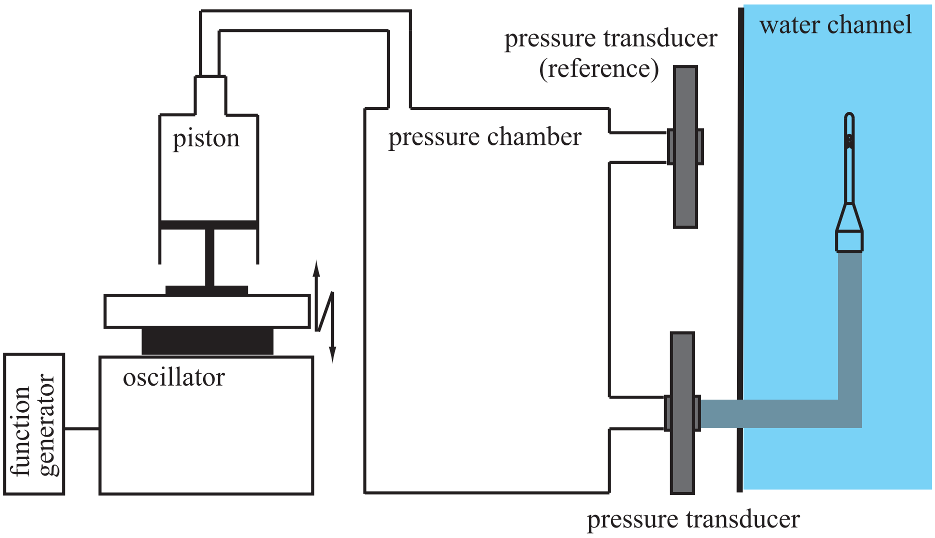

Figure 5.4: Schematics of system for calibration of dynamic response of pressure-measuring system.

and it was introduced into the reference port of the pressure transducer. The frequency and the amplitude of the pressure input were controlled by a function generator. The true fluctuating pressure signal was monitored by another pressure transducer for reference, and the amplitude ratio A and the phase delay $\Delta\theta$ were evaluated by comparing the pressure signals measured simultaneously by these two pressure transducers.

Figure 5.5 presents the time sequences of the oscillatory pressure in the pressure chamber measured in the dynamic response calibration, comparing the signals measured by the main and reference transducers. The calibrated pressure-measuring sys-

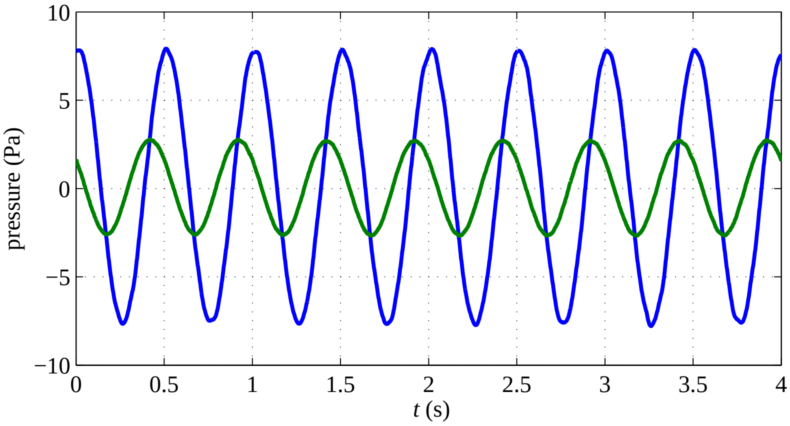

Figure 5.5: Time sequences of oscillatory pressure in the pressure chamber measured in dynamic response calibration: blue, main pressure transducer; green, reference pressure transducer. The calibrated pressure-measuring system comprised the DP45-1 and the probe-d20, the reference pressure transducer was the DP45-2, and the frequency of the input oscillatory pressure was 2 Hz.

tem consisted of the DP45-1 and the probe-d20, and the reference pressure transducer was the DP45-2. The frequency of the input oscillatory pressure was 2 Hz. It is shown that the pressure signal measured by the main pressure transducer was amplified, and a phase delay also occurred. The amplitude ratio and the phase lag between the signals measured by the main and reference pressure transducers were evaluated based on the Fourier coefficients at the input frequency as:

$$\begin{aligned} A(f_{\mathrm{ip}}) &= \sqrt{\frac{B_{\mathrm{m}}(f_{\mathrm{ip}})B^*_{\mathrm{m}}(f_{\mathrm{ip}})}{B_{\mathrm{s}}(f_{\mathrm{ip}})B^*_{\mathrm{s}}(f_{\mathrm{ip}})}}, \qquad (5.7)\\ \Delta\theta(f_{\mathrm{ip}}) &= \tan^{-1}\left(\frac{B_{\mathrm{s}}(f_{\mathrm{ip}})B^*_{\mathrm{m}}(f_{\mathrm{ip}})+B^*_{\mathrm{s}}(f_{\mathrm{ip}})B_{\mathrm{m}}(f_{\mathrm{ip}})}{j\left(B_{\mathrm{s}}(f_{\mathrm{ip}})B^*_{\mathrm{m}}(f_{\mathrm{ip}})-B^*_{\mathrm{s}}(f_{\mathrm{ip}})B_{\mathrm{m}}(f_{\mathrm{ip}})\right)}\right), \qquad (5.8)\end{aligned}$$

where f_{ip} stands for the frequency of the input oscillatory pressure, and B_{m} and B_{s} are the Fourier coefficients of the pressure signals measured by the main and sub pressure transducers, respectively.

The dumping ratio ζ and the natural frequency ω_{n} were evaluated based on the measured profiles of A and $\Delta\theta$. The natural frequency ω_{n} was obtained as the frequency at which $\Delta\theta$ was $\pi/2$ by interpolating the measured variation of $\Delta\theta$. The dumping ratio ζ was evaluated from the profile of the amplitude ratio A as

$$\zeta = \sqrt{\frac{1-\sqrt{1-A_{\mathrm{max}}^{-2}}}{2}}, \qquad (5.9)$$

where A_{max} is the maximum value of A. Equation (5.9) cannot be used in the case where the measuring system is overdamped and the profile of A does not have a maximum value. In such a case, the optimal value of ζ was obtained by fitting Eq. (5.3) to the measured profile of A using “`fminsearch`”, which is function for optimization, available in MATLAB®.

The dynamic response of the pressure-measuring system was investigated for various combinations of the SP-probe and the pressure transducer, and the values of ζ and ω_{n} are summarized in Table 5.2. The measured variation of A and $\Delta\theta$ are compared for cases with DP45-1 and various SP-probes in Fig. 5.6 and for cases with the probe d20 and various pressure transducers in Fig. 5.7. The circles stand for the measured values, and the solid lines represent the profiles obtained by Eqs. (5.3) and (5.4) with the calibrated values of ζ and ω_n in Table 5.2. Although only the values of A and $\Delta\theta$ at vicinity of the natural frequency were used for evaluation of ζ and ω_n, the profiles drawn by Eqs. (5.3) and (5.4) are in good agreement with all the measured val-

Table 5.2: Dumping ratio and natural frequency of various pressure-measuring systems. R, I and C are given in mm^3/Pa, $\times 10^{-2}$kg/mm^4 and mm^3/Pa.

	DP45-2				DP45-1				DP103			
SP-probe	air	d10	d15	d20	air	d10	d15	d20	air	d10	d15	d20
ζ	1.5	0.41	0.20	0.16	1.9	0.52	0.24	0.20	4.0	1.1	0.55	0.46
ω_n	19.7	17.4	19.3	20.3	12.1	11.7	13.2	13.7	2.88	3.52	4.58	4.78
R	1.6	0.49	0.21	0.16	1.7	0.46	0.19	0.15	1.4	0.325	0.122	0.098
I	2.7	3.4	2.8	2.5	3.6	3.8	3.0	2.8	6.1	3.8	2.4	2.2
C	0.0967				0.192				1.96			

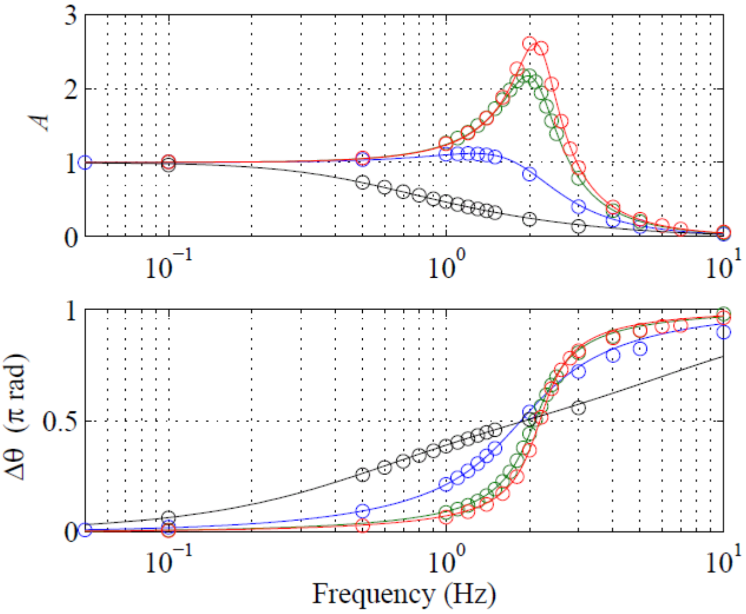

Figure 5.6: Dynamic response of pressure measuring systems with DP45-1 and various SP-probes: blue, probe-d10; green, probe-d15; red, probe-d20; black, probe-air. Circle plots and solid line show the measured values and the fitted profiles, respectively.

ues throughout entire the calibrated frequency range, which indicates that the model Eq. (5.1) approximates well the behavior of the present pressure-measuring system.

Comparing the dynamic response of the pressure-measuring systems with different SP-probes shown in Fig. 5.6, one can obviously see that the resonance peak magnitude of A became smaller as the SP-probe becomes thinner. Especially in the case with the probe-air, the system was overdamped and the evaluated value of the damping ratio ζ was much larger than those of the system with the other SP-probes. On the other hand, the variations of $\Delta\theta$ crossed $\Delta\theta = \pi/2$ around 2 Hz regardless of size of the SP-probe, indicating that the natural frequency ω_n was affected only weakly by size of the SP-probe.

The results presented in Fig. 5.7 indicate that the compliance C significantly changes both ζ and ω_n. As C increases, the natural frequency ω_n was shifted toward the lower frequency region, and also the system became more damped. This can be

Figure 5.7: Dynamic response of pressure measuring systems with probe-d20 and various pressure transducers: blue, DP45-2; green, DP45-2; red, DP103

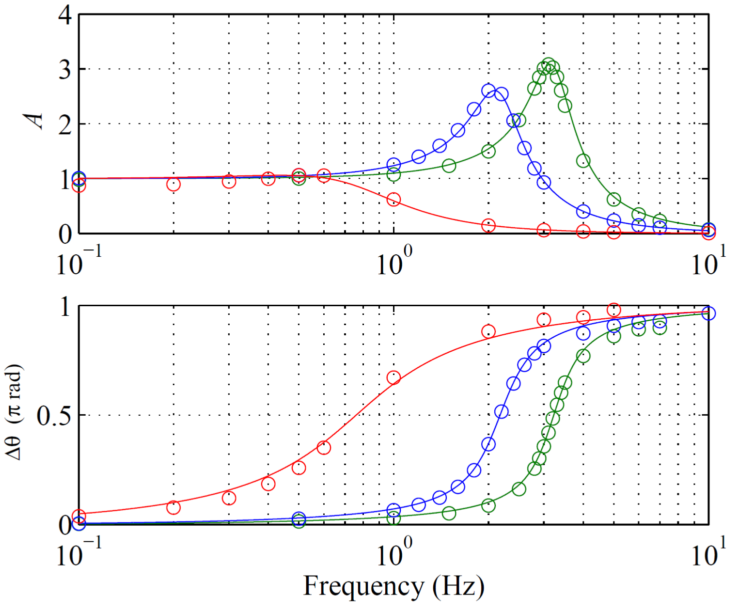

explained by Eq. (5.2) as C appears in both ζ and ω_n.

The fluid resistance R and the inertance I were also evaluated based on Eq. (5.2), and the values are summarized in Table 5.2. One can see that R significantly increased as the tube of the SP-probe became thinner, indicating that R primarily represents the effect of the viscosity of the water inside the tube of the SP-probe. Hence, the size of the SP-probe mainly affected the damping ratio ζ through the value of R, and did not the natural frequency ω_n because R does not appear in ω_n (see Eq. (5.2)). On the other hand, I was relatively insensitive both to the size of the SP-probe and to the compliance of the pressure transducer.

5.4.2 Step-response test

Response to a step input was examined for further investigation on the dynamic response of the pressure-measuring systems. A sudden pressure drop was generated using a system schematically sown in Fig. 5.8. The SP-probe of the pressure-measuring system to be calibrated was fixed in the water phase in a pressure box. A T-shape tube was connected to the air phase in the pressure box at one end and to a piston at another end, and the other end was closed by a membrane of soap solution. The pressure in the air phase in the pressure box was kept higher than the atmospheric pressure by the piston, and sudden pressure drop was generated by breaking the membrane of soap solution.

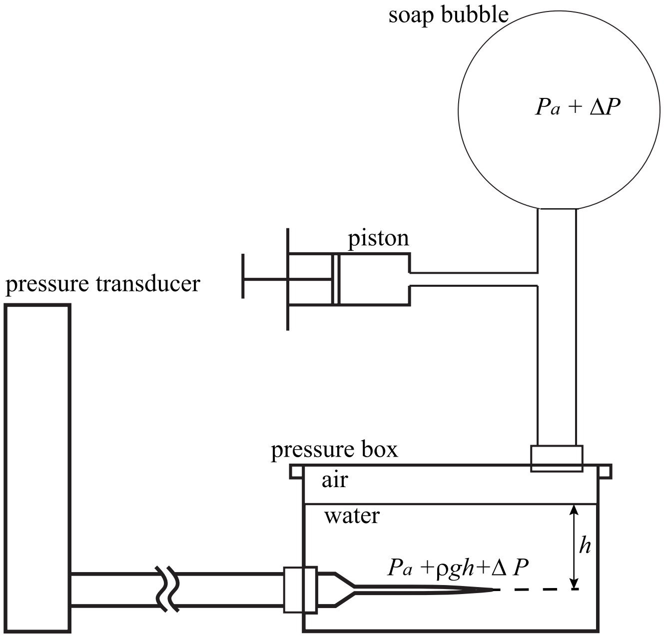

Figure 5.8: Schematics of system for step-response test.

The behavior of the measuring system against the step input is described by the following differential equation:

$$\frac{d^2 p_\mathrm{m}}{dt^2} + 2\zeta\omega_\mathrm{n}\frac{dp_\mathrm{m}}{dt} + \omega_\mathrm{n}^2 p_\mathrm{m} = 0. \tag{5.10}$$

Equation (5.10) can be easily solved, and the analytical step response of the pressure-measuring system is obtained as:

$$\frac{p_\mathrm{m}}{p_0} = \begin{cases} e^{-\zeta\omega_\mathrm{n}t}\left(\cos qt + \dfrac{\zeta\omega_\mathrm{n}}{q}\sin qt\right) & (\zeta < 1) \\ \dfrac{p_2}{p_2 - p_1}e^{-p_1 t} - \dfrac{p_1}{p_2 - p_1}e^{-p_2 t} & (\zeta > 1) \end{cases}, \tag{5.11}$$

where p_0 is the height of the step input, and q, p_1 and p_2 are respectively defined as:

$$\begin{aligned} q &= \omega_\mathrm{n}\sqrt{1-\zeta^2}, \\ p_1 &= \omega_n(\zeta + \sqrt{\zeta^2 - 1}), \\ p_2 &= \omega_n(\zeta - \sqrt{\zeta^2 - 1}). \end{aligned}$$

Figure 5.9 presents the step response of the measuring systems with DP45-1 and various SP-probes, comparing those measured and predicted by Eq. (5.11). The measured responses are indicated by the blue, green, cyan, and red lines for the probe-d20,

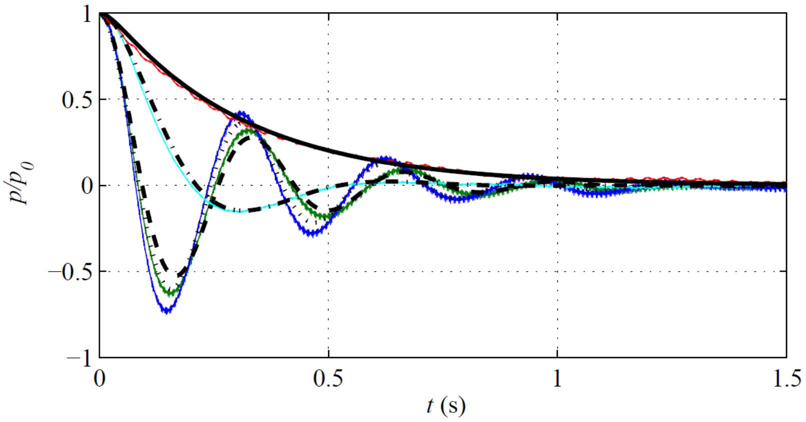

Figure 5.9: Comparison of measured and predicted step response of pressure-measuring system with DP45-1. Probe-d20, blue and "· · ·"; probe-d15, green and "— —"; probe-d10, cyan and "— · —"; probe-air, red and "—".

d15, d10, and air, and it is shown that step response of the system with the probes-d10, d15, and d20 showed the overshoot, but that of the system with the probe-air was overdamped and did not oscillate. The step responses predicted by Eq. (5.11) with the values of ζ and ω_n in Table 5.2 are also presented in Fig. 5.9 by the black dotted, dashed, chained, and solid lines for the probe-d20, d15, d10, and air. The predicted step response for the case with the probes-air and d10 were in strong agreement with the measured step responses, and those for the case with probes-d15 and d20 also agreed fairly well with the measured step response while certain underestimate of overshoot can be seen. This results also supports consistency of the present calibration results.

5.4.3 Effect of tube on dynamic characteristics of systems

The present pressure-measuring system has tubing with a certain length between the SP-probe and the the pressure transducer, unlike those used in the measurements in air, where the transducer is directly embedded to the SP-probe. The dynamic characteristics of such a pressure-measuring systems may depend on the length and/or the shape such as straight, curved, or looped. In this subsection, such effect of the tubing is addressed by the step-response test.

Effect of tubing length The effect of the tubing length was examined by comparing the step response for different tubing lengths. Three tubes were used for comparison: tubes with lengths of 0.46 m, 0.96 m and 1.9 m. It should be noted that the tube with length of 0.96 m was identical to that used in the main experiment.

Table 5.3: Parameters of pressure-measuring system with different tubing length.

L (m)	ζ/ζ_0	$\omega_\mathrm{n}/\omega_\mathrm{n0}$	R/R_0	I/I_0
0.46	1.1	1.26	0.94	0.86
0.96	1	1	1	1
1.9	0.94	0.76	1.23	3.73

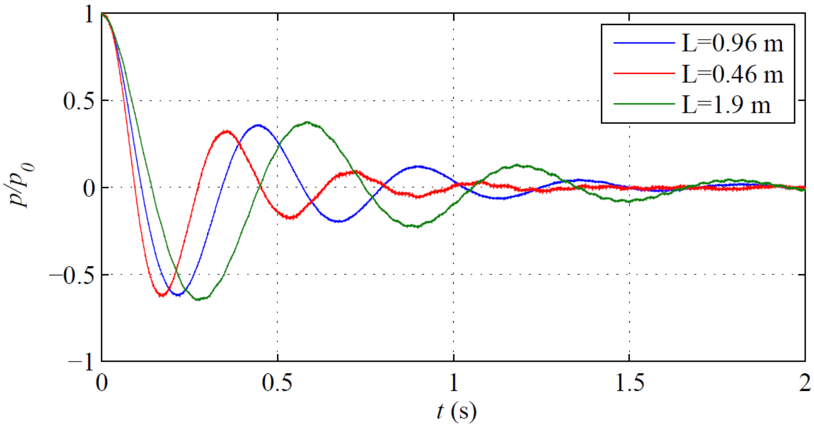

Figure 5.10: Step response of pressure measuring systems with probe-d20, DP45-1 and tubing with different lengths.

Figure 5.10 compares the step responses of the pressure-measuring systems with the DP45-1, the probe-d20, and the three different tubes. It is shown that the step response was clearly affected by the length of the tubing. The parameters of the dynamic response for each case were evaluated by fitting Eq. (5.11) to the measured step response, and the obtained values are summarized in Table 5.3. The values are scaled by those in the case of the tubing length being 0.96 m. It is shown that both R and I increased as the tubing length increased. The increase of R was attributable to increase of the area of inner wall of the tube, where the viscous drag acted on the oscillating fluid inside the tubing. The increase of I was simply interpreted as the increase of the fluid mass inside the pressure-measuring system.

The natural frequency of the system ω_n moved toward the lower frequency range as the tubing length increased due to the increasing I (see Eq. (5.2)). The damping ratio ζ was the function of both R and I, and decreased as the tubing length increased because the variation of I was more significant than that of R. Thus, the tubing length affects both the damping ratio and the natural frequency of the pressure-measuring system through the fluid inertance I.

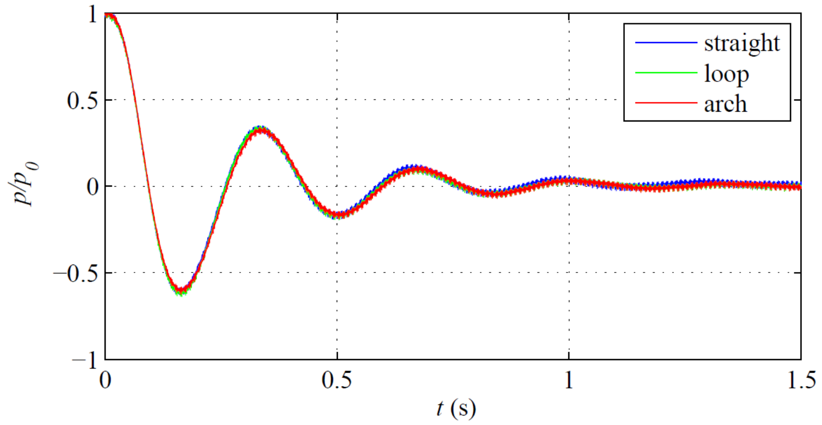

Figure 5.11: Step response of pressure measuring systems with same SP-probe, tubing, pressure transducer but different shape of tubing.

Effect of tubing shape The effect of shape of the tubing is examined. The step responses of the pressure-measuring system composed of same SP-probe, same pressure transducer, and same tube was measured and compared for different three tube shapes: straight, looped, and arched. The step response measured with different tubing shape are compared in Fig. 5.11. It is indicated that the step responses were almost identical to each other and the tubing shape did not affect the dynamic characteristics of the pressure-measuring system.

5.5 Fluctuating Pressure Measurement in a Wake of a Circular Cylinder

5.5.1 Experimental condition

Fluctuating pressure measurement was performed in a wake of a circular cylinder. The measurement was undertaken in a closed-loop water channel. A circular cylinder with the diameter D of 20 mm was placed in a free steam of the water channel, and the free stream velocity was fixed at $U_\infty = 0.28$ m/s. The temperature of the water was 39°C during the measurement. The origin of the Cartesian coordinates was placed at the center of the cylinder and the $x-$ and $y-$axes were taken in the streamwise and transverse directions, respectively. The Reynolds number based on U_∞ and D, $Re = U_\infty D/\nu$, was 7800, and the measurements were conducted at $x/D = 6$.

The main SP-probe was placed in the wake, and the secondary SP-probe, which had the same geometry as the main probe, was placed at the same streamwise location

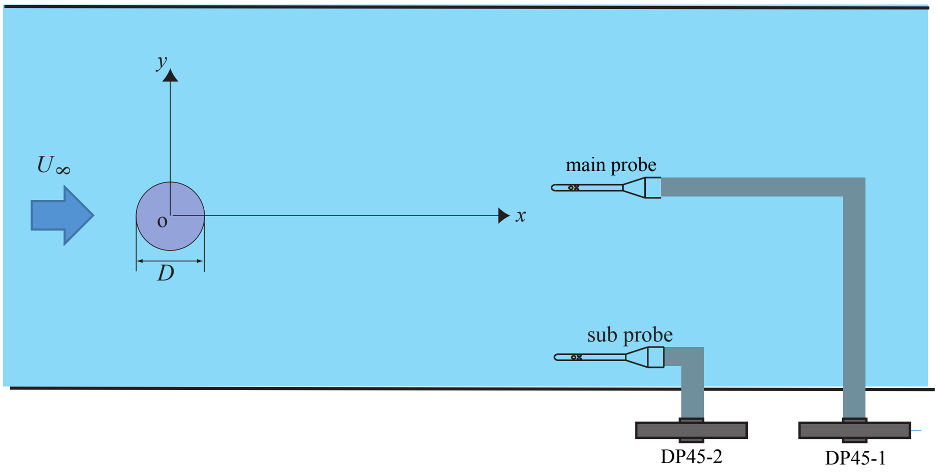

Figure 5.12: Measurement conditon.

but outside the wake to monitor the background noise on the fluctuating pressure. The background noise on the pressure signal measured by the main probe was reduced by the same manner proposed by Naguib et al. (1996). The DP45-1 was used with the SP-probes d15 and d20, but the DP45-2 was used for with the SP-probe d10 and air, because of the better dynamic response of the pressure-measuring system with the DP45-2. A sampling rate and sampling time at each measurement point were 100 Hz and 300 s, respectively.

The signals of fluctuating pressure were corrected based on the calibration results of the dynamic response of the pressure-measuring system by the procedure described below. Applying the Fourier transform to the measured pressure signals, we evaluated the complex Fourier coefficient at n-th Fourier mode B_n. The amplitude change and the phase delay at n-th frequency f_n caused by the dynamic response of the SP-probe, namely A_n and $\Delta\theta_n$, were evaluated by Eqs.(5.3) and (5.4) with the values of ω_n and ζ in Table 5.2. Using these values of A_n and $\Delta\theta_n$, B_n was corrected as

$$\hat{B_n} = \frac{B_n}{A_n\{\cos(\Delta\theta_n) + j\sin(\Delta\theta_n)\}}, \tag{5.12}$$

where j is the imaginary unity, and the pressure signals were reconstructed by applying inverse Fourier transform as

$$p = \sum_{n=1}^{N} \hat{B_n} \exp\left(-j2\pi f_n t\right). \tag{5.13}$$

As the sampling time was 300 s, the frequency resolution of the Fourier transform was $1/300$ Hz. Besides, a low-pass filtering a cut-off frequency of 8 Hz was applied to the

Figure 5.13: Distribution of mean pressure and at $x/D = 6$ in a wake of a circular cylinder: blue, d20; green, d15; red, d10; black, air.

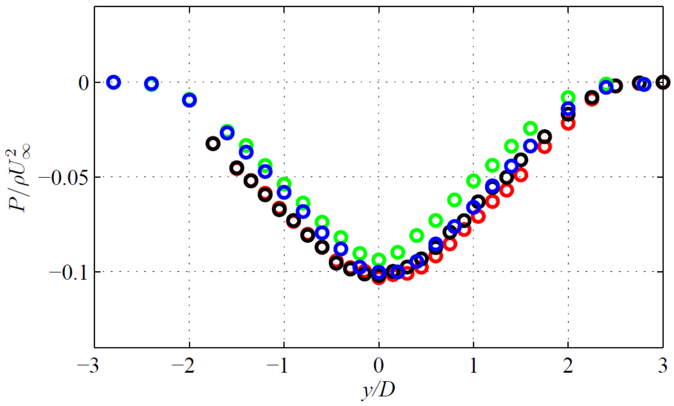

corrected pressure signals, in order to filter out the high-frequency noise. The FFT, interpolation, and low-pass filtering included in the above procedures were conducted by using the functions “`fft`”, “`interp1`”, and “`filtfilt`” available in the MATLAB® library.

It should be mentioned that the measurement location $x/D = 6$ belonged to the flow region associated with relatively strong velocity fluctuation, in which the pressure measurement by the SP-probe might be contaminated due to the cross flow effect described in Fig. 5.3. However, as the purpose in the present chapter is to develop a calibration technique of dynamic response of a system for pressure measurement in water, the overall accuracy of the pressure measurement is not addressed, and, instead, a focus is put on correction of the measured pressure signal based on the result of the dynamic-response calibration.

5.5.2 Results and discussion

The distributions of the mean pressure P at $x/D = 6$ measured by the four different SP-probes are presented in Fig. 5.13. The values are scaled by ρU_∞^2, and the mean pressure values at $y/D = 3.0$ are taken to be zero. It should be also mentioned that the pressure in the range of $y/D < -2.0$ was not measured by the probes d10 and air due to the limitation of the traverse equipment. The profile of P measured by all the SP-probes show symmetric profiles with respect to $y/D = 0$ and take the minimum of about $-0.1\rho U_\infty^2$ at the wake center. The agreement between these results is reasonably good.

Figure 5.14a presents the distributions of the root-mean-square of the pressure fluctuation obtained from the uncorrected pressure. The values of the pressure fluctuation p' are scaled by ρU_∞^2. The profiles of the uncorrected p' measured by the various SP-probes show much different distributions. Those measured by the probes d10, d15, and

Figure 5.14: Distribution of pressure fluctuation at $x/D = 6$ in a wake of a circular cylinder: (top) uncorrected, (bottom) corrected. Colors indicate same SP-probes as in Fig. 5.13

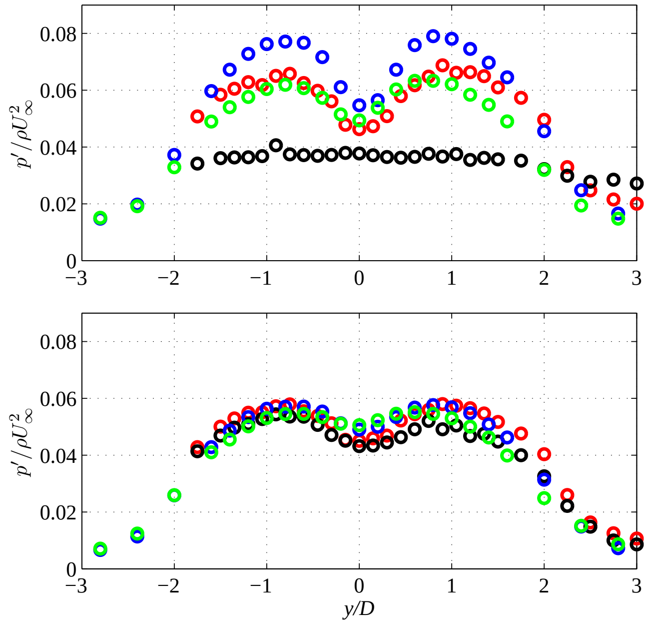

d20 indicate the two peaks of the pressure fluctuation located beside the wake center, but the peak magnitude is different from each other. On the other hand, the profile of p' measured by the probe-air shows much smaller value and has no peak of fluctuation.

Figure 5.14b presents the profiles of the pressure fluctuation p' evaluated from the pressure corrected based on the calibration results of the dynamic response of the pressure-measuring system. The profiles of p' measured by the four SP-probes are in good agreement with each other despite of the profiles much different from each other before the correction. Especially, the result measured by the probe-air was drastically changed by the correction; two peaks of the fluctuation appears at $y/D = \pm 1$.

Figure 5.15 presents the power spectrum density (PSD) of the fluctuating pressure at $y/D = -1.0$, comparing the results measured by the various SP-probes. The profiles of the PSD of the uncorrected pressure are show in Fig. 5.15a. All of the profiles measured by the four different SP-probes have a significant peak at $f = 2.6$ Hz, which corresponds to the Strouhal number $S_t = fD/U_\infty$ of 0.186. This peak was obviously caused by the Karman vortices shed from the cylinder. The difference between the results measured is significant in the frequency range 1 Hz $\leq f$, including the vortex shedding frequency. The PSDs measured by the probe-d10, d15, and d20 have the broad hill, which was caused by the resonance. On the other hand, the profile of the PSD measured by the probe-air does not show such broad increase because the system with the probe-air is overdamped.

In Fig. 5.15b, it is shown that the PSDs of the measured pressure are in good agree-

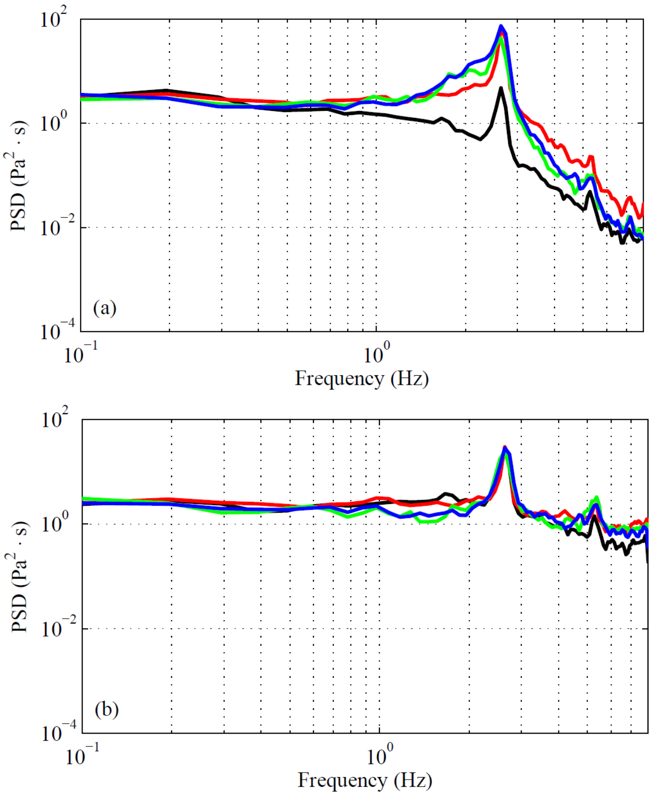

Figure 5.15: Power spectra density of pressure fluctuation measured at $y/D = -1.0$: (top) uncorrected, (bottom) corrected; blue, d20; green, d15; red, d10; black, air.

ment with each other after the correction. The broad hill apparent in the profiles of the uncorrected PSD measured by the SP-probe d10, d15 and d20 disappear although the significant peak by the Karman vortex shedding still remain. The profile of the PSD measured by the probe air also drastically changed by the correction. This agreement between the pressure fluctuation by the correction supports validity of the present measurement technique.

In order to further examine the measurement results, the probability density function (PDF) of fluctuating pressure was investigated at $y/D = 1.0$ and 3.0; the former was the location where the pressure fluctuation reached a local maximum, while the latter was outside the wake region where the pressure fluctuation is so weak that basically only the background noise was measured. Figure 5.16 presents the PDFs at these locations measured by the four SP-probes after the correction of the dynamic response was made. The results measured by the four different SP-probes agree well with each other. The PDFs measured at the edge of the wake $y/D = 3.0$ are concentrated around $p/\rho U_\infty^2 = 0$, while the PDFs measured at the peak location $y/D = 1.0$ show smooth distributions with a notable negative skewness. Both distributions are smooth and free from scratch noise of any kind. Based on these observations, we consider that the noise level of the pressure measurement was sufficiently small.@ The pressure fluctuation

Figure 5.16: Probability density function of fluctuating pressure: (a) measured at $y/D = 3.0$, (b) measured at $y/D = 1.0$. Colors indicate same SP-probe as in Fig. 5.13

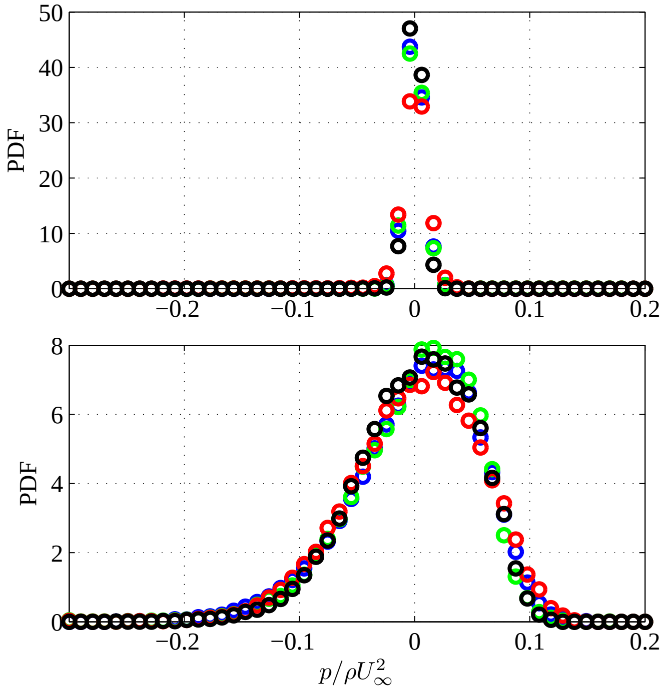

at $y/D = 1.0$ was about $0.052\rho U_\infty^2$ (evaluated as the average of results by the four SP-probes), while that measured at $y/D = 3.0$ was 0.0081. Consequently, the signal-to-noise ratio of the pressure measurement was roughly evaluated to be 6.6-to-1.

The appropriateness of the correction based on the present calibration results is also supported by the higher moment of the pressure fluctuation. Figure 5.17 presents the distribution of the skewness factor of the pressure fluctuation, defined as $S \equiv \overline{p^3}/p'^3$, comparing the profiles evaluated from the measured pressure signals before and after the correction. The profiles of S evaluated without the correction show the negative values of skewness across the wake, and have two negative peaks located at $y/D = \pm 2$. Among the results, those measured by the probe-air shows much larger magnitude of the skewness than those measured by the other probes in the center region of the wake. On the other hand, the profiles of S evaluated with the correction are in fairly good agreement with each other, which also supports the appropriateness of the correction on the measured pressure based on the calibration results.

As shown in the above discussion, the measured fluctuating pressure was examined from different aspects including the second- and third-moments, PSD, and PDF, and these results measured by the four different pressure-measuring systems showed a clear consistency with each other. These observations supports a fair reliability of the present method of dynamic-response calibration.

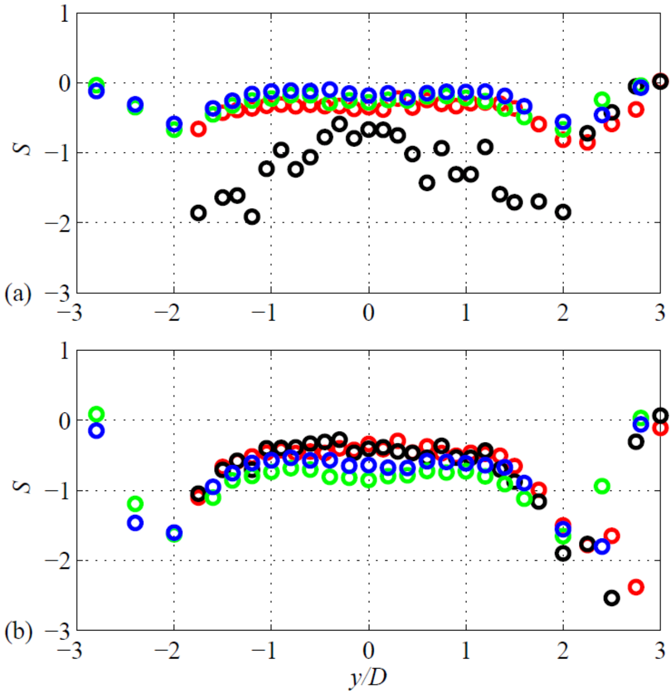

Figure 5.17: Distribution of skewness factor at $x/D = 6$ in a wake of a circular cylinder: (top) uncorrected, (bottom) corrected. The colors indicate same SP-probe as in Fig. 5.13

5.6 Summary of This Chapter

A technique for fluctuating static-pressure measurement at an arbitrary point in turbulent flow in water was developed using a pressure-measuring system comprising an SP-probe, a strain-gauge-type pressure transducer, and a tube connecting them. A model of behavior of the pressure-measuring system was introduced, and a calibration technique for determining the parameters in the model equation was developed. The fluctuating pressure measurement was performed in a wake of a circular cylinder. The frequency range of the present measurement technique was $0 \leq f \leq 8$ Hz, and the spatial resolution was from $2.4 \times 2.4 \times 3.2$ mm^3 to $1.0 \times 1.0 \times 0.4$ mm^3, depending on the SP-probe. The signal-to-noise ratio was approximately 6.6-to-1. The pressure related statistics measured by four different pressure-measuring systems, including the second- and third-moments, power spectrum density, and probability density function, were in good agreement with each other, after the correction based on the dynamic-response calibration. This demonstrates that the fluctuating hydraulic-pressure was successfully measured by the developed technique and fluctuating pressure at an arbitrary point in water is possible.

Chapter 6

Hybrid Method of PIV-Based Pressure Evaluation and Direct Measurement by Static-Pressure Probes

6.1 Motivation

Certain successful results of the velocity-pressure correlation have been obtained by the direct measurement method, where the miniature pressure probe is combined with a hot-wire probe, by the several earlier studies (Naka and Obi, 2009; Naka et al., 2006; Sakai et al., 2007; Terashima et al., 2012; Tsuji et al., 2007) and the previous chapters of this thesis. However, this measurement technique is limited to the single-point measurement; in addition, it cannot be applied to the flow region where instantaneous flow direction has large angle of attack to the probe axis, such as a high turbulence intensity region or a recirculation region, mainly due to error in the pressure measurement caused by the cross-flow effect.

On the other hand, the PIV-based pressure evaluation, by which instantaneous pressure filed is numerically derived from instantaneous velocity field measured by PIV, has been intensively studied in recent years (e.g., Ghaemi et al., 2012; Liu and Katz, 2006; Obi and Tokai, 2006; Pröbsting et al., 2013; van Oudheusden, 2013), as mentioned in Sect. 1.2. Thanks to the non-intrusive nature of PIV measurement, this method can be applied to flow regions where the direct measurement techniques cannot be used. It is also quite useful for investigating the pressure-related statistics, in that both the instantaneous fields of velocity and pressure are obtained.

Despite such great advantages, there remain issues of the PIV-based pressure evaluation that need to be further addressed, such as specification of the boundary condition. Information of velocity primarily gives the Neumann-type boundary condition as the pressure gradients are supplied by evaluating the terms in the momentum equation, while some extra efforts are required to identify the Dirichlet-type boundary condition; the most straightforward way is to directly measure the pressure in the PIV measurement domain, which has never been attempted in earlier studies (at least, to the best of the author′s knowledge) partly due to the technical difficulties in measuring fluctuating pressure. Alternatively, in some of the earlier studies, the pressure on the boundary was estimated from the measured velocity data by assuming a potential flow or a steady flow (e.g., De Kat and van Oudheusden, 2012; Ghaemi et al., 2012; Ishii et al., 2008; Pröbsting et al., 2013).

The PIV-based pressure evaluation has another shortcoming, in that the pressure evaluation is easily affected by the noise involved in PIV data (Charonko et al., 2010; De Kat and van Oudheusden, 2012). The equation used to derive pressure, such as the Poisson equation for pressure, contains spatial and temporal derivatives of instantaneous velocity, the evaluation of which amplifies the effect of the measurement noise in PIV data.

In this chapter, it is aimed to improve these shortcomings of the PIV-based pressure evaluation method by combining it with direct single-point measurement by the SP-probes. The technique for fluctuating pressure measurement in liquid flow developed in the previous chapter is combined with time-resolved planar PIV measurement, and instantaneous velocity field and fluctuating pressure at single point are measured simultaneously. The shortcomings of the PIV-based pressure evaluation, such as the low signal-to-noise ratio and the specification of the pressure value, is overcome by using the pressure signals directly measured by the SP-probe as reference to extract the pressure data of the coherent structure and to specify the pressure value. Simultaneous measurement of fluctuating velocity and pressure was performed in a turbulent wake behind a circular cylinder, where the recirculation region exists and the direct measurement technique for the velocity-pressure correlation measurement cannot be applied. The pressure-related statistics such as the velocity-pressure correlation and the pressure-strain correlation were evaluated, and their roles in the transport of the Reynolds stresses were investigated.

6.2 Evaluation of Instantaneous Pressure Field

6.2.1 Basic Equation and Boundary Condition

There are several ways to numerically reconstruct the pressure field from the measurement data of the PIV, such as directly integrating of the pressure gradient obtained based on the momentum equation (e.g., Liu and Katz, 2006) and solving the Poisson equation for pressure (e.g., De Kat and van Oudheusden, 2012; Ghaemi et al., 2012; Obi and Tokai, 2006; Pröbsting et al., 2013). Charonko et al. (2010) compared several numerical methods and reported that solving Poisson equation is more robust to the noise involved in the PIV data than the other numerical method. In the present study, the Poisson equation for pressure was used for numerically valuating pressure.

Based on the Navier-Stokes equation for the incompressible flow, the pressure gradient is obtained as

$$\frac{\partial \tilde{p}}{\partial x_i} = -\rho \left(\frac{\partial \tilde{u}_i}{\partial t} + \tilde{u}_j \frac{\partial \tilde{u}_i}{\partial x_j} \right) + \mu \frac{\partial^2 \tilde{u}_i}{\partial x_j^2}, \tag{6.1}$$

where ρ is density of the fluid, and u_i and p are instantaneous velocity and pressure, respectively. When the flow field of interest is fairly homogeneous in the z-direction, the two-dimensional approximation can be applied, and the pressure gradient in the x- and y-directions are approximated as:

$$\frac{\partial \tilde{p}}{\partial x} \simeq -\rho \left(\frac{\partial \tilde{u}}{\partial t} + \tilde{u} \frac{\partial \tilde{u}}{\partial x} + \tilde{v} \frac{\partial \tilde{u}}{\partial y} \right), \tag{6.2}$$

$$\frac{\partial \tilde{p}}{\partial y} \simeq -\rho \left(\frac{\partial \tilde{v}}{\partial t} + \tilde{u} \frac{\partial \tilde{v}}{\partial x} + \tilde{v} \frac{\partial \tilde{v}}{\partial y} \right), \tag{6.3}$$

where u and v are the velocity components in the x- and y-directions, respectively. It should noted that the viscous terms of Eq. (6.1) are omitted under the assumption of sufficiently high Reynolds number. Taking divergence of the pressure gradients, one obtains the 2-D approximated Poisson equation for pressure:

$$\begin{aligned} \frac{\partial^2 \tilde{p}}{\partial x^2} + \frac{\partial^2 \tilde{p}}{\partial y^2} = \frac{\partial}{\partial x} \left[-\rho \left(\frac{\partial \tilde{u}}{\partial t} + \tilde{u} \frac{\partial \tilde{u}}{\partial x} + \tilde{v} \frac{\partial \tilde{u}}{\partial y} \right) \right] \\ + \frac{\partial}{\partial y} \left[-\rho \left(\frac{\partial \tilde{v}}{\partial t} + \tilde{u} \frac{\partial \tilde{v}}{\partial x} + \tilde{v} \frac{\partial \tilde{v}}{\partial y} \right) \right]. \end{aligned} \tag{6.4}$$

The source terms on the right-hand-side can be evaluated from the PIV data. Hence, one can obtain the instantaneous pressure field from the PIV data by numerically solving Eq. (6.4) with the proper boundary condition.

The boundary conditions are specified by virtue of Eqs. (6.2) and (6.3), which provides the Neumann-type condition. It should be mentioned that one needs reference pressure to specify the pressure values; in the present study, instantaneous pressure directly measured by the SP-probe is used as the reference, as will be described in Sect. 6.3.4.

6.2.2 Extraction of Data of Coherent Structure from PIV Data

Measurement noise involved in PIV data greatly affects the evaluation of instantaneous pressure field, because the source terms of Eq. (6.4) include temporal and spatial derivatives of instantaneous velocity. In order to separate the meaningful data of coherent structure from the noise, the proper orthogonal decomposition (POD) was applied as performed by Charonko et al. (2010).

The pressure gradients were evaluated from the PIV data by Eqs. (6.2) and (6.3), and the POD was applied to the data set of the velocity and the evaluated pressure gradient. After the POD was applied, the fluctuating velocities and the pressure gradients associated with the coherent structures can be extracted by reconstructing the PIV data using only the several lowest modes as:

$$\hat{\tilde{u}}_m = U + \sum_{k=1}^{m} a_i(t)\eta_k, \tag{6.5}$$

$$\hat{\tilde{u}}_m = V + \sum_{k=1}^{m} a_i(t)\xi_k, \tag{6.6}$$

$$\widehat{\frac{\partial \tilde{p}}{\partial x}}_m = \frac{\partial P}{\partial x} + \sum_{k=1}^{m} a_i(t)\phi_k, \tag{6.7}$$

$$\widehat{\frac{\partial \tilde{p}}{\partial y}}_m = \frac{\partial P}{\partial y} + \sum_{k=1}^{m} a_i(t)\psi_k. \tag{6.8}$$

where $\overline{[]}$ stands for the averaged values, $\hat{[]}_m$ for the instantaneous quantities reconstructed from the lowest m POD modes, η_k, ξ_k, ϕ_k, and ψ_k are the k-th POD bases of the velocities and the pressure gradients, and $a_k(t)$ is the k-th POD coefficient common to all the POD bases. The proper value of m was determined based on the reference signal directly measured by the SP-probe, as described in Sect. 6.3.4. The reconstructed pressure gradients $\hat{\partial} p/\partial x_m$ and $\hat{\partial} p/\partial y_m$ were used to evaluate the content of $\partial/\partial x[]$ and $\partial/\partial y[]$ in the right-hand-side of Eq. (6.4) and to specify the boundary condition. The reconstructed velocities $\hat{u}_m$ and $\hat{v}_m$ were used to evaluate the pressure-related statistics in Sect. 6.5.

6.2.3 Numerical Methods

Equation (6.4) was discretized by means of the finite volume method with second order accuracy. Denoting by P the node at which the equation to be solved is discretized and those surrounding it by E, S, W, and N, a discrete form of the Poisson equation is

$$\frac{\Delta y}{\Delta x}(\phi_E+\phi_W)+\frac{\Delta x}{\Delta y}(\phi_N+\phi_S)-2\left(\frac{\Delta x}{\Delta y}+\frac{\Delta y}{\Delta x}\right)\phi_P=S, \tag{6.9}$$

where S is the source terms in the right-hand-side, which was evaluated as

$$S=\left[\frac{\partial}{\partial x}\left(\widehat{\frac{\partial \tilde{p}}{\partial x}}_m\right)+\frac{\partial}{\partial y}\left(\widehat{\frac{\partial \tilde{p}}{\partial y}}_m\right)\right]\Delta x\Delta y, \tag{6.10}$$

with Δx and Δy being the grid spacing in the x- and y-directions, respectively. The temporal and spatial derivatives in the source term S were evaluated based on the PIV data using the central-difference-scheme with second order accuracy.

The numerical solution was obtained by the successive over-relaxation (SPR) method. The iterative procedure was continued until the residual became 1/1000 of that at the first iteration. The iteration number necessary for convergence was 10,000.

6.3 Experiment

6.3.1 Flow System

The test section is schematically shown in Fig. 6.1. The measurements were undertaken in a closed-loop water channel with a cross-sectional area $W \times H$ being 330×140 mm^2 (W and H are the width and the height of the cross section, respectively). A circular cylinder, which had a diameter D of 20 mm and spanned the height of the channel, was placed in the test section; consequently the aspect ratio D/H and the blockage coefficient D/W were 0.14 and 0.061, respectively. The origin of Cartesian coordinates was fixed at the center of the cylinder, and the x, y, and z axes were taken in the streamwise, transverse, and spanwise directions. The measurement domain of the PIV was placed immediately behind the cylinder, $0.6 \leq x/D \leq 4.5$, $-2.1 \leq y/D \leq 1.9$. The temperature of the water was 25°C during the experiment.

Figure 6.1: Schematics of test section.

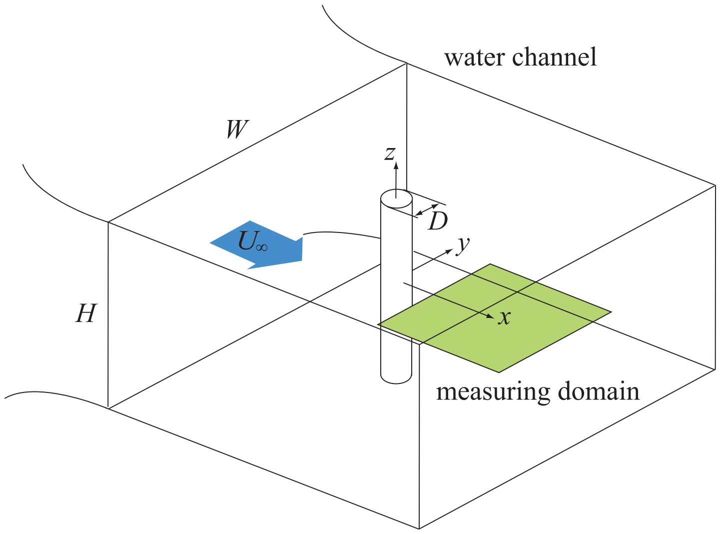

Figure 6.2: Static-pressure probe for direct single-point measurement of fluctuating pressure.

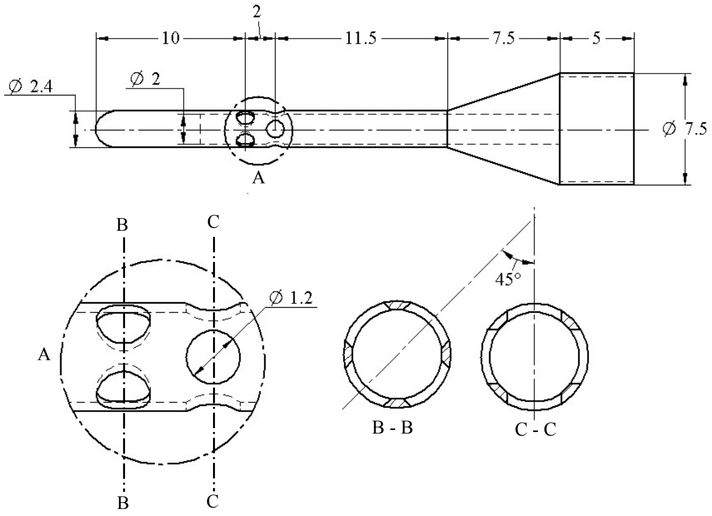

The free-stream velocity U_∞ was 0.28 m/s with turbulence intensity of 3%, and the Reynolds number based on D and U_∞ was 7800. The vortex shedding frequency was 2.6 Hz, corresponding to the Strouhal number $S_t = fD/U_\infty$ of 0.19.

6.3.2 Direct Single-Point Measurement of Fluctuating Pressure

The direct single-point measurement of fluctuating pressure was conducted by means of the technique developed in Sect. 5. The SP-probe 20 was employed (the schematics is shown in Fig. 6.2). As will be described later, three SP-probes were used for simultaneous measurement with a planar PIV: two SP-probes were used as the main probes located inside the measurement domain of the PIV for simultaneous measurement, and the other SP-probe was a sub probe for monitoring a background noise loaded on the pressure signals measured by the two main SP-probes. The pressure-measuring system developed in Chap. 5 was used; the SP-probes were connected to pressure transducers mounted outside the water channel by plastic tubes with a length, inner diameter, and thickness of 0.96 m, 6 mm, and 0.5 mm, and the DP45-1 and 2 were used with the two main SP-probes and the sub SP-probe, respectively. The signals from the pressure transducer was acquired by a 16-bit DAQ board (PCI 6221, National Instruments).

6.3.3 Velocity Measurement by PIV

Instantaneous velocity field was captured by means of a time-resolved planar PIV. A high-speed camera (FASTCAM SA3 model, Photron) with an 85 mm lens (Nikkor 85 mm f2.8D, Nikkon) was combined with a continuous laser (LYPE2-SG-WL532CW LYPE) with a wave length and a maximum output power of 532 nm and 2 W, respectively. The resolution of the high-speed camera was 1024×1024 pixel^2. White Nylon 12 particles, with a mean diameter and a specific gravity were 90 μm and 1.02, respectively, were used as a tracer.

The acquired images were processed by a house-made three-step algorithm based on the FFT-based cross-correlation method, in which the basic PIV, the discrete-window-shift PIV, and the central-difference-image-correction method (Wereley and Gui, 2003) were applied in the first, second, and third step with increasing spatial resolution. Size of the interrogation area was 48×48 pixel^2 in the first and second steps, and 20×20 pixel^2 in the third step, which corresponds to spatial resolution of 1.63×1.63 mm^2. The data points were located with overlap ratio of 50%, and 99×97 data points were in the PIV measurement domain. The sub-pixel displacement was evaluated based on the Gaussian fitting. The outliers were detected by the median filtering (Westerweel, 1994), and replaced by the average of the velocity vectors at surrounding eight neighbor data points; the typical number of the detected outliers was less than 0.1% of the data points.

The overall accuracy of the house-made PIV algorithm was addressed by Suryadi (2007) using artificial particle images by Okamoto et al. (2000), and uncertainty in evaluation of the particle displacement was found to be approximately 0.2 pixel, which corresponds to 3% of U_∞.

6.3.4 Simultaneous Measurement of Velocity and Pressure

Measurement system The system for simultaneous measurement of velocity and pressure is schematically shown in Fig. 6.3. Two SP-probes were employed; the SP-probes 1 and 2 were located at $(x_1/D,\ y_1/D) = (4.3,\ 1.0)$ and $(x_2/D,\ y_2/D) =$

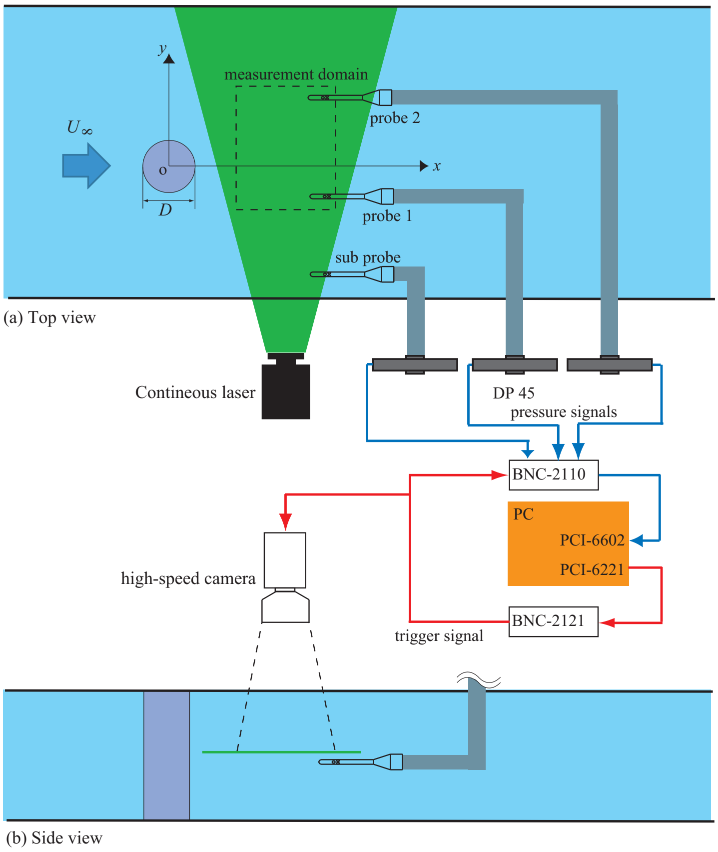

(a) Top view

(b) Side view

Figure 6.3: System of simultaneous measurement of velocity and pressure by time-resolved planar PIV and SP-probes.

$(4.3, -1.9)$, respectively, where velocity fluctuation was relatively moderate in the measurement domain of the PIV and the accuracy of the pressure measurement was retained. According to velocity measurement by the PIV, fluctuations of flow angle at the location of the SP-probes 1 and 2 were 19° and 7.0°, respectively. Consequently, uncertainties of the pressure measurement by the SP-probes 1 and 2 were 3.3% and 0.2% of ρU_∞^2, according to Fig. 5.3. The pressure signals measured by the SP-probe 2 were used as reference for the PIV-based pressure evaluation as explained later, and those measured by the SP-probe 1 were used for validation of the evaluated pressure. In addition, a third SP-probe for monitoring the background noise was placed at the same streamwise location but outside the wake. Based on the pressure signals measured by the sub SP-probe, the background noise loaded on the signals measured by the main SP-probes were canceled by the optimal filtering scheme (Naguib et al., 1996). The SP-probes were fixed 10 mm below the laser sheet to avoid reflection of the laser.

Spanwise coherence of the flow field was first examined by a two-point pressure measurement. Figure 6.4 presents fluctuating pressure measured at two points located at the position of SP-probe 2 (x_2, y_2) and spatially separated by a spanwise distance of 10 mm. As shown, the time sequences of the fluctuating pressure at the two points are

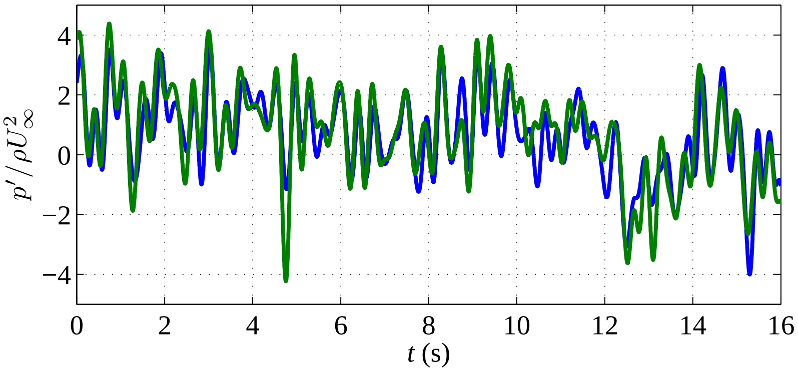

Figure 6.4: Time sequences of fluctuating pressure measured at two points located at the position of SP-probe 2 $(x_2,\ y_2)$ and spatially separated in spanwise direction by 10 mm distance.

Figure 6.5: Timing chart of simultaneous measurement of velocity and pressure.

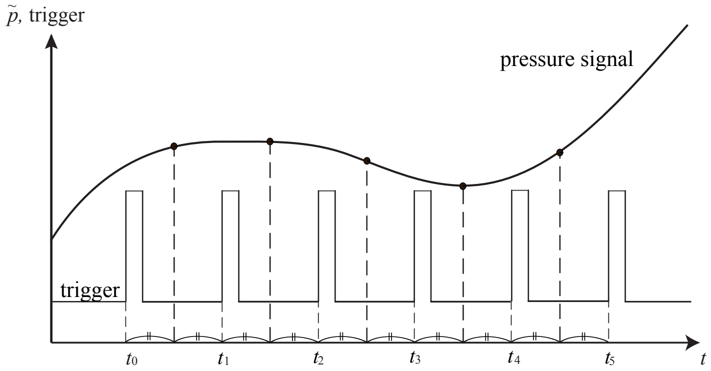

quite similar to each other, and the correlation coefficient between them is 0.83. This indicates a sufficient degree of spanwise coherence of the flow structure, and justifies the use of the pressure signal directly measured by the SP-probe 2 as reference for pressure evaluation based on the PIV measurement. The spanwise coherence was also investigated at the position of the SP-probe 1 $(x_1,\ y_1)$ by the same manner, and the correlation coefficient between the pressure signals is 0.63.

Synchronization of PIV and direct pressure measurement Synchronization of the PIV measurement and the pressure measurement by the SP-probes was operated by a 32-bit PC. The PC generated a pulse to trigger the recording of images by the high-speed camera. The trigger signal was recorded with the pressure signal with a sampling rate of 10 kHz, so that pressure samples acquired simultaneously with image acquisition by the high-speed camera can be extracted from the measured pressure signals by the rising edge of the trigger signal.

The samples of instantaneous pressure acquired simultaneously with velocity measurement by the PIV were extracted from the measured pressure signals in the post processing. As schematically shown in Fig. 6.5, the trigger signals and the pressure signals were recorded together by the PC. The timing of image acquisition by the PIV corresponds to those of the rising edges of the trigger signals, which occur at $t = t_0$, t_1, $t_2 \cdots$. As the i-th velocity field was evaluated from the $i-1$th and ith images, the samples of instantaneous pressure acquired simultaneously with the PIV measured were those measured at $t = (t_0+t_1)/2$, $(t_1+t_2)/2$, $(t_2+t_3)/2\cdots$.

Reference pressure signals for PIV-based pressure evaluation The value of m in Eqs. (6.5)-(6.7) was determined based on the pressure signals directly measured by the SP-probe 2. Reference streamwise pressure gradient was approximately evaluated as

$$\frac{\partial \tilde{p}_{\mathrm{spp}}}{\partial x} \simeq -\frac{1}{\tilde{u}}\frac{\partial \tilde{p}_{\mathrm{spp}}}{\partial t}, \tag{6.11}$$

where $\tilde{p}_{\mathrm{spp}}$ stands for the instantaneous pressure directly measured by the SP-probe 2, and $\tilde{u}$ is the instantaneous streamwise velocity measured by the PIV at the same position. The value of m was determined so that $\widehat{\partial p/\partial x_m}$ at $(x_2,\ y_2)$ has high correlation with $\partial \tilde{p}_{\mathrm{spp}}/\partial x$.

The values of the instantaneous pressure evaluated by numerically solving Eq. (6.4) were specified by the instantaneous pressure directly measured by the SP-probe 2 as

$$\tilde{p}_{\mathrm{cor}}(x,y,t) = \tilde{p}(x,y,t) - \left(\tilde{p}(x_2,y_2,t) - \tilde{p}_{\mathrm{spp}}(t)\right). \tag{6.12}$$

6.4 Result

6.4.1 Velocity Measurement and the POD Analysis

Figure 6.6 presents a sample of instantaneous velocity field measured by the PIV. The black arrows indicate the pattern of the flow direction and the color shows the magnitude of the velocity $\sqrt{\tilde{u}^2+\tilde{v}^2}$ scaled by the free-stream velocity U_∞.

The instantaneous pressure gradients were evaluated from the PIV data using Eqs. (6.2) and (6.3), and the POD bases of the velocities and pressure gradients ξ, η, ϕ and ψ were obtained by means of the snapshot POD (Sirovich, 1987). In the

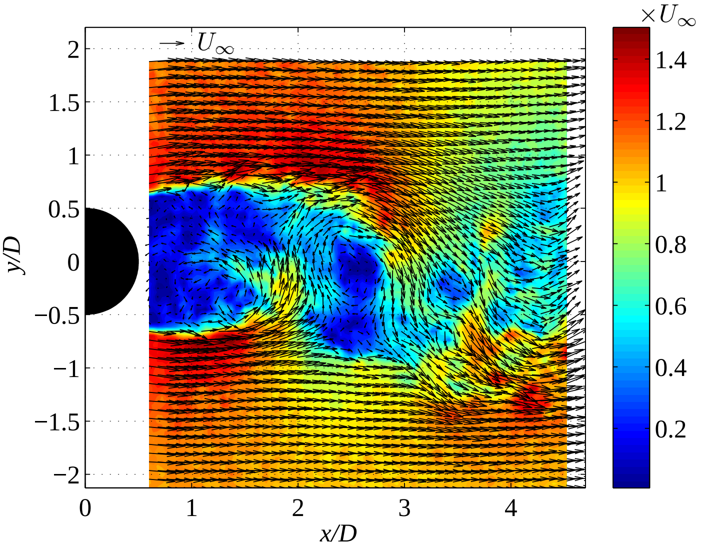

Figure 6.6: Instantaneous velocity field; color indicates $\sqrt{u^2+v^2}$ and black arrows show pattern of flow direction.

snapshot POD analysis, a matrix of the PIV data X was used:

$$X = \begin{bmatrix} \left\{ u \right\}_{t_0} & \left\{ u \right\}_{t_t} & \cdots & \left\{ u \right\}_{t_{n-1}} & \left\{ u \right\}_{t_n} \\ \left\{ v \right\}_{t_0} & \left\{ v \right\}_{t_1} & \cdots & \left\{ v \right\}_{t_{n-1}} & \left\{ v \right\}_{t_n} \\ \left\{ \frac{\partial p}{\partial x} \right\}_{t_0} & \left\{ \frac{\partial p}{\partial x} \right\}_{t_1} & \cdots & \left\{ \frac{\partial p}{\partial x} \right\}_{t_{n-1}} & \left\{ \frac{\partial p}{\partial x} \right\}_{t_n} \\ \left\{ \frac{\partial p}{\partial y} \right\}_{t_0} & \left\{ \frac{\partial p}{\partial y} \right\}_{t_1} & \cdots & \left\{ \frac{\partial p}{\partial y} \right\}_{t_{n-1}} & \left\{ \frac{\partial p}{\partial y} \right\}_{t_n} \end{bmatrix}, \tag{6.13}$$

where $\{\}_{t_i}$ stands for a column vector obtained by sorting the data of instantaneous distribution of the velocity or pressure gradient at $t = t_i$ into one column. Then, the following eigen value problem of a symmetric matrix $Q_X = X^T X$ was solved:

$$Q_X \gamma_k = \lambda_k \gamma_k, \tag{6.14}$$

where λ_k and γ_k are the k-th eigen value and vector, respectively. The POD bases in Eqs. (6.5)-(6.8) were contained in the eigen vector γ as

$$\begin{bmatrix} \eta_k^T & \xi_k^T & \phi_k^T & \psi_k^T \end{bmatrix}^T = X\gamma_k \Big/ \sqrt{\lambda_k}\,. \tag{6.15}$$

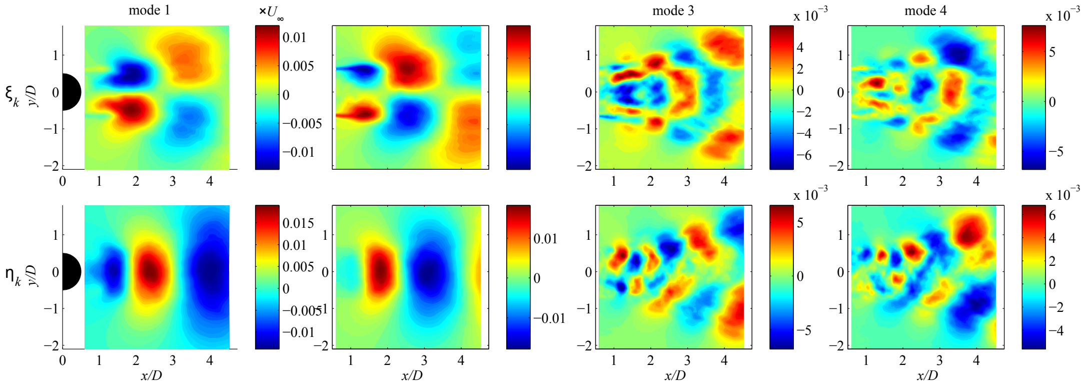

Figure 6.7: POD base of fluctuating velocity ξ and η.

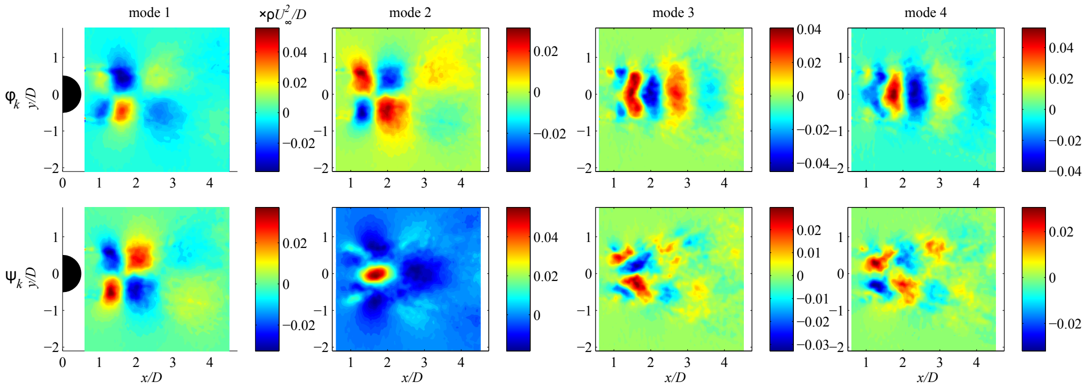

Figure 6.8: POD base of fluctuating pressure gradient ϕ and ψ.

The eigen value λ_k and the eigen vector γ_k were evaluated by numerically solving the eigen value problem Eq. (6.14) using a function "`eig`", available in MATLAB® library.

Figures 6.7 and 6.8 present the evaluated POD bases of the fluctuating velocities and pressure gradients. For each component, the first four modes are shown for instance. All the POD bases show symmetric distributions with respect to $y/D = 0$.

Figure 6.9 shows the fluctuating component of the streamwise pressure gradient at $(x_2,\ y_2)$, comparing those measured by the SP-probe 2 ($\partial p_{\mathrm{spp}}/\partial x$) and evaluated from the PIV data with/without the POD ($\widehat{\partial p}/\partial x_5$, for instance, and $\partial p/\partial x$). It is indicated that the PIV result without the POD $\partial p/\partial x$ showed much larger amplitude of fluctuation than the result by the SP-probe $\partial p_{\mathrm{spp}}/\partial x$. On the other hand, the result obtained from the first five POD modes $\widehat{\partial p}/\partial x_m$ agreed well with $\partial p_{\mathrm{spp}}/\partial x$.

Figure 6.10 shows the amplitude ratio of $\widehat{\partial p}/\partial x_m$ to $\partial p_{\mathrm{spp}}/\partial x$ and the correlation

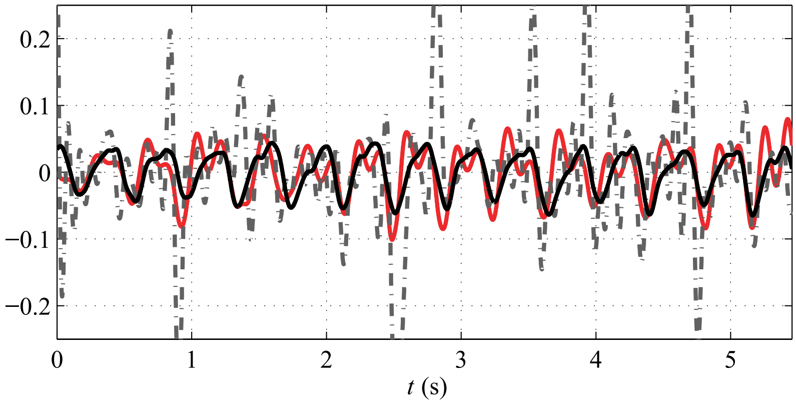

Figure 6.9: Fluctuation of streamwise pressure gradient at $(x_2,\ y_2)$; black solid line, $\partial\hat{p}/\partial x_5$ (PIV, with POD, modes 1-5 are taken into account); gray chained line, $\partial p/\partial x$ (PIV, without POD); red solid line, $\partial p_{\mathrm{spp}}/\partial x$ (SP-probe 2).

coefficient between them, which are respectively defined as:

$$A = \sqrt{\overline{\left(\frac{\partial\hat{p}}{\partial x_m}\right)^2} \Big/ \overline{\left(\frac{\partial p_{\mathrm{spp}}}{\partial x}\right)^2}}, \tag{6.16}$$

$$C = \frac{\overline{\dfrac{\partial\hat{p}}{\partial x_m}\dfrac{\partial p_{\mathrm{spp}}}{\partial x}}}{\sqrt{\overline{\left(\dfrac{\partial\hat{p}}{\partial x_m}\right)^2}\,\overline{\left(\dfrac{\partial p_{\mathrm{spp}}}{\partial x}\right)^2}}}. \tag{6.17}$$

The amplitude ratio monotonically increased as the number of POD modes taken into account increased, and became about unity around the mode 5. It is shown that the correlation coefficient had quite large value about 0.6 around mode 5, and decreased with the number of POD modes taken into account. Therefore, it was reasonable to determine that the first five POD modes should be taken into account for the pressure evaluation. Figure 6.11 shows the cumulative sum of the first m-th eigen values scaled by the total energy. The sum of the eigen values of the first five POD modes was about 50% of the total energy, which implies that the pressure gradients evaluated from the PIV data without special treatment were seriously contaminated by the noise.

6.4.2 Evaluation of Instantaneous Pressure Field

As described in Sect. 6.2.1, instantaneous pressure field was evaluated by virtue of Eq. (6.4), under assumption that the flow phenomena under investigation has a suf-

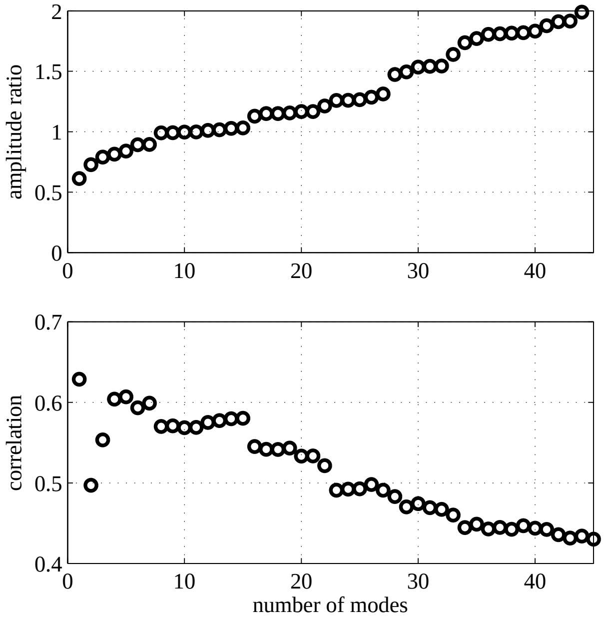

Figure 6.10: Variation of amplitude ratio and correlation coefficient between $\partial\hat{p}/\partial x_m$ and $\partial p_{\mathrm{spp}}/\partial x$

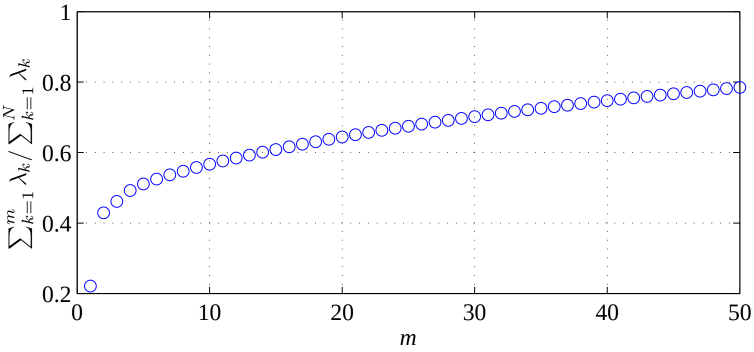

Figure 6.11: Cumulative sum of eigen values; N is the total number of POD modes.

ficient degree of two-dimensionality in the z-direction. In order to justify the use of Eq. (6.4) for evaluation of instantaneous pressure field in this study, a residual of the two-dimensional continuity equation, $\partial u/\partial x + \partial v/\partial y$, was investigated. Figure 6.12 presents the residual magnitude of the continuity equation of the mean-velocity field and the residual fluctuation of the continuity equation of the fluctuating velocity field obtained with/without the POD. It is shown by Figs. 6.12a and b that the measured mean-velocity field sufficiently satisfied a two-dimensional continuity, while the instantaneous field obtained without the POD did not as indicated by the significant fluctuation of the residual. Such significant fluctuation of $\partial u'/\partial x + \partial v'/\partial y$ was due to both the motion of the three-dimensional small-scale vortices and the effect of noise

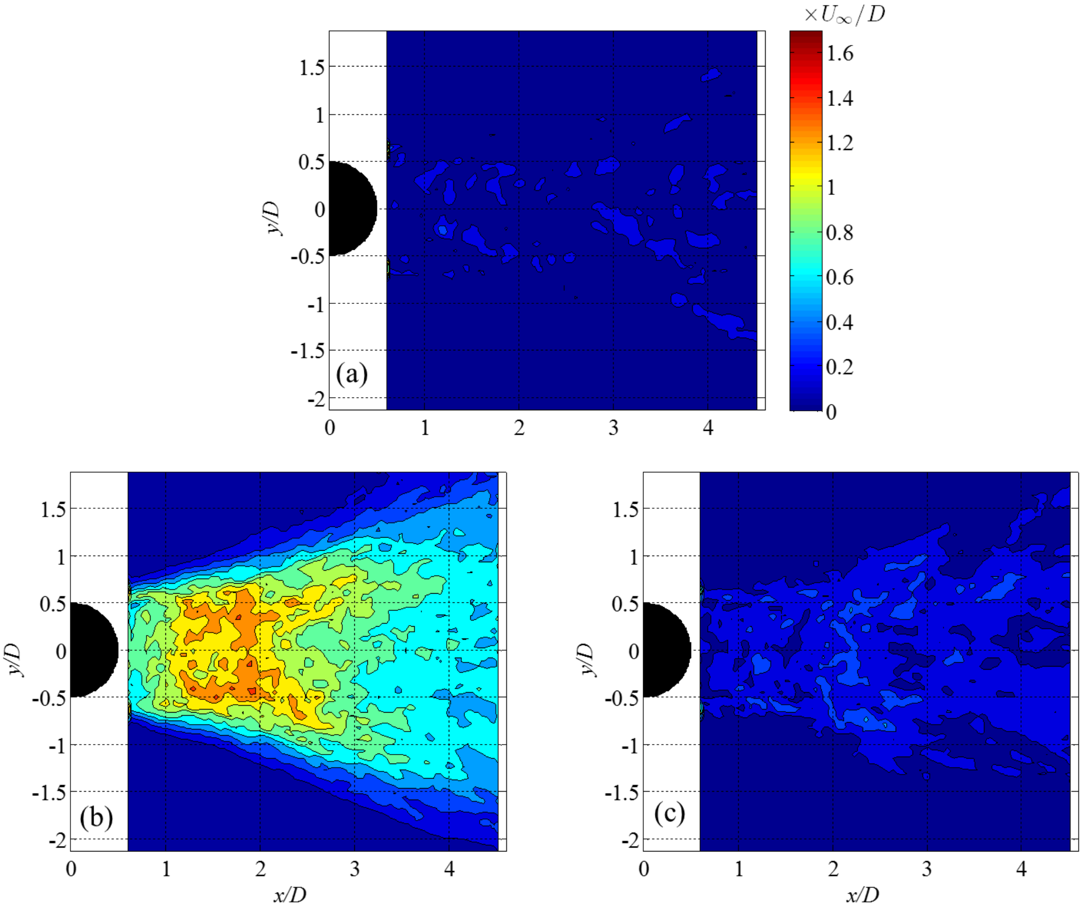

Figure 6.12: Two-dimensional divergence of velocity field: (a) divergence magnitude of mean velocity field $|\partial U/\partial x + \partial V \partial y|$; (b) fluctuation of divergence obtained without POD $\sqrt{(\partial u/\partial x + \partial v/\partial y)^2}$; (c) fluctuation of divergence obtained with POD $\sqrt{(\partial \hat{u}_5/\partial x + \partial \hat{v}_5/\partial y)^2}$ (the first five modes were taken into account).

involved in the PIV measurement. On the other hand, as shown in Fig. 6.12 c, the POD analysis drastically reduced the residual fluctuation to the same order as the residual of the continuity equation of the mean velocity field, which indicates that the fairly two-dimensional flow structure was successfully extracted by the POD. It is therefore reasonably considered that the use of Eq. (6.4) was appropriate to evaluate instantaneous pressure based on the POD-applied velocity fields.

Now, the source terms in Eq. (6.4) were evaluated using $\widehat{\partial p}/\partial x_5$ and $\widehat{\partial p}/\partial y_5$, and the instantaneous pressure field was evaluated by numerically solving it. The values of the evaluated pressure were specified by using Eq. (6.12) based on the reference pressure directly measured by the SP-probe 2. Figure 6.13 shows the instantaneous pressure field evaluated from the velocity shown in Fig. 6.6, comparing those evaluated with/without the POD. The streamlines drawn by smoothly connecting velocity

Figure 6.13: Instantaneous pressure distribution evaluated from PIV data; (a) without POD, (b) with POD, mode 1-5 are taken into account.

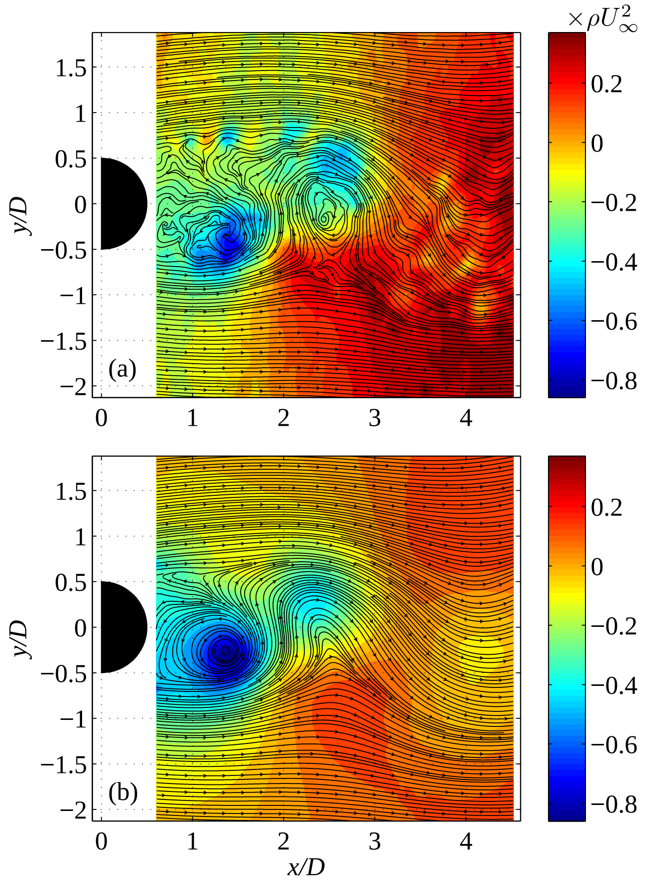

vectors are shown together. In both cases, the location of the minima of the pressure corresponded to the pattern of the streamlines, but the pressure distribution and the streamline pattern were smoother in the case with the POD than that without the POD.

Figure 6.14 shows the fluctuating pressure at $(x_1,\ y_1)$, comparing those directly measured by the SP-probe 1 and evaluated based on the PIV data. It is shown that the fluctuating pressure evaluated from PIV data without the POD had higher-frequency fluctuations than the directly measured data, and the amplitude of the high-frequency fluctuations in the PIV data without the POD was much larger. The correlation coefficient between them was 0.53. On the other hand, the fluctuating pressure evaluated with the POD showed a very similar pattern to the direct measurement result by the SP-probe 1, and the correlation coefficient between them was improved to 0.74. The fluctuation of pressure evaluated based on the PIV data and directly measured by the SP-probe 1 were $0.055\rho U_\infty^2$ and $0.062\rho U_\infty^2$, respectively. The difference between them was $0.007\rho U_\infty^2$, and it was on the same order as that of the uncertainty in the direct pressure measurement by the SP-probe 1 mentioned in Sect. 6.3.4. Therefore, the uncertainty in the pressure evaluation was approximately $0.007\rho U_\infty^2$, which corresponded

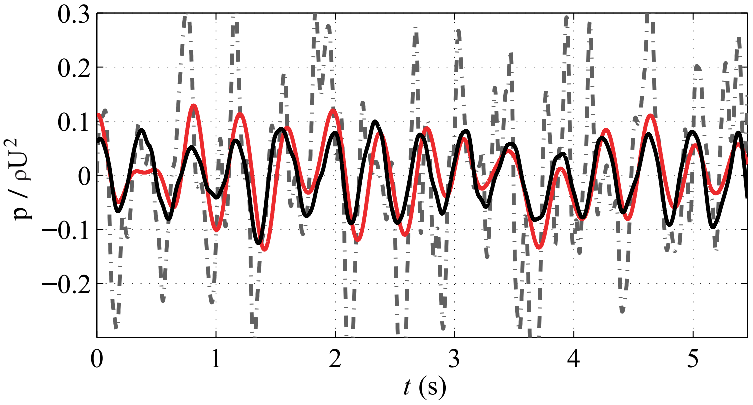

Figure 6.14: Fluctuating pressure at (x_1, y_1); black solid line, PIV with POD, mode 1-5; gray chained line, PIV without POD; red solid line, SP-probe 1.

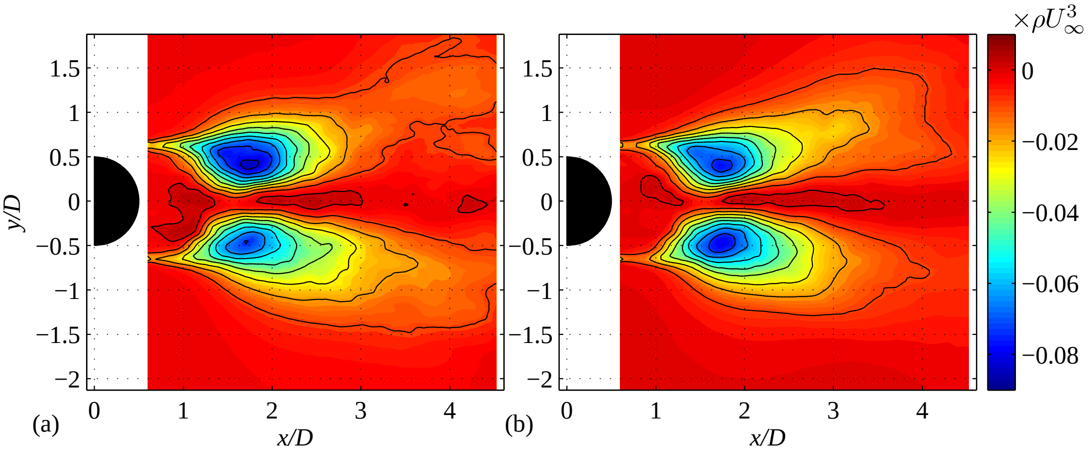

Figure 6.15: Distribution of velocity-pressure correlation $\overline{up}$: (a) without POD; (b) with POD, modes 1-5 were taken into account.

to 13% of the evaluated pressure fluctuation.

The velocity-pressure correlations $\overline{up}$ and $\overline{vp}$ were evaluated based on the measurement results, and are shown in Figs. 6.15 and 6.16, comparing those obtained with/without the POD. The results with the POD were evaluated taking into account the POD modes 1-5. It is shown that the velocity-pressure correlation $\overline{up}$ were mainly negative in the entire wake region, and showed a symmetric distribution with respect to $y/D = 0$ with two significant negative peaks located immediately behind the circular cylinder, $(x/D,\ y/D) = (1.5,\ \pm 0.5)$. The peak magnitude of $\overline{up}$ was about $0.09\rho U_\infty^3$. On the other hand, the velocity-pressure correlation $\overline{vp}$ showed an anti-symmetric distribution with negative values in $y/D \leq 0$ and positive values in $y/D \geq 0$, and the peak magnitude was approximately $0.025\rho U_\infty^3$, relatively small as compared to that of $\overline{up}$.

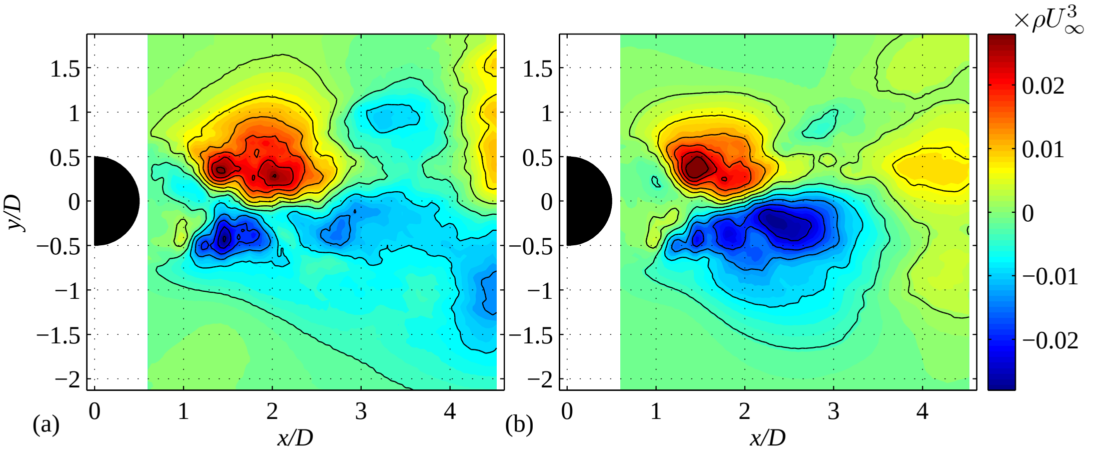

Figure 6.16: Distribution of velocity-pressure correlation $\overline{vp}$: (a) without POD; (b) with POD, modes 1-5 were taken into account.

Comparing the results obtained with/without the POD, one can see that the results of the velocity-pressure correlation measurement were improved by the hybrid method, in that distributions of $\overline{up}$ and $\overline{vp}$ obtained with the POD analysis were more symmetrical with respect to $y/D = 0$ than those obtained without the POD.

It was demonstrated that the instantaneous pressure field was successfully derived from the PIV data by using the instantaneous pressure directly measured by the SP-probe as the reference signals. The pressure-related statistics in flow regions where the direct measurement technique cannot be applied are now accessible by the present method. In the next section, the pressure-related statistics evaluated by the present hybrid method are further examined, and the role of the pressure-related statistics in transport of the Reynolds stresses in the flow region immediately behind a circular cylinder is investigated.

6.5 Discussion

6.5.1 Validation/Verification of Pressure-Related Statistics

The pressure-related statistics are further validated and verified in the following, in order to further examine reliability of the present measurement results. Figure 6.17 shows the distribution of the mean pressure P, the root-mean-square of the pressure fluctuation p' and the magnitude of the mean pressure gradient, defined as $\sqrt{(\partial P/\partial x)^2 + (\partial P/\partial y)^2}$. The mean pressure is shown with streamlines evaluated

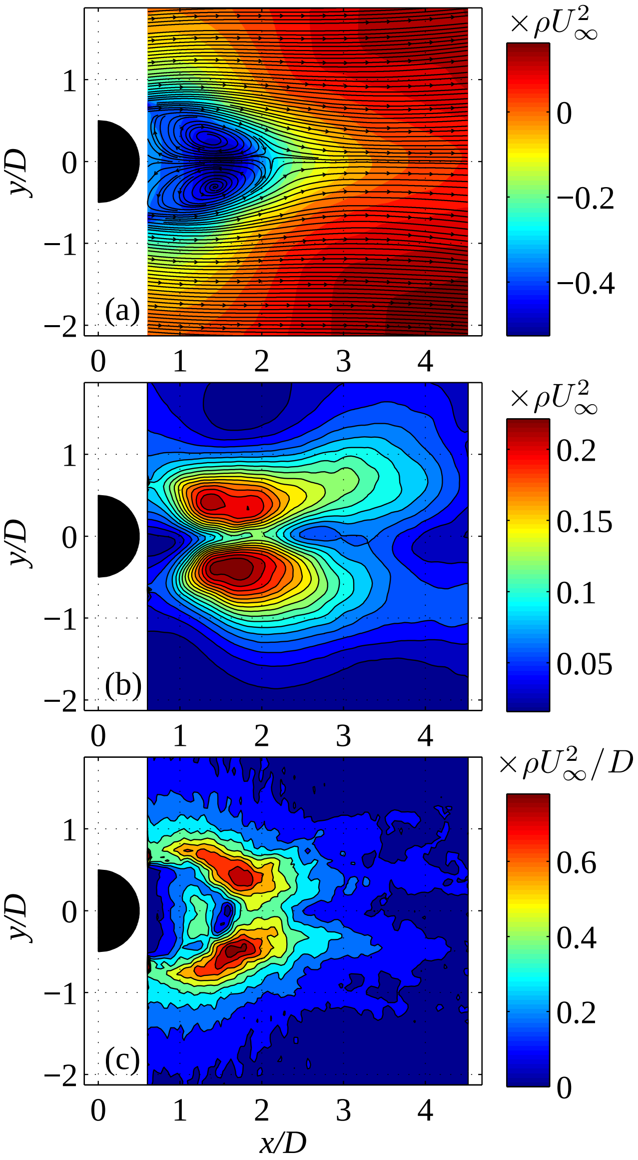

Figure 6.17: Distribution of pressure statistics obtained based on PIV result with POD; (a) mean pressure P, (b) pressure fluctuation p', (c) pressure gradient $\sqrt{(\partial P/\partial x)^2+(\partial P/\partial y)^2}$.

from the mean velocity distributions. It is shown that the mean pressure had the minimum inside a recirculation region and recovered in the downstream. The pressure fluctuation showed a symmetric distribution with respect to $y/D = 0$ and had two significant peaks located downstream of the cylinder around $(x/D,\ y/D) = (1.5,\ \pm 0.5)$. Comparing with the mean pressure gradient shown in Fig. 6.17c, one can see that the peak locations of p' corresponded to those of the peak of the mean pressure gradient. These peak locations of the pressure fluctuation and the mean pressure-gradient corresponded to those of $\overline{up}$ (see Fig. 6.15).

The signal-to-noise ratio of the evaluated pressure is now estimated by the similar manner to those described in previous chapters. It is reasonably considered that

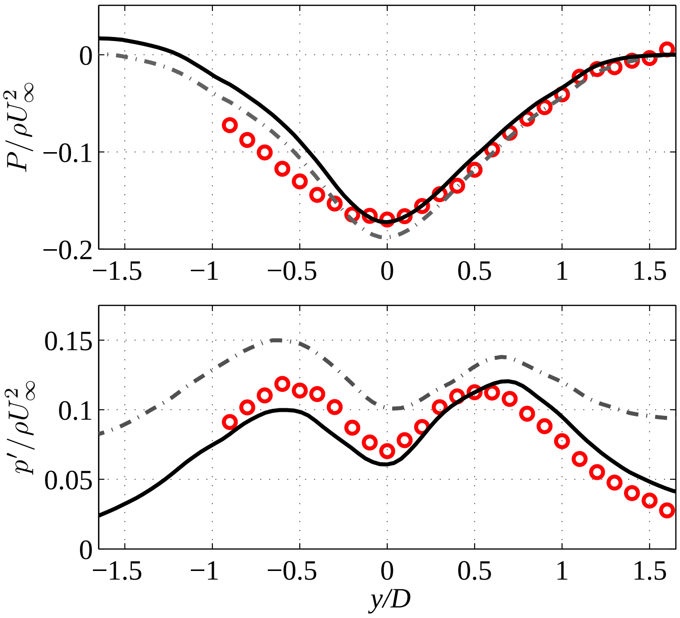

Figure 6.18: Distribution of mean pressure and pressure fluctuation at $x/D = 3$; black solid line, PIV with POD; gray chained line, PIV without POD; red circle, SP-probe.

the upstream corner of the measurement domain $(x/D,\ y/D) = (0.6,\ -2.1)$ is a location far enough from the shear layer to assume the pressure fluctuation measured here to be mainly the background noise. In Fig. 6.17b, the pressure fluctuation at this location was $0.016\rho U_\infty^2$, and the maximum pressure fluctuation was $0.23\rho U_\infty^2$ at $(x/D,\ y/D) = (1.7,\ -0.37)$. Consequently, the signal-to-noise ratio was approximately 14-to-1, while that of the pressure evaluation without the POD was evaluated by the same manner to be 2.6-to-1. Hence, the signal-to-noise ratio of the pressure evaluation was significantly improved by the hybrid method.

The profiles of the mean pressure and the pressure fluctuation at $x/D = 3$ are presented in Fig. 6.18, comparing those obtained based on the PIV and those directly measured by the SP-probe. The pressure in $y/D \leq -1$ was not measured in the direct measurement because of the limitation of the equipment to traverse the SP-probe. The cross-flow error contained in the mean pressure measured by the SP-probe was corrected based on the observation on the cross-flow effect in described in Fig. 5.3. The mean flow angle against the SP-probe was evaluated from the PIV data by

$$\phi = \tan^{-1}\left(\frac{v'}{U}\right), \tag{6.18}$$

and the values of the mean pressure were corrected as

$$P_{\mathrm{cor}} = P - C_p(\phi), \tag{6.19}$$

where $C_p(\phi)$ was obtained by interpolating the profile of the pressure coefficient shown in Fig. 5.3. It is shown in Fig. 6.18 that the use of POD in the pressure evaluation did not make a significant difference in the mean pressure profile, and those results obtained based on the PIV data were in strong agreement with the result of the direct measurement by the SP-probe. On the other hand, the fluctuation of pressure evaluated by the PIV data with the POD was smaller than that obtained without the POD, and agreed more reasonably with the result of the direct measurement.

Next, the statistics related to correlation between the velocity and pressure fields are further investigated. In order to verify them, a focus is made on a relationship between pressure-related terms in the transport equation of the Reynolds stresses $\overline{u_i u_j}$ introduced in the following. The fluctuating pressure originally appears in the transport equation of the Reynolds stress as the velocity pressure-gradient correlation Π_{ij}, which is defined as

$$\Pi_{ij} = -\frac{1}{\rho}\left(\overline{u_i \frac{\partial p}{\partial x_j}} + \overline{u_j \frac{\partial p}{\partial x_i}}\right). \tag{6.20}$$

In the framework of the Reynolds-stress closure, Π_{ij} is often decomposed as

$$\Pi_{ij} = D^p_{ij} + \phi_{ij}, \tag{6.21}$$

where D^p_{ij} and ϕ_{ij} are the pressure diffusion and the redistribution, which are respectively defined as:

$$D^p_{ij} = -\frac{1}{\rho}\left(\frac{\partial \overline{u_i p}}{\partial x_j} + \frac{\partial \overline{u_j p}}{\partial x_i}\right), \tag{6.22}$$

$$\phi_{ij} = \overline{\frac{1}{\rho} p \left(\frac{\partial u_i}{\partial x_j} + \frac{\partial u_j}{\partial x_i}\right)}. \tag{6.23}$$

The decomposition of Π_{ij} into D^p_{ij} and ϕ_{ij} has been conventionally preferred because of an important physical meaning of ϕ_{ij}; the trace of ϕ_{ij} is zero, and consequently ϕ_{ij} does not appear in the transport equation of the turbulent kinetic energy, which implies that ϕ_{ij} *redistributes* energy among the Reynolds stresses (e.g., Pope, 2000).

Equation (6.21) is now used to verify the velocity-pressure correlation and the pressure-strain correlation obtained in the present study. The velocity pressure-gradient correlation Π_{ij} was evaluated using only the non-POD-applied velocities by virtue of Eqs. (6.2) and (6.3), while the pressure diffusion D^p_{ij} and the redistribution ϕ_{ij} were evaluated using the POD-applied velocities $\hat{u_5}'$ and $\hat{v_5}'$ and the pressure p'

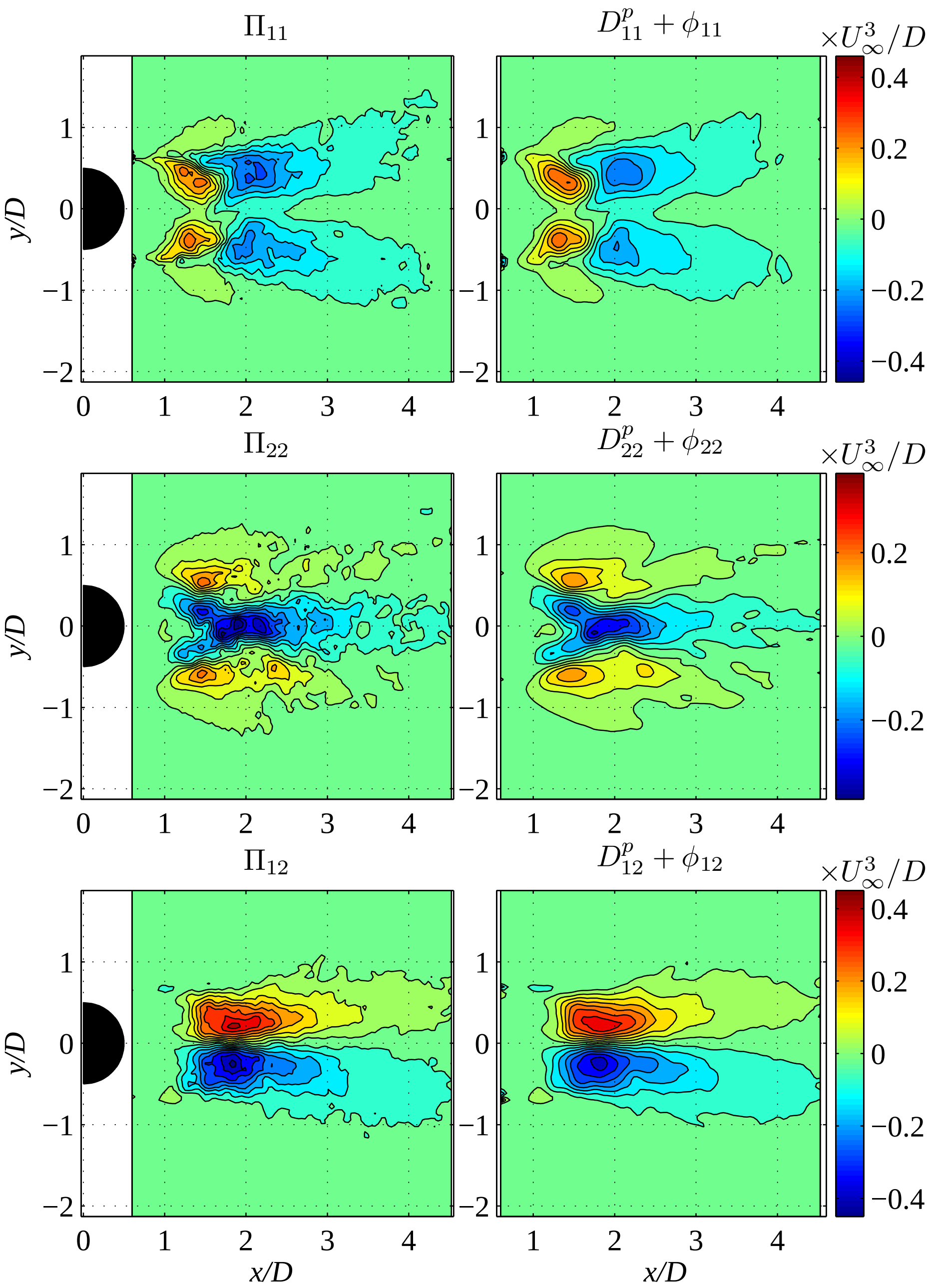

Figure 6.19: Comparison between the left-hand and right-hand sides of Eq. (6.21).

obtained by numerically solving Eq. (6.4); and whether Eq. (6.21) was satisfied was examined. It should be emphasized that p' to be examined was used only in evaluation of the right-hand-side of Eq. (6.21), but not used in evaluation of the left-hand-side.

Figure 6.19 shows a comparison between the distribution of Π_{ij} and $D^p_{ij} + \phi_{ij}$ of the transport equation of Reynolds stresses. It is shown that sums of the pressure diffusion and the redistribution are in quite good agreement with the velocity pressure-gradient correlations for all components of the Reynolds stresses. The correlation coefficients between them were 0.98 between Π_{11} and $D^p_{11}+\phi_{11}$, 0.98 between Π_{22} and $D^p_{22}+\phi_{22}$ and 0.99 between Π_{12} and $D^p_{12}+\phi_{12}$, which supports the consistency of the pressure-related statistics evaluated in the present study.

6.5.2 Transport Equation of Reynolds Stress

The role of the pressure-related terms in the transport of the Reynolds stresses is now focused. The transport equation of the Reynolds stresses $\overline{u_i u_j}$ is written as

$$C_{ij} = P_{ij} + \left(D^t_{ij} + D^p_{ij}\right) + \phi_{ij} + \varepsilon_{ij}, \tag{6.24}$$

where P_{ij}, C_{ij}, D^t_{ij} are the production rate, the convection, and the turbulent diffusion. It should be noted that the viscous diffusion in Eq. (6.24) is omitted because of sufficiently high Reynolds number. For evaluation of the pressure related terms, the fluctuating velocities reconstructed from the first five POD modes, namely $\hat{u}_5$ and $\hat{v}_5$, and the pressure evaluated based on them were used. The other terms without the fluctuating pressure, P_{ij}, C_{ij}, and D^t_{ij} were also evaluated based on the POD-applied velocities for fair comparison with the pressure-related terms. For simplicity, the notation $\hat{[]}_5$ is omitted in the following discussion; for example, $\overline{\hat{u}_5 p}$ and $\overline{\hat{u}_5 \hat{v}_5^2}$ are simply written as $\overline{up}$ and $\overline{uv^2}$. In the following, each terms in the transport of the Reynolds stresses $\overline{u^2}$, $\overline{v^2}$ and $\overline{uv}$ were evaluated and the balance between them was investigated.

6.5.2.1 Transport of Reynolds normal stress $\overline{u^2}$

Each term in the transport equation of the Reynolds streamwise normal stress u^2 was evaluated as:

$$\begin{aligned}
P_{11} &= -2\left(\overline{u^2}\frac{\partial U}{\partial x} + \overline{uv}\frac{\partial U}{\partial x}\right), && (6.25)\\
C_{11} &= -U\frac{\partial \overline{u^2}}{\partial x} - V\frac{\partial \overline{u^2}}{\partial y}, && (6.26)\\
D^t_{11} &= -\frac{\partial \overline{u^3}}{\partial x} - \frac{\partial \overline{u^2 v}}{\partial y}, && (6.27)\\
D^p_{11} &= -\frac{2}{\rho}\frac{\partial \overline{up}}{\partial x}, && (6.28)\\
\phi_{11} &= \overline{\frac{2}{\rho}p\frac{\partial u}{\partial x}}, && (6.29)\\
\varepsilon_{11} &= -P_{11} + C_{11} - D^t_{11} - D^p_{11} - \phi_{11}. && (6.30)
\end{aligned}$$

It should be noted that the dissipation rate ε_{11} was indirectly evaluated as a residual on the transport equation, while the other terms were directly evaluated from the measurement results. Figure 6.20 presents the distribution of the streamwise normal Reynolds stress $\overline{u^2}$ and the evaluated terms in the transport equation. It is shown that the distribution of $\overline{u^2}$ had two broad hills around $(x/D,\ y/D) = (2, \pm 0.5)$, and also had two thin regions with high intensity of fluctuation located upstream of the two broad hills. The former was consequence of the periodic motion of the large vortices shed from the cylinder, while the latter was the turbulence produced in the shear layer separated from the cylinder.

The production rate P_{11} had the significant positive values at the locations corresponding to the thin shear layer separated from the cylinder and the broad hills of $\overline{u^2}$. On the other hand, P_{11} also showed two significant negative peaks inside the recirculation region located around $(x/D,\ y/D) = (1.3,\ \pm 0.5)$, and the peak magnitude was as large as that of the positive peaks in the downstream. This significant negative production was caused by the second termin Eq. (6.25); the Reynolds shear stress $\overline{uv}$ showed the opposite sign inside the recirculation region to that of $\overline{uv}$ in the downstream region (see Fig. 6.22).

Focusing on the pressure-related terms, one can obviously see that the pressure diffusion D^p_{11} mainly compensated for the production rate P_{11}; it showed a quite similar distribution to that of the production rate P_{11}, which had two significant positive peaks located around $(x/D,\ y/D) = (2,\ \pm 0.5)$ and two negative peaks inside the recirculation region $(x/D,\ y/D) = (1.3,\ \pm 0.5)$. The distribution of D^p_{11} indicates that the streamwise normal stress $\overline{u^2}$ produced by P_{11} in the downstream region of the recirculation region was transported upstream by D^p_{11} and expended by the sink of P_{11} located inside the recirculation region.

On the other hand, the redistribution ϕ_{11} had a relatively minor contribution as compared to the pressure diffusion. It was mainly negative in the entire region of the measurement domain, and showed relatively large magnitude values in the regions corresponding to the thin shear layer separated from the cylinder and two broad hills of $\overline{u^2}$, which indicates an energy exchange from $\overline{u^2}$ to the other components of the Reynolds normal stresses.

For the other terms, the turbulent diffusion D^t_{11} was not as large as the pressure diffusion, but partly compensated for the production rate. The convection term indicates that $\overline{u^2}$ produced in the thin shear layer separated from the cylinder was transported downstream by the mean flow. The dissipation rate ε_{11} indirectly evaluated from the other terms mainly took negative values, which is consistent with the definition of ε_{11}

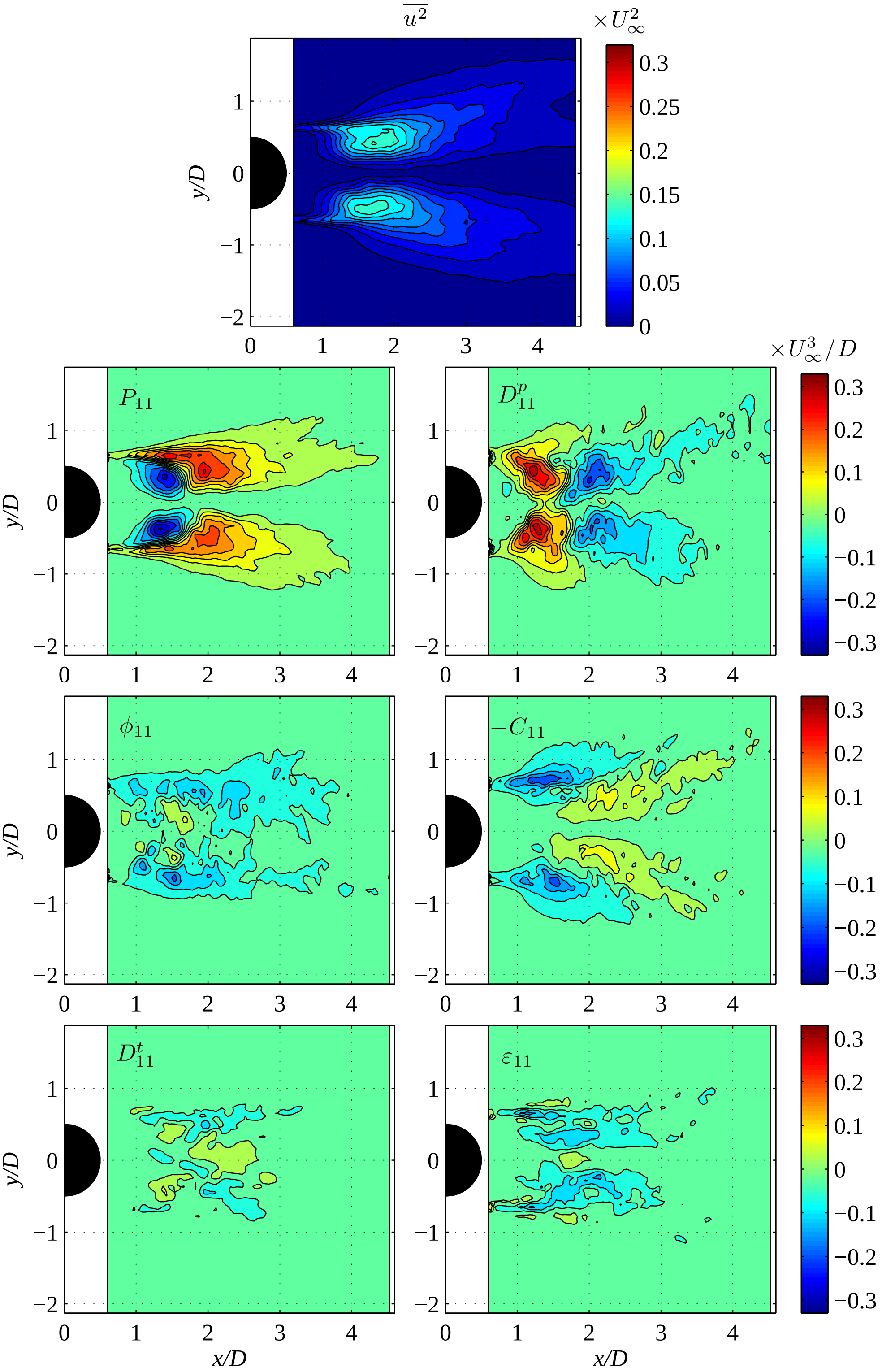

Figure 6.20: Distribution of Reynolds stress $\overline{u^2}$ and balance in transport equation.

and supported the validity of the evaluation of the other terms based on the present experimental result.

6.5.2.2 Transport of Reynolds normal stress $\overline{v^2}$

Terms in the transport equation of the Reynolds transverse normal stress $\overline{v^2}$ were evaluated for the measurement results as:

$$
\begin{aligned}
P_{22} &= -2\left(\overline{uv}\frac{\partial V}{\partial x}+\overline{v^2}\frac{\partial V}{\partial y}\right), && (6.31)\\
C_{22} &= -U\frac{\partial \overline{v^2}}{\partial x}-V\frac{\partial \overline{v^2}}{\partial y}, && (6.32)\\
D_{22}^{t} &= -\frac{\partial \overline{uv^2}}{\partial x}-\frac{\partial \overline{v^3}}{\partial y}, && (6.33)\\
D_{22}^{p} &= -\frac{2}{\rho}\frac{\partial \overline{vp}}{\partial y}, && (6.34)\\
\phi_{22} &= \frac{2}{\rho}\overline{p\frac{\partial v}{\partial y}}, && (6.35)\\
\varepsilon_{22} &= -P_{22}+C_{22}-D_{22}^{t}-D_{22}^{p}-\phi_{22}. && (6.36)
\end{aligned}
$$

The distribution of the lateral component of the normal Reynolds stress $\overline{v^2}$ and the terms in the transport equation are shown in Fig. 6.21. The Reynolds stress $\overline{v^2}$ showed a single significant peak at $(x/D,\ y/D) = (2.0,\ 0)$, and the peak magnitude was about two times larger than that of the streamwise normal stress $\overline{u^2}$. This significant lateral velocity fluctuation in excess of the streamwise velocity fluctuation was consequence of the periodic motion of the large-scale vortex shed from the cylinder.

The production P_{22} had a single significant peak at $(x/D,\ y/D) = (2.0,\ 0)$, and this was caused by the normal stress $\overline{v^2}$ itself and the gradient of the mean velocity V in the y-direction (cf. the second term in Eq. (6.31)).

Comparing the evaluated terms in the transport equation, one can see that the pressure diffusion D_{22}^{p} mainly compensated for the significant positive peak of the production P_{22}, and transported $\overline{v^2}$ from the wake center to the side. The redistribution was slightly negative in the wake center, but positive in the region along the shear layer separated from the cylinder, indicating that $\overline{v^2}$ received the energy from $\overline{u^2}$.

The turbulent diffusion D_{22}^{t} was relatively smaller than D_{22}^{p} but had similar contribution. The convection $-C_{22}$ was negative beside the significant peak of the production and positive in the downstream location. The distributions of D_{22}^{p}, D_{22}^{t}, and $-C_{22}$ indicate that $\overline{v^2}$ produced in the wake center was carried to the side of the peak location

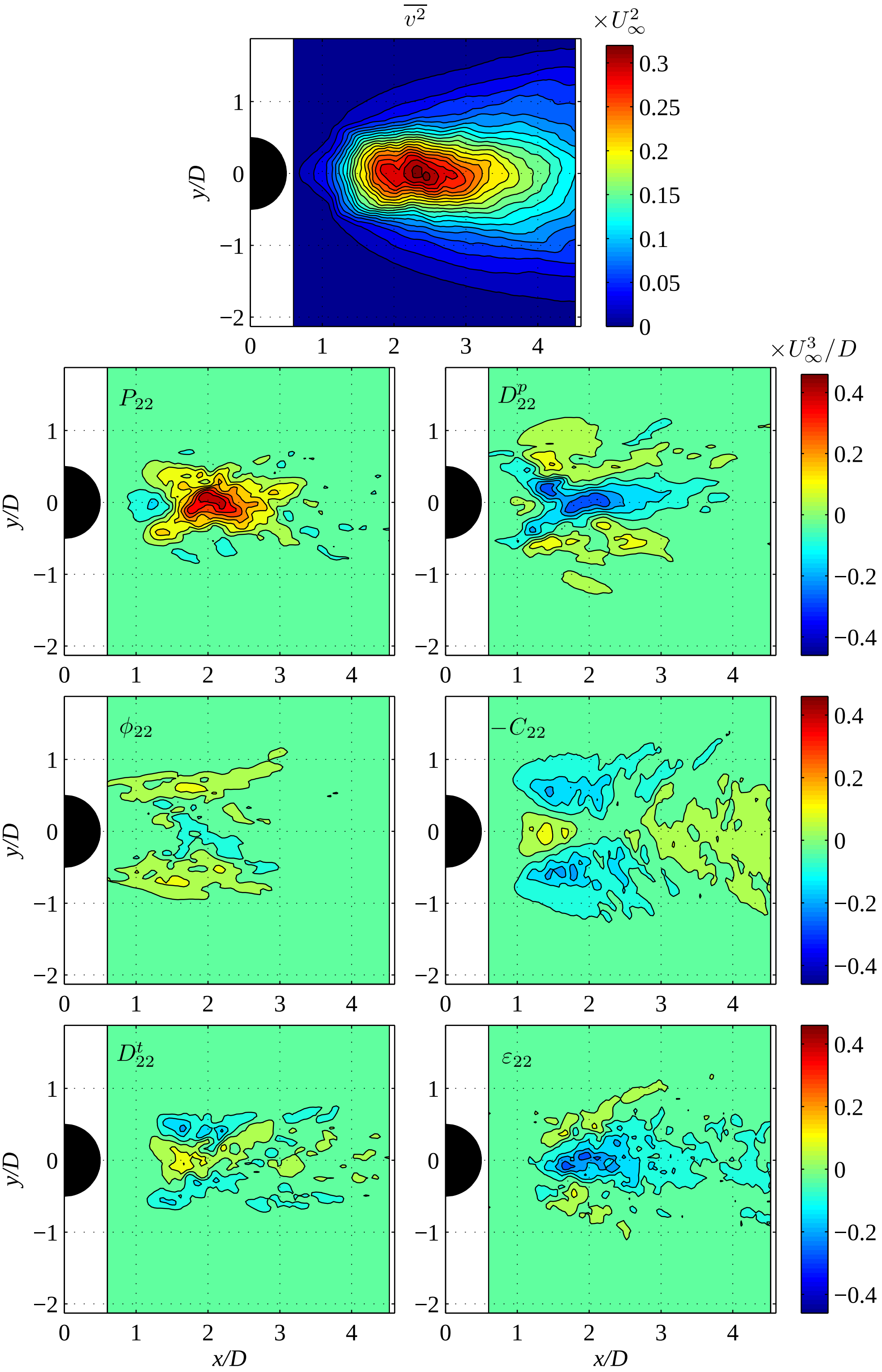

Figure 6.21: Distribution of Reynolds stress $\overline{v^2}$ and balance in transport equation.

of P_{22} by the diffusion terms, and then convected to the downstream by the mean flow.

6.5.2.3 Transport of Reynolds shear stress $\overline{uv}$

Next, the budget of the transport equation of the Reynolds shear stress $\overline{uv}$ was investigated. Each term in the transport equation was evaluated as:

$$P_{12} = -\overline{u^2}\frac{\partial V}{\partial x} - \overline{uv}\frac{\partial V}{\partial y} - \overline{uv}\frac{\partial U}{\partial x} - \overline{v^2}\frac{\partial U}{\partial y}, \tag{6.37}$$

$$C_{12} = -U\frac{\partial \overline{uv}}{\partial x} - V\frac{\partial \overline{uv}}{\partial y}, \tag{6.38}$$

$$D^t_{12} = -\frac{\partial \overline{u^2 v}}{\partial x} - \frac{\partial \overline{uv^2}}{\partial y}, \tag{6.39}$$

$$D^p_{12} = -\frac{1}{\rho}\left(\frac{\partial \overline{up}}{\partial y} + \frac{\partial \overline{vp}}{\partial x}\right), \tag{6.40}$$

$$\phi_{12} = \frac{1}{\rho}\overline{p\left(\frac{\partial u}{\partial y} + \frac{\partial v}{\partial x}\right)}, \tag{6.41}$$

$$\varepsilon_{12} = -P_{12} + C_{12} - D^t_{12} - D^p_{12} - \phi_{12}. \tag{6.42}$$

The Reynolds shear stress $\overline{uv}$ and the terms in the transport equation are presented in Fig. 6.22. The distribution of the shear stress $\overline{uv}$ was anti-symmetric with respect to $y/D = 0$. One can see clearly that the two primary peaks of the shear stress were located at the streamwise location of $x/D = 2.0$, showing the significant positive values in $y \leq 0$ and the negative in the other region. Furthermore, there were the other two peaks located inside the recirculation region, at $x/D = 1.3$, taking the opposite sign to that in the downstream region.

Investigating the distribution of the production rate P_{12}, one can easily see that the primary peaks of the shear stress $\overline{uv}$ located at $x/D = 2.0$ were maintained by the significant production at the corresponding location. However, there was no production that maintains the secondary peaks of $\overline{uv}$ inside the recirculation region.

Focusing on the pressure-related terms, one can see that both the pressure diffusion D^p_{12} and the redistribution ϕ_{12} were as large as the production rate P_{12}. Interestingly, the pressure diffusion D^p_{12} took different signs in the region along the thin shear layer separated from the cylinder and in the downstream region, where the periodic oscillatory motion of the large vortex was dominant. The distribution of D^p_{12} indicates that $\overline{uv}$ produced in the downstream location was transported to the shear layer in the upstream location. The redistribution of ϕ_{12} showed the anti-symmetric distribution with

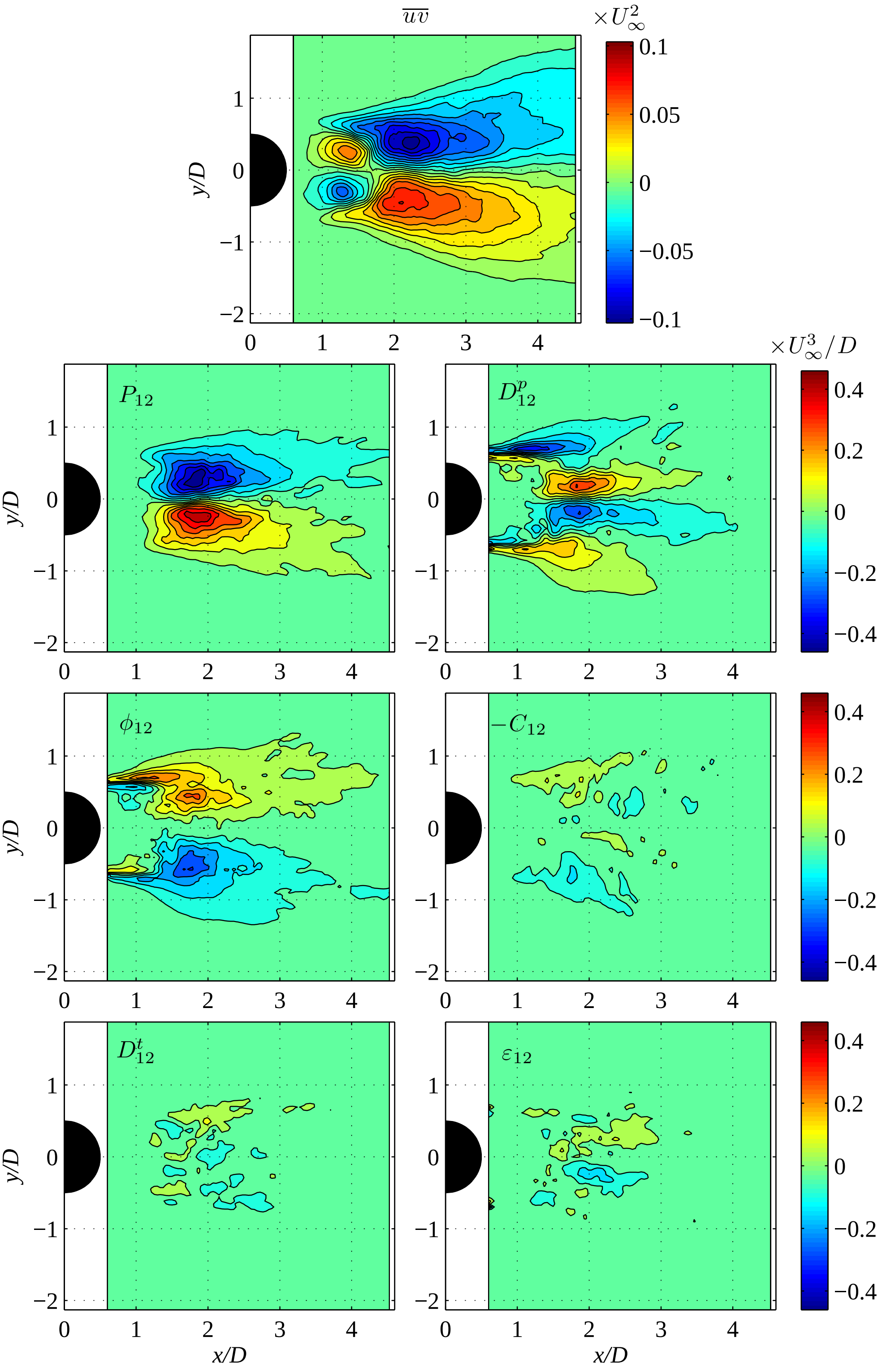

Figure 6.22: Distribution of Reynolds stress $\overline{u'v}$ and the balance in transport equation.

Figure 6.23: Distribution of Reynolds shear stress and balance in transport equation at $x = 1.3D$; (a) Reynolds shear stress $\overline{uv}$, (b) budget of transport equation; blue, P_{12}; green, $D^p_{12} + \phi_{12}$, red, D^t_{12}, cyan, others

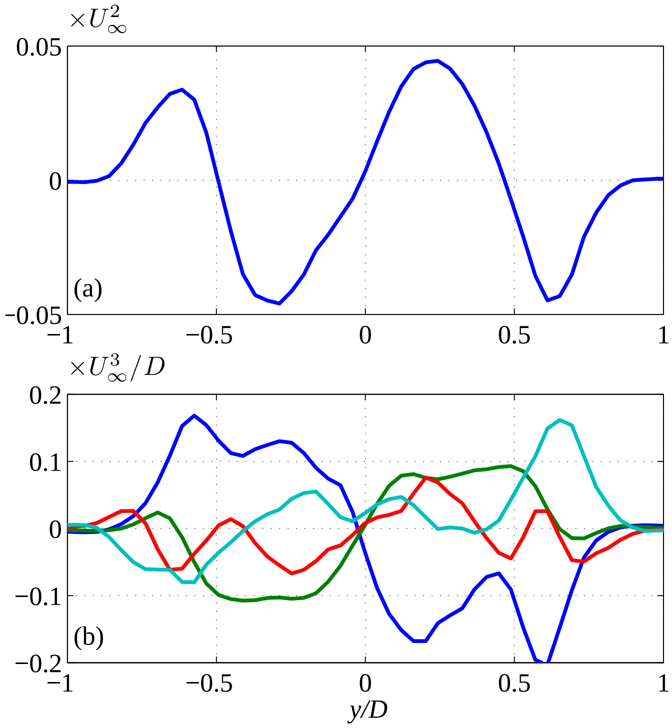

opposite sign to P_{12}. The sum of the pressure-related terms $D^p_{12} + \phi_{12}$ mainly compensated for P_{12} (see Fig. 6.19), which indicates that the shear stress $\overline{uv}$ produced by P_{12} was mainly expended by the redistribution of ϕ_{12} after being carried by the pressure diffusion D^p_{12}.

The other terms had only a minor role compared to the pressure-related terms. The convection $-C_{12}$ indicates the shear stress $\overline{uv}$ was slightly carried from the region along the thin shear layer to the downstream. The turbulent diffusion D^t_{12} was much smaller than the pressure diffusion D^p_{12}. The dissipation rates ε_{12} indirectly evaluated from the other terms was also reasonably small, which also supports consistency of the present measurement results.

As mentioned above, the Reynolds shear stress $\overline{uv}$ showed secondary peaks inside the recirculation region, although the production that maintained them was not observed. Figure 6.23 present the profile of $\overline{uv}$ and the terms in the transport equation at $x/D = 1.3$ across the peaks of $\overline{uv}$ in the recirculation region. As shown in Fig. 6.23a, $\overline{uv}$ inside the recirculation region took the negative and positive values in $-0.5 \leq y/D \leq 0$ and $0 \leq y/D \leq 0.5$, respectively. The peaks located outside $-0.5 \leq y/D \leq 0.5$ was caused by the thin shear layer separated from the cylinder.

In Fig. 6.23b, it is shown that P_{12} was not the source, but was rather the sink of $\overline{uv}$ in the recirculation region. On the other hand, the pressure-related terms $D^p_{12} + \phi_{12}$ mainly supplied the shear stress. The turbulent diffusion D^t_{12} was not as large as the pressure-related terms, but partly supported the profile of $\overline{uv}$. The other terms did not have significant contribution in the recirculation region. Thus, the two peaks of $\overline{uv}$ in the recirculation region were maintained mainly by the pressure-related terms.

6.6 Summary of This Chapter

In this chapter, a hybrid method of the PIV-based pressure field evaluation and direct single-point measurement by SP-probes was developed. Pressure fluctuation associated with large-scale vortex structure was extracted from PIV data by means of the POD, and the instantaneous pressure directly measured by the SP-probe was used for reference to determine valid number of POD modes to be taken into account for the pressure evaluation.

The hybrid method was applied to measurement in a very near wake of a circular cylinder. The extracted fluctuating pressure from the PIV data by the hybrid method was quite in strong agreement with direct measurement results. The signal-to-noise ratio of the pressure evaluation was significantly improved from 2.6-to-1 to 14-to-1 by the hybrid method, and the uncertainty of the pressure evaluation was 13%. The verification on the evaluated pressure-related statistics using the relationship between the pressure related terms in the transport equation of the Reynolds stresses indicated certain consistency of the present measurement results of the pressure-related statistics. Thus, the pressure-related statistics in flow regions where the direct measurement technique cannot be applied is now accessible.

By the investigation on budget of the transport equations of the Reynolds stresses, it was revealed that the pressure-related statistics have significant contributions to transport of the Reynolds stresses. In particular, the Reynolds shear stress in the recirculation region is found to be maintained mainly by the pressure-related statistics.

Chapter 7

Summary and Conclusion

7.1 Technical Achievements for Development in Measurement Techniques

In the present thesis, the series of work aiming at further development in techniques for simultaneous measurement of fluctuating velocity and pressure were done on the three different topics:

1. Validation of the existing measurement technique, in which a miniature static-pressure probe are combined with a hot-wire probe
2. Development of a technique for simultaneous measurement of three velocity components and fluctuating pressure
3. Development of a hybrid method of PIV-based pressure evaluation and direct single-point measurement of static pressure by the SP-probes

Achievements of the present study on each topic are summarized below.

1. Validation of the existing measurement technique

Aiming at validation of the existing measurement method, the measurement results obtained by a combination of a miniature static-pressure probe (SP-probe) and an X-type hot-wire probe (X-probe) were compared with reference data obtained by a large-eddy simulation (LES). The measurement results of the pressure fluctuation and the velocity-pressure correlation were in fairly good agreement with the computational results, and the reliability of the existing technique was confirmed. In addition, it was revealed that the measurement of the velocity-pressure correlation $\overline{vp}$ is extremely sensitive to a small time lag between the velocity and pressure signals and the geometrical configuration of the pressure-sensing holes of the SP-probe. Therefore, it can be reasonably considered that the measurement method in which a Pitot-tube-type pressure probe is combined with a hot-wire probe is a reliable method for simultaneous measurement of fluctuating velocity and pressure, but special attention is necessary for measurement of correlation between the transverse velocity component and pressure.

2. **Measurement in three-dimensional turbulent flow**
   A new probe system comprising a bent-type total pressure probe (TP-probe) and a triple-sensor hot-film probe (THF-probe) was developed for simultaneous measurement of three velocity components and pressure in three-dimensional turbulent flow. The spatial resolution of the new combined probe was equivalent to that of single use of the THF-probe: a sphere with a diameter of 3.0 mm. The frequency range and the signal-to-noise ratio of the fluctuating pressure measurement were $25 \leq f \leq 600$ Hz and 6-to-1, respectively; the frequency range was equivalent to that of the fluctuating pressure measurement by the SP-probe, while the signal-to-noise ratio was smaller that of the measurement by the SP-probe due to indirect measurement of static pressure. The pressure fluctuation measured by the new probe system was validated by a comparison with a reference results provided by single use of the SP-probe, and they were in good agreement with each other. The measurement results of velocity-pressure correlations were also found to be consistent with the Reynolds stresses, which supports a reliability of measurement by the newly proposed technique. Therefore, the newly proposed probe system is useful for simultaneous measurement of fluctuating velocity and pressure in three-dimensional turbulent flow.

3. **Hybrid measurement method of PIV and SP-probes**
   A hybrid method of the PIV-based pressure evaluation and direct single-point pressure measurement by the SP-probes was developed, aiming at improving the shortcomings of the PIV-based pressure evaluation such as a low signal-to-ratio and specification of boundary condition. The proper orthogonal decomposition was applied to the PIV data in order to extract pressure fluctuation caused by the large-scale vortex structure, and the number of the POD modes used to reconstruct the pressure field was determined based on the pressure signals directly measured by the SP-probes. The signal-to-noise ratio of the PIV-based pressure evaluation was significantly improved from 2.3-to-1 to 14-to-1, by the hybrid method. The fluctuating pressure obtained by the hybrid method strongly agreed

with the reference direct measurement results by single use of the SP-probe, which indicates validity of the measurement by the hybrid method. The velocity-pressure and pressure-strain-rate correlations obtained by the hybrid method were also examined by focusing on the relationship between the pressure-related terms of the transport equation of the Reynolds stresses, and consistency with the velocity pressure-gradient correlation was confirmed. Therefore, it is reasonable to consider that the reliability of the PIV-based pressure evaluation was significantly improved by hybrid with direct pressure measurement by the SP-probe.

Thus, applicable range of the technique for simultaneous measurement of fluctuating velocity and pressure was significantly expanded and reliabilities of the measurement techniques were also strengthened in the present study. The direct point-measurement technique is now applicable to both two- and three-dimensional turbulent flow fields. Simultaneous measurement of instantaneous velocity and pressure fields is also possible by the hybrid method.

7.2 Role of Pressure-Related Statistics

Turbulent Wingtip Vortex

The role of the velocity-pressure correlation in a turbulent wingtip vortex flow was investigated evaluating the terms in the transport equation of the turbulent kinetic energy and the Reynolds stresses. The pressure-diffusion was found to be much larger than the turbulent diffusion and play a significant role in the transport equation of the turbulent kinetic energy. This significant contribution of the pressure diffusion was produced by the unsteady motion of the wingtip vortex with directional preference.

Near Wake of Circular Cylinder

The velocity-pressure correlation was measured at different streamwise locations in a near wake of a circular cylinder by different approach. The pressure diffusion in the transport equation at $x/D = 10$ (x is streamwise coordinate axis and D is the cylinder diameter) measured by the direct measurement technique was found to be comparable to the other terms.

The pressure-related statistics were also investigated in the flow region immediately behind a circular cylinder. In the transport equation of all the Reynolds stress components, the pressure diffusion was found to play a distinct role. Especially, the Reynolds shear stress shows characteristic peaks inside the recirculation region while the normal stresses were almost zero, and this distribution of the shear stress were found to be maintained mainly by the pressure diffusion and the redistribution.

In both flow fields, the pressure-diffusion was found to play an important role in the transport equation of the turbulent kinetic energy and the Reynolds stresses, and the significant importance of the pressure diffusion was a consequence of strong pressure fluctuation caused by motion of the large-scale vortices. Thus, investigation on the velocity-pressure correlation is crucial to understand the structure of such complex turbulent flows from the view point of the Reynolds-averaging framework.

7.3 Direction for Further Development of Measurement Technique

Direct Measurement Technique

A probe configuration comprising the TP-probe and THF-probe provided the measurement results with a certain reliability, but a room for improvement remained in the relatively narrow measuring range of the cross-flow angle on the velocity measurement. In the velocity measurement, a certain influence by the narrow acceptance range of the THF-probe was observed, and it may have contaminated the static-pressure measurement. Therefore, it may further improve the quality of the simultaneous measurement of velocity and pressure to enlarge the measurement range of flow angle by, for example, using a four-sensor hot-wire/film probe, which has larger acceptance range.

Measurement Method Based on PIV and SP-Probe

Although certain successful results were obtained by the proposed hybrid method, the POD procedure extracted only the pressure fluctuations caused by the largest vortex structure, and the higher POD modes not taken into account for the pressure evaluation may contain the meaningful information of the pressure fluctuation by the smaller structure.

One of the possible reasons is that the POD analysis may not be the best decomposition method to extract the pressure fluctuation related to the vortex structures from the measurement noise. As the POD bases are perpendicular to each other, the smaller structure may not be successfully extracted by the POD. Use of other decomposition method, such as the dynamic mode decomposition, may result in further improvement the extraction of meaningful data from the measurement noise.

Furthermore, in the present study, the 2D approximation was used in the pressure evaluation. While this approximation was valid for the largest structure, it may not for the smaller structure. Therefore, use of the 3D velocity measurement method, such as the tomo-PIV, may result in further improvement in capturing the pressure fluctuation caused by the smaller structure.

Bibliography

Abe, S., Okamoto, K., Madarame, H., 2004. The development of piv-psp hybrid system using pressure sensitive particles. Meas. Sci. Technol. 15, 1153–1157.

Adrian, R. J., Meinhart, C. D., Tomkins, C. D., 2000. Vortex organization in the outer region of the turbulent boundary layer. J. Fluid Mech. 422, 1–54.

ASME PTC 19.1, 1985. Measurement uncertainty.

Aydin, I., 1998. Evaluation of fluctuaitng pressure measured with connection tubes. J. Hydraul. Eng. 124-4, 413–418.

Bailey, S. C. C., Taboularis, S., 2006. Effects of free stream turbulence on wing-tip vortex formation and near fileld. J. Aircraft 43-5, 1282–1291.

Baur, T., Köngeter, J., 1999. Piv with high temporal resolution for the determination of local presure reductions from coherent turbulent phenomena. In: Proceedings of the 3rd international workshop on particle image velocimetry, Santa Barbara, USA.

Beaudan, P., Moin, P., 1994. Numerical experiments on the flow past a circular cylinder at a sub-critical Reynolds number. Tech. rep., CTR Annual Research Breifs, NASA Ames/Stanford University.

Bernard, P. S., Wallace, J. M., 2002. Turbulent flow; analysis, measurement and prediction. Wiley & Sons, Ic.

Birch, D., Lee, T., 2005. Investigation of the near-field tip vortex behind an oscillating wing. J. Fluid Mech. 544, 201–241.

Boesch, G., Vo, H. D., Savard, B., Tchatchouang, C. W., Mureithi, N. W., 2010. Flight control using wing-tip plasma actuation. J. Aircraft 47, 1836–1846.

Brown, G. L., Roshko, A., 1974. On density effects and large structure in turbulent mixing layers. J. Fluid Mech. 64, 775–816.

Browne, L. W. B., Antonia, R. A., Chua, L. P., 1989. Calibration of X-probes for turbulent flow measurement. Exp. Fluids 7, 201–208.

Bruns, J. M., Dengel, P., 1998. A miniature triple hot-wire probe for wall bounded flows. Exp. Fluids 24, 479–488.

Cantwell, B. J., 1981. Organized moton in turbulent flow. Annu. Rev. Fluid Mech. 13, 457–515.

Charonko, J., King, C., Smith, B., Vlachos, P., 2010. Assesment of pressure field calculations from particle image velocimetry measurements. Meas. Sci. Technol. 21, 105401.

Chow, J., Zilliac, G., Bradshaw, P., 1997. Turbulence measurement in the near field of a wingtip vortex. Tech. rep., NASA Technical Memorandum, 110418.

Craft, T. J., Gerasimov, A. V., Launder, B. E., 2006. A computational study of the near-field generation and decay of wingtip vortices. Int. J. Heat Fluid Flow 27, 684–695.

De Kat, R., van Oudheusden, B. W., 2012. Instantaneous planar pressure determination from PIV in turbulent flow. Exp. Fluids 52–5, 1089–1106.

Devenport, W. J., Rife, M. C., Liapis, S. I., Follin, G. J., 1996. The structure and development of a wint-tip vortex. J. Fluid Mech. 312, 67–106.

Donovan, F. M., Mcllwain, R. W., Mittmann, D. H., Taylor, B. C., 1994. Experimental correlations to predict fluid resistance for simple pulsatile laminar flow of incompresible ffluid in rigid tubes. Trans. ASME J. Biomech. Eng. 116, 516–521.

Donovan, F. M., Taylor, B. C., Su, M. C., 1991. one-dimensional computer analysis of oscillatory flow in rigid tubes. Trans. ASME J. Biomech. Eng. 113, 476–484.

Duraisamy, K., Rmasamy, M., Baeder, J. D., Leishman, J. G., 2007. High resolution comutational and experimental study of rotary wing-tip vortex formation. AIAA J. 45, 2593–2603.

Eckelmann, H., 1989. A review of knowledge on pressure fluctuation. Hemisphere, New York.

Elsinga, G. E., Scarano, F., Wieneke, B., van Oudheusden, B. W., 2006. Tomographic particle image velocimetry. Exp. Fluids 41-6, 933–947.

Fuchs, H., 1972. Measurement of pressure fluctuations within subsonic turbulent jets. J. Sound Vib. 22-3, 361–378.

Fujisawa, N., Nakamura, K., Srinivas, K., 2004. Interaction of two parallel plane jets of different velocities. Journal of Visualization 7, 135–142.

Fujisawa, N., Tanahashi, S., Srinivas, K., 2005. Evaluation of pressure field and fluid forces on a circular cylinder with and without rotational oscillation using velocity data from piv measurement. Meas. Sci. Technol. 16, 989–996.

Geddes, L. A., Athens, W., Aronson, S., 1984. Measurement of the volume displacement of blood pressure transducer. Med. Biol. Eng. Comput. 22, 613–614.

George, W. K., Beuther, P. D., Arndt, R. E. A., 1984. Pressure speactra in turbulent free shear flow. J. Fluid Mech. 148, 155–191.

Gerontakos, P., Lee, T., 2006. Near fied tip vortex behind a swept wing model. Exp. Fluids 40, 141–155.

Ghaemi, S., Ragni, D., Scarano, F., 2012. PIV-based pressure fluctuation in the turbulent boundary layer. Exp. Fluids, DOI 10.1007/s0034–012–1391–4.

Giovanangeli, J. P., 1988. A new method for measuring static pressure fluctuations with application to wind-wave interaction. Exp. Fluids 6, 156–164.

Gurka, R., Liberzon, A., Hefetz, D., Rubinstein, D., Shavit, U., 1999. Computation of pressure distribution using PIV velocity data. In: Proceedings of the 3rd international workshop on particle image velocimetry, Santa Barbara, USA.

Haase, W., Braza, M., Revell, A., 2009. DESider - a European effort on hybrid RANS-LES modelling (Results of the European-Union Funded Project, 2004-2007). Springer-Verlag Berlin Heidelberg.

Hansen, A. T., 1950. Pressure measurement in th human organism. Acta Physiol. Scand. 19, 306–331.

Heyes, A. I., Jones, R. F., Smith, D. A., 2004. Wandering of wing-tip vortices. In: Symp. on the Applications of Laser Technical Memorandum, 110418.

Hinze, J. O., 1959. Turbulence. McGraw-Hill.

Ho, C. M., Huerre, P., 1984. Perturbed free shear layers. Annu. Rev. Fluid Mech. 16, 365–424.

Hosokawa, S., Moriyama, S., Tomiyama, A., Takada, N., 2003. PIV measurement of pressure distribution about single bubbles. J. Nucl.Sci. Technol. 40, 754–762.

Hoyas, S., Jimenez, J., 2006. Scaling of the velocity fluctuations in turbulent channels up to $re_\tau = 2003$. Phys. Fluids 18, 011702.

Hussain, A. K. M. F., 1983. Coherent structures - reality and myth. Phys. Fluids 26, 2816–2850.

Hussain, A. K. M. F., Hayakawa, M., 1987. Eduction of large scale organized structures in a turbulent plane wake. J. Fluid Mech. 180, 193–229.

Hussain, A. K. M. F., Zaman, K. B. M. Q., 1987. An experimental study of organizaed motion in the turbulent plane mixing layer. J. Fluid Mech. 159, 85–104.

Iida, A., Otaguro, T., Kato, C., Shimode, S., 1999. Analysis of aerodynamic sound source with measurement of static-pressure fluctuation. JSME International Journal, Series B 42-4, 596–604.

Ishida, T., Toyoda, K., Tao, H., Shirahama, T., 1995. Study of yaw-angle characteristics of static pressure probe. In: Fluid Engineering Division Conference of the Japan Society of Mechanical Engineering (in Japanese).

Ishii, T., Suryadi, A., Obi, S., 2008. The pressure-velocity correlation in the turbulent wingtip vortex flow. In: Proceedings of 7th JSME-KSME Thermal and Fluids Engineering Conference.

Iwamoto, K., Kasagi, N., Suzuki, Y., 2005. Direct numerical simulation of turbulent channel at $re_\tau = 2320$. In: 6th Symp. on Smart Control of Turbulence.

Jeong, J., Hussain, F., Schoppa, W., Kim, J., 1997. Cohrent structures near the wall in a turbulent channel flow. J. Fluid Mech. 332, 185–214.

Johansson, P. S., Andersson, H. I., 2005. Direct numerical simulation of two oppsing wall jets. Phys. Fluids 17, 055109.

Jones, W. P., Launder, B. E., 1972. The prediction of laminarizatioin of with a two-equation model of turbulence. Int. J. Heat Mass Transfer 15, 301–314.

Jørgensen, F. E., 1971. Directional sensitivity of wire and fibre-film probes. DISA Info. 11, 31–37.

Jørgensen, F. E., 2002. How to measure vortices turbulence with hot-wire anemometers - a practica guide. Dantec Dynamics Website; http://www. dantecdynamics.com/Download/pdf.files/practicalguide.pdf.

Kasagi, N., Sumitani, Y., Suzuki, Y., Iida, O., 1995. Kinematics of the quasi-coherent vortical structure in near wall turbulence. Int. J. Heat Fluid Flow 16, 2–10.

Kida, S., Yanase, S., 1999. Turbulence Mechanics (in Japanese). Asakura-shoten.

Kim, J., Moin, P., Moser, R. D., 1987. Turbulence statistics in fully developed channel flow at low Reynols number. J. Fluid Mech. 177, 133–166.

Kimura, F., Khalil, G., Zettsu, N., Xia, Y., Callis, J., Gouterman, M., Dalton, L., Dabiri, D., Rodriguez, M., 2006. Dual luminophore polystyrene microsheres for pressure-sensitive luminescent imaging. Meas. Sci. Technol. 17, 1254–1260.

Kimura, F., McCann, J., Khalil, G., Dabiri, D., Xia, Y., Callis, J. B., 2010. Simultaneous velocity and pressure measurment using luminescent microspheres. Rev. Sci. Instrum. 81, 064101.

Klein, C., Engler, R. H., Henne, U., Sachs, W. E., 2005. Application of pressure-sensitive paint for determination of the pressure field and calculation of the force and moments of models in a wind tunnel. Exp. Fluids 39, 475–483.

Kline, S. J., Reynolds, W. C., Schraub, F. A., Runstadler, P. W., 1967. The structure of turbulent boundary layers. J. Fluid Mech. 30, 741–773.

Kobashi, Y., 1957. Measurement of pressure fluctuation in the wake of circular cylinder. J. Phiys. Soc. Jpn. 12–5, 533–543.

Kobashi, Y., Kono, N., Nishi, T., 1960. Improvement of pressure pickup for the measurements of turbulece characteristics. J. Aerospace Sci. 27, 149–151.

Kraichnan, R. H., 1959. The structure of isotropic turbulence at very high reynolds numbers. J. Fluid Mech. 5, 497–543.

Kravchenko, A. G., Moin, P., 2000. Numerical studies of flow over a circular cylinder at $\mathrm{Re}_d = 3900$. Phys. Fluids 12, 403–417.

Launder, B. E., Reece, G. J., Rodi, W., 1975. Progress in the development of a reynolds stress turbulece closure. J. Fluid Mech. 68, 537–566.

Ligeza, P., Socha, K., 2007. Optimization of an algrithm for measurements of velocity vector components a three-wire sensor. Rev. Sci. Instrum. 78, 105104.

Liu, X., Katz, J., 2006. Instantaneous pressure and material accelaration measurements using a four-exposure piv system. Exp. Fluids 41, 227–240.

Lourenco, L. M., Shih, C., 1993. Characteristics of the plane turbulent near wake of a circular cylinder, a particle image velocimetry study. Published in Beaudan and Moin (1994).

Lueptow, R. M., Breuer, K. S., Haritonidis, J. H., 1988. Computeraided calibration of X-probes using a look-up table. Exp. Fluids 7, 201–208.

Lumley, J. L., 1978. Computational modeling of turbulent flows. Adv. Apll. Mech. 18, 123–176.

Ma, X., Karamanos, G. S., Karniadakis, G. E., 2000. Dynamics and low-dimensionality of a turbulent near wake. J. Fluid Mech. 410, 29–65.

MacLachlan, B. G., Kavandi, J. L., Callis, J. B., Goutarman, M., Green, E., Khalil, G., Burns, D., 1993. Surface pressure field mapping uisng luminescent coatings. Exp. Fluids 14, 33–41.

Margaris, P., Gursul, I., 2006. Wing tip vortex control using synthetic jets. The Aeronautical Journal 110-1112, 673–681.

Mittal, R., Moin, P., 1997. Suitability of upwind-biased finite-difference schemes for large-eddy simulation of turbulent flows. AIAA J. 35, 1415.

Mumford, J. C., 1982. The structure of the large eddies in fully developed turbulent shear flows. J. Fluid Mech. 118, 241–268.

Nagano, Y., Tagawa, M., 1990. A structual turbulence model for triple products of velocity and scalar. J. Fluid Mech. 215, 639–657.

Naguib, A. M., Gravante, S. P., Wark, C. E., 1996. Extraction of turbulent wall pressure time-series using an optimal filtering scheme. Exp. Fluids 22, 14–22.

Naka, Y., 2009. Simultaneous measurement of fluctuating velocity and pressure in turbulent free shear flows. Ph.D. thesis, Graduate School of Science and Technology, Keio University, Japan.

Naka, Y., Obi, 2009. Velocity-pressure correlation measurements in complex free shear flows. Int. J. Heat Fluid Flow 4–1, 107–115.

Naka, Y., Omori, T., Obi, S., Masuda, S., 2006. Simultaneous measurement of fluctuating velocity and pressure in a turbulent mixing layer. Int. J. Heat Fluid Flow 27, 737–746.

Nasseri, M., Nitsche, W., 1991. A probe for measuring pressure fluctuatins in flows. In: Proceedings of Instrumentation in Aerospace Simulation Facilities (ICASF '91).

Norberg, C., 1987. Effects of Reynolds number and low-intensity freestream turbulence on the flow around a circular cylinder. Tech. rep., Department of Applied Thermodynamics and Fluid Mechanics, Chalmer University of Technology, Sweden Rep.

Obi, S., Tokai, N., 2006. The pressure-velocity correlation in oscillatory turbulent flow between a pair of bluff bodies. Int. J. Heat Fluid Flow 27, 768–776.

Okada, S., Hiraoka, K., 2003. Experimental studies of reduction of the wing tip vortex by suction. AIAA Paaper 2003-3533.

Okamoto, K., Nishio, S., Saga, T., Kobashi, T., 2000. Standard iimage for particle-image velocimetry. Meas. Sci. Technol. 11, 685–691.

Ong, J., Wallace, L., 1996. The velocity field of the turbulent very near wake of a circular cylinder. Exp. Fluids 20, 441–453.

Orszag, S. A., 1970. Analytical theories of turbulentc. J. Fluid Mech. 41, 363–386.

Parnaudeau, P., Carlier, J., Heitz, D., Lamballais, E., 2008. Experimental and numerical studies of the flow over a circular cylinder at Reynolds number 3900. Phys. Fluids 20, 085181.

Pope, S. B., 2000. Turbulent Flows. Cambridge University Press.

Pröbsting, S., Scarano, F., Bernardini, M., Pirozzoli, S., 2013. On the estimation of wall pressure coherence using time-resolved tomographic piv. Exp. Fluids 54, 1567.

Robinson, S. K., 1991a. Coherent motion in the turbulent oundary layer. Ann. Rev. Fluid Mech. 23, 601–639.

Robinson, S. K., 1991b. The kinematics of turbulent boundary layer structure. Tech. rep., NASA TM-103859.

Roseman, H., Stäger, R., Kreplin, H. P., 1996. Development and application of a quadruple hot-wire technique for turbulent flows. Meas. Sci. Technol. 7, 1477–1491.

Sakai, Y., Moriguchi, Y., Tanaka, N., Yamamoto, M., Kubo, T., Nagata, K., 2007. On characteristics of velocity and pressure field in two-dimensional turbulent jet. Journal of Fluid Science and Technology 2-3, 611–622.

Schlatter, P., Örlü, R., 2010. Assessment of direct numerical simulation data of turbulent boundary layers. J Fluid Mech. 659, 116–126.

Schoppa, W., Hussain, F., 2002. Coherent structure generation in near-wall turbulence. J. Fluid Mech. 453, 57–108.

Shirahama, Y., Toyoda, K., 1993. Development of the probe to measure static-pressure fuctuations. Trans. Jpn. Soc. Mech. Eng. Series B (in Japanese) 59, 3381–3387.

Sirovich, L., 1987. Turbulence and the dynamics of coherent structures. Parts I-III. Q. Appl. Math. XLV, 561–590.

Smith, C. R., Metzler, S. P., 1983. The characteristics of low-speed streaks in the near-wall region of a turbulent boundary layer. J. Fluid Mech. 129, 27–54.

Smith, L. M., Woodruff, S. L., 1998. Renormalization-group analysis of turbulence. Annu. Rev. Fluid Mech. 30, 275–310.

Speziale, C. G., Sarker, S., Gatski, T. B., 1991. Modeling the pressure-strain correlation of turbulence; an invariant dynamical ssystem approach. J. Fluid Mech. 227, 245–272.

Suga, K., 2004a. Improvement of second moment closure for turbulent obstacle flow and heat transfer. Int. J. Heat Fluid Flow 25, 776–784.

Suga, K., 2004b. Modeling the rapid part of the pressure-diffusion process in the reynolds stress transport equation. J. Fluids Eng. 126–4, 634.

Suryadi, A., 2007. Application of image distortion analysis with stereo particle image velocimetry on unsteady flow generated by flapping motion. Master's thesis, Keio University.

Tatsumi, T., Kida, S., Mizushima, J., 1978. The multiple-scale cumulant expansion for isotropic turbuence. J. Fluid Mech. 85, 97–142.

Taylor, B. C., Donovan, F. M., 1992. Hydraculic resistance and damping in cather-transcuer systems. IEEE Eng. Med. Biol. 0739-5175.

Terashima, O., Sakai, Y., Nagata, K., 2012. Simultaneous measurement of velocity and pressure in a plane jet. Exp. Fluids 53–4, 1149–1164.

Toyoda, K., Okamoto, T., Shirahama, Y., 1994. Eduction of vortical structures by pressure measurements in noncircular jets. Applied Scientific Research 53, 273–248.

Tropea, C., Yarin, A. L., Foss, J. F., 2007. Springer Handbook of Experimental Fluid Mechanics. Springer.

Tsuji, Y., Fransson, J. H. M., Alfredsson, P. H., Johansson, A. V., 2007. Pressure statistics and their scaling in high-Reynolds-number turbulent boundary layers. J. Fluid Mech. 585, 1–40.

Tsuji, Y., Ishihara, T., 2003. Similarity scaling of pressure fluctuation in turbulence. Phys. Rev. E 68, 026309.

van Oudheusden, B. W., 2013. Topical review; PIV-based pressure measurement. Meas. Sci. Technol. 24, 032001.

Violato, D., Moore, P., Scarano, F., 2011. Lagrangian and eulerian pressure field evaluation of rod-airfoil flow from time-resolved tomographic piv. Exp. Fluids 50, 1057–1070.

Wereley, S., Gui, L., 2003. A correlation-based central difference image correction (CDIC) method and application in a four-roll mill flow PIV measurement. Exp. Fluids 34, 42–51.

Westerweel, J., 1994. Efficient detection of spurious vvector in particle image velocimetry data. Exp. Fluids 16, 236–247.

White, F. M., 2006. Viscous Fluid Flow, Third Edition. McGraw-Hill.

Wilcox, D., 1993. Turbulence Modeling for CFD. DCW Industries and Griffin Printing, Glendale, Calif.

Willmarth, W. W., 1975. Pressure fluctuations beneath turbulent boundary layers. Annu. Rev. Fluid Mech. 7-1, 13–36.

Yao, Y. F., Thomas, T. G., Sandham, N. D., 2001. Direct numerical simulation of turbulent flow over a rectangular trailing edge. Theoret. Comput. Fluid Dyn. 14, 337–358.

Yoshizawa, A., 2002. Statistical analysis of mean-flow effects on the pressure-velocity correlation. Phys. Fluids 14-5, 1736–1744.

Zhou, Y., Antonia, R. A., 1993. A study of turbulent vortices in the near wake of a cylinder. Exp. Fluids 253, 643–661.

Appendix A

List of Instruments

Table A.1: List of Instruments used in experiment in air

Name	Manufacturer	Model	Specification
Thermometer	Nakamura-Rika-Kogyo	TA-5N	min scale: 1°C
Mercury Barometer	Shimadzu Corp.		Fortin type min scale: 0.1mmHg, 0.5°C
Blowing Wind Tunnel	Self-built		
Standard Pitot-tube	Okano-Seisakusho	LK-1	Coefficient: 1.00
Precision Pressure Difference Sensor	Validyne	DP45-18	pressure range: 0-35 mmH$_2$O
Precision Pressure Difference Sensor Amplifier	KRONE	PA-501	
Constant Temperature Anemometer (CTA)	Kanomax	1011	
Tempareture Unit	Kanomax	1011	
I-type Hot-Wire Probe	Kanomax	0251R-T5	Used in two-point correlaitn measuremeent mentinoed in Sect. 3.4.1
X-type Hot-Wire Probe	Dantec	55P64	
Triple Hot-Film Probe	Dantec	55R91	
Temperature Compensation Probe	Dantec		
Support for Dual Sensor Probe	Dantec	55H24	
Support for Triple Sensor Probe	Dantec	55H27	
Static-Pressure Probes	Self-Fabricated		
Bent-Type Toltal-Pressure Probes	Self-Fabricated		
Condenser Microphone	RION	UC-29	Sensitivity: 4.02 mV/Pa, Frequency Range: 5-10,0000Hz
Conversion Adapter	RION	UA-12	
Pre-Amp.	RION	NH-05	
Main-Amp	RION	UN-04	

Name	Manufacturer	Model	Specification
USB Sound Unit	Onkyo	SE-30	
Loudspeaker	YAMAHA	HS80M	
Quasi-anechoic box	self-fabricated		
Traversing Unit	Oriental Motor	SPF60	y and z-directions
Automatic Rotating Stage	Misumi	RMPG40	Used for Calibraton of X- and THF-probes, Resolution; 0.004°
Automatic Rotating Stage	Misumi	RMPG60	Used for Calibraton of X- and THF-probes, Resolution; 0.006°
Driver for Automatic Rotating Stage	Oriental Motor	DS507-2	
Low-pass filter	NF Corp.	3344	6th order Chevishev
A/D Converter Board	National Instruments	PCI-6221	Multifunction DAQ Board, Resolution: 16bit
BNC Terminal	National Instruments	BNC-2120	
Digital Micro Scope	Keyence	VH-6200	
Measurement Software	National Instruments	LabView 2010	
Signal Processing Software	The MathWorks	Matlab 2012a	
PC	Proside	Rack-Mount PC -500	CPU: Pentium4 2.66GHz, Main Memory: 1GB

Table A.2: List of Instruments used in experiment in water

Name	Manufacturer	Model	Specification
Closed-Loop Water Channel	Igarashi Industory Ltd.		
Strain-Gage-Type Pressure Transducer	Valydyne	DP45	Pressure Range: ±83 Pa (DP45-1) Pressure Range: ±158 Pa (DP45-2)
Precision Pressure Difference Sensor Amplifier	KRONE	PA-501	
Static-Pressure Probe	Self-Fabricated		
Low-pass filter	NF Corp.	3344	6th order Chevishev
A/D Converter Board	National Instruments	PCI-6221	Multifunction DAQ Board, Resolution: 16bit
BNC Terminal	National Instruments	BNC-2120	
Traversing Unit	Oriental Motor	LXM3010C	For traverse of SP-probes
High-Speed Camera	Photron	FASTCAM SA3 Model	Resolution 1034×1024 pixel^2
Lens	Nikkon	Nikkor 85 mm f2.8D	
Continuous Layser	LYPE	LYPE2-SG-WL532CW	wavelength: 532 nm Output Power: 2 W
Tracer Particle	Daicel-Evonik Ltd.	White Nylon 12	mean diameter 90 μm specific gravity 1.02
Measurement Software	National Instruments	LabView 2010	
Signal Processing Software	The MathWorks	Matlab 2012a	
PC for Operation of Direct Pressure Measurement	Proside	Rack-Mount PC-500	CPU: Pentium4 2.66GHz, 32-bit, Main Memory: 1GB
PC for Operation of PIV	T420	Lenovo	32 bit, Main Memory: 4 GB CPU: Intel(R) Core(TM) i5-2520M 2.50 GHz
PC for Data Processing	CTO server-C Custom	UNITCOM	CPU: Intel(R) Core(TM) i7-2600 3.4 GHz 32 bit, Main Memory: 8GB

Appendix B

Effect of Geometrical Configuration of Pressure-Sensing Holes of SP-probe

The measurement of $\overline{vp}$ was also found to be sensitive to the configuration of the pressure-sensing holes of the SP-probe. Figure B.1 shows the profiles of the pressure fluctuation p' and the velocity-pressure correlations $\overline{up}$ and $\overline{vp}$ measured by the probe d07-1 with three different circumferential orientation of the SP-probe: The SP-probe was rotated about its axis by the rotation angle ϕ as schematically shown in Fig. B.1a, and the velocity-pressure correlation measurements were repeated three times with different values of ϕ by 90°. One should note that the time lag between the velocity and pressure signals was not corrected for these results. It is shown in Fig. B.1 that the profiles of p' and $\overline{up}$ are identical to each other regardless of the circumferential

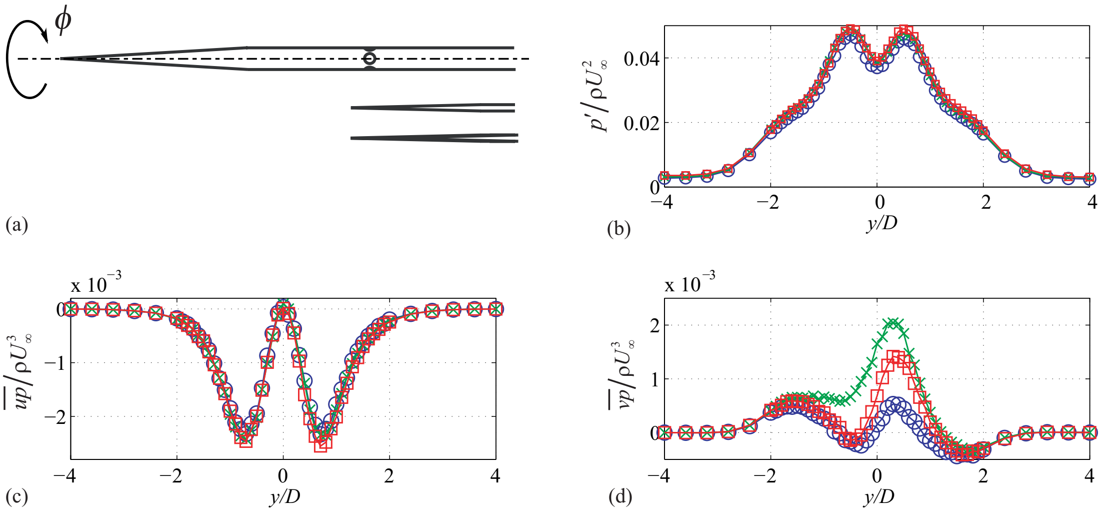

Figure B.1: Distribution of pressure-related statistics measured by probe d07-1 at $x/D = 10$ with three values of ϕ different form each other by 90°.

Figure B.2: Variation of pressure fluctuation and velocity-pressure correlation against ϕ measured by probe d07-1 at $(x/D,\, y/D) = (10,\, 0)$.

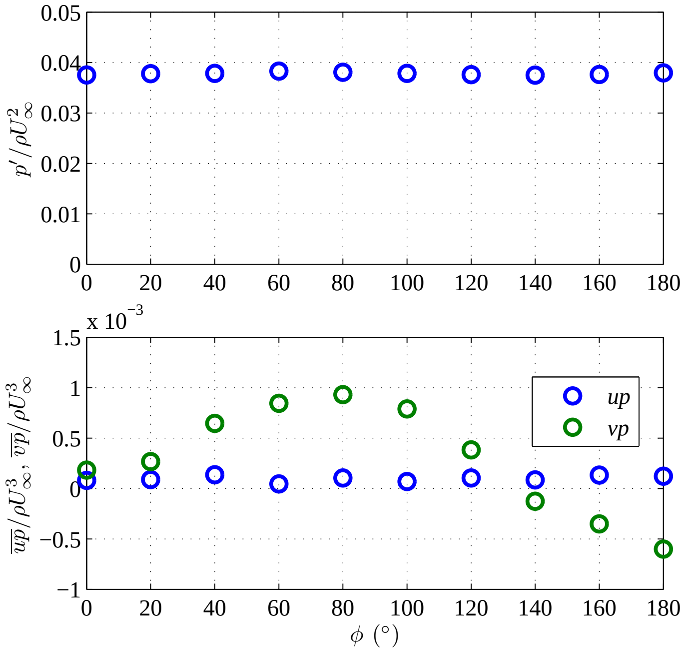

orientation of the SP-probe, but the profiles of $\overline{vp}$ are sensitively affected.

Figure B.2 shows the variation of the measured pressure fluctuation p' and the velocity-pressure correlations $\overline{up}$ and $\overline{vp}$ against the circumferential orientation the SP-probe ϕ. The results were measured by the probe d07-1 at the center of the wake. It is clearly shown that the measured values of p' and $\overline{up}$ are insensitive to ϕ, whilst those of $\overline{vp}$ show significant variation.

In order to further investigate the effect of the circumferential radiation angle ϕ, the PSDs of fluctuating pressure and real part of cross spectrum between p and v are shown in Figs. B.3 and B.4, respectively, comparing those measured at $\phi = 0°$ and 80°. As

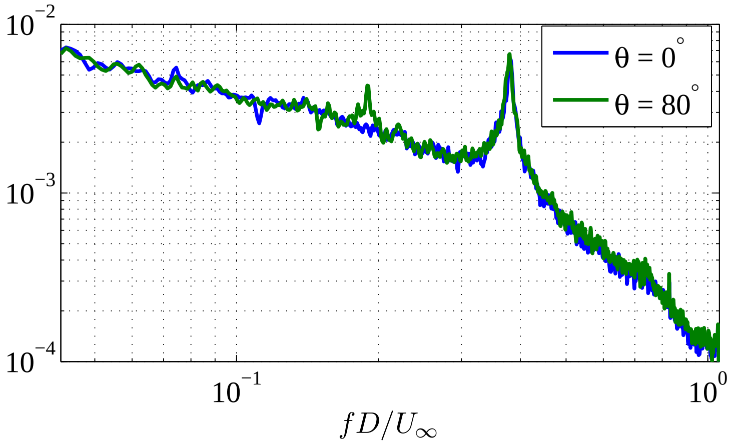

Figure B.3: PSD of fluctuating pressure measured by probe d07-1 at $(x/D,\, y/D) = (10,\, 0)$: blue, $\phi = 0°$; green, $\phi = 80°$.

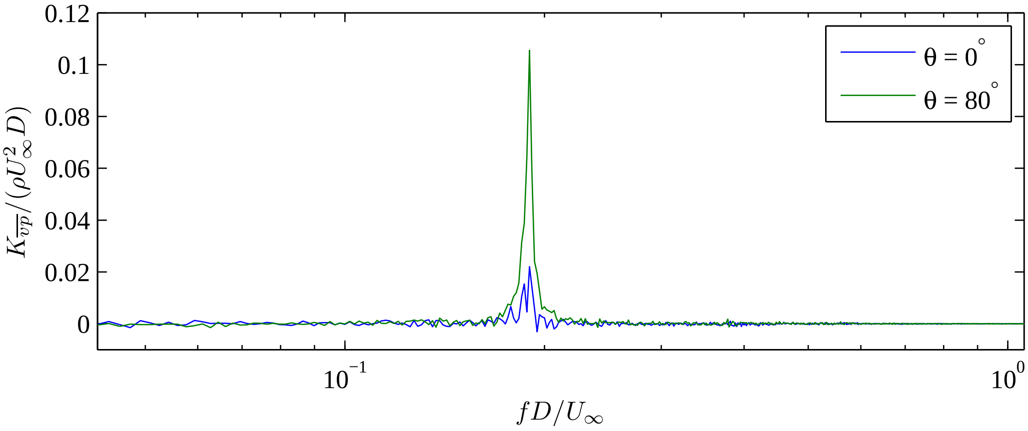

Figure B.4: Real part of cross spectrum between fluctuating velocity v and pressure p measured by the X- and d07-1 probes at $(x/D,\ y/D) = (10,\ 0)$: blue, $\phi = 0°$; green, $\phi = 80°$.

shown in Fig. B.3, the PSD of p measured at $\phi = 0°$ showed a significant single peak at $fD/U_\infty = 0.38$, similarly to the PSD profile of the fluctuating streamwise velocity u show in Fig. 3.21. On the other hand, the PSD profile of p measured at $\phi = 80°$ was similar to that at $\phi = 0°$, but had a small peak at the vortex shedding frequency $fD/U_\infty = 0.19$ as well as the primary peak at $fD/U_\infty = 0.38$. As the magnitude of the peak at $fD/U_\infty = 0.19$ was much smaller than that of the primary peak at $fD/U_\infty = 0.39$, the pressure fluctuation measured at $\phi = 80°$ was almost same to that measured at $\phi = 0°$ despite the difference between the PSD profiles.

Figure B.4 presents the profiles of real part of the cross spectrum between p and v. It is shown that, in the case of $\phi = 0°$, the fluctuating velocity v and pressure p were not correlated throughout the measured frequency range, because v and pressure p were fluctuating at different frequencies from each other; p was mainly fluctuating at $fD/U_\infty = 0.38$, while v was fluctuating at $fD/U_\infty = 0.19$ (see Figs. 3.21 and B.3). On the other hand, in the case of $\phi = 80°$, v and p had significant correlation at $fD/U_\infty = 0.19$. It is reasonable to consider that the small pressure fluctuation at $fD/U_\infty = 0.19$ shown in Fig. B.3 had a certain correlation with the fluctuating velocity v.

As shown in the above discussion, the variation of the measured velocity-pressure correlation $\overline{vp}$ with the circumferential rotation angle ϕ was attributable to the strange pressure fluctuation measured at the vortex frequency $fD/U_\infty = 0.19$. In the following, the relationship between this pressure fluctuation at the vortex shedding frequency and the geometrical configuration of the SP-probe is further discussed.

Figure B.5 shows a schematic explanation of the relationship between the geo-

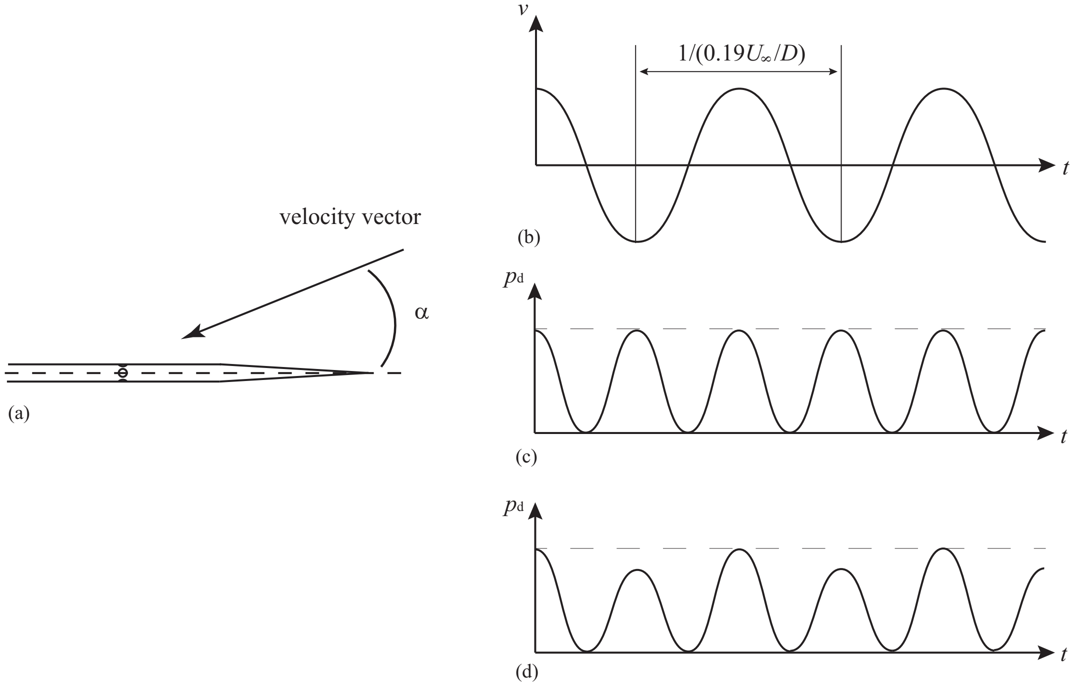

Figure B.5: Schematic explanation of effect of geometrical configuration of the SP-probe on velocity-pressure correlation measurement: (a) SP-probe exposed to velocity vector with angle of attack α; (b) fluctuation of v; true dynamic pressure fluctuation $p_{\mathrm{d},v}$; signal of $p_{\mathrm{d},v}$ measured by an SP-probe with non-axisymmetric sensitivity.

metrical configuration of the SP-probe and the velocity-pressure correlation measurement. As shown in Fig. B.5a, the SP-probe was exposed to velocity vector with a certain instantaneous flow angle α in the range of $-15^\circ \leq \alpha \leq 15^\circ$ during the measurement, and consequently the static-pressure measured by the SP-probe may contain a part of the dynamic pressure caused by the cross-flow velocity component v, namely $p_{\mathrm{d},v} = 0.5\rho v^2$. As the transverse velocity component v was fluctuating at the vortex shedding frequency $fD/U_\infty = 0.19$ with symmetric profile at the wake center (Fig. B.5b), the true dynamic pressure $p_{\mathrm{d},v}$ should be fluctuating at $fD/U_\infty = 0.38$ as schematically drawn in Fig. B.5c. However, if the sensitivity of the SP-probe to the cross-flow effect was asymmetric with respect to $\alpha = 0^\circ$ due to, for example, non-axisymmetric configuration of the pressure-sensing holes, the signal of $p_{\mathrm{d},v}$ actually measured by the SP-probe may be as such shown in Fig. B.5d. The signal of $p_{\mathrm{d},v}$ drawn in Fig. B.5c obviously has the power at $fD/U_\infty = 0.38$ but does not at $fD/U_\infty = 0.19$, and consequently does not have any correlation with v. On the other hand, the signal of $p_{\mathrm{d},v}$ in Fig. B.5d is also mainly fluctuating at $fD/U_\infty = 0.38$ similarly to that of $p_{\mathrm{d},v}$ in Fig. B.5c, but the waves with smaller and lager amplitude are alternatively repeated, which results in the lowest frequency component of the Fourier series being at

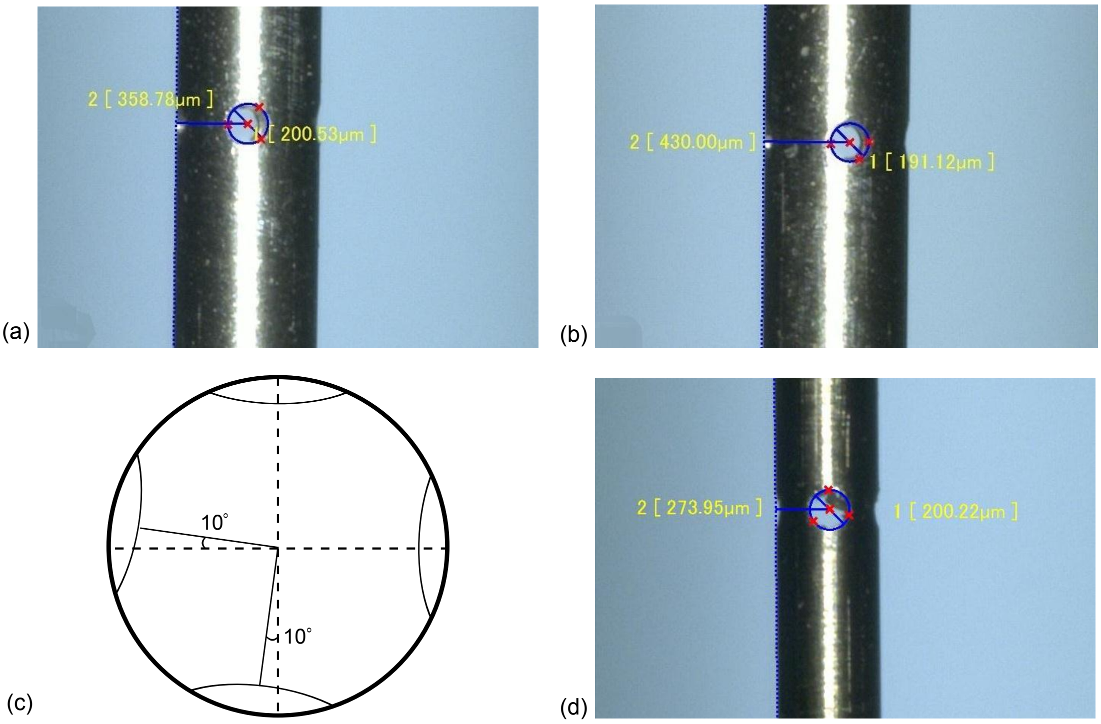

Figure B.6: Pressure-sensing hole of the SP-probe; (a) and (b) pressure-sensing holes of probe d07-1 at circumferential orientations different from each other by 90°, (c) schematics of hole configuration of probe 8, (d) pressure-sensing hole of probe d05-2.

$fD/U_\infty = 0.19$. Thus, the signal of $p_{\mathrm{d},v}$ drawn in Fig. B.5d may have a certain power not only at $fD/U_\infty = 0.38$, but also at $fD/U_\infty = 0.19$, as the pressure signal measured at $\phi = 0^\circ$ in Fig. B.3; and consequently it may have a certain correlation with v.

Next, the configuration of the four pressure-sensing holes of the SP-probe was investigated using a digital microscope. Figures B.6a and b compare configuration of the pressure-sensing hole of the probe d07-1 at two different circumferential orientations. There are two values indicated in each picture: the values denoted by 1 (value 1) are the measured diameter of the pressure-sensing hole, and those denoted by 2 (value 2) are the distance between the center of the hole and the edge of the surface of the probe which is marked by a blue broken line. In Fig. B.6a, one of the pressure-sensing hole is seen with the value 2 approximately being 0.35 mm. In Fig. B.6b, the probe d07-1 was rotated in the circumferential direction by 90°, and the measured value 2 is 0.43 mm. This difference of the value 2 between Figs. B.6a and b corresponds to deviation from the axisymmetric position by 10°, as schematically shown in Fig. B.6c. Such deviation of the configuration from axisymmetric form was observed in the probes d07-1, 2 and d10, which had a relatively large probe diameter d among the various SP-probes. For the probes with the diameter of 0.5 mm, the configuration of the pressure holes was relatively accurate, but some of them had burr on the pressure holes (the probe d05-2 is shown in Fig. B.6d, for instance). Such imperfect geometrical configuration of the pressure-sensing holes might result in the effect of the circumferential orientation of the SP-probe on the measurement of the velocity-pressure correlation $\overline{vp}$ shown in Fig. B.2. Thus, the measurement of the velocity-pressure correlation $\overline{vp}$ was also found to be quite sensitive to the configuration of the pressure sensing-holes, while the measurement of the fluctuating pressure and the velocity-pressure correlation $\overline{up}$ were, again, insensitive.

Appendix C

Simultaneous Measurement of Velocity and Pressure by the THF- and TP-Probes in a Wake of a Circular Cylinder

Simultaneous measurement of three velocity components and pressure by the THF- and TP-probes was performed in a turbulent wake of a circular cylinder prior to the measurement in a turbulent wingtip vortex, as a preliminary application of the measurement technique, and the measurement results were quantitatively compared with the experimental and computational results provided in Chap. 3. In this appendix, this preliminary measurement is described.

C.1 Experimental Condition

The measurements were undertaken in the same wind tunnel as in the experiments described in Chap. 3. Since the measurement volume of the THF-probe was much larger than that of the X-probe, a circular cylinder with diameter D of 20 mm was used in order to maintain the relative spatial resolution of the measurement. The free stream velocity U_∞ was 3 m/s, and the Reynolds number based on D and U_∞ was 3900. The definition of the coordinate system was same as in Chap. 3, and the measurement location was $x/D = 10$. The sampling rate and the integration time for evaluation of statistics were 10 kHz and 180 s, respectively.

The typical acceptance domain of the THF-probe is a corn with tip angle of 35°, and the shape of the acceptance domain is not axisymmetric with respect to the axis

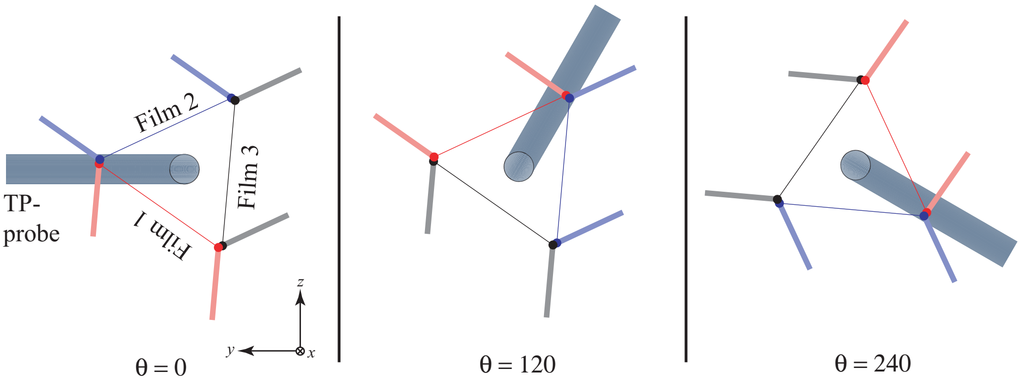

Figure C.1: Configuration of Combined probe in velocity-pressure correlation measurement

of the THF-probe due to the non-axisymmetric configuration of the three hot films. Therefore, in order to minimize such effect of non-axisymmetric configuration, the measurement results measured with three different circumferential orientation of the combined probe shown in Fig. C.1 were averaged to obtain statistics.

C.2 Results and Discussion

The mean streamwise velocity and the Reynolds stresses measured by the new combined probe are shown in Fig. C.2 with the reference data measured by the X- and SP-probes (d05-3, for instance) and predicted by the LES. All the results are scaled by the free stream velocity U_∞. It is shown in Fig. C.2a that the profile of the mean streamwise velocity U measured by the new combined probe had velocity deficit of $0.25U_\infty$ at the wake center, and agreed well with the other reference results.

The Reynolds stresses measured by the new combined probe are presented in Figs. C.2b and c. It is shown by the results measured by the THF-probe that the transverse component $\overline{v^2}$ was the dominant among the Reynolds normal stresses, and the spanwise component $\overline{w^2}$ was as large as the streamwise component $\overline{u^2}$ in the center region of the wake. The results of $\overline{u^2}$ and $\overline{v^2}$ measured the new combined probe were in good agreement with the experimental reference data by single use of the X-probe. The computational results of $\overline{u^2}$ and $\overline{v^2}$ obtained by the LES also agreed well with the measurement results by the present experimental results, although a certain disagreement was seen between the results of the spanwise normal stress $\overline{w^2}$. As shown in

Figure C.2: Mean streamwise velocity and Reynolds stresses at $x/D = 10$ in a wake of a circular cylinder; ○ THF- and TP-probe, × X-probe, - LES; (a) mean streamwise velocity U, (b) Reynolds normal stresses $\overline{u^2}$ (blue), $\overline{v^2}$ (green), $\overline{w^2}$ (red), (c) Reynolds shear stress $\overline{uv}$.

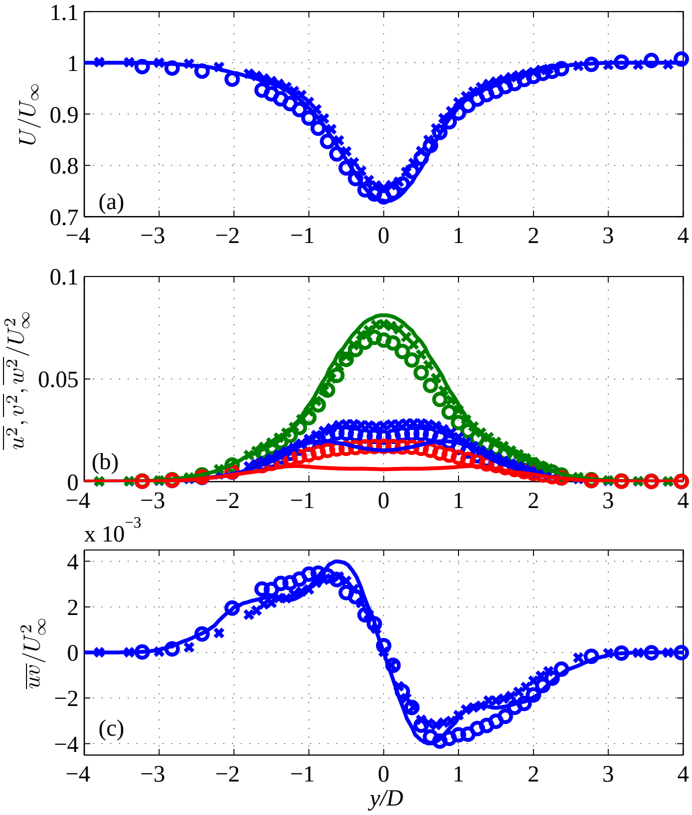

Figure C.3: Power spectra of fluctuating velocity u and v measured by the THF-probe at the wake center.

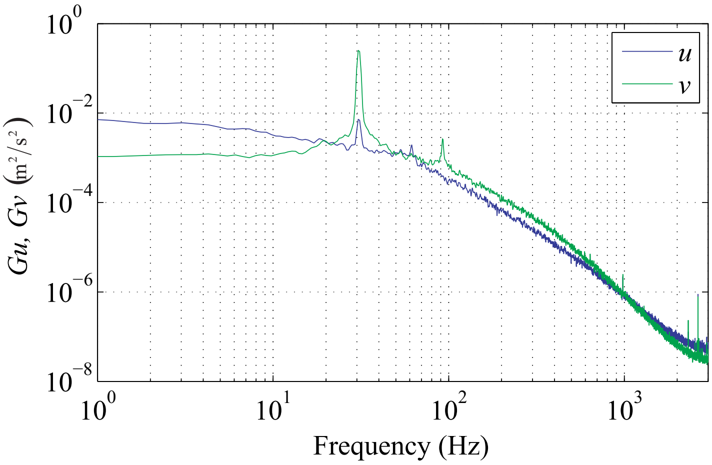

Fig, C.2c, the results of the Reynolds shear stresses $\overline{uv}$ measured by the present combined probe showed an anti-symmetric profile with respect to $y/D = 0$, and it was also in quite good agreement with the other reference results.

Figure C.3 shows the typical PSDs of the fluctuating velocities u and v measured by the THF-probe in the presence of the TP-probe at the center of the wake. The PSD of v showed a significant peak of the velocity fluctuation at the frequency $f = 30$ Hz, which was the vortex shedding frequency corresponding to the Strouhal number of 0.2, and

Figure C.4: Distribution of pressure-related statistics at $x = 10D$. ○, THF- and TP-probe; ×, X- and SP-probe (d05-3, for instance); -, LES.

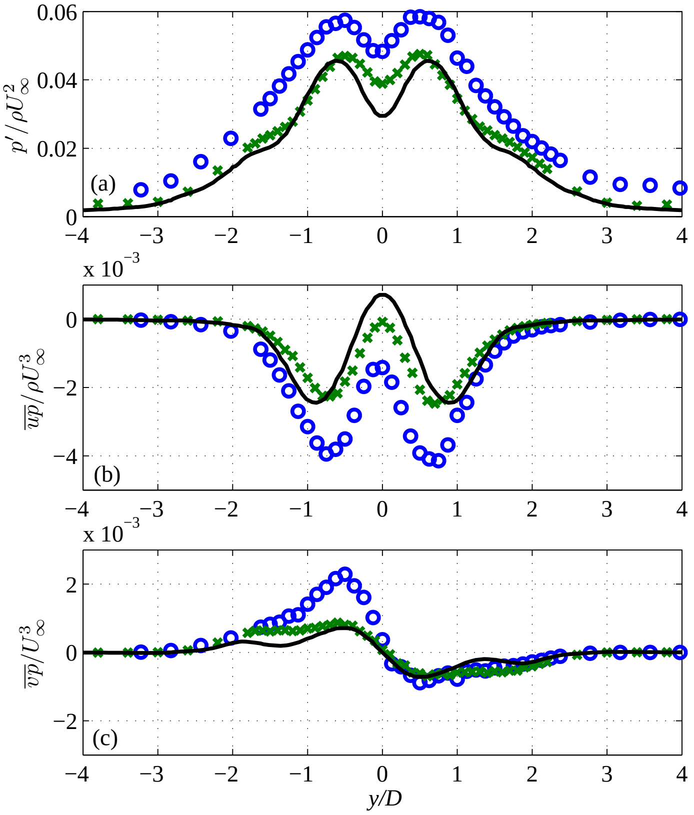

the PSD of u also indicated a peak of the fluctuation at the vortex shedding frequency $fD/U_\infty = 0.2$ as well as at $fD/U_\infty = 0.4$, although the measured location is the center of the wake.

Figure C.4 presents the pressure-related statistics measured by the new combined probe, comparing them with those measured by the X- and SP-probe and predicted by the LES. It is show that the results measured by the new combined probe were in qualitative agreement with the reference results, although certain quantitative discrepancy was indicated; the pressure fluctuation and the velocity-pressure correlation $\overline{up}$ measured by the present method showed two peaks beside the center of the wake similarly to the reference results, but the magnitudes were larger than those of the reference data throughout the wake. The velocity-pressure correlation $\overline{vp}$ measured by the new combined probe changed its sign across the wake similarly to the reference data, but the profiles was not anti-symmetric about $y/D = 0$ with the magnitude of the positive peak located at $y = -0.5D$ being two times larger than those of the reference results.

The possible cause of the discrepancy between the pressure-related statistics is further investigated below. Evaluation of static-pressure fluctuation by Eq. (4.3) requires accurate measurement of both the total- and the dynamic-pressure fluctuations. As the

Figure C.5: Coherence and phase lag between total pressure fluctuation measured by TP-probe and dynamic pressure fluctuation measured by THF-probe.

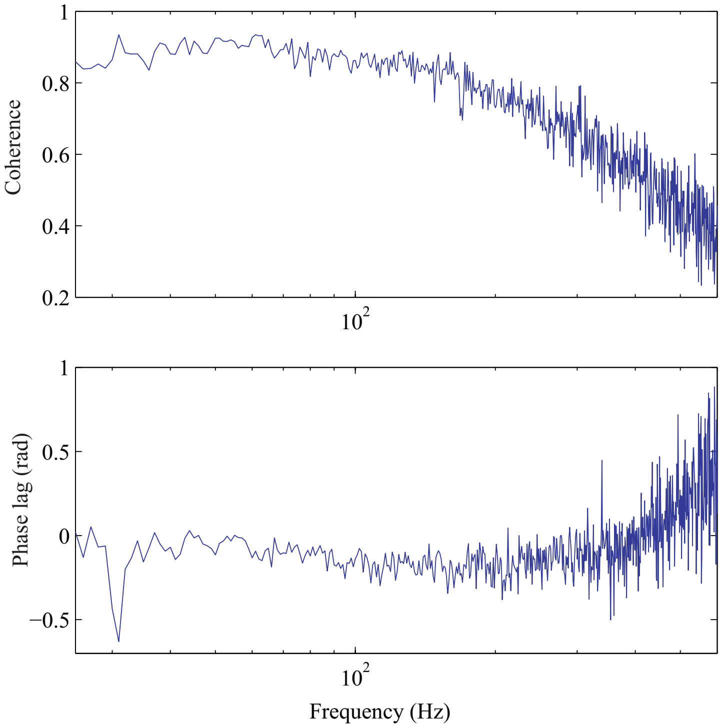

dynamic-pressure fluctuation is usually much larger than the static-pressure fluctuation, the measured total- and dynamic pressure fluctuations should be highly correlated with each other. In order to investigate the correlation between the total- and dynamic-pressure fluctuations directly measured by the new combined probe, the coherence and the phase lag between them were evaluated as

$$\mathrm{coh} = \frac{|S_{p_t p_d}|^2}{S_{p_t^2} S_{p_d^2}} \tag{C.1}$$

$$\Delta\theta = \tan^{-1}\left[\frac{\mathcal{I}(S_{p_t p_d})}{\mathcal{R}(S_{p_t p_d})}\right],, \tag{C.2}$$

where $S_{p_t p_d}$ is the cross spectrum between the total- and dynamic-pressure fluctuation, and $\mathcal{R}$ and $\mathcal{I}$ stands for the real and imaginary part of a complex quantity, respectively. The coherence coh can be interpreted as the correlation coefficient between two signals at each frequency.

Figure C.5 presents the coherence and the phase lag between the total- and the dynamic-pressure fluctuations. It is shown that coh indicated high correlation between the total- and dynamic-pressure fluctuations in the low frequency range around the vortex shedding frequency, but the phase lag $\Delta\theta$ was about -0.7 rad at the vortex shedding frequency. This implies that the total and the dynamic pressure may not be in balance, which may results in overestimation of the static-pressure fluctuation and the

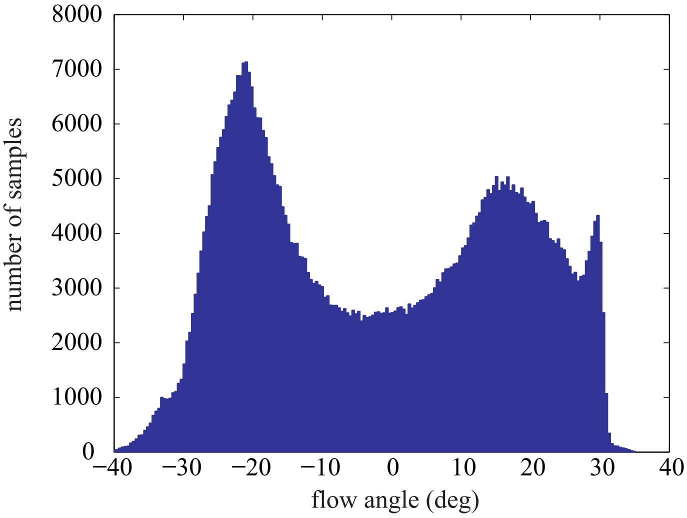

Figure C.6: Histogram of instantaneous angle of attack of velocity vector against THF-probe at center of wake.

velocity-pressure correlation $\overline{up}$.

The phase lag between the total- and dynamic-pressure fluctuations may be attributable to the large fluctuation of the instantaneous angle of attack of the velocity vector which exceeded the range of the acceptance domain of the THF-probe. Figure C.6 shows the histogram of the instantaneous flow angle at the center of the wake evaluated from the instantaneous velocity measured by the THF-probe as

$$\tilde{\phi} = \tan^{-1}\left(\frac{\sqrt{\tilde{v}^2+\tilde{w}^2}}{\tilde{u}}\right). \tag{C.3}$$

The histogram of $\tilde{\phi}$ did not show a symmetric profile with respect to $\tilde{\phi} = 0°$, although it was measured at the wake center; furthermore, a strange peak appeared near 30°. As the limit of the flow-angle range of the acceptance domain was approximately ±35°, the strange peak was attributable to the samples outside the acceptance domain. The phase lag between the total- and dynamic-pressure fluctuations shown in Fig. C.5 may be due to such inaccurate velocity measurement.

Although certain quantitative discrepancy was observed, the measurement results obtained by the combined probe were in qualitative agreement with the reference results. One should note that the time lag between the signals of velocity and pressure was not corrected in this measurement, while the correction was necessary in the experiment described in Chap. 3 to achieve good agreement between the experimental and computational results. The reason of the agreement may be because of the different experimental condition from that of the experiment described in Chap. 3. As the cylinder diameter and the free-stream velocity were twice and half of those in the experiment described in Chap. 3, respectively, the typical time-scale of the fluid motion in the present experiment was four times larger than that in the reference experiment. Therefore, even if a time lag as large as that observed in the reference experiment existed also in the present experiment, the influence should be four times smaller. Hence, the fairly good agreement between the present and the reference results was achieved without the time-lag correction.